Wideband Excitation Signals for Fast Impedance Spectroscopy of Biological Objects

JAAN OJARAND

TALLINN UNIVERSITY OF TECHNOLOGY
Faculty of Information Technology
Thomas Johann Seebeck Department of Electronics

Dissertation was accepted for the defence of the degree of Doctor of Philosophy in Engineering on November 29, 2012.

Supervisor: Professor Mart Min
                 Thomas Johann Seebeck Department of Electronics,
                 Faculty of Information Technology, Tallinn University of Technology

Co-supervisor: Dr. Ing. habil. Uwe Pliquett
                 Institute for Bioprocessing and Analytical Measurement Techniques
                 Heilbad Heiligenstadt, Germany

Opponents: Professor Ørjan Grøttem Martinsen
                 University of Oslo

                 Professor Alvo Aabloo
                 University of Tartu

Defence of the thesis: December 21, 2012

European Union
European Social Fund   Investing in your future

Lairiba ergutussignaalid bioloogiliste objektide kiiretoimelise bioimpedants-spektroskoopia jaoks

JAAN OJARAND

ABSTRACT

Exciting an object with an electrical signal and measuring the reaction parameters yields useful information about the properties of the object or changes to the properties. Electrical impedance characterises the object under study when electrical current and voltage are used as the excitation and reaction (response) signals. Impedance is the measure of opposition to an alternating current impeding the current flow through the object. For the determination of the relationship between measured signal parameters and the characteristics of the object, the equivalent circuit as an electrical model of the object is used. Excitation signal must cover the full range of frequencies in which the values of the elements of the equivalent circuit are changing to fit these values with the electrical model.

When studying single cells, a good quality measurement results have been obtained using intracellular recording or patch-clamp technique. These techniques, however, having considerable impact on the cell, need complicated equipment and are time consuming. Current thesis work considers a situation where the excitation signals are applied and the response signals are collected using electrodes, which are in direct contact with the object or the liquid surrounding it. The later aproach is more suitable for the lab-on-a-chip devices, their developement has been boosted during last decade.

The objective of the thesis is to design efficient excitation signals for the bioimpedance measurements, where single cells and conglomerations of cells are mainly considered as an object. The main criterium of the excitation signal efficiency is the signal-to-noise ratio (SNR) in the response signal achieved in measurements. The second important value is the speed of measurement. Third, the energy efficiency of the excitation signal is also considered to be valuable.

In **the first chapter** an overview of the electrical impedance and bioimpedance (EBI) is given. Equivalent circuit model of the cellular tissue is discussed.

In **the second chapter** the properties of the typical microfluidic device and the main factors which complicate the measurement are described and analysed. First limited amplitudes of the excitation voltage and current are considered. These are caused by several factors, including sensitivity of the object to the excitation level (including temperature sensitivity through warming effect), nonlinearities of the object, impact of the interfacial double layer near the electrodes, safety regulations, limiting constraints to power supply voltages and energy consumption.

The next main complicating factor is the limited measurement time as the properties of the object change or the object itself moves, e.g., cells flowing fast between the electrodes of the microfluidic device. In the last part of the chapter different excitation voltage and current limitations are compared and the conclusions about the properties of suitable excitation signals are drawn. One important observation is that the required properties of the excitation signal differ considerably in the low frequency and high frequency areas. It is also shown that, in the case when the electrodes are very close to each other, a temperature rise due to the heating effect may become a limiting factor to the amplitude of the excitation signal in the high frequency range. The results of the calculations presented in this

chapter show that the rotation of assymmetrically shaped cells will produce a significant variation of measurement readings.

In **the third chapter**, the properties of the wideband excitation signals with a dense distribution of spectral components are analysed. Dependency of the mean RMS value of magnitudes on the number of frequency components and deviations from the mean value are calculated and illustrated. It may be concluded that the mean power spectrum of all signals considered, except the short waveforms, decays almost proportionally to the number of frequency components. A novel nonlinearly modulated short chirp signal with a flat magnitude spectrum and 23% better energy efficiency than comparable linearly modulated chirps is also introduced in this chapter.

In **the fourth chapter** the properties of the wideband signals which may have a sparse distribution of the frequency components are described and analysed. A well-known signal of this class is a multisine waveform (later here as multisine). In the first section of the chapter, a novel method for the minimization of the crest-factor (CF) of the multisine is presented. As in case of other known methods, the computed CF may be guaranteed to be only local optima, however, the systematic variation of the initial parameters, which is possible due to the spare algorithm, ensure the CF value very close to the global minimum.

In the second section of the chapter the properties of the binary multifrequency signals (BMS) and two novel methods for the shaping their spectra are described. The first method is based on enumeration of all possible variations of a waveform, however, unlike with similar methods, the number of variations is significantly reduced (at least 200 times). The second method is based on the use of multisine waveform with the desired frequency components. Unlike other known methods, it uses only one DFT in each step of iteration.

In the third section of the chapter the properties of optimized multisines and BMS with the same spectral distributions are compared and illustrated. The main conclusion is that the mean RMS value of the optimized BMS is always higher than the RMS of similar multisine and this difference increases considerably in case of spectrally sparse distributions.

In the fourth section of the chapter a novel multipart time separated multifrequency excitation signal is presented which is derived from the conclusions of the second chapter. Computer simulation shows that the RMS of two-part excitation signal is around 1.3 times higher than the RMS of the BMS covering the same bandwith.

The sensitivity, resolution and SNR of measurements depend also on the structure of the measurement circuitry and on properties of the parts of it. The mechanical design (design and placement of electrodes, dimensions of the connections, shielding, etc.) influences the results too. A description of the microfluidic device, with a brief discussion of topics mentioned, is provided in the last chapter of the thesis and appendix D. Signal processing of the response signals is out of the scope of this thesis.

KOKKUVÕTE

Uuritav objekt, mida mõjutatakse elektrilise signaaliga, avaldab sellele vastumõju, mille parameetreid mõõtes saame informatsiooni objekti omaduste ja nende omaduste muutuste kohta. Impedants iseloomustab objekti vastumõju objekti läbivale vahelduvvoolule. Objekti omaduste seostamine mõõdetud vastussignaali parameetritega toimub selle elektrilise mudeli kaudu. Selleks, et leida mudelile vastava aseskeemi elementide väärtusi, peab ergutussignaal katma kogu sagedusriba (spektri), kus uuritavad omadused ja muutused avalduvad.

Seni on üksikrakkude impedantsi mõõtmisel häid tulemusi saadud lahendustega, kus mõõteelektroodi sisaldav mikropipett kas torgatakse raku sisse või fikseeritakse rakumembraani pinnal. Nende lahenduste puuduseks on objekti tugev mõjutamine, katse keerukus ja aeganõudvus. Antud töös on lähtutud olukorrast, kus ergutussignaalide rakendamine ja vastussignaalide registreerimine toimub objektiga või seda ümbritseva vedelikuga kokkupuutes olevate elektroodide kaudu. Selline lahendus sobib paremini ka kiip-labori seadmetele, mille arendamine toimub viimasel aastakümnel kasvavas tempos.

Käesoleva väitekirja põhieesmärgiks on tõhusamate ergutussignaalide leidmine bioloogiliste objektide impedantsi mõõtmiseks, kusjuures peamiselt on arvestatud üksikute rakkude ja nende kogumitega. Olulisemaks tõhususe näitajaks on antud juhul mõõtmiste signaal-müra suhe, kuid teise olulise näitajana tuleb arvesse mõõtmiste kiirus. Lisaks on arvesse võetud ka ergutussignaalide omadustega seotud energiatarvet.

Esimeses peatükis antakse ülevaade bio-impedantsi ja selle elektrilise mudeli omadustest ja seostest.

Teises peatükis antakse ülevaade üksikrakkude impedantsi mõõtmise tüüpilisest lahendustest ning mõõtmisega kaasnevatest probleemidest. Esimeseks oluliseks probleemiks on ergutussignaali pinge ja voolu amplituudide piirangud, millel on mitmeid põhjusi: objektides ning elektroodide ja vedeliku liideses tekkivad ebalineaarsused, objektide tundlikkus (sh. soojenemist tekitatud temperatuuri tõusule), ohutusnõuded ning lisaks ka mõõteseadme piiratud toitepinged ja energiatarve. Teiseks oluliseks probleemiks on mõõtmiste aeg, mis on piiratud kas objekti enda omaduste muutuste või ka objekti liikumise tõttu, näiteks rakkude kiire liikumine mõõteelektroodide vahel mikrofluidik-seadme kanalis. Peatüki lõpuosas on võrreldud erinevatest põhjustest tingitud pinge ja voolu amplituudide piiranguid ja tehtud järeldused sobivate ergutussignaalide omaduste kohta. Üks oluline tähelepanek on, et nõuded ergutussignaalide omadustele on madalatel ja kõrgetel sagedustel erinevad. Seejuures on näidatud, et juhul kui elektroodide vahekaugus on väga väike, võib kõrgematel sagedustel signaali amplituudi piiravaks teguriks osutuda ka vedeliku soojenemisest tekkiv temperatuuri tõus. Selles peatükis esitatud arvutuste tulemused näitavad veel, et ebasümmeetrilise kujuga rakkude pöörlemine elektroodide vahel toob kaasa mõõtetulemuste suure varieerumise.

Kolmandas peatükis on analüüsitud lühikese kestusega, tiheda spektriga lairiba ergutussignaalide omadusi. Sealhulgas on pakutud välja uudne, ebalineaarse modulatsiooniga lühike siristussignaal (ingl. k. „chirp signal") mille spekter on

soovitud sagedusribas ühtlasema kujuga kui analoogsetel lineaarse modulatsiooniga siristussignaalidel. Lisaks on uudsel signaalil soovitud sagedusribas oleva energia ja koguenergia suhe kuni 23% parem. Peatükis on võrreldud erinevate tiheda spektriga lairiba ergutussignaalide spektrikomponentide keskväärtuse sõltuvust sagedusribast ning selle keskväärtuse deviatsiooni. Üldjärelduseks on, et uuritud pikemate signaalide spektrikomponentide keskväärtuse võimsustihedus langeb proportsionaalselt sageduskomponentide arvu suurenemisega.

Neljas peatükk käsitleb ergutussignaale, mille spektrid võivad koosneda ka ainult hõredalt jaotatud komponentidest. Tuntud selle klassi esindaja on multisiinus, mis koosneb sinusoidaalsete signaalide summast. Neljanda peatüki esimeses osas on kirjeldatud uudset meetodit multisiinuse tipp-faktori (ingl. k. „crest-factor") minimeerimiseks. Sarnaselt teiste tuntud meetoditega garanteerib ka uus meetod ainult lokaalsete miinimumide leidmise, kuid tänu algoritmi ökonoomsusele saab algparameetrite süstemaatilise varieerimise teel leida ka globaalsele miinimumile väga lähedasi tulemusi.

Neljanda peatüki teises osas on kirjeldatud binaarset multisagedussignaali (BMS) ja esitatud kaks meetodit selle signaali spektri kujundamiseks. Esimese meetodi, mis põhineb signaali kuju variatsioonide läbivaatamisel, uudsuseks, võrreldes varasemate sarnaste meetoditega, on variatsioonide arvu oluline vähendamine (tüüpiliselt üle 200 korra). Teine meetod põhineb soovitavate spektrikomponentidega multisiinuse kasutamisel ning selle eeliseks on algoritm, mis vajab igal arvutustsükli sammul ainult ühte Fourier' teisendust. Peatüki kolmandas osas võrreldakse samade spektrijaotustega optimeeritud multisiinuste ja BMS-ide omadusi. Peamiseks järelduseks on, et optimeeritud BMS-i spektrikomponentide keskväärtus on alati suurem kui vastavate omadustega multisiinuse komponentide efektiivväärtused ning see vahe kasvab hõredamate spektrikomponentide jaotuste korral oluliselt.

Lähtudes teises peatükis esitatud järeldusest, et madalate ja kõrgete sageduste alas on nõuded ergutussignaalidele erinevad, on neljanda peatüki neljandas osas esitatud kaheosalise, ajaliselt eraldatud ergutussignaali näide. Võrreldes ühe, sama sagedusriba katva BMS-ga, on kaheosalise signaali spektrikomponentide võimsused ligi 1,6 korda suuremad.

Viiendas peatükis ja lisas D on lühidalt käsitletud mõõteskeemi üldstruktuuri ja selle osade lahenduste mõju mõõtmiste tundlikkusele, eraldusvõimele ja signaalmüra suhtele. Analüüsitud on ka konstruktiivsete tegurite (elektroodide konstruktsioon ja paigutus, ühendused, ekraneerimine, sümmetreerimine) mõju ning esitatud eksperimentaalse diferentsiaalse mõõteskeemiga mikrofluidik-seadme kirjeldus, mille lahendused põhinevad tehtud järeldustel. Peatüki viimases osa tutvustatakse lühidalt uut kompaktset impedantsi mõõteseadet, kus kasutatakse BMS ergutussignaale. Vastussignaalide töötlust antud töös põhjalikumalt ei käsitleta.

ACKNOWLEDGEMENTS

This work would not have been possible without a support and valuable advice of my colleagues and friends from ELIKO Competence Centre and Thomas Johann Seebeck Department of Electronics of the Tallinn University of Technology. The professional, creative and enthusiastic atmosphere encouraged me to carry on with my studies. There are many people somehow involved in the process of creation of this work. The following is only a very short list: Dr. Raul Land, Dr. Paul Annus, Dr. Toomas Parve, Dr. Toivo Paavle, Dr. Athanasios Giannitsis. Thank you all.

My special thanks go to my supervisor Prof. Mart Min who has greatly supported and adviced me during my studies and my co-supervisor Dr. –Ing. habil. Uwe Pliquett whose great experience guided me into the world of biological cells and cytometry.

I highly appreciate the valuable suggestions done by the Prof. Emeritus Enn Velmre and Dr. Ahto Palm-Leis who have helped to enhance this thesis and made it more readable.

Thank you all once again. It has been a pleasure and honour to have the opportunity to cooperate with you and learn from you.

Finally, I would like to thank my family for the support and understanding that helped me through the exciting but difficult task of writing this thesis.

CONTENTS

ABBREVIATIONS

Frequent abbreviations used in the thesis.

AC	alternating current
BMS	binary multifrequency signal
CF	crest factor
CPE	constant phase element
DC	direct current
DFT	discrete Fourier transform
DSP	digital signal processing
EBI	electrical bioimpedance
FFT	fast Fourier transform
FCI	frequency components of interest
MLS	maximum length sequence
SUT	sample under test
PCB	printed circuit board
PBS	phosphate buffered saline
RMS	root mean square
SNR	signal to noise ratio

1. INTRODUCTION TO ELECTRICAL IMPEDANCE AND BIOIMPEDANCE

1.1 Electrical impedance and electrical bioimpedance (EBI)

1.1.1 Introduction

The first known version of the relationship between applied voltage, body resistance, and flowing current, later called as Ohm's law, was described by Henry Cavendish in 1781. Most of his electrical experiments did not become known until they were collected and published by J. C. Maxwell a century later, in 1879. Cavendish's was experimenting with Leyden jars with different electric potentials and glass tubes of varying diameter and length filled with salt solution. He measured the current by noting how strong was the shock he felt, when closing the loop with his body.

The relationship between the voltage, current and resistance was studied by the German physicist George Simon Ohm and formulated in 1827 (Ohm, 1827). Ohm began his research with the electrochemical cell, invented by Alessandro Volta. Since voltaic piles ecxhibited large changes of voltage in time, it made experiments difficult to repeat. Major breakthrough came probably when Estonian-German physicist Thomas Johann Seebeck discovered thermoelectricity in 1821. G. S. Ohm used thermocouples in his experiments, as they provided a more stable voltage source, (Velmre, 2010), (Geddes, 1996).

Passive electric properties of substances can be analyzed using wireless methods or with direct galvanic contact with the object. In the first case information is gathered from interaction with electromagnetic waves. An object is usually placed near the single antenna, or opened transmission line, between two antennas, inside the waveguide or resonant cavity. Information is in the changes of amplitude and phase of the response signal, polarization and spectral content. Dielectric multi-parameter measurement are required and question arises how to correlate the direct measurement variables at various frequencies and the originally desired information about constituents or properties of material and thus calibrate the instrument (Kraszewski, 2005). This method suits for substances and materials with significant moisture content and the properties of that depend on it. Pure water has a characteristic relaxation frequency of approximately 20 GHz (Kaatze, 2005) and relativly small antennas could be used as the dimensions of the antennas depend on the wavelenght of electromagnetic waves. Hovewer, if only moisture content is a question, lower frequencies could be also used, e.g. 1 MHz was used for moisture determination in wheat, which was placed between the plates of a capacitor (Nelson and Trabelsi, 2011).

The inductive coupling method have been also introduced for measurement and recording of electrical bioimpedance, e.g. (Scharfetter, Lackner, and Rosell, 2001), or (Vedru and Gordon, 2010), where the heart was probed with Foucault currents induced in the cardiac area by high-frequency magnetic fields.

The current thesis deals with a situation where the excitation signals are applied and the response signals are collected using electrodes, which are in direct contact with the object or liquid surrounding it.

Analyzing the electrical response which is caused by the electrical excitation allows one to determine passive electrical properties of an object. In contrast to the passive case, objects can also generate electricity, e.g. heart tissue, and it could be monitored using electrocardiograph (ECG). This, so called endogenic electricity is not a topic of the current work, however, in some cases it can influence the measurements of passive electrical properties.

In case of simple homogeneous samples and fixed measurement conditions passive electrical properties are common for the whole object and they characterize properties of the material, e.g., permittivity ε – a property of a dielectric medium that describes how it affects an electric field; it is determined by how much the material polarizes in response to an electric field. If the object is not uniform, a more cpmplicated electrical equivalent circuit model could represent it. Also variations of the measurement conditions can be reflected in the model, for instance, dependency of the permittivity of the material on the frequency of the electric field. In practise, however, „equivalency" of the model and object is difficult to obtain and it is often far from ideal. As it is briefly discussed in the next section, equivalent circuit models are ambiguous in most cases, i.e. the same property could be modeled with different circuits. In general, when more parametres such as the mobilities of positive and negative charge carriers and generation–recombination parameters are considered several additional ambiguities appear (Macdonald, 2012). Prior knowledge about the nature of the object allows one to choose a more adequate variant and to use simpler models. Elements of the model which have a small influence on the properties of interest can be disregarded. Complexity of the model can be also reduced by fixing of the values of some variables which are less informative.

Determination of the parametres of the elements of the electrical equivalent circuit model allows one to describe electrical properties of an object. The real goal of the measurements, however, is often the determination of other properties which are correlated with the electrical properties of the obejct. Examples: permittivity ε could characterize the moisture content of the material since the permittivity of pure water is high compared to permittivity of other common materials; bio-impedance of the tissue at low frequencies could characterize ischemia since cell edema, caused by the lack of oxygen, constrains the extracellular space and, consequently, narrows the low frequency current path (Gersing, 1998), (Ivorra, et al., 2005). The current thesis is not focusing on correlation issues of the models, though use of proper models is considered.

1.1.2 Impedance and complex numbers

Impedance is the ratio between voltage and current. In general it applies to both direct current (DC) and alternating current (AC) cases however, in case of using AC there are other mechanisms impeding the flow of current besides the resistance to

DC, the induction of voltages in conductors self-induced by the magnetic fields of currents (inductance) and the electrostatic storage of charge induced by voltages between conductors (capacitance). The impedance $\dot{Z}$ caused by these two effects is collectively referred to as reactance X, which forms the imaginary part of complex impedance whereas resistance R forms the real part. Usage of complex numbers results in following equation:

$$\dot{Z} = R + j\dot{Z} = \operatorname{Re}\dot{Z} + j\operatorname{Im}\dot{Z} \tag{1.1}$$

where j is the imaginary unit defined as $j = \sqrt{-1}$ The lenght of the vector $|\dot{Z}|$ (also named magnitude and modulus) can be calculated as

$$\left|\dot{Z}\right| = \sqrt{\operatorname{Re}\dot{Z}^2 + \operatorname{Im}\dot{Z}^2} \tag{1.2}$$

and phase angle as

$$\varphi = \arctan(\operatorname{Im}\dot{Z} / \operatorname{Re}\dot{Z}) \tag{1.3}$$
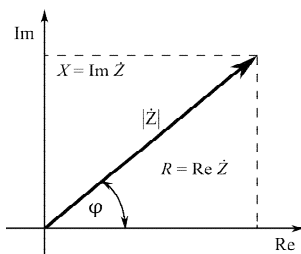

Figure 1. The impedance vector and its real and imaginary parts

In the case of biological objects inductancies are usually very small which allows to neglect them in eletrical models. Since the reactance of the capacitance C is expressed as $\operatorname{Im}\dot{Z} = -1 / j\omega C$ the phase angle φ is negative. In phasor diagrams for capacitive circuit it is convenient to mirror the image over the real axis and denote it with a − sign near imaginary axis. The $\omega = 2\pi f$ denotes the angular frequency.

1.1.3 Wessel diagrams of the simple RC circuits

Considering a simple circuit, R and C in series, impedance can be expressed as $\dot{Z} = R - 1 / j\omega C$. If $\operatorname{Re}\dot{Z} = R$ and $\operatorname{Im}\dot{Z} = -1 / j\omega C$ are known for a single frequency it is possible to calculate impedance $\dot{z}$ at any frequency, since impedance values on a complex plane fall on a strait line parallel to the imaginary axis at a distance of R from it, starting at $-j\infty$ ($\omega = 0$) and ending at the real axis at R when $\omega = \infty$ (Fig. 2a). If R and C are connected in parallel, impedance can

also be calculated at any frequency and impedance values draw a semicircle in a complex plane as it is shown in Fig. 2b.

These diagrams are called Wessel diagrams after the Norwegian mathematician Caspar Wessel. He was first to publish this suitable presentation of complex numbers in 1797. However, the same presentation is often called Argand diagram instead, since Wessel's paper, written in danish, went unnoticed until 1897. Carl Friedrich Gauss derived the same geometric representation of complex numbers in 1796, but it went unpublished until 1831 (Merino, 2006). Use of the terms Nyquist diagram or Nyquist plot is also common.
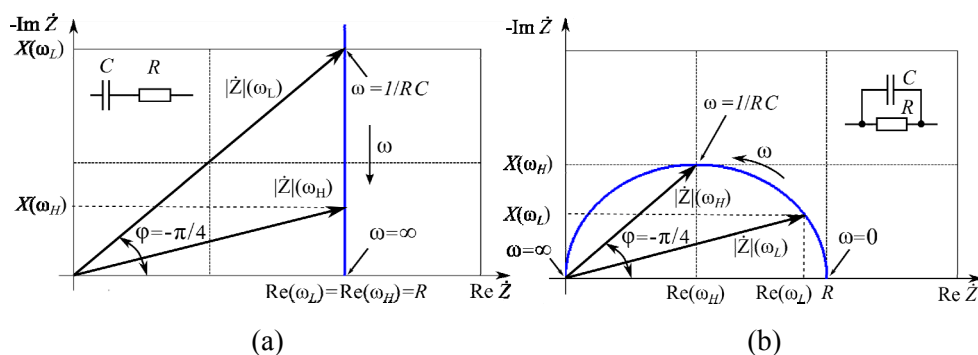

Figure 2. Wessel diagrams of the series *RC* circuit (a), and parallel *RC* circuit (b); two vectors of the complex impedance at lower frequency ω_L and higher frequency ω_H are shown for both cases

If it is not known whether the connection is series or parallel, the situation is slightly more complicated. In case where the resistance of the series circuit is equal or grater than the resistance of parallel circuit, both the values of *R* and *C* and the connection mode of the circuit could be found by one measurement (Fig. 3a). If this exceptional condition is not fulfilled, there will be intersection of the impedance curves as illustrated in Fig. 3b.

At the intersection points impedances of the serial and parallel *RC* circuits are equal. Equivalent values of *R* and *C* for the serial and parallel circuits exist for every single frequency. As a consequence, to determine the connection mode at least two impedance values at different frequencies are needed.

The situation gets more complicated if additional elements are included. Wessel diagram in Fig. 4a illustrates two configurations with one additional resistor, *2R-1C*, and Fig. 4b two configurations with one additional capacitor, *2C-1R*.

Values of the elements can be recalculated for the same impedance for both configurations. Matching of the impedances is achievevable for all frequencies, unlike in case of two element *RC* circuits, and Wessel diagrams are the same for both equivalent configurations. Values of the elements shown in Fig. 3 and 4 are illustrative and can be recalculated for different initial ratios.
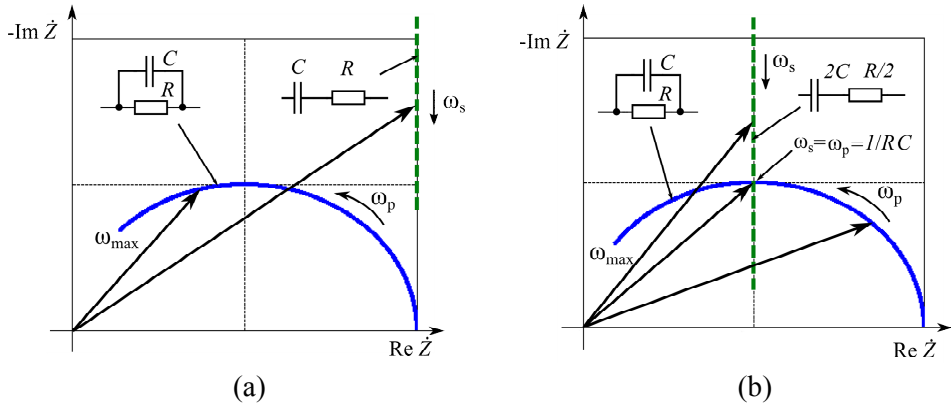
Figure 3. Wessel diagrams of the series (dashed line) and parallel *RC* circuits (solid line) for the different ratios of the values of *R* and *C*
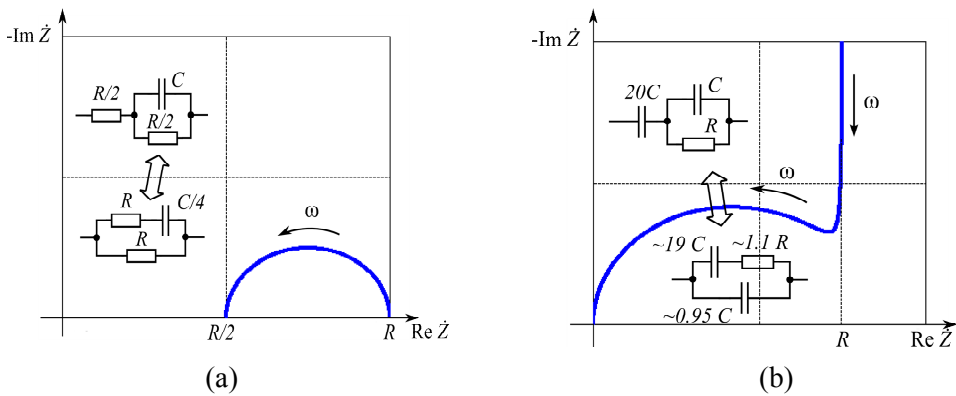
Figure 4. Wessel diagrams of equivalent *2R-1C* circuits (a) and *2C-1R* circuits (b)

Excact configuration of the three element *RC* circuit can not be found even measuring impedance at multiple frequencies however, if the configuration is known, impedance values at multiple frequencies are still necessary for calculating of values of all *RC* elements.

Electrical models of real objects consist usually more than three componets, and the interpretation of measurement results becames harder. Even so, undestanding of the reaction of the circuits with two and three *RC* componets is useful since more complicated circuits can be often simplified to these elementary cases. For instance, living tissue can be modeled as a conglomeration of three element *RC* circuits connected in series and in parallel. However, as it is briefly discussed in the next sections, in some cases electrical models of the objects may consist elements which differ from ideal *R* and *C*.

Instead of impeding it can be interpreted that certain objects or substances are admitting current. Admittance is an inverse of the impedance $\dot{Y} = 1 / \dot{Z} = \operatorname{Re}\dot{Y} + j\operatorname{Im}\dot{Y} = G + jB$, where G is conductance, and B susceptance. As admittance is just the reciprocal of impedance it contains the same amount of data, however, in some calculations it is easier to use impedance terms while in other calculations admittance is more convenient. It is also pointed out in (Grimnes and Martinsen, 2008) that presentation of the data should agree with the nature of the object. Resistance R is not the inverse of conductance G, and reactance X is not the inverse of susceptance B, therefore, by choosing either of these two expressions, a physical model of the process involved is inevitably selected at the same time. Immittance is the combined term for both impedance and admittance.

1.1.4 Bode plots

Instead of using Wessel diagrams, there are other ways to present impedance data at different frequencies. Magnitude of the impedance $\left|\dot{Z}\right|$ in decimal logarithmic scale and phase angle φ can be plotted versus the decimal logarithm of frequency. Such plots are called Bode plots after Hendrik Wade Bode who devised this method in the 1930s for graphing gain and phase-shift plots.

In Fig. 5 and Fig. 6 PSpice modeling results of the *4R-2C* circuit (Fig. 5a) are presented. As seen in Fig. 5b, only half of the points are located in the main part of the diagram. The rest of the points are concentrated near both ends of the curve and are not separable in this scale. Nonuniform distribution of the frequency points leads to the roughness of the curve in the middle part of the diagram.

(a)   (b)
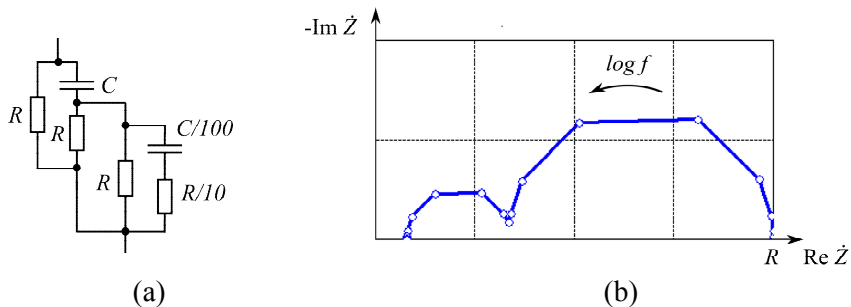
Figure 5. *4R-2C* circuit (a) and its Wessel diagram (b); R = 10 kΩ, C = 2 nF and 20 frequency points from 10 Hz to 1 GHz are used

In the Bode plot Fig. 6a all frequency points are well distinguishable. However, since the phase plot uses nonlogarithmic scale, more points are nessessary for obtaining a smooth curve. Replacing the phase data with an imaginary part data allows to get best result in the current situation as it is illustrated in Fig. 6.b.

(a)   (b)

Figure 6. Bode plots of the impedance using magnitude and phase (a), real and imaginary components (b); parameters of the circuit and the frequency range are the same as in Fig. 5

Wessel diagrams provide compact presentation of impedance data, Bode plots with several graphs, however, can present more information.

1.1.5 Conductors and insulators

Objects can be roughly classified as conductors and insulators according to their electrical properties. In the classical meaning dielectric is a perfect insulator which is not conducting and allow static electric fi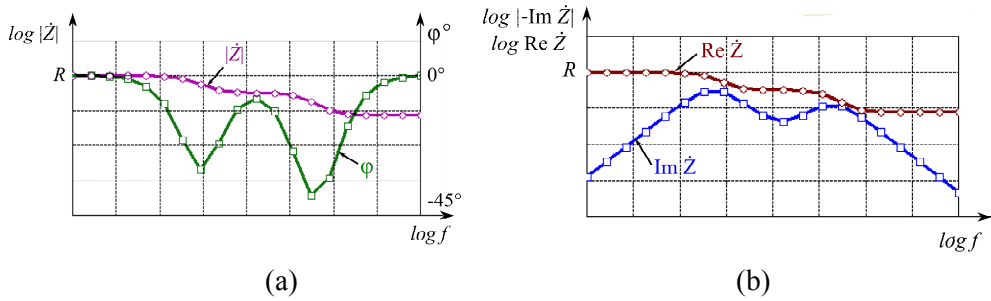eld to penetrate it. Ideal conductors to the contrary do not allow static electric field penetration. Real objects are neither perfect insulators nor perfect conductors. The permittivity ε – a property of a dielectric medium that determines how well it transmits an electric field is frequency dependent.

Materials can by grouped according to whther the capacitive (displacement) current is larger than the in-phase current, $\omega C > G$ or $f > \sigma / 2\pi\varepsilon$, where G is conductance and σ is conductivity. According to this definition, saline solution ($\sigma = 1$ S/m, $\varepsilon = 80 \times 8 \times 10^{-12}$) is a conductor for $f < 250$ MHz and a dielectric for $f > 250$ MHz. This definition is frequency dependent. More generally material can be classified as a dielectric if it has an ability to store energy capacitevly, not only dissipate it (Grimnes and Martinsen, 2008).

1.2   Equivalent circuit model of cellular tissue

1.2.1 Introduction

Electrical properties of tissue can be interpreted in different ways: tissue may be considered as a volume conductor or a dielectric. In the frequency range below 100 kHz most tissues are predominantly electrolytic conductors. However, with high resolution techniques it is possible to extract important capacitive, that is

dielectric, properties even at low frequencies, e.g. 10 Hz (Grimnes and Martinsen, 2008). At higher frequencies the dielectric properties of tissue will dominate.

Herman Schwan, H. Fricke, K.C. Cole, H. Curtis and others (Schwan H. P., 1999) defined three frequency regions α, β and γ of the dielectric properties of biological materials from the observed main dispersions of the permittivity and the conductivity illustrated in Fig. 7.
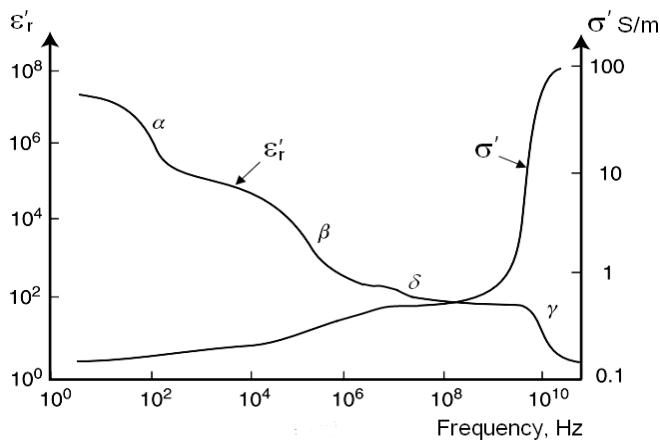

Figure 7. Dispersion regions, idealized. ε_r' is the real part of relative permittivity and σ' is the real part of conductivity; modified from (Grimnes and Martinsen, 2008)

A number of additional dispersions of small magnitude were found later at the tail of the β-dispersion (Stoy, Foster, and Schwan, 1982). This, so called δ-dispersion is caused by proteins, protein-bound water, and cell organelles such as mitochondria. At the highest frequencies tissue properties become more and more equal to that of water. Pure water has a characteristic relaxation frequency of approximately 20 GHz (Kaatze, 2005).

Displacement of charges and the polarization in a material do not occur instantly. If frequency is low then all charges have enough time to change their position, and polarization is maximal. But with frequency increase the polarization and permittivity will decrease. This time dependence may be characterized by introducing the concept of relaxation. Peter Debye used it referring to the time required for dipolar molecules to orient themselves (Debye, 1929). Relaxation time depends on the polarization mechanism. Electronic polarization is fastest, this process occurs on the atomic level when the electric field displaces the electron density relative to the nucleus it surrounds. Large organic molecules like proteins may have a particularly large permanent dipole moment because of the large distance between the charges. Since they are large and with a complex bonding, the rotation and twist can be relatively slow. However, interfacial relaxation may be the most important process and with the longest mean relaxation times of the order of seconds (Grimnes and Martinsen, 2008). Each polarizable entity within the

tissue will exhibit its own characteristic response and thus a distribution of relative permittivities will give rise to a complex function of frequency (Pethig and Kell, 1987):

$$\dot{\varepsilon}(\omega) = \varepsilon_\infty + (\varepsilon_s - \varepsilon_\infty) / (1 + j\omega\tau) \qquad (1.4)$$

where ε_∞ is the high frequency permittivity at which the polarizable entities are unable to respond, ε_s is the low frequency permittivity where polarization is maximal, and τ is the characteristic relaxation time of the tissue under study.

1.2.2 Origin of α-dispersion

Although α-dispersion of biological tissues was observed early, in 1950 (Schwan H. P., 1999), direct studies on the tissues were difficult. There are several theories and assumptions about the origin of the α-dispersion. Gerhard Schwartz (Schwartz, 1962) used theories of electric double layers to describe the measured α-dispersion of particle suspenions. He considered the case where counterions are free to move laterally but not transversally on the particle surface. When an external field is applied, the system will be polarized since the counterions will be slightly displaced relative to the particle. The reestablishment of the original counterion atmosphere after the external field is switched off will be diffusion controlled, and this will lead to a permittivity dispersion. Schwarz's theory was successfully accounted for the amplitude of the dispersion by (Foster and Schwan, 1989). It was also proposed (Fatt and Falck, 1964) that the measured α-dispersion of muscle cells originates from polarization of the entrance of these channel systems. This was discussed by (Foster and Schwan, 1989), (Schwan and Takashima, 1991) who concluded that probably both the polarization of the channel system and counterion polarization at the cell surface were responsible for the α-dispersion. Tissue is anisotropic medium because of the orientation of cells, macromembranes, and organs. In some tissues, such as the myocardium, cells are electrically connected through gap junction channels. Gap junctions channels are physical structures formed by large proteins on the bilayer lipid membrane that connect the intracellular media of adjacent cells (Ivorra A. , 2003). These gap junctions can produce an α-dispersion in some tissues, e.g., in porcine liver at about 7 Hz, which vanishes when the gap junctions close (Gersing, 1998). Antoni Ivorra's modelling results with his *Bioimpedance Simulator* agree with this theory.
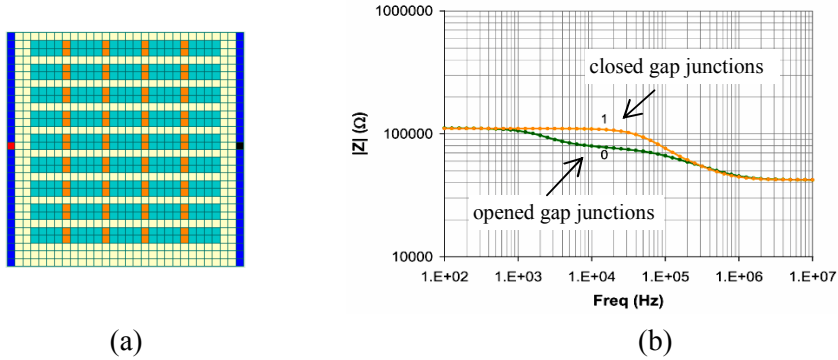
(a)   (b)

Figure 8. Model map of the tissue sample with gap junctions (a) and Bode plots
of the impedance magnitude (b); gap junctions are marked with orange squares
and electrodes with blue lines; adapted from (Ivorra A. , 2003)

In the simulation the following parametres were used: pixel size 25 µm × 25 µm,
slab thickness 20 µm, electrode resistivity 0 Ω cm, intra- and extracellular resistivity
100 Ω cm, membrane capacitance 1 µF/cm^2, gap junctions resistance
1 Ω cm^2 ⇒ 100 Ω cm^2, gap junction separation 1 µm.

In recent experiments by Grimnes and Martinsen using non-invasive Ag/AgCl
surface electrodes with different segments of living human body, α-dispersion was
found in all cases, whereby large alpha dispersions were found where the distance
between the electrodes and muscle masses was small. Centre frequencies of the
α-dispersion were in the range from 6 to 100 Hz. Previous experiments with fish
muscles have demonstrated that α-dispersions are the first to disappear when tissue
dies (Grimnes and Martinsen, 2010).

1.2.3 Origin of β-dispersion

The β-dispersion is mostly due to membrane systems, which separate regions
having different dielectric constants and electrical conductivities, resulting in an
interfacial polarization causing Maxwell-Wagner type relaxation.The accumulation
of charges of opposite sign on both sides of the interfaces create large induced
dipole moments. (Schwan and Takashima, 1991) calculated Maxwell-Wagner
β-dispersion parametres for typical cell suspensions using two cell sisez (with the
radiuses 1 μm and 10 μm) and got dispersion of a large magnitude at frequencies
between 0.1 to 10 MHz. Centre frequency of the β-dispersion region was inversely
proportional to the size of cells.

1.2.4 Recent models of dielectric response of cell suspensions

Recently (Prodan, Prodan, and Miller, 2008) have developed a model that takes into
account the presence of a charge distribution at both the cell membrane interfaces.
In the case of spherical cells, authors have given an analytical solution for the

dielectric response, which accounts for both the α- and β-dispersions. Analysis show that the conductivities of the medium and of the intracellular fluid control the length of the beta plateau, while the membrane thickness controls the height of the beta plateau. In the alpha region, the membrane potential controls the height of the alpha plateau while the mobility of the surface charges accumulated at the cell's membrane controls the length of the alpha plateau. It is pointed out that, for a given cell concentration and geometry, the low-frequency alpha dielectric response correlates with the magnitude of the cellular membrane potential. Authors suggest also to use dielectric spectroscopy for the label free and non-invasive monitoring of membrane potential.

Most of the biological cells have a geometry that deviates from a spherical. (Di Biasio, Ambrosone, and Cametti, 2010) extended the model of Prodan et al. to nonspherical cells, in particular to ellipsoidal cells, both for prolate and oblate shape. Authors have derived a general analytical solution for a biological cell suspension in the presence of both the α- and β-dispersions without the restriction of negligible small membrane conductivity. It is rather difficult to extract α-dispersion effect from the measurement data since in aqueous solutions electrode polarization effect overshadows it. As a consequence, dielectric analysis of biological cell solutions is mostly limited to the β-dispersion area, ignoring the fact that at lower frequencies also α-dispersions occurs. Authors have pointed out that this may not be completely correct since the two dispersions, even if falling in well-separated frequency ranges, influence each other. A certain degree of mutual influence exists, especially for a value of the membrane conductivity of $\sim 10^{-8}$ to 10^{-9} S/m .

1.2.5 Cole-Cole equation and constant phase element (CPE)

A simplified electrical model of the tissue and its equivalent circuit is shown in Fig. 9. At low frequencies excitation current flows through the extracellular space since the reactance of the cell membranes is high. At high frequencies excitation current flows also throw the cells since the reactance of the cell mebrames becomes low. Three-element *2R-C* equivalent circuit, Fig. 9b is known as Cole type B circuit. Experimental evidence collected by Kenneth S. Cole and Robert H. Cole show that the correct description of the complex permittivity of many objects cannot be achieved using eqn. (1.4). It was found that the locus of the complex dielectric constant in the complex plane is a circular arc with endpoints of the axis of reals and center below this axis and an empirical equation representing the situation was proposed (Cole and Cole, 1941):

$$\dot{\varepsilon}(\omega) = \varepsilon_{\infty} + (\varepsilon_S - \varepsilon_{\infty}) / (1 + j\omega\tau_S)^{1-\alpha} \qquad (1.5)$$

Symbols ε_0 an τ_0 of the original equation are replaced here with ε_S and τ_S for the compatibility.

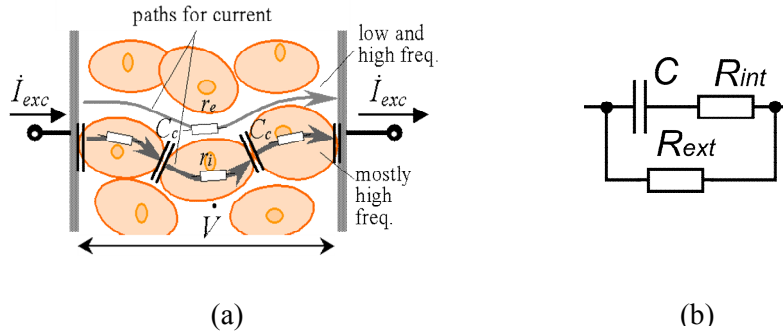(a)   (b)

Figure 9. Essentials of formation of the EBI (a), and the 3-element equivalent circuit (b); adapted from (Min, Parve, Annus, and Paavle, 2006)

Many works are concerned with the meaning of α and the resulting equivalent circuits. The Cole–Cole equation presupposes usage of so-called constant phase element (CPE). The impedance of this element is usually called Warburg impedance after Emil Warburg who is credited with the first solution to the diffusion equation at the boundary, which is related to the diffusional (or mass transfer) impedance of electrochemical systems. The boundary is usually considered to be an electrode - electrolyte interface, however, it is also stated that the appearance of the Warburg-like impedance can be attributed to the action of the more mobile or more-reactive species in screening the applied electric field, allowing diffusion to dominate the motion of the remaining species (Franceschetti and Macdonald, 1979).

As already noted in the description of the α-dispersion, electric double layers can appear also around the particles, which are placed in suspensions.

(a)   (b)
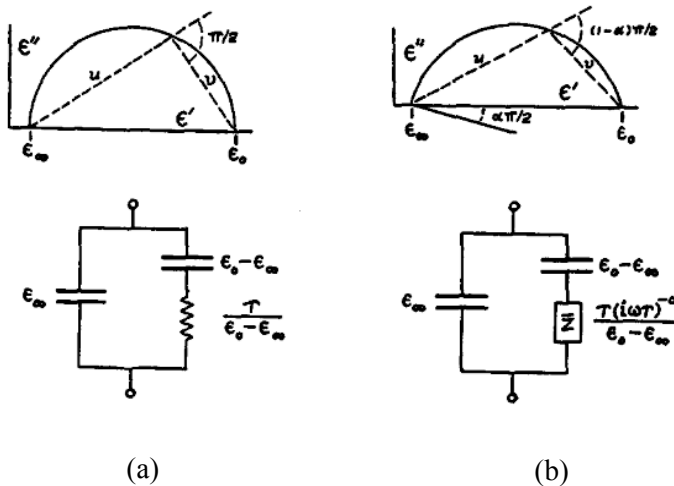
Figure 10. Theoretical complex plane loci of the complex dielectric constant and equivalent circuits for dielectrics; Debye theory (a), and as required by experimental evidence (b); adapted from (Cole and Cole, 1941)

The Warburg impedance is a complex quantity having equal real and imaginary parts, its magnitude proportional to the reciprocal of the square root of the frequency:

$$| \dot{Z}_W | = A_W / \sqrt{\omega} \qquad (1.6)$$

where A_W is the Warburg coefficient which can be calculated using equations presented for instance in (Pliquett, et al., 2010).

Warburg impedance is represented by a straight line at 45° to the axis in the Wessel diagram. It must be noted that Warburg impedance was initially defined for the infinite thickness of the diffusion layer. A more general finite length Warburg impedance does not have the same constant phase character (Macdonald, 1987) and in more general representation the admittance of the CPE can be expressed as

$$\dot{Y} = k(j\omega)^{\alpha} \qquad (1.7)$$

where $0 \leq \alpha \leq 1$ and k is a coefficient. In the form of impedance it can be rewritten as

$$\dot{Z} = 1 / \dot{Y} = 1 / k(j\omega)^{\alpha} \qquad (1.8)$$

The impedance locus of the CPE in Wessel diagram is a straight line at an angle of $\varphi = \alpha(-\pi / 2)$ to the real axis. If the coefficient $\alpha = 1$ then the impedance of the CPE equals to the impedance of the capacitor and if $\alpha = 0$, then CPE behaves as a resistor. Please note that the fractional power term of the CPE α, and α-dispersion belong to different categories. In case of measuring impedance of the tissue with microelectrodes the value of α could be around 0.8 (Mercanzini, Colin, Bensadoun, Bertsch, and Renaud, 2009).
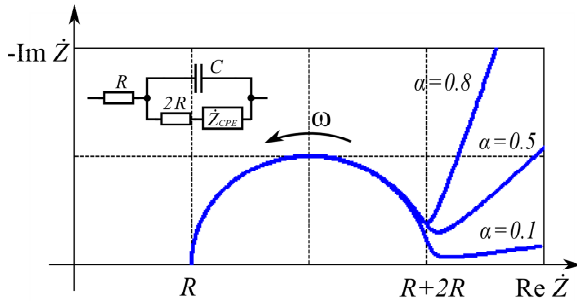

Figure 11. Wessel diagram of the equivalent *2R-1C* circuit
with CPE and different values of α

It is shown in (Grimnes and Martinsen, 2008) that by defining $(\varepsilon_S - \varepsilon_\infty) = \Delta\varepsilon$, the Cole–Cole equation (1.5) may equally well be written as equivalent capacitance equation:

$$C = C_\infty + \frac{\Delta C}{1 + (j\omega\tau_0)^{1-\alpha}} \qquad (1.9)$$

and use of permittivity implies that the model is changed from regarding tissue as a conductor (*2R–1C* model) to regarding tissue as a dielectric (*1R–2C* model). Since with fixed component values these two equivalent circuits cannot be made to have the same frequency dependence, the Cole-Cole model contradicts with the structure of the tissue (Fig. 9). An improved alternative model is already proposed by Grimnes and Martinsen (Grimnes and Martinsen, 2005):

$$\dot{Z} = R_\infty + \frac{1}{G_{var} + G_1(j\omega\tau_z)^\alpha} \qquad (1.10)$$

Here τ_Z is a free variable (nominal time constant) but conductancies G_1 an G_{var} are not, $G_1 = G_{var}$. The time constant as a dependent variable is expressed by eqn. (1.11) where τ_{Zm} is the time constant changing with changing conductance. If G_{var} increases, the time constant τ_{Zm} decreases in accordance with relaxation theory:

$$\tau_{Zm} = \frac{1}{\omega_{Zm}} = \tau_Z \left(\frac{G_1}{G_{var}}\right)^{1/\alpha} \; or \; G_1 = \frac{G_{var}}{(\tau_Z\omega_{Zm})^\alpha} \qquad (1.11)$$
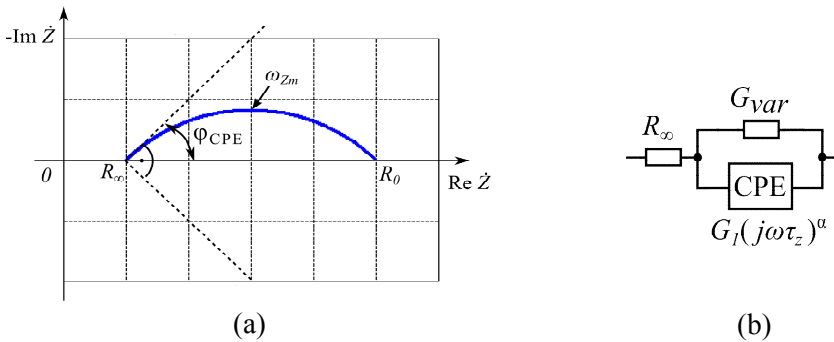
Use of this method is illustrated in Fig. 12.

Figure 12. Example of the Wessel diagram (a) and dispersion model in accordance with eqn. (1.10), (b); parameters R_∞, φ_{CPE} and ω_{Zm} can be found from the shape of the arc and if these values are put into eqn.(1.11), variations in, for example, α and G_1 can be followed separately

The physical meaning of the parameter α is still not clearly undestood. Many authors suggest that it is caused by the heterogeneity of cell size and shape in a living tissue, e.g. (Foster and Schwan, 1989). Random (or pseudorandom) distribution of relaxation times will indeed produce an impedance spectrogram similar to the effect of CPE. For instance, as it is descibed in (Valsa and Vlach, 2011), the parallel connection of series RC branches with recursive parameters offers any phase angle in the range between − 90° and 0°. There are other structures which can provide similar results (Nikovski, 2011). However, as noted by Antoni Ivorra (Ivorra, et al., 2005), to produce α values around 0.8 a very broad distribution of relaxation times would be necessary that cannot be related to the actual heterogenity of tissues in terms of cell size and shape. As an altenative he proposed that the α value is mainly related to the morphology of the extra-cellular spaces which depend on the morphology of the cells.

To measure the electrical impedance of the tissue, impact of the electrodes must be also considered as part of the overall electrical model. Modelling of the properties of the electrodes is discussed briefly in the following chapter.

1.3   Summary of the chapter

In the first introductory chapter the descriptions of electrical impedance and electrical bioimpedance (EBI) are provided.

The limitations of simple *RC* equivalent circuit models are illustrated in the Section 1.1.3 with the Wessel diagrams.

In the Section 1.1.4 it is shown that even though the Wessel diagrams allow compact representation of impedance data, Bode plots with two graphs present more detailed information.

The equivalent circuit model of the cellular tissue is discussed in the second part of the chapter. Origins of different dispersion areas of EBI and the *constant-phase element* (CPE) are discussed.

2. INTRODUCTION TO THE IMPEDANCE CYTOMETRY AND STATEMENT OF THE PROBLEM

2.1 Equivalent circuit model of impedance cytometry

Measurement of the electrical impedance offers a non-invasive method for counting, identifying and monitoring cellular function. Potential applications are ranging from the simple cell counting and label-free identification of different cell types to detecting changes in cell morphology and physiological properties. Cells solutions, or even single cells, could flow in the channel of the microfluidic device (flow cytometry) or be trapped for continuous recording of impedance data. Comprehensive overview of the microfluidic impedance-based flow cytometry is presented in (Cheung, et al., 2010) and in (Sun and Morgan, 2010) for the single-cell microfluidic impedance cytometry.

Description of the microfluidic device with a differential front-end circuitry which was designed during PhD studies is presented in appendix D.

2.1.1 Simplified electyrical model of single cell in a microfluidic device

A simplified electrical model of a single cell in suspension between the electrodes and its equivalent circuit is shown in Fig. 13.
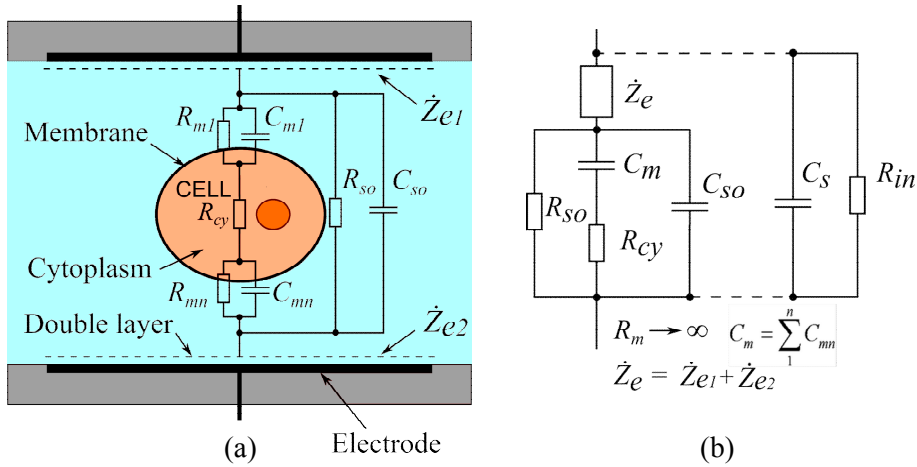
Figure13. Simplified electrical model of a single cell in suspension between the electrodes (a), and its equivalent circuit (b)

C_s is a stray the capacitance of the connections between the electrodes and impedance measurement instrument front-end. This capacitance includes also an input capacitance of the front-end electronics. R_{in} is the input resistance of the measurement circuitry depending on the method and components used. R_m and C_m

are the resistance and capacitance of the cell membrane, respectively. The cell membrane resistance is generally much greater than the reactance of the membrane and is ignored in the equivalent circuit. Likewise, the capacitance of the cell cytoplasm is also ignored since its reactance is usually very small compared to the cell cytoplasm resistance R_{cy}. The value of the cell membrane resistance is between $1 M\Omega$ μm^2 to 100 $G\Omega$ μm^2 and the typical capacitance around $0,01$ $pF/\mu m^2$ (Borkholder, 1998). If the diameter of the cell $d = 10$ μm, then $C_m \approx 3$ pF. For the same cell size typical value of R_m is reported to be 100 MΩ (Sun, Bernabini, and Morgan, 2010). In certain cases, the cell membrane conductance and cytoplasm capacitance cannot be ignored and a complete equivalent circuit model must be used. The cell contains organelles (nucleus, mitochondrions and others) which could produce δ-dispersion at the tail of the β-dispersion as it was mentioned in the Section 1.2 (see Fig. 7).

R_{so} and C_{so} are the bulk resistance and capacitance of the suspension between the electrodes, respectively, approximate values of which can be calculated as

$$R_{so} = 1/G_{so} = k_g / \sigma \tag{2.1}$$

$$C_{so} = \varepsilon_r \varepsilon_0 / k_g \tag{2.2}$$

where G_{so} is the conductance in S (Siemens), σ is conductivity in S/m, ε_r is the relative permittivity of the solution, ε_0 is the permittivity of free space (8.854×10^{-12} F/m) and k_g is the geometry factor of the measuremet chamber (also called cell constant). For the simple measurement chamber geometries like plane parallel plates $k_g = l/A$, where l is a distance between the plates and A is their surface area. For the physiological saline solution $\sigma \approx 1$ S/m and $\varepsilon_r \approx 70$ (Grimnes and Martinsen, 2008). Using values $l = 30 \mu m$ and $A = 200 \times 200 = 4 \times 10^4$ μm^2 as in developed microfluidic device (appendix D), $R_{so} = 750\Omega$ and $C_{so} = 0.83$ pF.

Conductivity of the electrolyte depends on its concentration, and in case of using strong electrolytes (the substances, in aqueous which ionize almost completely into ions) like KCl this relationship is almost linear up to 2 mol/L (Pliquett, 2010). Saline solutions with lower concentration gives lower conductivity, e.g., KCl with concentration 10 mM/L has conductivity 0.14 S/m. The conductivity and permittivity of the electrolyte depend also on chemical compsosition and temperature. The temperature dependence of conductivity of most ions in aqueous solution is about 2.0 %/°C. This high temperature dependence results from the decrease in viscosity of water with temperature. (Grimnes and Martinsen, 2008).

The cell constant calculated as $k_g = l/A$ provide estimate values of the values of R_{so} and C_{so} since the actual electric field extends from the sides of the electrodes and the distribution of it is not uniform there. If more complicated shapes of the electrodes are used, calculations of the shell constant becomes difficult. Therefore, the experimental determination of k_g using a test medium with known electrical properties and fixed environmental conditions is commonly used. Use of numerical simulations like finite element method (FEM), allows to predict and compare the

properties of different electrode shapes. In (Wang, Wang, and Jang, 2010) it is shown, that parallel plate electrodes provide better sensitivity and sensing area in comparison to other shapes.

Substituting a spherical cell with a right parallelepiped equivalent volume, approximate value of the cytoplasm resistance R_{cy} can be easily calculated as

$$R_{cy} = l / \sigma_{cy} A \tag{2.3}$$

where l is a lenght of the sample and A is the surface area. Real biological cells, however, are more similar to prolate spheroids (Di Biasio, Ambrosone, and Cametti, 2010). For a simplification of calculations we can substitute a sphere with a radius r_s with a cylinder of equivalent volume, where d_c is a diamiter, r_c is a radius and h_c is a hight of the cylinder respectivly. Defining a shape factor $k_{sh} = h_c/d_c$ the volumes of the sphere and cylinder are equal if

$$\frac{4}{3}\pi r_s^3 = \pi r_c^2 h_c = 2k_{sh}\pi r_c^3 \tag{2.4}$$

Dividing both sides of the eqn. (2.4) by $4/3\pi r_c^3$ diameter d_c and hight h_c of the equivalent cylinder can be derived as

$$d_c = \frac{d_s}{\sqrt[3]{1.5k_{sh}}} \tag{2.5}$$

$$h_c = k_{sh}d_c \tag{2.6}$$

Substituting a spherical cell with $d = 10$ μm and inner conductivity $\sigma_{cy} = 1$ S/m with a cylinder of equivalent volume (523 μm^3) and different shape factors (Fig. 14), give values of the diameter d_c, hight h_c, and resistance of the cytoplasm R_{cy} shown in Table 1.

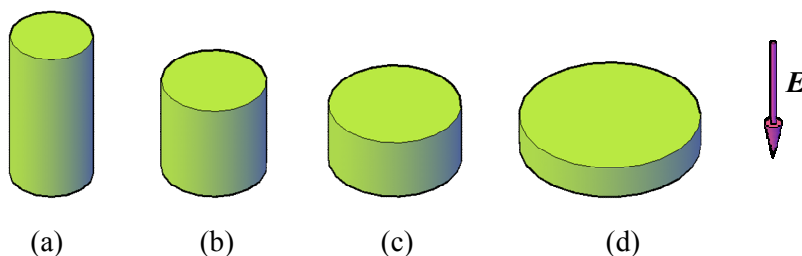(a)   (b)   (c)   (d)

Figure 14. Cylinders with equal volume and different shape factors k_{sh}

The shapes of real biological cells differ also from the shape of the cylinder and in case of nonspherical objects their resistance depends on the orientation in the space between the electrodes. However, calculated values could be used for a rough

estimation of the range of cytoplasm resistance R_{cy}. Here the resistance of a cytoplasm is handled as a resistance of a self-contained volume.

Table 1. Cytoplasm resistance R_{cy} dependence on shape factor k_{sh}

Case	Shape factor, k_{sh}	Diameter d_c, μm	Hight h_c, μm	Resistance R_{cy}, kΩ
a	2.0	6.9	13.9	371
b	1.0	8.7	8.7	146
c	0.5	11.0	5.5	58
d	0.2	15.0	3.0	17
e*	0.25	8.0	2.0	20

* - case e represents simplified shape of a typical human erythrocyte. It is not shown in Fig. 14 since the volume of it is about 10 times less (around 50 μm^3).

2.1.2 Transmembrane potential and characteristic frequency of polarization

A potential difference at the cell membrane generated by the external electric field E of the excitation depends on the shape and size of the cells, on their orientation to the electrical field, on the frequency and strength of the field, but furthermore on the membrane properties and on the conductivities inside and outside the cells.

In (Maswiwat, Wachner, Warnke, and Gimsa, 2007) simplified equations for calculations of transmebrane potentials in ellipsoidal cells of rotational symmetry are provided. Equations for the cylindrical shapes are also derived. In cace where homogeneous electric field E is oriented along axis c (see Fig. 15) maximum membrane potential differences along semiaxis a, $\Delta V_{m,a}$ and along semiaxis c, $\Delta V_{m,c}$ can be calculated as

$$\Delta V_{m,a} = \frac{(a+2c)aE}{(a+c)\sqrt{1+f^2/f_{c,a}^2}} \tag{2.7}$$

$$\Delta V_{m,c} = \frac{(a+2c)E}{2\sqrt{1+f^2/f_{c,c}^2}} \tag{2.8}$$

where E is the external electric field strenght V/m along axis c and f, $f_{c,a}$, $f_{c,c}$ stand for the external field frequency and the characteristic frequency of membrane polarization along semiaxis a and c, respectively. Capacitive bridging decreases the membrane impedance at higher frequencies. Characteristic frequency is defined as a frequency where the transmembrane potential is decreased by a factor of $\sqrt{2}$ or -3 dB compared to the low frequency value (near 0 Hz). Characteristic frequencies

along the semiaxes *a* and *c* can be calculated using following equatiotions given in (Maswiwat, Wachner, Warnke, and Gimsa, 2007):

$$f_{c,a} = \frac{1}{2\pi a \, C_{me}(1/\sigma_i + c/(a+c)\sigma_e)} \tag{2.9}$$

$$f_{c,c} = \frac{1}{2\pi a \, C_{me}(1/\sigma_i + c/(a+c)\sigma_e)} \tag{2.10}$$

where σ_i and σ_e are the internal and external conductivities in S/m. C_{me} stands for the area specific membrane capacitance in F/ m^2.

(a)   (b)   (c)
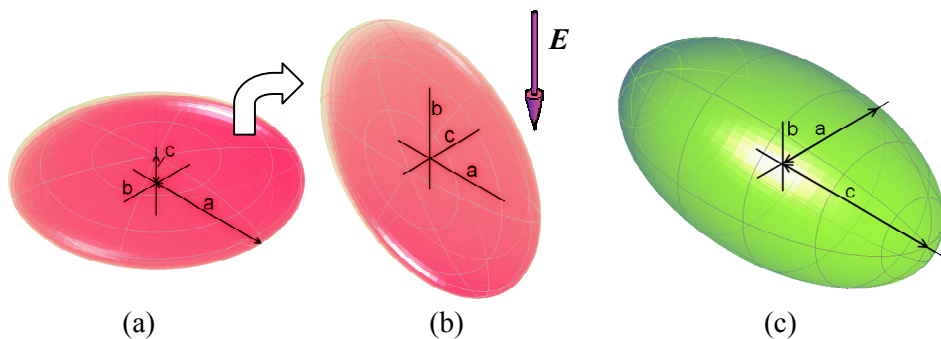
Figure 15. Cells with oblated (a), (b) and prolated (c) ellipsoidal shapes in external electric field *E* ; rotational axis of all shapes is *c*, dimensions along *a* and *b* axis are equal

In Fig.16 Bode plots of maximum membrane potentials for these ellipsoidal cell shapes are shown. Membrane potentials are calculated using eqn. (2.7) - (2.10) and following initial values: internal and external conductivities $\sigma_i = \sigma_e = 1$ S/m, conductivity of the membrane $\sigma_m = 1\times10^{-8}$ S/m, thickness of the membrane $d = 5$ nm, relative permittivity of the cell membrane $\varepsilon_m = 10$, distance between the parallel plate electrodes $l = 50$ μm, excitation voltage applied to the electrodes $V_{ext} = 50$ mV, $C_{me} = (\varepsilon_m \varepsilon_0)/d = 17.7$ mF/m^2 (0.018 pF/μm^2) and $E = V_{ext}/l = 1000$ V/m. ε_0 is the permittivity of free space.

Figure 16. Bode plots of the maximum transmembrane potentials $\Delta V_{m,c}$ of the cells with a shape and direction of the electric field vector shown in Fig. 15; cells (a) and (b) have the same dimensions but cell (b) is rotated 90 degrees around axis a

Cells (a) and (b) represent simplified shape of a typical human erythrocyte with a diameter $d_c = 2a = 8$ μm and thickness $h_c = 2c = 2$ μm. (c) represents typical Chinese Hamster Ovarian (CHO) cell. In reality CHO cells (and many many others) have quiet ir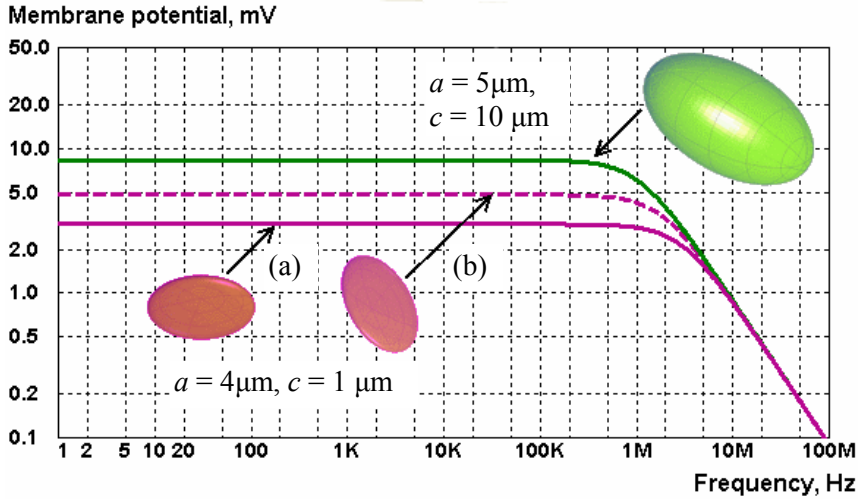regular shape, e.g., as illustrated in (Gözen, Dommersnes, Czolkos, Jesorka, Lobovkina, and Orwar, 2010). In recent research the membrane is found to exhibit fractal behavior which correlates with its capacitance (Wang, Becker, and Gascoyne, 2010). Real human erythrocyte differs also slightly from a disk or oblated ellipsoid, it is biconcave shaped.

Even if the shape of the cell is regular (but not spherical), a maximum membrane potential and its characteristic frequency depends significantly on the orientation of the cell in the electric field. These parametres vary 1.6 times if the cell with oblated ellipsoidal shape shown in Fig. 16 rotates between the electrodes. In case of large geometrical unsymmetry of cells, e.g. muscle fibers, influence of the orientation is large.

Membrane capacitance depends on the cell type. For instance, membrane capacitance of the muscle fibers is stated to be substantially large compared to the membrane capacitance of the typical nerve cells which is around 0.01 pF/μm² (Brown, 2001). Takashima gives 0.07 … 0.1 pF/μm² for the tubular membrane of the sceletal muscle (Takashima, 1985) and Huang 0.09 … 0.11 pF/um² for the frog striated muscle fibres (Huang, 1993).

2.2   Electrodes and electrode-electrolyte interface

2.2.1 Double layer and double layer capacitance

Interfacial impedance of the electrode system is an important part of the electrical model in EBI measurements. When a metal and electrolyte come into contact, a space charge region is formed in the electrolyte at the interface. The atoms at a metal surface in electrolytic contact are ionized that yield a rigid double layer on the surface of the electrode (Helmholtz-layer). The double layer can be interpreted as a capacitor, where one plate is represented by the charges in the metal, and the other by the ions in the solution.
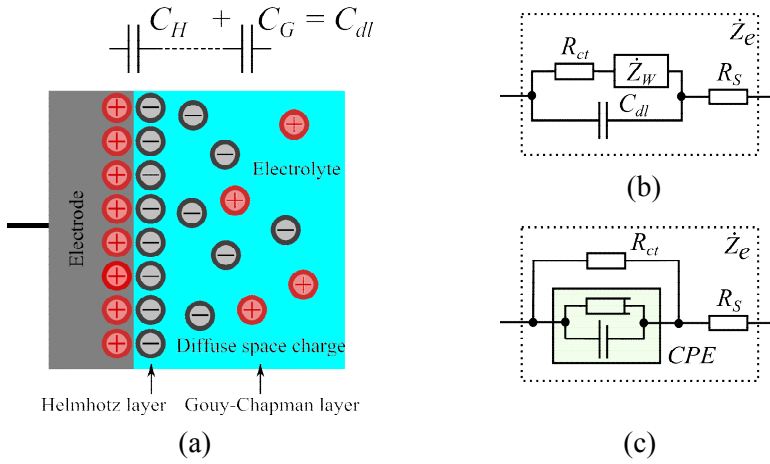
Figure 17. Simplified electrical model of a electrode-electrolyte interface (a) and variants of its equivalent circuit (b) and (c); the meaning of the symbols C_H, C_G, C_{dl}, R_{ct}, R_s and CPE is explained below

The capacitance C_H per unit area (F/m^2) is determined by the relative permittivity of electrolyte ε_r, the area of the interface, and the distance of the outer Helmholtz plane from the metal electrode d_{OHP}:

$$C_H = \varepsilon_0 \varepsilon_r / d_{OHP} \qquad (2.11)$$

The low value of $\varepsilon_r = 6$ for oriented water dipoles at the interface (in practice it can be as high as 78) and an outer Helmholtz plane distance of 0.5 nm (both for physiological saline at 25°C), yielding a lowest Helmholtz capacitance of 0.14 pF/µm^2 (Borkholder, 1998).

The electrostatic forces vanish with increasing distance of ions to the metal but they are sufficient to keep a diffuse layer (Gouy–Chapman layer). The differential capacitance per unit area (F/m^2) can be calculated by:

$$C_G = \frac{\varepsilon_0 \varepsilon_r}{L_D} \cosh\left(\frac{zV_0}{2V_t} \right) \qquad (2.12)$$

where L_D is the Debye lenght, V_0 is the potential at the electrode ($x = 0$, x is the distance from the electrode), z is the valence of the ions (number of electrons involved in the redox reaction) and V_t is the thermal voltage kT/q (here k is the Boltzmann constant, T is the absolute temperature and q is the charge on an electron). For most physiological saline solutions the width of the diffuse layer L_D is below 1nm. As the potential at the electrode is increased, the ions in the diffuse layer are pulled toward the electrode (electrical forces dominate over thermal). This affects the hyperbolic cosine term in eqn. (2.12) resulting in an increase in C_G and the series combination of $C_H + C_G$ becomes dominated by the smaller C_H term. With very low potential (near zero) and dilute electrolyte solutions, the total interfacial capacitance may be dominated by C_G (Borkholder, 1998).

2.2.2 Butler-Volmer equation

The electron transfer at the surface of a metal electrode yields conduction between metal and the electrolyte as described by the Butler-Volmer equation. Using symbols V_t and z described above:

$$I = J_0 A \left(e^{\frac{(1-\beta)z}{V_t}(E-E_{eq})} - e^{\frac{-\beta z}{V_t}(E-E_{eq})} \right) \qquad (2.13)$$

The electrode current I is function of the electrode potential E (measured against the H^+-electrode, also called overpotential), J_0 is the exchange current density (exchange current per unit area) and A is the electrode area. E_{eq} is the electrode potential when the total current is zero, i.e. the electrochemical equilibrium is reached. When $E = E_{eq}$, no chemical reaction takes place and the charge transfer resistance R_{ct} is infinite. Symmetry factor β can be determined from the V/I-slope in voltammetry experiments (Pliquett, et al., 2010). J_0 depends on the material properties of the electrode, the electrolyte composition, resulting oxidation-reduction reaction and is often determined experimentally by measuring the charge transfer resistance around the equilibrium potential of the electrode in the electrolyte of interest. Approximate value of J_0 is 2×10^{-9} A/cm^2 for the gold electrodes in buffered saline (Borkholder, 1998) and 8.5×10^{-8} A/cm^2 is reported for the platinum electrodes (Franks, Schenker, Schmutz, and Hierlemann, 2005).

In Fig. 18 relative current densities calculated using Butler-Volmer equation are shown.
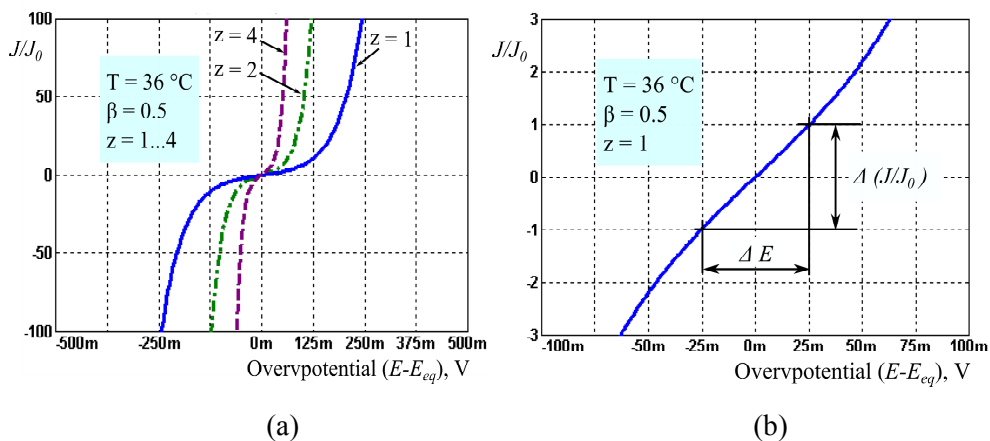
Figure 18. Relative current densities calculated using Butler-Volmer equation for the large overpotential range and different valences of z (a), and for smaller overpotential range (b), where the linear region may be used for charge transfer resistance calculation

If the exchange current density J_0 is known, the charge transfer resistance R_{ct} can be calculated as

$$R_{ct} = V_t / J_0 A z \tag{2.14}$$

For the rectangualr gold plated electrodes with the side lenght $l = 200$ μm ($A = 4 \times 10^{-3}$ cm^2), $z = 1$, $V_t = 26.3$ mV (T=309.15 °K) and $J_0 = 2 \times 10^{-9}$ A/cm^2, approximate value of the R_{ct} is 4 GΩ. This value will decrease in case of larger electrodes or if platinum is used ($z = 4$).

From Fig. 18 it is evident that in case of symmetrical system ($\beta = 0.5$) almost linear behavior can be achieved only then the voltage drop on the electrodes is kept below ± 50 mV. This limiting value will decrease with increasing valence z while increasing with increasing temperature.

2.2.3 Warburg impedance and CPE

When applying AC electric field, ions, as charged particles will move in response to this electric field resulting from varying their spatial concentration. As the frequency of excitation is increased, it becomes more difficult for the ions to follow the field. At sufficiently high frequencies, they are not able to follow the field at all, resulting in this diffusional impedance tends towards zero. This frequency dependent diffusional impedance within the Gouy-Chapman layer is known as a Warburg impedance which is already described in the Section 1.2.5.

In addition to the diffusion of the ions, roughness of the surface of the electrodes plays also an important role in formation of the CPE. Real electrodes are not

perfectly smooth, they have microscopic roughness due to scratches, pits, etc. Moreover, roughening the electrode surface mechanically or by using electrochemical treatments that produce a porous or fractal electrode surface is usually desirable to get a large effective surface area. The impedance of such porous surface may be modeled by an infinite series of parallel R-C circuits. This type of distribution of the relaxation times will lead to the effect of CPE (Lasia, 1999).

In case of smaller electrodes and low overpotential, the charge transfer resistance R_{ct} is high and the Warburg impedance due to the diffusion of ions have small impact. For instance, if $A < 1mm^2$, it is hardly detectable (Pliquett, et al., 2010). Many authors, e.g. (Franks, Schenker, Schmutz, and Hierlemann, 2005), (Mercanzini, Colin, Bensadoun, Bertsch, and Renaud, 2009), (Malleo, Nevill, Van Ooyen, Schnakenberg, Lee, and Morgan, 2010) have excluded the series Warburg impedance and using equivalent circuit Fig. 17c, with R_{ct} and Z_{CPE} connected in parallel. In case where surface of the electrodes is smooth, the phase angle of the imaginary component of this CPE is is usually not -45° degrees (as in case of Warburg impedance) but closer to -90° degrees. The corresponding coefficient α (eqn. (1.7)) is usually between 0.8 to 0.95. As already noted, one possible reason of the constant phase impedance is the roughness of the electrodes. In case of porous electrodes values of $\alpha \approx 0,5$ have frequently been observed, however, for rough electrodes of relatively low roughness factors this approach is inappropriate. In the latter case capacitance dispersion is due to the non-uniformity of the surface atom layer and to specific adsorption and/or adsorption-related processes (Pajkossy, 2005). At higher overpotentials there are limitations to the use of simple model of the CPE (Wang and Pilon, 2012), however, in bioimpedance measurements use of higher ovepotentials is limited anyway.

2.2.4 Spreading resistance

Spreading resistance R_s models the effects of the spreading of current from the localized electrode to a distant counter electrode in the solution and it depends on dimensions of the electrode and measurement chamber. In the case of parallel plate electrodes with a size of measurement chamber $R_s = 0$. In opposite case, where small electrode is in a big chamber, electric field lines will concentrate near to the electrode, thereby creating a high resistance in that region. In the last case spreading resistances for the circular electrode R_{sc} and for the rectangular electrode R_{sr} can be calculated using following equations adapted from (Borkholder, 1998):

$$R_{sc} = 1 / (2d\,\sigma)$$
(2.15)

$$R_{sr} = \frac{\ln(4l / w)}{\sigma\,\pi\,l}$$
(2.16)

where σ is the conductivity of the electrolyte and d is a diameter of the circular electrode, l is lenght and w is width of the rectangular electrode respectivly (in cm).

2.2.5 Limit voltages and currents of linearity

As illustrated in Fig. 18, in case of highly polarizable electrodes made of noble metals such as platinum or gold, the linear part of the transfer characteristic is very limited. To avoid nonlinearities, current through the electrodes is also limited, especially for the microelectrodes, and the impedance of the electrodes at lower frequencies is high. Schwan reported in (Schwan H. , 1968) that the current density through the electrodes has a significant effect on the interface values the system exhibits. The non-linearity will appear in decreased value of the interface resistance and increased value of the interface capacitance with increasing current density. Schwan has also suggested a limit current of linearity, which has been defined as values at which the series equivalent capacitance and resistance of the interface impedance deviate by a certain percent (generally 10%) from their small signal, linear values. For a 1 cm^2 Pt electrode in KCl solution nonlinear range begun from current of 0.4 mA which corresponds to current density of approximately 0.4 mA/cm^2. The measurement frequency used was 100 Hz. Schwan and colleagues also observed that the following empirical relationship of the limit current of linearity i_L is valid over wide frequency ranges:

$$i_L = B\omega^{\alpha} \tag{2.17}$$

where where B is a constant particular to the electrode system, and α is the fractional power which appears in eqn. (1.7). This means that the limiting current of linearity is significantly higher at higher frequencies. In (Ron, et al., 2008) current densities of linearity 0.6 mA/cm^2 and 2.4 mA/cm^2 were measured for the Pt-black electrodes at frequencies 100 Hz and 1 kHz respectively. Measurements were carried out using using parallel-plate electrodes with a surface area of 0.7 cm^2 and conductivity of Dulbecco's Modified Essential Medium (DMEM) around 9 mS/cm. It must be pointed out that the current density depends also on the geometry of the electrodes. Even in case of using parrallel plate electrodes, current density is higher at the edges if the measurement chamber is larger than the electrodes.

At very low frequencies, such that $\omega > 0$, the voltage limit of linearity, V_L, approximates to the voltage at which the charge transfer resistance R_{ct} decreases by a certain percent (generally 10%) from its small signal value and can been calculated using the Butler-Volmer equation as illustrated in Fig. 18. Nonlinearity occurs at $V_L \approx 40/z$ mV, where z is the valence of the ions. The log (f) versus V_L plot is a straight line over a wide frequency range. As the gradient of this straight portion is large, V_L increases only very slightly with frequency (McAdams, Lackermeier, McLaughlin, Macken, and Jossinet, 1995).

2.2.6 Electrodes with increased effective area

Interfacial resistance and capacitance cause changes in the measurement signals. It is therefore important that the values of these components of the model be such that the signal to be measured is not significantly distorted. Electrodes with porous or

fractal surface have an increased effective area which provides a hihger current density and lower impedance due to the increased double layer capacitance. The most common electrochemical method, so called platinum black treatment gives about 200 times large effective area compared to bright platinum, however, poor reproducibility and potential biotoxibility have limited the its use. Other materials such as iridium oxide and conducting polymer – polypyrrole/polystyrenesulphonate (PPy/PSS) have been reported to increase the effective capacitance of the electrode against bright platinum by factors of approximately 75 and 790, respectively (Malleo, Nevill, Van Ooyen, Schnakenberg, Lee, and Morgan, 2010). Approximate effective interfacial capacitance C_{dl} and parameter $α$ of the CPE in phosphate buffered saline (PBS) with conductivity of 1.6 S/m are shown in Table 2.

Table 2. C_{dl} and parameter $α$ of the CPE for different electrode materials *

	Platinum	Platinum black	Iridium oxide	PPY/PSS
C_{dl}, pF/μm^2	0.3	67	22	259
α	0.93	0.74	0.68	0.76

*Adapted from the supplemental material of (Malleo, Nevill, Van Ooyen, Schnakenberg, Lee, and Morgan, 2010).

Carbon nanotube composite coatings with lower impedance have been introduced recently. Tip electrodes with geometrical area of 900 μm^2 had impedance at 1 kHz no more than 25 kΩ (Baranauskas, et al., 2011).

2.2.7 Nonpolarizable electrodes

Electrodes made of noble metals are relatively inert, it is difficult for them to oxidize and dissolve. Thus current passing between the electrode and the electrolyte changes the concentration primarily of ions at the interface. The electrical characteristics of such an electrode show a strong capacitive effect, the charge transfer resistance is high (Neuman, 2000). There are also 'nonpolarizable' electrodes, which use the electrochemical equilibrium between a metal and its hardly soluble salt, e.g. Ag/AgCl. The electrode potential depends on the activity of the counterion but is almost insensitive to the activity of the metal ions. In order to keep the counterion activity constant, the electrode is usually mounted in an extra compartment within a defined electrolytic environment with ionic connection (e.g., glassfrit) to the object. Ag/AgCl- electrode is often used as a reference electrode, for instance, in redox- or ion selective measurements (e.g., pH) or in cyclic voltammetry (Pliquett, 2010). These electrodes have a relativly large value of exchange current density, a very low value of charge transfer resistance R_{ct} and are widely used in sensitive surface bio-potential measurements. However, due to complicated assembly the use of Ag/AgCl in miniaturized electrode systems is limited. In this case it is often easier to expose the silver chloride directly to the SUT (sample under test). However, there are several drawbacks. If the electrolyte is stirred, (e.g., in microfluidic system), AgCl dissolves (Pliquett, et al., 2010). Rapid

degradation of subcutaneously implanted Ag/AgCl electrodes electrodes is also reported (Moussy and Harrison, 1994). Dilute solutions of a variety of silver compounds have strong bacteriocidal properties and in some cases, e.g. in the presence of smooth muscle, could become toxic (Jackson and Duling, 1983). Light changes the properties of silver chloride since it is light-sensitive. Ag/AgCl electrodes could be protected by coating with different polymers (Shinwari, Zhitomirsky, Deen, Selvaganapathy, Deen, and Landheer, 2010), (Pliquett, et al., 2010). However, this influences also electrical properties of the electrodes.

2.2.8 Stability and noise of electrodes

Thermal noise of the electrodes can be calculated following the standard Johnson noise equation for the RMS voltage noise of a resistor:

$$V_{rmsN} = \sqrt{4kT R_N \Delta f} \qquad (2.18)$$

where k is the Boltzman constant ($1.38 \ 10^{-23}$ J/K), T is the absolute temperature in Kelvin, R_N is the real part of the electrode impedance, in ohms, and Δf is the bandwidth of interest.

The electrodes suffer also from electrochemical noises from different origins. Impurities adsorbed by an electrode is one source of noises. However, even if the electrodes are clean, dissimilarity of electrodes will produce some noise. The electrochemical noise of a virtually still interface can reach noise voltage values as high as tens of microvolts up to tens of millivolts (Riistama, 2010).

At hihger frequencies instability in the dc-electrode potential would probaly not disturb the measurements. However, when measuring at low frequency, e.g. below 10 Hz, it can not be negleted. The potential stabilizes with moderate current through the electrode (Pliquett, et al., 2010). In case of measuring biomedical signals from the body surface the noise at low frequencies is much higher than the equivalent thermal noise generated in the impedance of the electrodes and skin. When an electrolyte is applied to the electrode metal, an initially unstable contact potential develops. The RMS value of this noise decreases approximately exponentially in time and stable contact potential is reached within 1 min in case of using Ag/AgCl electrodes. When plain silver or stainless steel is used stabilisation occurs after about 1 to 3 hours (Huigen, Peper, and Grimbergen, 2002). Stabilisation time of five minutes is used for experiments with gold electrodes in PBS solution (McAdams, Jossinet, Subramanian, and McCauley, 2006).

The noise of the electrodes depends on electrode area. It is found that the voltage noise power is characterized by a $1/f^{\alpha 1}$ spectrum in the low frequency range. The value of α_1 is observed to be double that of the CPE coefficient α. The noise resistance is thus inversely related to the electrode area (McAdams, Jossinet, Subramanian, and McCauley, 2006). In that article McAdams and colleagues

suggested that the source of this noise is due to the charge transfer resistance R_{ct}, and that the frequency dependence is due to R_{ct} being connected in parallel with the frequency dependent CPE. Recent studies are confirming this theory (Yao and Gillis, 2012). Use of porous electrode surfaces increases the effective interfacial area and reduces the noise level almost proportionally (Urbanova, Li, Vytras, Yvert, and Kuhn, 2011).

2.2.9 Capacitive electrodes

Insulating electrodes, also known as capacitive electrodes, allow impedance measurement without galvanic contact. In (Cahill, Land, Nacke, Min, and Beckmann, 2011) a sensor that measures the conductivity of the liquid in the capillary using the impedance spectrum over the frequency range rom 1 to 10 MHz is presented.

The advantage of this type of electrodes is the constant capacitive coupling of the sensor electrodes to the solution. However, since the thickness of the insulation is usually much more than the thickness of the Helmholtz-layer in electrolytic contact (which is around 1 nm for the typical physiological saline solutions) a coupling capacitance is low and it can't be increased by increasing the effective surface area as in case of electrolytic contacts. This leads to high impedance values of the electrodes at low frequencies resulting in low sensitivity of measurements of the impedance of the SUT. However, advanced capacitive sensors, e.g. Plessey Semiconductors Electric Potential Integrated Circuit (EPIC) sensors with a coupling capacitance 1 nF and input resistance 20 GΩ allow to cover a frequency range from 0.1 Hz to 10 kHz (Plessey Semiconductor, 2011). The surface area of these sensors is around 1… 3 cm^2. In case of microelectrodes the low coupling capacitance still remains a critical limiting factor.

2.2.10 Bipolar and tetrapolar electrodes

The simplest configuration for impedance measurement is a two electrode interface. In this case impedance of the sample under test (SUT) and the impedance of the electrodes are connected in series (Fig.16 (a)). Since the impedance of the electrodes varies and depends on several factors, this affects the measurent considerably, especially at low frequencies where the impedance of the electrodes could be higher than the impedance of the SUT. One way out is to use electrodes with large effective surface area. The second way is to use separate electrodes for the voltage monitoring and application of current. This method is usually known as the Kelvin, or 4-wire method, however for eliminating of the electrode-electrolyte impedance errors it was first introduced by physicist and inventor Gabriel Lippmann in 1876 (Geddes, 1996).

Since in the tetrapolar system the voltage is monitored with separate electrodes (Fig. 18 (b)), it is almost insensitive to the impedance of the current electrodes. Assuming that the input impedance of the voltage monitoring circuitry is very high and the

voltage monitoring electrodes are identical, tetrapolar electrode system is commonly believed to be immune to the influence from electrode polarization impedance.
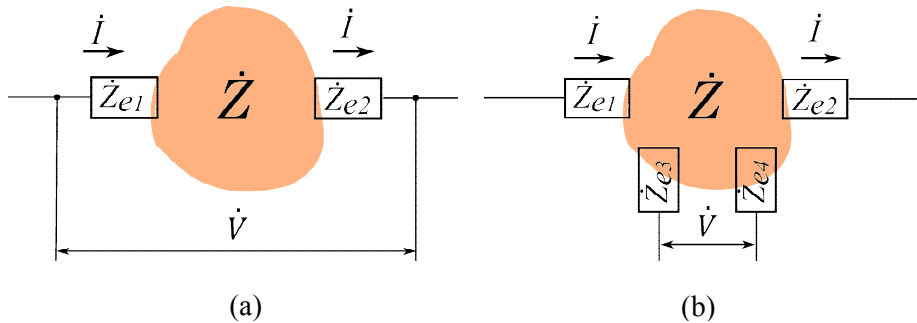

(a)   (b)

Figure 19. Impedance measurement with two electrodes (a), and with four electrodes (b)

However, in practice there are several pitfalls which spoil the idealized situation. At first, both the current source and the potential measuring circuits are not ideally floating, one lead of the current carrying electrodes may be grounded and the voltage monitor inputs are also referenced to the same ground (connection with a dashed line in Fig. 20). Studies of several authors (Grimnes and Martinsen, 2007), (Mazzeo and Flewitt, 2007) show that the parasitic impedances degrade the compensation of the electrode polarization of a tetrapolar interface, especially at hihger frequencies. It is also pointed out that voltages at the inputs of the voltage monitor amplifier are not equal and parasitic impedances Z_{S1} and Z_{S2} yield an asymmetric current at the monitor electrodes (Pliquett, 2010). Symmetrical excitation source, where the potential at the applicator electrodes is complementary with respect to zero allows to minimize these assymetry effects (Pliquett, Schönfeldt, Barthel, Frense, Nacke, and Beckmann, 2011), (Ojarand, Giannitsis, Min, and Land, 2011).

The second pitfall ot the tetrapolar electrode system is that the sensitivity of the impedance measurement depends significantly on the placement of the electrodes. As it is pointed out in (Grimnes and Martinsen, 2007), not only the volume between the voltage monitoring electrodes is measured, but there could be also areas with negative sensitivity (between the current carrying electrodes and voltage monitoring electrodes). Negative sensitivity means that if the impedivity is increased in these zones, lower total impedance will be measured.

Supply source

$\dot{Z}_{e1}$

$\dot{Z}_{e3}$

$\dot{Z}$

$\dot{V}$

Supply source

2

+

+

Diff. amp.

1

$\dot{I}$

$\dot{Z}_{e4}$

−

−

$\dot{V}_{out}$

Supply source

$\dot{Z}_{e2}$

$\dot{Z}_{S1}$

$\dot{Z}_{S2}$

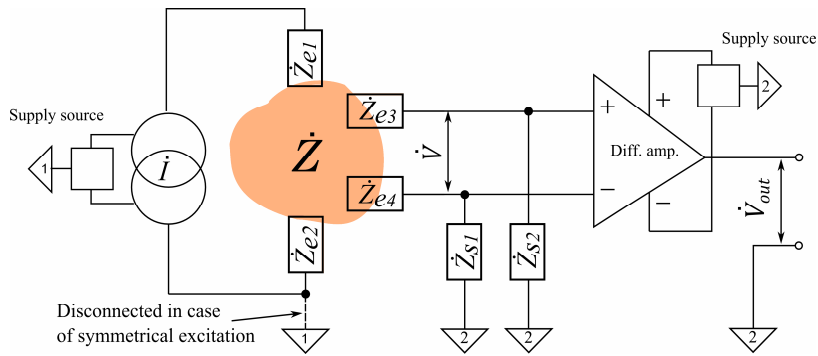Disconnected in case
of symmetrical excitation

1

2

2

2

Figure 20. Simplified equivalent circuit of the tetrapolar impedance measurement system

In case of microfluidic devices it is often hard to find a proper place for the tetrapolar electrode system. Both pairs of electrodes can be positioned collinearly along the same side of the microfluidic channel. A drawback of this coplanar arrangement is that the current density and electric field become very inhomogeneous. If the electrodes, however, are placed opposite each other across both sides of the microfluidic channel, the electric field between the electrodes will be nearly uniform in the middle part of electrodes, good sensitivity and larger sensing area can be achieved (Wang, Wang, and Jang, 2010). In this case, howerer, it is difficult to position the parallel voltage sensing electrodes between the current electrodes as in the classical four-electrode setup since they will disturb the flow of the liquid and cells in the channel. To minimize the values of parasitic impedances it is important to keep the connections as short as possible. Advantage of two-electode system is that it needs less space.

Besides using four electrodes as a classical tetrapolar system, two pairs of electrodes can be also used for a differential measurement. In this case, SUT is placed only between one pair of the electrodes and the second pair of electrodes is used as a reference. If the electrode pairs are identical and have similar placement in the measurement chamber, both, the impedance of the electrodes and the impedance of the liquid surronding the SUT can be compensated. Moreover, also the parasitic impedances can be compensated if fully symmetric measurent circuitry is used as in front-end electronics decribed in appendix D. however, the efficiency of the compensation is limited by the identity of the measurement and reference electrodes and the circuitry connected to the electrodes. Materials of the electrodes, dimensions and properties of the surfaces of the electrodes, and parasitic impedaces connected to the electrodes must be identical for both pairs of electrodes for the total compensation.

2.3   Sensitivity of biological objects

2.3.1 Membrane potential and excitable cells

Biological objects are sensitive to the electomagnetic field. If the excitation signal exceeds some characteristic level, properties of the object could change significantly. Some cells like nerve and muscle cells can react on electrical trigger signals, e.g. the motor nerve axon has voltage gated sodium and potassium channels in the mebrane. Change of the membrane potential in tens of millivolts could change the state of the ion channels of the cell membrane.

If the excitatory stimulus is strong enough, the transmembrane potential reaches the threshold, the critical firing level (CFL), and the membrane produces a characteristic electric impulse, as it is shown in Fig. 21a. An initial depolarization of the cell membrane and opening of sodium channels allows inflow of sodium ions Na^+. This increase in inward current causes further depolarization. Since additional depolarization activates more sodium channels this yield a positive feedback loop which leads to a rapid rise of the current of Na^+ ions. There are also voltage-gated potassium channels that become activated by membrane depolarization, however,
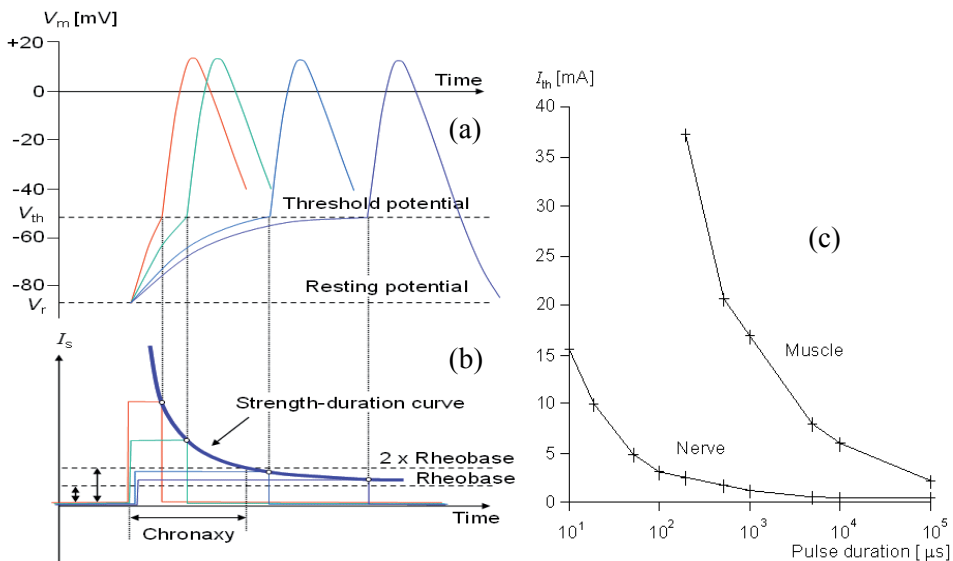

Figure 21. The response of the membrane (a) to various stimuli of changing strength and duration (b) (for simplicity threshold potential is shown to be independent on stimulus duration) and experimentally determined strength-duration relationship dependency for motor nerve and the muscle stimulation (c); adapted from (Malmivuo and Plonsey, 1995)

43

increasing flow of potassium ions K^+ from inside to outside returns the intracellular potential to its resting value. These channels are much slower than voltage gated sodium channels. After the peak of Na^+ current is reached, more slowly.

Once activation has been initiated, the membrane is insensitive to new stimuli, no matter how large the magnitude. This phase is called the absolute refractory period. Near the end of the activation impulse, the cell may be activated, but only with a stimulus stronger than normal. This phase is called the relative refractory period (Malmivuo and Plonsey, 1995)The polarized cell is positively charged at the external cell surface. Some negative charge, in order of 0.5 pC is needed to recharge a single cell to approach the firing level. Since with extracellular electrodes there is no direct access to the cell interior, the current density near the cell surface is therefore the basic parameter.

A pacemaker pulse is also given as current and pulse duration, that is in reality an electric charge (Grimnes and Martinsen, 2008). The level of current strength which will just elicit activation after a very long stimulus is called rheobase. The minimum time required for a stimulus pulse twice the rheobase in strength to trigger activation is called chronaxy (Fig. 21.b).

A current from an external current carrying electrode in the order of 2 mA during 1 ms is needed to stimulate a motor nerve and above 15 mA for a muscle during the same time as it is shown in Fig. 19c (Malmivuo and Plonsey, 1995). These current values illustrate a relative sensitivity of different cells. Real thresold current depends on the type and dimensions of the cell as well on the distance of the electrodes. In (Gustafsson and Jankowska, 1976) a stimulus thresold current around 5 µA with duration of the pulses 0.2 ms at near soma positions is reported for the motoneurones and spinal border cells of the cat. Stimulus thresold current around around 10 µA was recorded at near-dendrites positions about 150 µm away. Duration of the pulses in these experiments was 0.2 ms. In (McIntyre and Grill, 2002) a stimulus amplitude of 35 µA with duration of the pulses 0.1 ms is reported for the somatic motoneurons controlling external urethral sphincter (EUS), with its cell body near the electrode.

At higher frequencies of the stimulation pulses cell membranes are not able to react in a regular way. As it is reported in (Tai, de Groat, and Roppolo, 2005) a nerve membrane conduction can be blocked when the stimulation frequency is above 4 kHz. In this article it is concluded that the activation of potassium channels, rather than inactivation of sodium channels, is the possible mechanism underlying the nerve conduction block. At frequncies from 4 to10 kHz a block thresold current increases from 7 mA to 20 mA when distance of the electrode from the nerve axon is 100 µm.

In the frequency range between 4 and 64 MHz reversible deformation of the muscle fibre membrane was observed with excitation voltage of 100-400V at the distance of electrode about 50 µm. Such deformation was accompanied by a membrane depolarization and an increase of cytosolic free calcium (Dal Maschio, Canato, Pigozzo, Cipullo, Pozzato, and Reggiani, 2009). Unfortunately not much information is available about the relationship of the low level excitation current and the cell behavior in the MHz range.

2.3.2 Membrane electroporation (MEP)

When sufficiently high electric field is applied to the cell, nano-pores develop in the cell membrane also in case of non-excitable cells (cells without voltage gated ion channels). Electroporation can be either reversible or irreversible, depending on parameters of the electric signal. It is stated that MEP is a threshold phenomenon: the induced transmembrane voltage imposed by external electric field should reach a critical value between 200 mV and 1V to trigger formation of transient aqueous pores in the cell membrane (Weaver, 2000). Threshold level, however, depends on the shape and duration of the electric signal. Experiments show that with longer pulses lower amplitudes are needed to maintain roughly the same fraction of electroporated cells and train of shorter pulses can replace a longer pulse. It is even suggested that there might be no threshold (Pucihar, Krmelj, Reberšek, Napotnik, and Miklavčič, 2011). Membrane capacitance change is small so that the main electrical result is decreased barrier resistance. Pores are nevertheless widely separated, occupying only about 0.1% of the electroporated membrane area (Weaver, 2000).

If the electropration voltage or current ramp is applied to the cellular membrane of a single Chinese Hamster Ovary (CHO) cells, the membrane conductance increases nonlinearly with field strength reaching saturation. Experiments show also that under hyperpolarising conditions the probability of appearance of occasional step-like jumps is significantly higher than under depolarising conditions (Krassen, Pliquett, and Neumann, 2007).

Since in EBI measurements a level of the excitation signals is usually kept less than a thresold level of MEP, more detailed description of this phenoma is beyond the scope of this thesis, but it is worth keeping in mind that transmembrane potential above 200 mV (or even less) may change the properties of cells substantially.

2.3.3 Temperature sensitivity and Joule heating

For all living organisms, temperature only moderately above the respective optimum growth temperature represent a challenging problem for survival. One of the most amazing aspects of the heat shock response is that it is triggered by a temperature increase of just a few degrees. A small increase in temperature can cause protein unfolding, entanglement, and unspecific aggregation (Richter, Haslbeck, and Buchner, 2010). For the mammalian cells a broad classification places a heat stress in the temperature range 39 … 42 °C for a duration of 15 - 20 minutes in the mild category, whereas a shock in the temperature range of 43 … 45 °C for the same durations will be considered severe (Cates, et al., 2011).

The major component of cellular membranes is phospholipids. Assuming that a lipid can only be found in one of two states – solid-ordered or disordered – the (chain) melting point, T_m , can be defined as the temperature at which the ground state and the excited states are equally likely. For most natural lipids the melting temperatures are in the biologically relevant temperature regime (−20 °C to +60 °C) and in general biological membranes have a transition temperature approximately 15 °C below the organism's temperature (Blicher, 2011).

Assuming that electrical energy is transformed into heat completely the maximum increase of temperature of the liquid in the measurement chamber ΔT_{so} during the excitation signal t_{exc} can be calculated as

$$\Delta T_{so} = \frac{E_{exc}}{\rho_e W_{so} c_{pe}} = \frac{V_{exc}^2 t_{exc}}{R_{so} \rho_e W_{so} c_{pe}} \tag{2.19}$$

where E_{exc} is the energy of the excitation signal, ρ_e the density of the liquid, W_{so} the volume of the liquid in the measurement chamber, c_{pe} the specific heat capacity of the liquid, V_{exc} the excitation voltage (RMS), and R_{so} the resistance of the liquid between the electrodes.
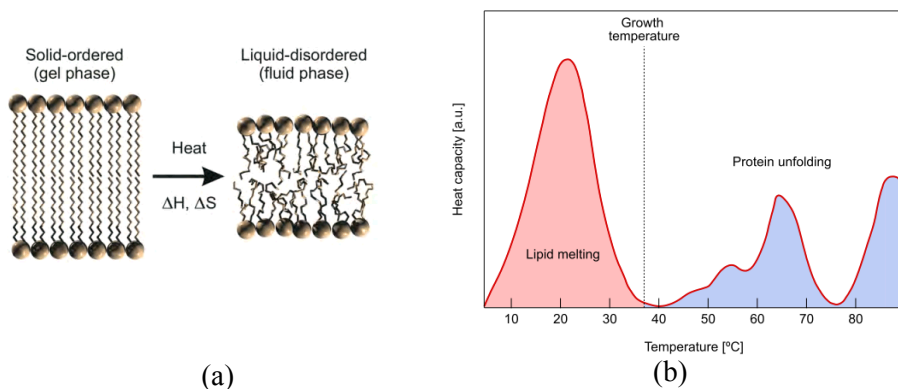

Figure 22. (a) chain-melting transition of a phospholipid bilayer - when going from low to high temperature there is an increase in the enthalpy, Δ H, and the entropy, Δ S; (b) the calorimetric profile of an intact native bacterial membrane; adapted from (Blicher, 2011)

Using distance between the electrodes $l = 30$ µm and surface area of electrodes $A = 200 \times 200 = 4 \times 10^4$ µm^2 (as in developed microfluidic device, appendix D), $\rho_e = 1000$ kg/m^3, $c_{pe} = 4186$ J/(kg K), $V_{exc} = 50$ mV and resistance of the liquid $R_{so} = 750\Omega$ (as calculated in the Section 2.1.1), a temperature rise caused by the excitation signal with a duration of 1 s is around 0.66 K. This temperature calculation is simplified to include only heat generation in the measurement chamber; in reality, part of the heat is spread out through the electrodes and walls of the measurement chamber. In case of microfluidic devices part of the heat is also carried away by the flowing fluids. Therefore use of the eqn. (2.19) gives a conservative estimate of the maximum temperature rise.

When using voltage excitation, current through the cytoplasm of the cells increases with a frequency. Since the membrane isolates the cytoplasm from the surrounding fluid, temperature inside the cells may be higher. Using a disk shaped cell

representing typical human erythrocyte (Fig. 14d and Table 1, case e) maximal electrical energy transformed into heat $E_{cy.max}$ during the excitation signal t_{exc} equals

$$E_{cy.max} = \frac{V_{cy}^2 t_{exc}}{R_{cy}}$$
(2.20)

where V_{cy} is a voltage applied to the cytoplasm and R_{cy} is a resistance of the cytoplasm. Assuming that the conductivities of the cytoplasm and external fluid are equal, distribution of the electric field at high frequencies is uniform and

$$V_{cy} = \frac{V_{exc} h_c}{l}$$
(2.21)

where, l is a distance between the parallel-plate electrodes and h_c is a hight of the disk-shaped cell. If the tempearture of the surrounding fluid remains unchanged during the excitation, the temperature difference at the membrane of the cell ΔT_{me} can be calculated as

$$\Delta T_{me} = E_{cy.max} R_{t.me}$$
(2.22)

$$R_{t-me} = \frac{d}{\kappa_{me} A_{me}} = \frac{d}{\kappa_{me} 2\pi (d_c^2 + d_c h_c)}$$
(2.23)

where $R_{t.me}$ is a thermal resistance, d is a thickness, κ_{me} is thermal conductivity, and A_{me} is a surface area of the membrane respectivly. Substitution of following values: $t_{exc} = 1$ s, $R_{cy} = 20$ kΩ, $V_{exc} = 50$ mV, $l = 30$ μm, $h_c = 2$ μm, $d_c = 8$ μm (as in Table 1, case e), $d = 5$ nm, $\kappa_{me} = 0.2$ W/(m K) into eqn. (2.20) - (2.23) gives $V_{cy} = 3.3$ mV, $E_{cy-max} = 551$ pJ, $R_{t-me} = 166$ K/W and $\Delta T_{me} = 91$ nK. Thermal conductivity of the mebrane is taken here to be equal to typical thermal conductivity of fat. Due to the small electrical energy transformed into heat inside the cell, the transmembrane temperature difference caused is negligible. Even if the electrodes are very close to the single cell (so that $l = h_c = 2$ μm and $V_{cy} \approx V_{exc} = 50$ mV), transmembrane temperature difference rises only 20 μK (however, the temperature rise of the surrounding liquid calculated under similar conditions using eqn. (2.19) is over 100 K!). In case of $l = 10$ μm, the temperature rise of the liquid is up to 6 K .

The temperature dependence of conductivity of most ions in aqueous solution is about 2.0 %/°C (see Section 2.1.1).

If the membrane of the cell contains pores when current density in the pores depends on the excitation energy and conductivity of the surrounding medium. In case where the conductivity of the suroundig medium is low, or the excitation energy is high, then increased current density will cause local heating near the pores (Gowrishankar and Weaver, 2003), (Pliquett, Gallo, Hui, Gusbeth, and Neumann, 2005).

2.3.4 Safety regulations

In-vivo EBI measurements usually comply with the International Electrotechnical Commission (IEC) standard (IEC60601-1 (ed 3.0), 2005). Most medical devices are classified as Type BF or Type CF. Type BF devices have conductive contact with the patient but not the heart. Type CF is designated for devices and parts directly contacting the heart.

The standard specifies a ''patient auxiliary current'' limits in normal conditions in the frequency range from DC to 1 kHz shown in Table 3. From 1 kHz to 100 kHz, the current levels linearly increase with frequency. Above 100 kHz, the currents are limited to the same maximum value as at 100 kHz.

Table 3. Safe current limits (RMS) in normal conditions for the frequencies below 1 kHz according to the IEC60601-1

Leakage current type	Type BF	Type CF
Patient auxiliary current (DC), μA	10	10
Patient auxiliary current (AC), μA	100	10

Safe current limits in normal conditions $I_{s.n}$ in the frequency range from 1 kHz to 100 kHz can be calculated

$$I_{s.n}(f) = I_{s.1k} \ f \tag{2.24}$$

where $I_{s.1k}$ is the safe current limit at 1 kHz and f is the frequency for calculating the maximum safe current in kHz. IEC60601-1 standard establishes also the maximum current values under a single fault condition (SFC) which are 5 times higher than the values shown in Table 3. Single fault conditions (e.g., interrupted earth connection) are specified under clause 8.1 of the standard.

Use of eqn. (2.24) gives maximum safe AC RMS excitation current 10 mA at frequencies ≥100 kHz in normal conditions and non-cardiac applications (type BF).

2.4   Outline of the problems and potential solutions

Electrical impedance is an informative property of biological objects allowing to caharacterize other properties of these objects as described in the Sections 1.2-2.1. However, several requirements and limitations must be considered when measuring electrical bioimpedance (EBI). Generalized structure of the typical EBI measurement system is depicted in Fig. 23. An excitation signal source (generator of excitation waveform) has inputs for timing and duration control (from t_1 to t_n) and for frequency range setting (from f_1 to f_k). The signal from this generator is used as an input excitation for the complex impedance $\dot{Z}$ under study, as well as a reference signal source. Discrete Fourier transform (usually FFT) is employed for obtaining the amplitude and phase spectra $|\dot{Z}(f)|$ and $\Phi(f)$ of the impedance $\dot{Z}$. As an alternative, real and imaginary parts of the spectra $\mathrm{Re}\dot{Z}(\omega)$, $\mathrm{Im}\dot{Z}(\omega)$ may be used for

calculation. Usually the signal passes also a signal-conditioning block for the amplification, filtering and signal level matching (which is not shown here) before the signal processing is performed.

2.4.1 Time dependency of the bioimpedance

In some cases, the properties of the object are changing relativly fast, e.g. in cardiovascular system or in cytometry, when the nerve cells are fired. In later case
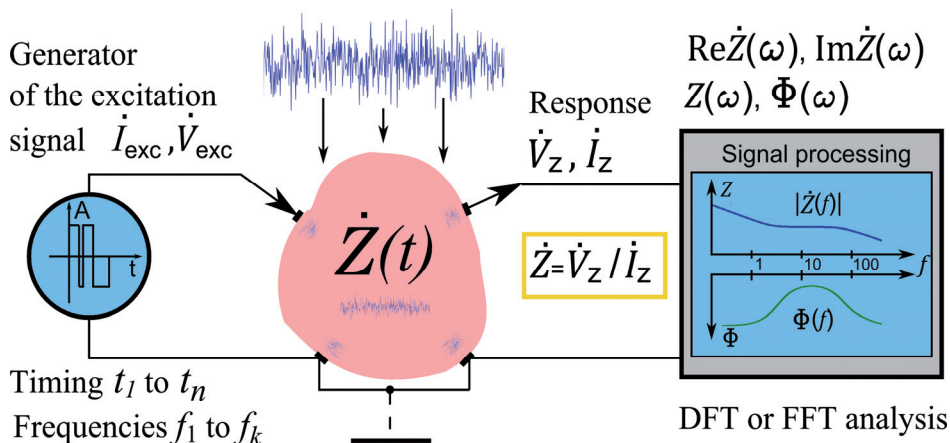

Figure 23. Depiction of the structure of the EBI measurement system

the intracellular potential and cell membrane conductance change in about one millisecond (Malmivuo and Plonsey, 1995). To follow these changes the duration of the measurement cycle must be shorter. Another typical situation, which requires fast measurement is a microfluidic device where the droplets or cells are flowing within microfluidic channels. Since the dimensions of the channel and the electrodes are small, productivity of system depends highly on the duration of the measurement cycle.

In order to apply Fourier transform to non-stationary signals, it must be processed in a short-time windows, so that within each window the signal may be assumed to be time-invariant. The windows must overlap, otherwise some information is lost which was contained in the separate time segments (Karrenberg, 2007).

The Fourier uncertainty principle states that minimal product of signal spreading in time domain and frequency domain

$$\Delta t \, \Delta \omega \geq 0.5 \qquad\qquad (2.25)$$

where the minimal number 0.5 corresponds to the gaussian function. However, in the case of any non-gaussian signal the product $\Delta t \, \Delta \omega$ becomes much greater than

the lowest limit 0.5, e.g. for a train of pulses $\Delta t\,\Delta\omega$ tends to the value of 7.582 if the number of pulses tends to infinity (Udal, Kukk, and Velmre, 2009). Using this limiting value and frequency f instead of angular frequency ω ($f = \omega / 2\pi$), eqn. (2.25) can be rewritten as

$$\Delta f \geq \frac{7.582}{2\pi\,T_s} \geq \frac{1.2}{T_s} \tag{2.26}$$

where Δf is a frequency resolution and T_s is a duration of the signal. This considered task is of the field of *time-limited asynchronous spectral measurements*.

In synchronized measurements, where it is possible to assure the integer number of signal periods within the time window, the resolution limit is defined as $\Delta f = 1/T_s$. To ensure an exact calculation of the signal spectrum the following requirements have to be fulfilled (Rauscher, 2008):

- the signal must be periodic (period T_p)
- the observation time $N\,t_s$ must be an integer multiple of the period T_p of the signal where N is lenght of DFT, i. e. total number of samples used for calculation of Fourier transform, and t_s is a sampling period.

Not fullfilling these requirements results in amplitude and phase errors of the signal spectrum.

Measurement time may be also limited by the heating effects as described in Section 2.3.3, since the energy content of the excitation signal is proportional to its duration.

2.4.2 SNR, limiting voltage and current of excitation signal

A well-known characteristic of the quality of a measurement is the signal-to-noise ratio SNR, given by square root of the ratio of the signal power P_S over the power of noise P_N

$$SNR = \sqrt{\frac{P_S}{P_N}} \tag{2.27}$$

with

$$P_S = \frac{1}{T}\int_0^T s^2(t)dt \tag{2.28}$$

$$P_N = \sigma^2 \tag{2.29}$$

where s is a determinstic signal, T denotes the duration of the signal and σ is a variance of the additive noise.

The following main noise sources affect the impedance measurement:
- noises of the excitation signal source
- noises of electrodes
- external noises
- noises of the object
- noises of the signal conditioning circuitry.

Noises of the excitation signal source consist noises of the signal source (e.g. noises of the active and passive components of the current source). When using voltage source with an additional resistor, thermal noise of this resistor is added.

Noises of the electrodes embody thermal noise of the real part of the electrode impedance and electrochemical noise (see Section 2.2.8).

There are many sources of external noises since the environment is polluted with different electromagnetic fields.

Noises of the object depend on its nature. One source is a thermal noise of the real part of the impedance. In case of biological objects rotation and fluctuation of the cells in the measurement chamber produce random changes of the EBI (see Section 2.1.2). Gating of the ion channels in the cell membranes could also produce random changes in the impedance of the cells.

Noises of the signal conditioning circuitry depend mainly on the noise properties of the first stage (in the following stages these noises will be repeated and usually also amplified).

When combining noises of different origins into a total noise expression, the method of addition must be carefully considered. For example, if two noises with RMS-values σ_a and σ_b exist together, the RMS -value of the total noise, σ_T, is given by (Alkemade and Snelleman, 1978):

$$\sigma_T = \sqrt{\sigma_a^2 + \sigma_b^2 + 2C\sigma_a\sigma_b} \qquad (2.30)$$

where C is a correlation coefficient; C ranges between $C = 1$, in the case of complete statistical correlation, and $C = 0$ in the case when both noises are completely uncorrelated. It must be noted that some statistical correlation may excist even if noises are produced by different objects, e.g. two resistors influenced by fluctuations of temperature.

When the noise is correlated neither with the signal nor with itself across trials, averaging yields an improvement of the SNR. If σ is the amount of RMS noise in a set of n samples, the RMS noise of the average $\sigma_{avg} = \sqrt{1/n}$. However, this improvement of the SNR comes in a cost of measurement time which increases by factor of n.

To measure unknown impedance, as depicted in Fig. 23, we can use one of two simple approaches: either we apply a known voltage excitation across the object and then measure the current flowing through it, or we inject a known current into that object and measure the voltage across it. We can also measure both

values, current and voltage simultaneously. There are also other methods, like bridge balancing etc, which are not described here.

Measuring both, the voltage and current, is probably a good choise in wideband EBI measurements since the bandwith of the real current sources is limited and voltage sources usually can not be used without current limiting.

From the definition of SNR (eqn.(2.27)) it is obvious that it can be improved in two ways – by increasing the power of useful signal and by decresing the power of noise signals. Considering that some noises are almost unavoidable (e.g. noises of the object and thermal noises of the resistors) and reduction of other types of noises (e.g. noises of the electrodes and external noises) have also limitations, increased power of the excitation signal is desired. However, the power of the excitation signal is limited since both, the voltage and current of the excitation signal are limited by several factors summarized in the Table 4. In the right column of the table the section numbers are given where more detailed description of the limiting factor can be found.

Table 4. Limitations of the voltage and current of the excitation signal

Limiting factor	V_{exc}	I_{exc}	Reference
Nonlinearity caused by the electrodes	80 mV [1]	0.16 mA , f = 100 Hz [2] 6.6 mA, f = 1 MHz [2] 41 mA, f = 10 MHz [2]	s. 1.5.5
Critical firing level of excitable cells	20 mV [3]	5-10 µA [4]	s. 1.6.1
Electroporation of cells	400 mV [5]	n/a	s. 1.6.2
Joule heating	50 mV [6]	67 µA [6]	s. 1.6.3
Safety regulations for in-vivo measurements	n/a	10 µA, DC and cardiac [7] 100 µA, $f \le$ 1 kHz 10 mA, $f \ge$ 100 kHz	s. 1.6.4

[1] – double voltage drop (amplitude) of the gold-plated electrode

[2] – gold plated electrodes with the surface area of 4×10^4 µm^2, α = 0.8, B = 1

[3] – deviation of cell mebrane voltage from its resting potential; excitation voltage limit depends on the position of the cell between the electrodes

[4] – approximate value with electrodes in the tissue near the cell (< 150 µm)

[5] – double cell mebrane voltage; excitation voltage limit depends on the position of the cell between the electrodes

[6] – parallel-plate electrodes with surface area of 4×10^4 µm^2, gap between the electrodes 30 µm, conductivity of the liquid 1 S/m; duration of the excitation signal 1 s, excitation voltage 50 mV RMS, excitation frequency 10 MHz, static fluid, maximum temperature rise of the liquid < 0,7 K

[7] – DC current limit for all in-vivo measurements and AC current limit for cardiac measurements for the frequencies $\le$ 1 kHz

Limit voltages and currents of linearity have been defined as values at which the series equivalent capacitance and resistance of the interface impedance deviate 10% from their linear values. At low frequencies most of the excitation voltage drops on the electrodes.

Limit voltage of linearity depends on material of the electrodes, the electrolyte composition and the thermal voltage $V_t = kT/q$ (where k is the Boltzmann constant, T is the absolute temperature and q is the charge on an electron). If the material of the electrode, electrolyte composition and temperature are fixed, the limit voltage is almost constant. If the lower deviation from linear values is desired lower excitation voltage should be used.

At higher frequencies, where the charge-transfer resistance of the electrodes is short-circuited by a double layer capacitance of the electrodes, most of the excitation voltage drops on the resistance of the liquid causing heating of it. In the current setup maximum temperature rise is below 0.7 K if the excitation voltage is 50 mV, however this temperature rise is significantly lower if the liquid is flowing or if the the measurement chamber is large than the electrodes. On the other hand, in case of using voltage source the temperature grows in power of two when the distance between the electrodes is decreased, since both, the volume and resistance of the liquid between the electrodes are decreasing.

Similarly to the limit voltage of linearity, the limit current of linearity depends on material of the electrodes, the electrolyte composition, and the thermal voltage V_t, but also on the current density of the electrodes. At higher frequencies, where capacitive current due to the double layer capacitance increases, the limit current of linearity increases according to the eqn. (2.17). Coefficient α in this equation characterizes the CPE effect which is correlated with a roughness of the electrodes (see Table 2 in the Section 2.2.6). Electrodes with a porous or fractal surface have signicantly large effective area which increases the limit current of linearity and this limit starts from lower frequencies (due to the increased double layer capacitance). Drawback of such electrodes is that the large variance of the effective surface area limits their use in tetrapolar and differential measurement circuitres as the efficiency of the compensation of errors and synphase signals is limited by the identity of the electrodes (see Section 2.2.10).

Critical firing level of the excitable cells is an unstable condition which depends on several factors (e.g. on previous state of the cell). At higher frequencies (> 4 kHz) and excitation currents (> 7 mA), cell membranes are not able to react in a regular way but may be blocked (see Section 2.3.1). Excitation voltage and current limits depend on the measurement conditions (distance and shape of the electrodes, dimesions and orientation of the cell, conductivity of the medium etc.). Calculations of the membrane voltages are discussed in the Section 2.1.2 and some examples for the current setup are shown in Fig. 16.

Voltage and current limits of electroporation depend on the membrane voltages and measurement setup as in case of excitable cells, however, since these limits are significantly higher they are usually avoided in EBI measurements.

It can be concluded that for the typical measurement conditions described in Section 2.1.1 and Fig. 13, the excitation voltage is limited to around 50 mV due to

the nonlinearities arising in the electrode-electrolyte interface in the low frequency range and Joule heating of the liquid in the higher frequency range.

The current limit depends on the object: it is in the range from 10 μA to 200 μA in the low frequency area and up to 40 mA at 10 MHz. However, if the excitation voltage V_{exc} is fixed to the 50 mV, the maximum current through the liquid depends on its resistance. In case where $R_{so} = 750\ \Omega$ the real part of I_{exc} can not exceed 67 μA. Some capacitive current I_c passes also through the stray capacitances C_{so} and C_s (see Fig.13):

$$I_c = \frac{V_{exc}}{1/2\pi f(C_{so} + C_s)} = V_{exc} 2\pi f(C_{so} + C_s) \qquad (2.31)$$

In case where $C_{so} + C_s = 3$ pF, $I_c = 9.4$ μA at 10 MHz.

To increase the excitation current I_{exc} at higher frequencies, large excitation voltage is needed, which leads to the increased heating of the liquid between the electrodes. Since according to the eqn. (2.20) temperature rise is proportional to the duration of the excitation signal t_{exc} and square of the excitation voltage V_{exc}^{2}, doubling of the V_{exc} (which improves SNR two times) may be compensated with a 4 times shorter t_{exc}. Since the averaging of 4 measurement samples could also improve the SNR two times (if the noise is uncorrelated), the advantage of doubled V_{exc} is a shorter measurement time. Another choise for keeping temperature rise at the same level during fixed t_{exc}, if V_{exc} is doubled, is doubling of the distance l between the electrodes, however in this case I_{exc} remains the same, SNR improves only $\sqrt{2}$ times and the sensitivity of the EBI measurements is lower.

2.4.3 Frequency range of EBI measurements

To characterise the properties of biological objects usually frequencies where α and β-dispersions appear must be covered. In some cases, only one dispersion area is considered, e.g. in the single-cell cytometry, since the capacitance and conductivity of the cell membrane and conductivity of the cytoplasm influencing mainly the β-dispersion area. However, in this case some part of lower frequency area must be also included, since α-dispersion changes the plateau from which the β-dispersion starts (see Section 1.2.4). Cumulative RMS noise of voltage or current to be measured is proportional to the bandwith.

2.4.4 Potential solution for improving SNR and speed of EBI measurements

As it already discussed in previous sections, SNR and speed of EBI measurements are contradicting parametres, which are limited by several factors. In case of fast measurements, which is dictated by fast changes of the properties of the object (SUT), the frequency range (bandwith) of interest must be covered in a short timeframe; or in other words – fast impedance spectroscopy must be performed.

Minimum appropriate measurement time depends also on the relaxation time-constants of the SUT. As a rule of thumb, the observation time must be at least 3 times longer than the largest time-constant of the SUT, otherwise some information will be lost and the measurement error increases (this simplified rule is based on the fact that response of the single R-C circuit to the excitation step reaches 95 % from its final value during 3τ, where time-constant $\tau = 2\pi RC$). Lowest frequency of the available spectra and the frequency resolution of the spectra are inversely proportional to the observation time as described in the section 2.4.1.

Since the sequential measurements at many separate frequencies require more time due to the longest relaxation time-constant of the SUT, a wideband excitation signal which covers a range of frequencies is usually preferred for fast wideband measurements. However, as it is shown in the next chapter, a power of different frequency components of the wideband signals is less than the power of the single sinusoidal signal with the same amplitude.

Taking into account that both the amplitude and duration of the excitation signal are limited, one solution for improving SNR of the fast EBI measurements is use of the wideband excitation signals (waveforms) with the best power at the frequencies of interest. Comparison of different wideband signals and methods for adjusting properties of some most suitable signals are discussed in the next chapters of the thesis.

The second possibility for improving SNR of the fast EBI measurement is optimizing the structure of EBI measurement circuitry. Overall SNR depends on the contribution of all parts. SNR of measurement circuitries with current and voltage sources using different excitation signals are briefly discussed in the fifth chapter of the thesis.

2.5   Summary of the chapter

Electrical models and correponding equivalent circuit models of the single cell and electrodes are discussed in first sections of the second chapter.

In Section 2.1.2 it is shown that a transmembrane potential of cells depends significantly on the orientation of cells in electric field. This leads to variation of EBI in case where cells are rotating, e.g. in the channel of microfluidic device.

In Section 2.2 properties of the electrodes and limitations caused by electrode-electrolyte interface are discussed. One solution for decreasing of the impedance of electrode-electrolyte interface and increasing a limit current of linearity is use of electrodes with increased effective area. However, as pointed out in Section 2.2.10 this will decrease a positive effect of another solutions – use of tetrapolar electrodes and symmetrical measurement circuitry.

In Section 2.3 the limitations originated by the sensitivity of biological objects are discussed. In Sections 2.3.4 and 2.4 it is shown that in case where electrodes, which are placed in a typical physiological saline solution, are close to each other, heating of the solution may become a major limiting factor of increase of the exitation current at higher frequencies. This limits also the quality of the measurements since the higher excitation current corresponds to the better SNR.

In Section 2.4 the limiting factors influencing the fast and wideband EBI measurement are summarized and the use of wideband excitation signals (waveforms) with the highest power at the frequencies of interest is picked out as one of main solutions for achieving a better SNR of EBI measurements.

3. SPECTRALLY DENSE WIDEBAND EXCITATION SIGNALS

3.1   Introduction

3.1.1 Classification of signals

There are many ways that signals can be classified. A signal can be either continuous or discrete, and it can be either periodic or aperiodic. The combination of these two features generates the four categories (Smith, 1999):

aperiodic-continuous; for example, decaying exponentials and the Gaussian curve which signals extend to both positive and negative infinity without repeating in a periodic pattern

periodic-continuous; sine waves, square waves, and any waveform that repeats itself in a regular pattern from negative to positive infinity

aperiodic-discrete; these signals are only defined at discrete points between positive and negative infinity, and do not repeat themselves in a periodic fashion

periodic-discrete; these are discrete signals that repeat themselves in a periodic fashion from negative to positive infinity.

For improving of the SNR of EBI measurements it is important to concentrate the signal energy in a frequency range of interest. From this point of wiev signals may be classified in two classes by how the energy is distributed among spectral components. Benefit of the excitation signal with a dense frequency distribution is that it gives more detailed shape of the spectrum of the response signal. All the waveforms discussed in this chapter (except the rectangular wave waveform) have magnitudes over half-pover limit in all harmonic frequencies of the fundamental frequency $f_1 = 1/T_p$. Signals with a sparse frequency distribution, which belong to the second class, are discussed in the next chapter.

3.1.2 Discrete Fourier Transform (DFT)

Usually the simplest representation of a signal is as a function of time. For instance, a voltage or current changing over time. However, other representations of the signal, such as a frequency-domain function are useful. It shows how the signal characteristics are changing over a range of frequencies. Signals can be converted between time and frequency domains with mathematical operators known as transforms. The Discrete Fourier Transform (DFT) is a widely used invaluable tool when analysing signals or studying the response of a system to a signal. The use of DFT is also essential in a fast impedance spectroscopy. An efficient algorithm to compute DFT is called Fast Fourier Transform (FFT).

If one domain is discrete, the other domain must be periodic, and vice versa. Since the DFT views both domains as discrete, it must also view both domains as periodic. The samples in each domain represent harmonics of the periodicity of the opposite domain (Smith, 1999).

Real and imagiginary parts of the frequency domain signals Re$X[k]$ and Im$X[k]$ are calculated from the time domain signal $x[i]$ as

$$\operatorname{Re}X[k]=\sum_{i=0}^{N-1}x[i]\cos(2\pi ki/N) \tag{3.1}$$

$$\operatorname{Im}X[k]=\sum_{i=0}^{N-1}x[i]\sin(2\pi ki/N) \tag{3.2}$$

where the index i runs from 0 to N-1, while the index k runs from 0 to $N/2$ and N is a total number of samples. Alternatively, the frequency domain can be expressed in polar form:

$$\operatorname{Mag}X[k]=\sqrt{(\operatorname{Re}X[k])^2+(\operatorname{Im}X[k])^2} \tag{3.3}$$

$$\operatorname{Ph}X[k]=\arctan\left(\frac{\operatorname{Im}X[k]}{\operatorname{Re}X[k]}\right) \tag{3.4}$$

In polar notation, Mag$X[k]$ holds the amplitude of the cosine wave, while Ph$X[k]$ holds the phase angle of the cosine wave. Polar notation usually provides observers with a more figurative representation of the characteristics of the signal. Real and imaginary parts are more convinient for math computations (see Fig. 6 in the Section 1.2.4).

If the real signals are not periodic, DFT interprets them as periodic anyway, which leads to the distortions of the spectra. A signal $x(t)$ is periodic if:

$$x(t)=x(t+T_p) \tag{3.5}$$

The smallest positive value of T_p which satisfies this condition is the period. If a signal does not repeat itself after a fixed length of time, it is aperiodic. In order to be sure of signal periodicity it must be observed from infinite past to infinite future. Fortunately, this is not always neccesary. The periodicity of the signal may be foreknown, as in case if the signal is designed as periodical. This is typical of the impedance measurement excitation signals.

If some additional conditions are fullfilled, a spectrum of the periodical signal does not depend on the number of periods when performing digital signal processing (DSP). As already noted in the Section 2.4.1, the observation time $N\times t_s$ must be an integer multiple of the period T_p of the signal where N is lenght of DFT, i. e. , the total number of samples used for calculation of Fourier transform, and t_s is a sampling period. To follow these requirements, the sampling and excitation signals must be synchronized, and at least one period of the excitation signal must

be covered. If it is not pointed out otherwise, the signals discussed in the following sections of the thesis are periodical and meet the conditions described here.

Although only one period of a periodical signal could be used for the synchronous DFT, more periods allow averaging which improves a SNR.

3.1.3 Single frequency signals and wideband signals

The only signal with a spectrum of single line is a sine (or sinusoidal) waveform. Sinusoidal voltage in a basic form as a function of time $V(t)$ is:

$$V(t) = A\sin(\omega t + \Phi) \tag{3.6}$$

where A is the amplitude and Φ is the phase, which specifies where in its cycle the waveform begins at $t = 0$. A cosine wave is also "sinusoidal" waveform, since $\cos(x) = \sin(x + \pi / 2)$ which is a sine wave with a phase-shift of $\pi/2$.

An important characteristic of linear systems is how they behave with sinusoids, a property which is called sinusoidal fidelity: if the input to a linear system is a sinusoidal wave, the output will also be a sinusoidal wave, and at exactly the same frequency as the input. Sinusoids are the only waveform that have this property (Smith, 1999).

According to the Fourier principle, any real waveform can be produced by adding sine waves together. Conversely all other waveforms except the sinewave contain more than one spectral component. The shorter the time duration of a waveform the more components with different frequencies we need to build it, and so the wider the bandwidth. From this point of view, the inifinitly short, so called δ-pulse, is an ideal excitation signal for the fast impedance spectroscopy since it covers all frequencies in a shortest timeframe and, in addition, with the same amplitude. However, in practice there is a crucial drawback. If the amplitude of very short excitation pulses is limited and fixed, then amplitudes (magnitudes) of the frequency componets are very low. If the duration of the pulses is increased, magnitudes of the frequency componets are almost equal only in a short frequency range as illustrated in Fig. 24.

3.1.4 Energy, power and Parseval's relation

In case of true periodic signals their energy becomes infinite, and in most DSP textbooks use of average power over a single period is claimed to be necessary for characterization of this type of signals.

In practice measurement time is always limited, especially in case of fast impedance spectroscopy, and only limited number of signal periods are used. It may be claimed that such a signal cannot be treated as periodic, yet it is often nearly enough periodic. If the signal is periodic, all the properties of the signal during each period are the same, therefore all the information can be gathered during one period assuming that following conditions are also fullfilled:

- measurement is synhcronized as described in Sections 2.4.1 and 3.1.1

- noises are not causing signicant errors

If the noise is large, averaging over several periods allows to improve a SNR. Exact repetitiveness of following periods of the signal is ensured by the design of the signal. This is an important difference since in general case the repetitiveness of the signal is not known beforehand.

Considering that the power is a rate of energy use, periodic signals may be characterized by the energy content available during some time interval as well. If the period of the signal is normalized to the unit value of 1 s, the values of power and energy over this period are equal.

Since the time and frequency domains are equivalent representations of the same signal, they must have the same energy. This is called Parseval's relation, and for the DFT it is expressed:

$$\sum_{i=0}^{N-1}(x[i])^2 = \frac{2}{N}\sum_{k=0}^{N/2}(\mathrm{Mag}X[k])^2 \qquad (3.7)$$

where $x[i]$ is a time domain signal with i running from 0 to N-1, and $X[k]$ is its modified frequency spectrum, with k running from 0 to $N/2$. The modified frequency spectrum is found by taking the DFT of the signal, and dividing the first and last frequencies (samples 0 and $N/2$) by the square-root of two (Smith, 1999).

Energy and power of the signal are proportional to the RMS magnitude squared. Note, that energy in this representation is not exactly the same as the conventional notion of energy in physics since the time is normalized to the unit value of 1 s, and in our case of electrical signals, the load resistance of the signal source is normalized to the unit value of 1 Ω. This is convinient for comparison of different signals since a voltage signal across the resistor and a current signal through the resitor give the same energy and power values. In practical cases the real load resistances and the real durations of the signals must be used to calculate actual values of power and energy.

3.1.5 Normalized RMS magnitudes of spectral components

The amount of the signal energy in the specified frequency range compared to the total energy of a signal characterizes the energy efficiency of the signal. However, result of this comparison does not describe how the energy (or power) of the signal is distributed among the frequency components (bins) of the spectrum. As an example: the spectrum of the chirp waveform (Fig. 29a) contains all the frequencies in between f_0 and f_{fin} and maximum deviation of the RMS magnitudes from their mean value is moderate (below $\pm$ 30 %); the spectum of the rectagular waveform Fig. 25a contains only the fundamental frequency component and its odd harmonics with fast decaying RMS magnitudes (Fig. 25b).

To improve the SNR of the impedance measurement, higher RMS magnitudes of the frequency components of interest (FCI) are desirable. From this point of view RMS magnitudes of the FCI may be used as a figure of merit for the different excitation waveforms. The energy of a waveform depends on its RMS value and

duration and the RMS value on a waveform depends on its amplitude. For a graspable comparison of different waveforms some variables must be fixed. In our case it is reasonable to fix the amplitude to the unit values ± 1 and the duration to the unit value 1 second. Normalizing the duration of the signal against 1 s provides also a normalized presentation of the spectra since the fundamental frequency is a reciprocal of the duration of the signal T_p.

In general, RMS magnitudes of the FCI are not equal. The shape of a magnitude spectrum may be also decaying, rising or oscillating around some mean value. The mean value of the RMS magnitudes of the FCI is used here as a figure of merit in this general case. However, a deviation from the mean RMS value is an additional parameter which also influences the results of measurements. Therefore a lower deviation of the RMS magnitudes is commonly preferred in case the mean values are equal.

3.2   Periodic pulses and rectangular signals

3.2.1 Short pulses and rectangular wave waveform

One of the simplest excitation waveform is a short pulse (Fig. 24a), which has a broad band spectrum (Fig. 24b) with moderately declining RMS spectrum. Such a spectrum has also a DC component which is undesirable in EBI measurements. A bipolar pulse without a DC component and with the same energy content (Fig. 24c) has a different shape of the spectrum (Fig. 25d). For both spectra only the first 65 frequency bins are shown.

If not noted otherwise, the normalized period of the waveform T_p is divided in a n_{sp} sample points and the frequency resolution of the spectrum $\Delta f = 1/T_p$.

Another simple waveform is a rectangular signal with binary (+1 and -1) levels, shown in Fig. 25a. Since there are no parts with zero level in the waveform, the energy content in the time domain is maximal, and the energy in the frequency domain is higher than in case of short pulses. However, the sparse spectrum of this waveform contains only odd harmonics which are declining fast with frequency by $1/f$ rule (Fig. 25b). Such the simple waveform can be used, therefore, in some special cases, e.g. when the falling shape of the spectrum is the inverse of the shape of the spectrum of the SUT.
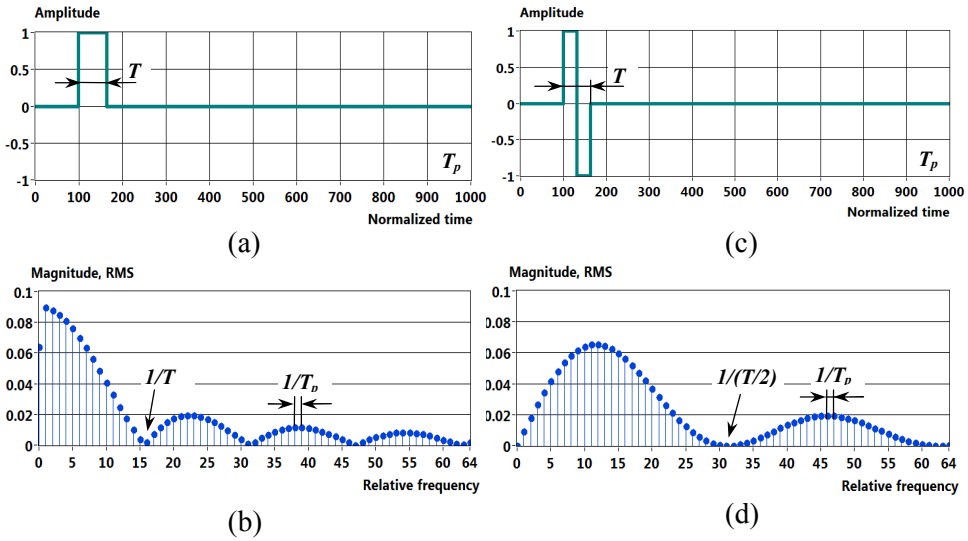
Figure 24. Waveforms (a), (c) and corresponding RMS spectra (b), (d) of the pulses with relative duration $T = (64/1000)\, T_p$
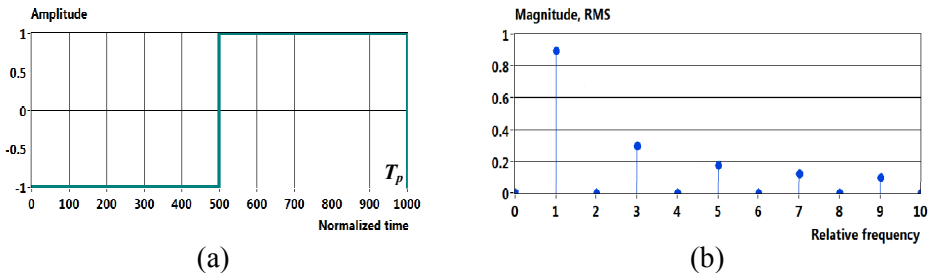

Figure 25. Waveform (a) and RMS spectrum (b) of a rectangular waveform; first frequency bin occupies 81 % and next frequency bins 3, 5, 7, 9 occupy 15 % of the total signal energy respectively

3.2.2 Shortened rectangular wave (SRW) waveforms

Classically sinusoidal excitation is used for impedance measurements. Similarly a good results can be achieved by using different piecewise continuous approximations of sinusoidal signals.

A drawback associated with later approach, is that harmonics content is very sensitive to level accuracies, and usually needs adjustments (Min, Parve, Kukk, and Kuhlberg, 2002). Higher harmonics of the simple square wave signal can be reduced by modifying the waveform as shown in Fig. 26. In case of "shortening" a rectangular wave by 23° magnitudes of the 3-rd and 5-th harmonics are supressed compared to the regular rectangular wave (RRW). The RMS value reaches 0.827

and the power of the first harmonic is 36.8 % higher compared to the sinusoidal wave.

The power of the first harmonic of the SRW shown in Fig. 26 is 15.6 % less compared with RRW. However, since the SRW contains zero level sections, the total energy of this waveform is 25.8 % less than of the RRW. This makes a SRW more energy efficient and useful for the applications where energy consumption is critical, e.g. battery-powered signal sources.

In cases where the energy efficiency is not of prime importance, the SRW waveforms can be optimized for a better suppression of harmonic components.
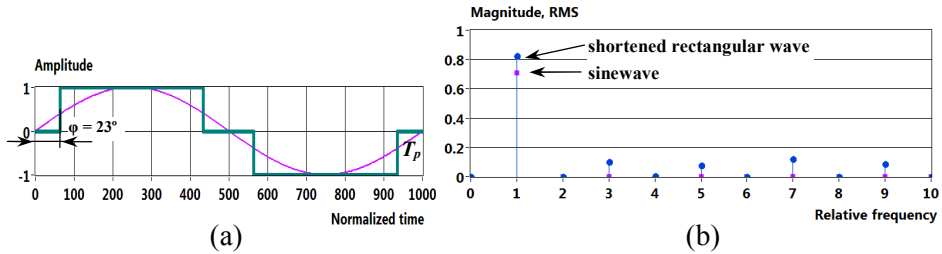

(a)   (b)

Figure 26. Waveform (a) and spectrum (b) of a ternary SRW optimized for concentrating the signal energy into the first harmonic component; the RMS value reaches 0.827 and seizes 92.3 % of the total energy; sinusoidal wave and its RMS magnitude are shown for comparison

Several ways to achieve this are discussed in (Annus, Min, and Ojarand, 2008), (Annus, Land, Min, and Ojarand, 2012), (Annus, Min, Märtens, and Ojarand, 2012). A more detailed description of these solutions is not provided here since they are mainly intended for single-frequency measurements.

3.2.3 Maximum length sequence (MLS)

A maximum length sequence (MLS) is a type of pseudorandom binary sequence which can be easily generated by an n-stage linear feedback shift register (LFSR), see example in Fig. 27a. A maximum-length LFSR produces an maximum length sequence (m-sequence). It cycles through all possible $N = 2^n - 1$ states within the n-stage shift register (except the state where all bits are zero). The MLS period $T_p = (2^n - 1)t_c$, where t_c is the period of the register clock.

The spectrum of the periodic MLS is a line spectrum with values only at frequencies $f = k/T_p$ where k is an integer. There is no power in the signal at the reciprocal of the clock pulse interval t_c or its integer multiples (Godfrey, 1991). The RMS magnitude spectrum follows the envelope of $sin\ (f)/f$ function and the values for a line spectrum of the MLS signal are given by

$$\text{Mag}\,X[k] = \frac{A\sqrt{2(N+1)}}{N}\frac{\sin(k\pi/N)}{k\pi/N}$$
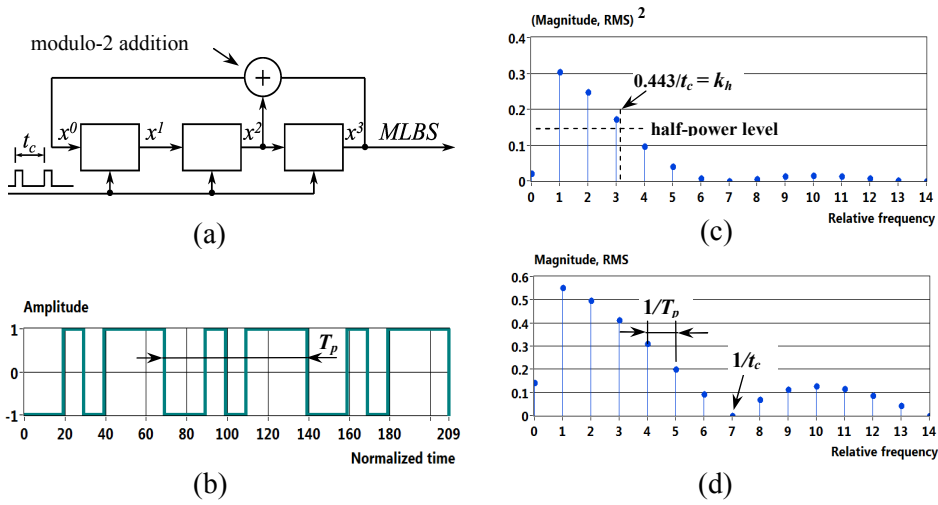
(3.8)

Figure 27. Simplified structure of the 3-bit LFSR (a), the waveform (b), power spectrum (c), and the magnitude spectrum (c) of the 3-rd order MLS

where A is the amplitude of the waveform, $k = 1,2,\ldots,(n_{sp}/2)\text{-}1$ and n_{sp} is a total number of sample points. The power spectrum (PSD) of the MLS signal can be calculated by squaring of the right side of the eqn. (3.8).

The number of pulses with opposite polarity in one sequence period T_p is almost equal (the difference equals one), i.e. Mag[0] = A/N. The half-power bandwidth of the signal occurs at a frequency of approximately $0.443/t_c$ (Godfrey, 1991). In the case of the 3-rd order MLS signal only the first three frequency bins (except the zero frequency) meet this condition (see Fig. 27c) and the energy content of these three spectral components is 72.4 % of the total signal energy. In the case of 6-th order MLS signal 27 frequency bins are in the half-power limit range and the energy content of these bins is 71.1 % of total signal energy.

As N becomes large, Mag[0] tends to zero and the spectrum becomes quite slow to decay to zero as number of frequency bins k increases. At the same time, according to the eqn. (3.8), magnitudes of all frequency componets Mag$X[k]$ are decreasing. That is, the shape of the magnitude spectrum becomes more flat as N increases and more frequency bins fall in the half-power limit range (useful frequency bins), however, the power of each frequency component decreases. A mean RMS value of all useful frequency bins is

$$\text{Mag}\,X_{0.5} \cong \frac{1}{k_h} \sum_{k=1}^{k=k_h} \frac{A\sqrt{2(N+1)}}{N} \frac{\sin(k\pi/N)}{k\pi/N} \qquad (3.9)$$

where k_h is the number of frequency bins which fall in the half-power limit range. Considering that $1/t_c = N$, k_h is a nearest integer number less or equal to 0.443 N.

Calculated mean RMS values for up to 8-th order MLS signal are shown in Fig. 28. It appears that the mean RMS levels tend to the value

$$\text{Mag } X_{0.5} = B \frac{4}{\pi} \frac{A}{\sqrt{2}} \frac{1}{\sqrt{k_h}} \tag{3.10}$$

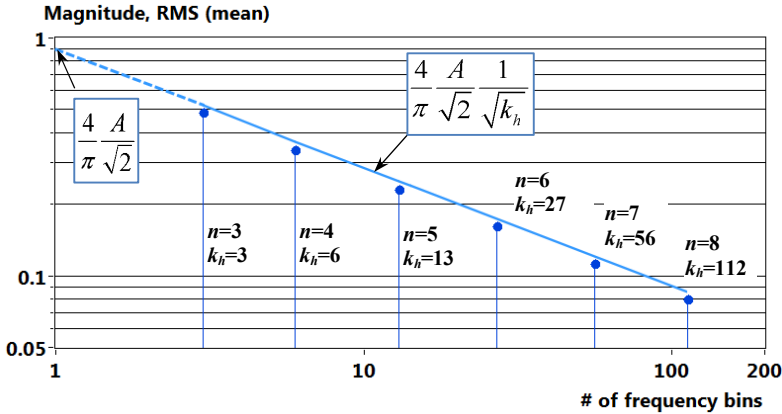where coefficient $B \approx 0.93$.

Figure 28. Dependency of the mean RMS magnitudes of the useful frequency components (bins) on a number of useful frequency bins k_h; n is an order of the corresponding MLS waveform and A is the amplitude of the waveform (± 1 in current case)

The RMS magnitude of the first frequency bin shown in Fig. 28 does not belong to the MLS but to thr rectangular signal shown in Fig. 25. It can be concluded that a mean value of RMS magnitudes of the half-power range frequency components of the MLS signal are decaying by a rate of $1/\sqrt{k_h}$ compared to the RMS magnitude of the fundamental frequency of the rectangular signal.

The MLS signal can be easily generated. However, since the distribution of the frequency components is dense, a power of these componets becomes low if a wide bandwidth is needed (and the amplitude of the waveform is limited). In case of a narrow bandwidth the drawback is a relativly fast decay of the magnitude spectrum as it is shown in Fig. 27.

3.3 Chirps

3.3.1 Introduction

The chirps as short-time frequency sweeps are widely used for different purposes. Also, using of chirp excitation is promising for fast estimation of complex bioimpedance in the medical studies (Nahvi and Hoyle, 2009). Usually, chirps are considered as signals of many cycles of sinusoidal oscillation with a changing „instantaneous" frequency. In the simples cases, the frequency of a chirp rises linearly (so-called up-chirp) or falls in the same manner (down-chirp). However, non-linear (quadratic, exponential, etc.) chirps have been used as well.

Generally, a sine-wave chirp signal with instantaneous phase $\theta(t)$ can be described mathematically as $V_{ch}(t) = sin(\theta(t)) = sin\left(2\pi \int f(t)dt\right)$, with "instantaneous" frequency $f(t) = (\theta(t)/dt)/2\pi$ (Fig. 29a).
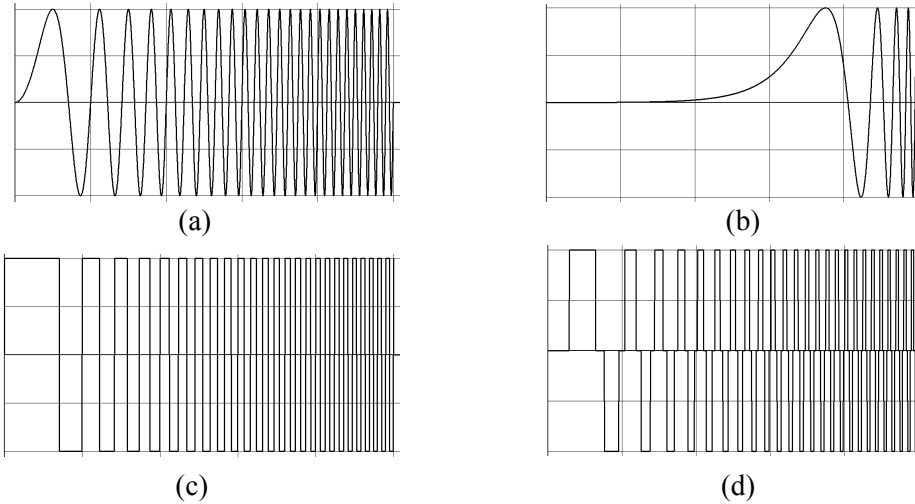

Figure 29. Selection of the chirp waveforms: $T_{ch} = 0.5$ ms, $f_0 = 0$ ($f_0 = 1$ Hz for (b)), $f_{fin} = 100$ kHz; adapted from (Paavle, Min, Ojarand, and Parve, 2010)

If the instantaneous frequency changes accordingly to some power function of n-th order, then this change (chirp rate) can be expressed as $k_{ch} = \left(f_{fin} - f_0\right)/T_{ch}{}^n$, where f_0 and f_{fin} are the initial and final frequencies, respectively, and T_{ch} is the pulse duration. This kind of chirp with unity amplitude expresses as

$$V_{ch}\left(t\right) = sin\left(2\pi\left(f_0 t + k_{ch} t^{n+1}/(n+1)\right)\right) \qquad (3.11)$$

In the case of $n = 1$ we have the linear chirp with constant rate $k_{ch} = (f_{fin} - f_0)/T_{ch}$. The rate of an exponential chirp (Fig. 29b) is defined as $k_{ch} = (f_2/f_1)^{t/Tch}$, and chirp of this type expresses as

$$V_{ch}(t) = \sin\left(2\pi f_0 T_{ch}(k_{ch} - 1)/\ln(k_{ch})\right) \qquad (3.12)$$

In practice, generating of discrete signals is more convenient. The adequate chirps are so-called signum-chirps with instant values $V_{sgn}(t) = \text{sign}(V_{ch}(t))$ (Fig.29c). In addition, the advantages of signum-chirps are the unity crest factor and higher energy content comparing with the respective sine-wave chirps of the same length. Unfortunately, the worse purity of spectrum accompanies (Fig. 33b). A method for supressing higher order harmonics of the signum-chirp is shortening the duty cycle by certain degrees per a quarter-period (Annus, Min, and Ojarand, 2008). In Fig. 29d, a chirp with 30° shortening is shown.

3.3.2 Minimum-length chirps

Usually, speaking about chirps, multi-cycle ones are regarded. However, chirps with a single cycle or even less can be generated, too.

It is evident that for a chirp of L cycles the instant phase must be $\theta(t) = 2\pi L$ at $t = T_{ch}$, where L can be an integer or fractional number of cycles. It follows from eqn. (3.12) that for n-th order power chirps the signal length is strongly determined (see nomogram in Fig. 30) as

$$T_{ch} = \frac{(n+1)L}{nf_0 + f_{fin}} \qquad (3.13)$$

Thus, in the case of single-cycle linear chirp the pulse duration is $T_{ch} = 2/(f_0 + f_{fin})$. This particular case is illustrated in Fig. 31. Similarly, one can show that for exponent chirp the duration of a pulse is (Fig.32)

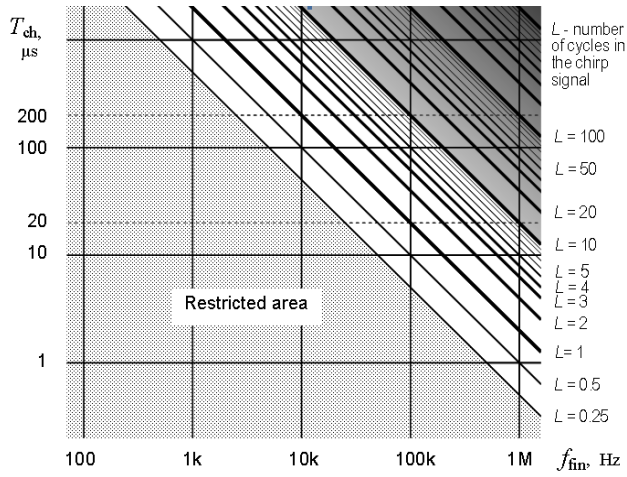$$T_{ch} = \frac{L}{f_{fin}} \ln \frac{f_{fin}}{f_0} \qquad (3.14)$$

Figure 30. Nomogram of relationship between the linear chirp duration T_{ch}, upper frequency f_{fin} ($f_0 = 0$) and number L of cycles for $n = 1$; adapted from (Paavle, Min, Ojarand, and Parve, 2010)
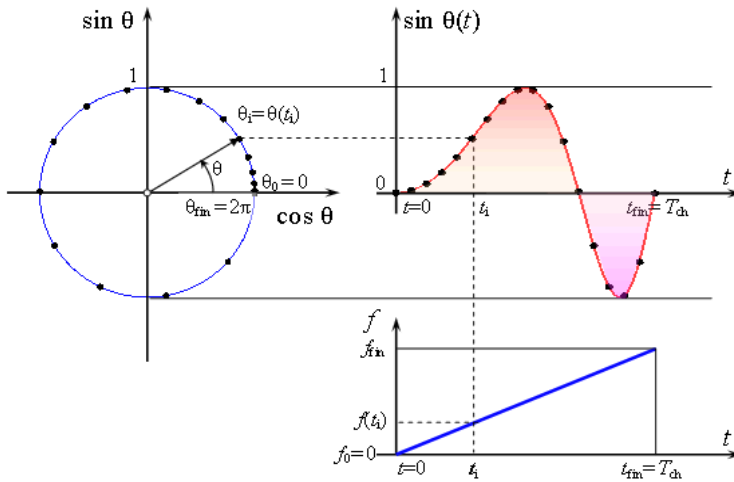

Figure 31. Waveform genesis of a single-cycle linear chirp at $f_0 = 0$; adapted from (Paavle, Min, Ojarand, and Parve, 2010)
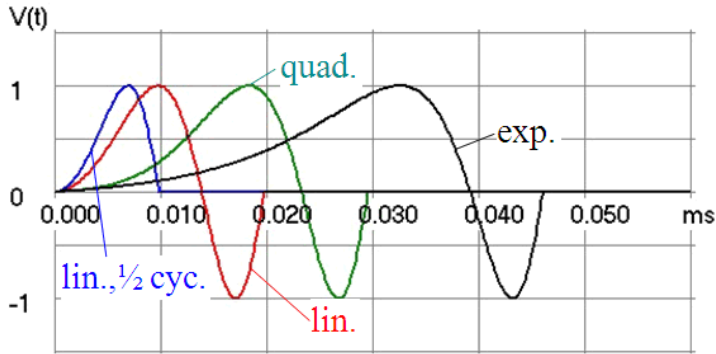
Figure 32. Comparison of linear, quadratic and exponent half- and single-cycle chirps with $f_0 = 1$ kHz and $f_{fin} = 100$ kHz; adapted from (Paavle, Min, Ojarand, and Parve, 2010)

Broadband short chirps accompany with a certain level of DC, which can be disturbing for some applications.

3.3.3 Spectral properties of the minimum-length linear chirps

The useful energy E_{BW}, corresponding to the chirp bandwidth $BW = f_{fin} - f_0$, is less than the total energy of a generated chirp E_{tot}, while the values both of them depend on the chirp length, waveform and spectral nature. In the case of sine-wave chirps with $L \rightarrow \infty$ the ratio $\delta_E = E_{BW}/E_{tot} \rightarrow 1$.

In Fig. 33 normalized magnitude spectra ($20\log(|V(f)|/|V(f_0)|$ vs. f) of the sine-wave and signum-chirps with different lengths L are shown. The shape of the spectra is oscillating and depends on the lenght L.

To improve the flatness of the spectrum, a kind of windowing of chirp pulses could be used, however, this accompanies with considerable loss of total energy and power of signals (Paavle, Min, Ojarand, and Parve, 2010).
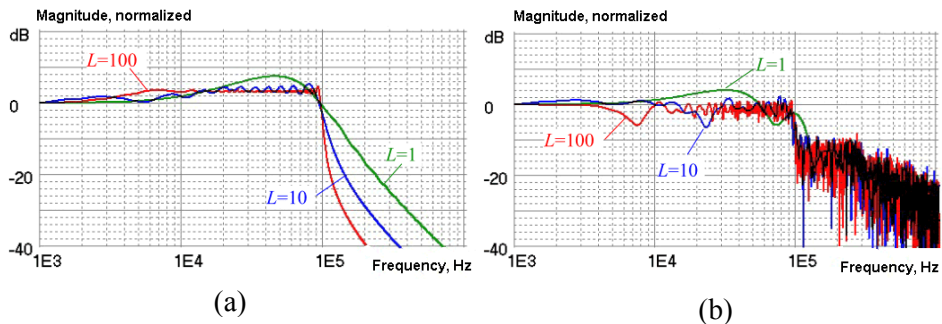

Figure 33. Magnitude spectra |Vch | of linear chirps from 0 to 100 kHz: (a) sine-wave chirps; (b) signum-chirps; adapted from (Paavle, Min, Ojarand, and Parve, 2010)

3.3.4 Spectral properties of the short nonlinear chirps

The following section is a brief summary of the paper presented in appendix A. (Ojarand, Annus, Land, Parve, and Min, 2010).

Unlike the linear chirp, which has a constant chirp rate, a nonlinear chirp has varying chirp rate during the excitation interval. Spectral properties of the chirp waveform depend on quickening (or slowing) of the frequency change i.e. acceleration or deceleration of the frequency change. If the growth (or reduction) of the frequency change is exponential then the frequency of the signal varies exponentially as a function of time t :

$$f_i(t) = k_{ch}^t f_0 \qquad (3.15)$$

The advantage of using an exponential relationship is in ease of realization, Fig. 34 depicts a simplified structure of the exponentially modulated chirp waveform source.

Output signal V_{ch} of the voltage controlled oscillator (VCO) can be expressed as follows:
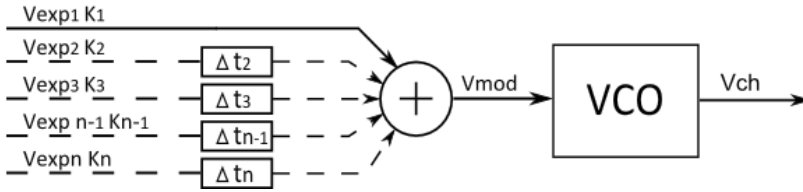
Figure 34. Exponentially modulated chirp waveform source

$$V_{ch} = V_p \sin(2\pi(f_0 t + \int_0^t K_f V_{mod} \, dt)) \qquad (3.16)$$

where V_p is a peak amplitude of the signal an K_f is the frequency sensitivity of the VCO in Hz/V. In current study V_p is kept constant at the 1V level. Peak value of the modulating signal V_{mod} is also kept at the 1V level. Input voltages V_{exp} can be expressed as

$$V_{exp} = V_o e^{kt} = V_o e^{t/\tau} \qquad (3.17)$$

where V_o express an initial voltage, k is growth constant and τ is the e-folding time ($\tau = 1/k$). In the simplest case only one exponentially changing voltage V_{exp} drives a VCO. However, it was found, that by combining two or more exponential signals with different growth factors it is possible to generate chirp waveforms with substantially steeper slope of spectral curve above the cut-off frequency, compared

to linearly modulated chirp or nonlinearly modulated chirp with one exponentially changing voltage V_{exp}. Waveforms and normalized spectra of the short chirps (so called „titlets") used for comparison are shown in Fig. 35.
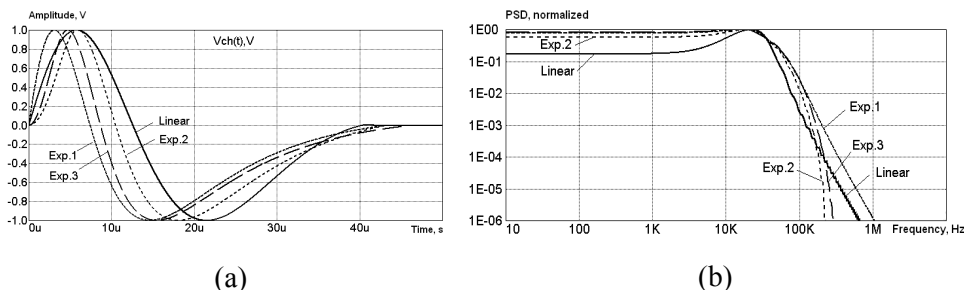

(a)   (b)

Figure 35. Titlet waveforms (a) and normalized power density spectra (b)

As it can be seen in Figs 35b, a multislope exponential modulating signal allows substantially steeper slope above the cut-off frequency. The cut-off frequency here is the frequency where the spectrum reaches a half-power limit (this is not the same as f_{fin} used in previous section).

PSD curves, where the spectra are normalized separately for each signal are not suitable for the comparison of the energy content of different signals since the maximum values are not equal. To compare the spectral content of different signals, they must be normalized against one of them. Calculation of the half-power limit energy content of the linearly and exponentially modulated short chirps shows that the waveforms Exp1 and Exp3 have 23 % more energy in the usable frequency range compared to its linear counterpart.

3.3.5 RMS magnitudes of normalized chirp signals

Chirp waveforms with different durations or spectra normalized to the maximum values of the spectra are not convenient for the comparison with other waveforms.

Fig. 36 shows the spectra of the sinusoidal and signum chirps, waveforms of which are normalized to the unit values. The amplitude and duration of the waveforms are ± 1 and 1 respectively.

In Fig. 37 the normalized waveform of the exponentially modulated short chirp and the corresponding spectrum are shown. This waveform is similar to the waveform Exp2 in Fig. 35a, however overall duration of the signal is fixed to 1. As a consequence, only five frequency bins (except DC) are over the half-power limit. If more frequency bins are desired, the observation period T_p must be increased although, this leads to the lower RMS magnitudes of the spectrum.

71
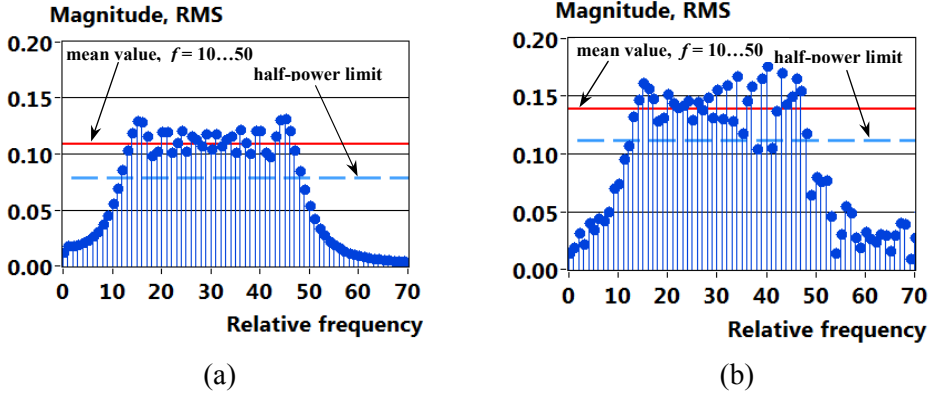
Figure 36. RMS spectra of the normalized sinusoidal chirp (a) and normalized signum chirp (b); relative frequency of both waveforms is changing from 10 to 50

In Fig. 38a and Fig. 39a dependency of the mean RMS magnitudes on a number of frequency bins are shown. Mean RMS values are calculated using all RMS magnitudes in the corresponding frequency range (including the values which are below the half-power limit). In Fig. 38b and Fig 39b deviations from the mean RMS values are shown. Deviation D is calculated relative to the running mean value of the magnitudes as $D = (((x_{max} - x_{min})/2)/x_{mean})100\,[\%]$.
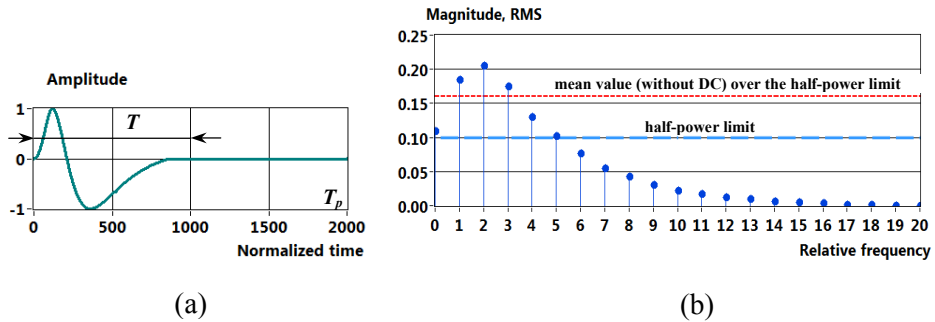
Figure 37. Normalised waveform of the exponentially modulated short chirp (a) and its magnitude spectrum (b); duration of the signal $T = (1000/2000)\,T_p$ and $T_p = 1$

Sinusoidal chirps

Magnitude, RMS (mean)

$$\dfrac{A}{\sqrt{2}}\,\dfrac{1}{\sqrt{k}}$$

# of frequency bins

Deviation from the mean magnitude, %

# of frequency bins

(a) (b)

Figure 38. Dependency of the mean RMS magnitudes on frequency range (number of frequency bins) (a) of the linear sinusoidal chirp, and corresponding relative deviation of the magnitudes from the mean magnitudes (b); frequencies are in the range from 10 to 50
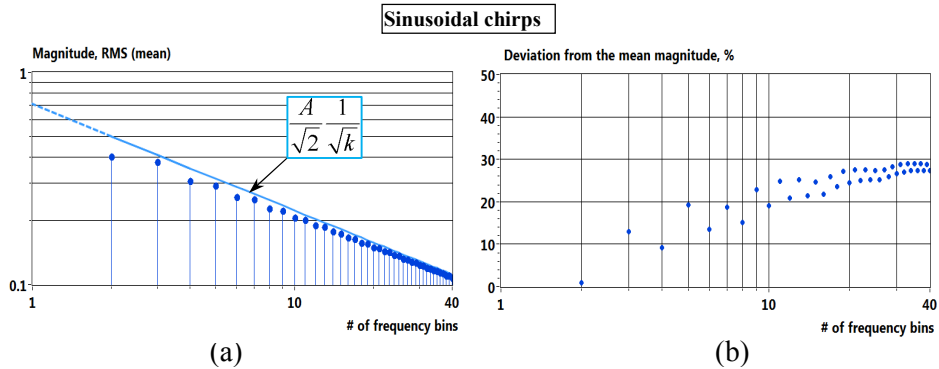

Signum chirps

Magnitude, RMS (mean)

$$\dfrac{4}{\pi}\,\dfrac{A}{\sqrt{2}}\,\dfrac{1}{\sqrt{k}}$$

# of frequency bins

Deviation from the mean magnitude, %

# of frequency bins

(a) (b)
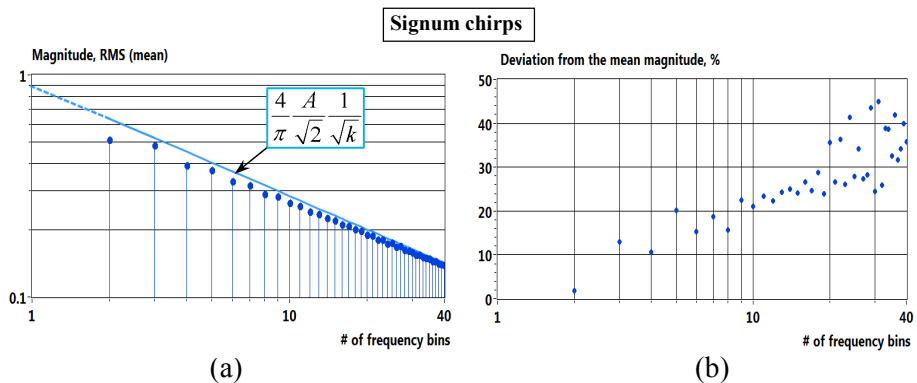
Figure 39. Dependency of the mean RMS magnitudes on frequency range (number of frequency bins) (a) of the linear signum chirp, and corresponding deviation of the magnitudes from the mean magnitudes (b); frequencies are in the range from 10 to 50

3.4 Conclusions of the chapter

Mean magnitudes of useful spectral components of the short rectangular pulses (Fig.24) and short chirps (Fig. 35, Fig 37) are lower, compared to other signals discussed here, since the waveforms with zero level sections contain less energy. Reducing a length of zero level sections does not solve the problem, since an increase of the waveform lenght T in the obseravtion period T_p accompanies with a narrower bandwith of the signal. For example: after setting $T = T_p$ for a signal shown in Fig. 37, only one (the first) frequency bin will be over the half-power limit. And vice-versa: decrease of T in the same observation period T_p accompanies

a wider and smoother magnitude spectrum, with more components over half-power limit, but the value of this limit and the magnitudes of the components will be lower proportionally to T/T_p.

Spectral components power of the rectangular waveform (Fig. 25) is concentrated into first the harmonic. 81% of total signal energy is focused there and RMS magnitude of it is 0.9. However, if the maximum energy efficiency is a goal, optimized shortened rectangular wave (SRW) waveform (Fig. 26) constitutes 92.3% of the total energy. Even so, RMS value of the first harmonic of SRW waveform reaches only 0.827. This means that the power of the first harmonic of the regular rectangular waveform is slightly higher.

RMS spectrum of MLS waveforms (Fig. 26) becomes quite slow to decay away as the number of frequency bins k increases. An analysis of this signal type shows that the mean value of the RMS magnitudes of the half-power range frequency components of the MLS signal are decaying at a rate of $1/\sqrt{k}$ compared to the RMS magnitude of the fundamental frequency of the rectangular waveform. Later RMS magnitude is higher by a factor of $4/\pi$ than the RMS magnitude of the sinusoidal waveform with the same amplitude. However, calculations show that the mean RMS magnitudes of the half-power range frequency components of the MLS signal are slighty less, by factor of $B \approx 0.93$.

An analysis of the chirp signals shows that a mean value of the RMS magnitudes of spectral components of the chirp signal is decaying at a rate of $1/\sqrt{k}$ compared to the RMS magnitude of the single frequency signal, where $k = |f_{fin} - f_0|$. Magnitudes of the spectral components of the rectangular waveform (signum chirp) are higher by a factor of $4/\pi$ compared to the sinusoidal chirp. It may be concluded, that the power of the spectral components of MLS and signum chirp waveforms is distributed almost similarly. Yet, there are also some differences. At first, the number of the spectral components of the MLS signal is fixed by its order n, and secondly, a shape of the spectrum is smooth with a fixed relative deviation near $\pm 15\%$ from its mean value (later is defined by the half-power limit). The relative deviation of the magnitudes of the signum chirp depends on its frequency range and reaches 3 times higher values (compared to the MLS) for the 30 frequency bins (Fig. 39b). A ripple of the magnitudes of the sinusoidal chirp is less (Fig 38b), however a mean magnitude is also less (by factor of $4/\pi$).

In Section 3.3.4 it is shown that nonlinearly modulated short chirps yield a flat spectrum shape and a higher energy efficiency compared to its linear counterpart. Nevertheless, as already explained at the beginning of a section a mean magnitudes of useful spectral components of the short chirps are lower, compared to other signals discussed in this chapter.

Considering that the power is proportional to the RMS magnitude squared, the mean power of spectral components over the 0.5 limit of the MLS and chirp signals decreases approximately by $1/k$ law and approximately by $1/k^2$ law in case of short pulses.

4   SPECTRALLY SPARSE WIDEBAND EXCITATION SIGNALS

4.1   Multisine waves

4.1.1 Spectrally dense and sparse signals

In the case of spectrally dense wideband excitation, a fixed amount of energy is distributed between a large number of frequency components k. Since the mean value of RMS magnitudes of these components decreases typically by $1/\sqrt{k}$ law (as it is shown in previous chapter), the magnitudes become low.

The advantage of the excitation signal with a dense frequency distribution is that it gives a more detailed shape of the spectrum of the response signal. However in cases where the spectrum of the response signal is smooth and characteristic changes fall into 1-2 frequency decades, as illustrated in Fig. 40, a waveform with 5 to 10 frequency components is sufficient.

(a)   (b)
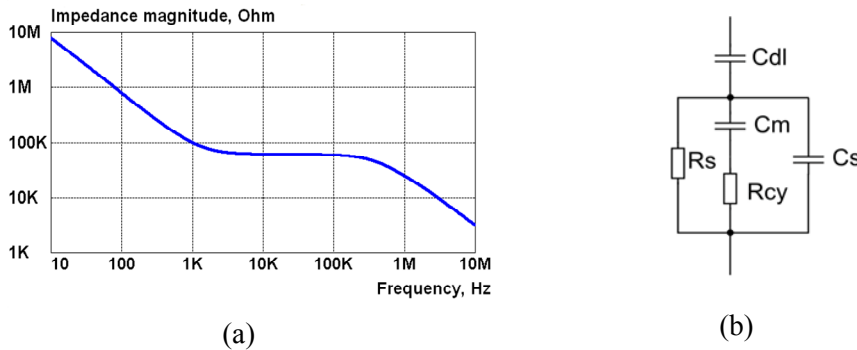
Figure 40. A magnitude spectrum of the impedance of a single cell in saline suspension shown in Figure13 (a) and simplified equivalent circuit (b); C_{dl} = 2 nF, C_m= 1 pF, C_s = 5 pF, R_s = 60 kΩ and R_{cy} = 100 kΩ

It should be noted that the rise of impedance in low frequency area is caused by the polarization of electrodes (double layer effect) and does not provide useful information about the properties of object. To enhance performance, it is reasonable to concentrate the signal's energy right on the specific frequencies of interest.

It is essential to accesss the information which characterizes the cell's structural properties and is related to β-dispersion area. In the current case this area is placed in between 20 kHz to several MHz. It is obvious, that equally spaced, dense frequency distribution is not adequate for this task.

Spectrally sparse signals possess discrete spectra with appropriate sparse distribution of frequency components of interest.

4.1.2 Basics

A well-known example of spectrally sparse signal is the multisine wave which in general case can be used also for dense frequency distribution. A multisinewave excitation (later here as multisine), $S_{exc}(t)$, between the frequencies f_1 to f_k, of k sinusoidal components can be expressed as

$$S_{exc}(t) = \sum_{i=1}^{i=k} A_i \cdot \sin(2\pi f_i + \Phi_i) \qquad (4.1)$$

where A_i is the amplitude of the i-th component, and Φ_i is the initial phase of the i-th component. If the amplitudes A_i of all components are assigned the same value, A_N, then, the RMS magnitudes of all components are equal each other and the RMS magnitude of the multisine becomes

$$M_{RMS} = \sum_{i=1}^{k} \sqrt{M_{RMS}^2(i)} = M_{RMS}(i)\sqrt{k} = \frac{A_N}{\sqrt{2}}\sqrt{k} \qquad (4.2)$$

In this case the RMS magnitude of the sum of the sine waves depends only on the number of components. However, the amplitude of the sum of the sinusoidal components depends also on the initial phase, Φ_i, of the components. The ratio of the peak value to the RMS value of the excitation signal is called peak factor (PF), or crest-factor (CF). The difference of these two factors is in the definition of the peak value. When using PF, the peak value is defined as $(V_{pk}{}^+ - V_{pk}{}^-)/2$, and when using CF, the peak value is defined by the maximum value of absolute values of the $V_{pk}{}^+$ and $V_{pk}{}^-$. Since in process of optimization the use of PF might cause significant asymmetry with respect to zero, especially when using just a few sinusoidal components (Ojarand, Land, and Min, 2012) CF is used later here.

   Varying the values of the initial phases allows one to find the lower CF values. There is much research done in an attempt to achiev the best set of phases, Φ_i, for multisines that contain up to 40 frequencies (Rees and Jones, 1991) or even more. Example of the multisine with 4 frequency components f_1, $3f_1$, $5f_1$, $7f_1$ and $A_i = A_N = 1$ is shown in Fig. 40.

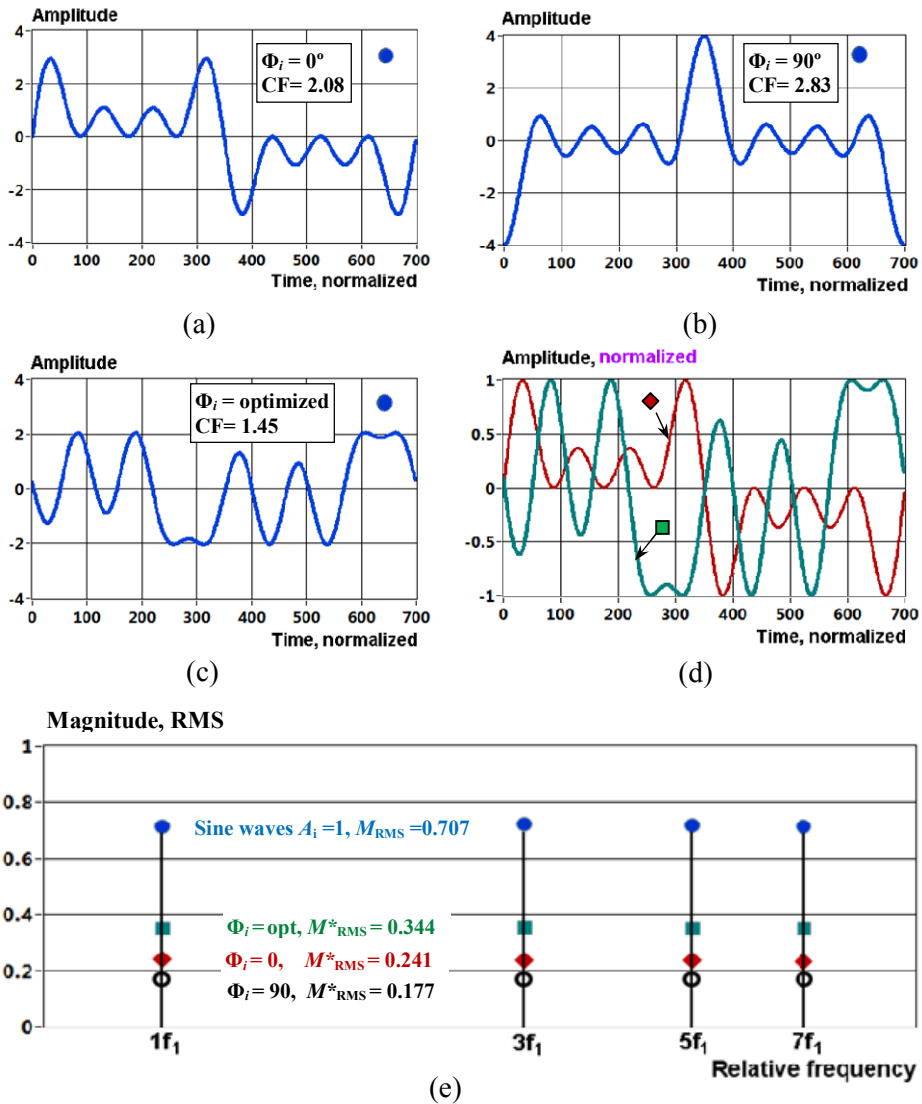Figure 41. Multisine with 4 sine wave components and frequencies f_1, $3f_1$, $5f_1$, $7f_1$ in cases where all initial phases are 0º (a), all initial phases are 90º (b) and initial phases are optimized for best CF (d); (d) - waveforms (a) and (c) after normalizing their amplitudes to ± 1V; (e) - magnitudes of the sine wave components A_i and normalized magnitudes of the multisines with different initial phases

4.1.3 Merit of the optimized multifrequency signal

In addition to the PF and CF there are more performance criteria like PIPS (Performance Index for Perturbation Signals) and others proposed for excitation. These are often also called perturbation signals.

The main motivation for searching signals with a lower CF is that the allowed maximum peak value of the excitation signal is given (fixed). We found that, in this case, normalizing the peak value of fixed length signals relative to A_N (which is taken equal to 1) with equal or near equal RMS magnitudes of frequency components allows compendious performance comparison with different multifrequency excitation waveforms (Ojarand, Land, and Min, 2012). The RMS values of the frequency components of a normalized multisine can be calculated as

$$M^*_{rms} = \frac{1}{\sqrt{2}} \frac{A_N}{Max(\left|A_i^+\right|, \left|A_i^-\right|)} \tag{4.3}$$

where M^*_{rms} denotes normalized RMS magnitude of the spectral components of the multisine waveform. More particularly, M^*_{rms} may be a RMS magnitude of voltage V^*_{rms} or current I^*_{rms}, depending on the type of exitation source. Normalized RMS magnitude shows how much magnitude of the frequency components is left if the amplitude of the sum of sine waves is kept in the unit limits ($\pm$ 1V). As illustrated in Fig. 41e, in case of 4 added sinewaves a normalised magnitude of the frequency components may be 4 times less (worst case) and also near 2 times less (best case) if the initial phases of the sinewaves are chosen properly (optimized). Normalized RMS magnitude of the multisine is directly related with its crest factor:

$$CF = \frac{A_N}{\sqrt{k} \cdot M^*_{rms}} \tag{4.4}$$

$$M^*_{rms} = \frac{A_N}{\sqrt{k} \cdot CF} \tag{4.5}$$

where k is a number of sinewaves (and frequency components). A multisine with minimum CF provides the highest normalized RMS magnitudes of the spectral components.

4.1.4 Maximum and minimum CF

Setting all the phases to 90 degrees gives the largest CF, since peaks of all the individual cosines line up (see Fig. 41b). If the amplitude A_i of all components are held at same value, A_N, then $A_{max} = k \times A_N$ and the maximum crest factor of the multisine can be found using eqn. (4.2) as

$$CF_{max} = \frac{A_{max}}{M_{RMS}} = \frac{k\,A_N\sqrt{2}}{A_N\sqrt{k}} = \frac{k\sqrt{2}}{\sqrt{k}} = \sqrt{2k} \qquad (4.6)$$

The minimum normalized RMS value can be found using eqn. (4.5) as

$$M*_{rms.min} = \frac{A_N}{\sqrt{2k}\sqrt{k}} = \frac{A_N}{k\sqrt{2}} = \frac{M_{rms.i}}{k} \qquad (4.7)$$

where $M_{rms.i}$ is a RMS magnitude of the single sinewave component.

Minimization of the multisine CF is not so straightforward it can be more formally stated as the minimization of a non-linear function (Rees, Jones, and Evans, 1992). There are several algorithms and methods proposed to overcome the problem, e.g. nonlinear Chebyshev approximation method (Guillaume, Schoukens, Pintelon, and Kollar, 1991) and geometric discrepancy criteria (Mittelmann, Pendse, Rivera, and Lee, 2006), however, computed solutions can only be guaranteed to be local optima.

There is also a simple equation proposed by Schroeder (Schroeder, 1970). In case of equal amplitudes A_i of the components k

$$\Phi_i = \Phi_1 - \frac{\pi\,i^2}{k} \qquad (4.8)$$

The Shroeder method produces better CF for the consecutive harmonic frequencies, e.g. for the 10 consecutive harmonics $i = [1, 2, 3, 4,...10]$ the Shroeder method gives CF = 1.89, when the best know optimization gives CF = 1.40 (difference 35 %). In case of non-consecutive frequency distributions, e.g. with 10 prime harmonics $i = [3, 5, 7, 11,13, 17, 19, 23, 29, 31]$ the Shroeder method gives CF = 2.24, when the best know optimization gives CF = 1.48 (a difference is 51 %). The best known values are calculated using the method described in the next section.

With a lower number of frequency components all the possible initial phase combinations can be checked for the best CF with a given phase resolution $\Delta\Phi$. A number of calculation steps for this exhaustive search is expressed as

$$n_{stp} = \left(\frac{360}{\Delta\Phi}\right)^{k-1} \qquad (4.9)$$

For the 5 frequency components and a phase resolution of 1 degree, the number of calculation steps is near 1.7×10^9 and the calculation lasts around 37 hours in case of using LabView software environment and a standard desktop PC. In case of 6 frequency components and the same phase resolution $n_{stp} \approx 6 \times 10^{12}$ and the calculation would last around 150 days. In case of large number of frequency components another possibility for finding initial phases, which are providing

better CF, is a search with randomly generated initial phases. Typical results of such a search are shown in Fig. 42.
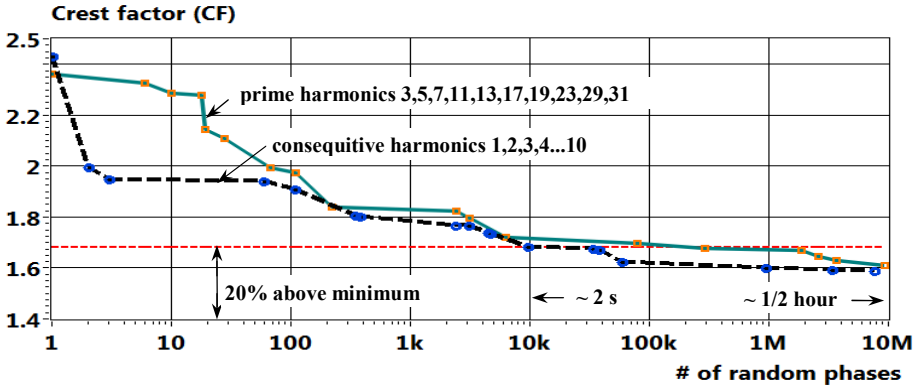

Figure 42. Samples of the dependency of the CF on a number of random initial phases of 10 added sinusoidal waves; consecutive harmonics 1, 2, 3, 4, ..., 10 - thick dashed line, and prime harmonics $i = [3, 5, 7, 11, 13, 17, 19, 23, 29, 31]$ – solid line; calculation time with 10^4 random phases takes around 2 s (LabView software, standard desktop PC)

The minimum value of CF depends on the distribution of frequency components. If the components are very sparse, CF tends to its maximum value $\sqrt{2k}$ (eqn. (4.6) since in some part of the waveform individual peaks are lining up, e.g. in case of logarithmic distribution of harmonics $i = [1, 10, 100]$, (Fig. 43). An exhaustive search using all phase combination with a resolution of 0.1 degrees gives a minimum CF = 2.40944, which is only 1.6 % below the maximum value.
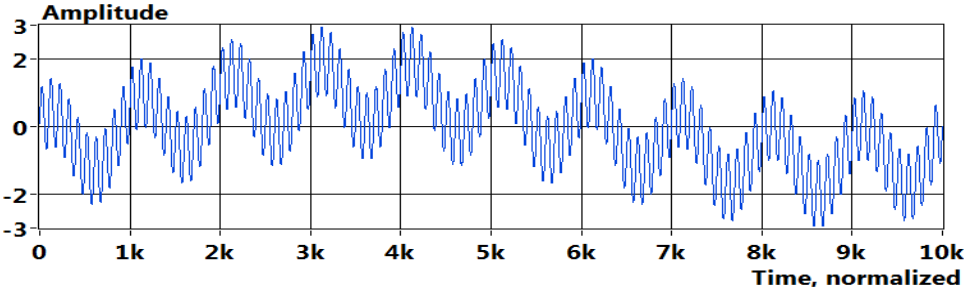
Figure 43. Waveform of the multisine optimized for the minimum CF with the harmonic components $i = [1, 10$ and $100]$

4.1.5 A novel empirical method for the minimization of CF

Examination of amplitude minimums of the multisines shows that typically there are several equal minimums if the combinations of initial phases are changing in the range from 0 to 360 degrees or more.
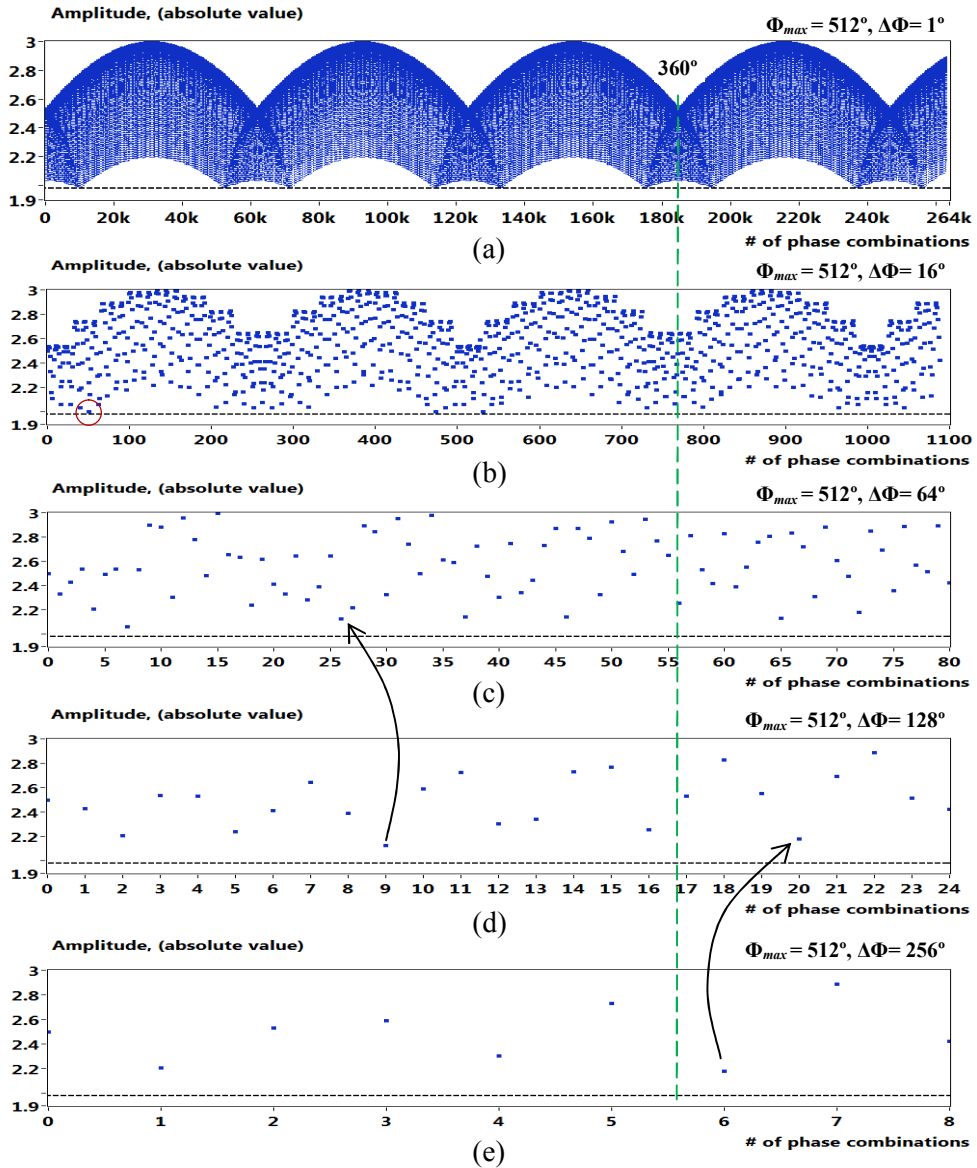
Figure 44. Dependency of the absolute values of the amplitudes of multisine with three consecutive harmonics $i = [1,2,3]$ in the combination of initial phases; initial phase of the third frequency component is fixed to 0 and other two are changing in the range from 0° to 512° with a different phase step $\Delta\Phi$ (a)-(e)

As an example, dependency of the absolute values of the amplitude of multisine with three consecutive harmonics $i = [1, 2, 3]$ in the combination of all initial phases is shown in Fig. 44. Points in the graphs represent the sums of the amplitudes of sinewave components with a unit amplitude ($A_i = 1$) and different initial phase

combinations Φ_{ij}, where i is a number of harmonic and j is a phase step number in the range from 0 to $j_{max} = \Phi_{max} / \Delta\Phi$. The initial phase of the third frequency component is fixed at 0 and the other two phases are changing in the range from 0 to j_{max} in a consecutive loops starting from the first component. It must be noted that a pattern of the amplitude values depends on the order of changing phases (e.g., 3, 2, 1 versus 1, 2, 3); however, the minimum level marked with a dotted line in Fig. 44 remains the same. In the current case, 12 equal minimums appear in the range from 0 to 360 degrees.

It was noticed that a pattern of amplitudes retains similarity when a phase step $\Delta\Phi$ is changing two times (or other base-2 number times). It was also found, that a phase combination corresponding to the minimum amplitudes with a large phase step appear also in the next pattern with a smaller phase step. As an example: a minimum at $ij = 6$ with the phases 512º- 0º- 0º and $\Delta\Phi = 256$º (Fig. 44e) excists also at $ij = 20$, $\Delta\Phi = 128$º (Fig. 44d). A minimum at $ij = 9$ with phases 128º-512º-0 and $\Delta\Phi = 128$ (Fig. 44d) excists also at $ij = 26$ and $\Delta\Phi = 64$ (Fig. 44c). Similar relationships were found with other distributions of frequency components. Observations described above led to the hypothesis, that the initial phases of the frequency components which produce a minimal amplitude of the sum could be found using sequential searches with limited number of phase steps. A remainder: in case of fixed amplitudes of the components, a minimum amplitude of the sum of sinewaves corresponds to the minimum CR and maximum normalized RMS magnitude $M^*_{rms.max}$).

Computer simulations with different frequency distributions proved that a recursive algorithm with 2 phase steps in each iteration can be used for finding near optimal initial phases of the sinewaves $\Phi_{min(i)}$. Fig. 45 gives a flowchart describing the algorithm. However, as with other known methods, computed phases can only be guaranteed to be local optima since the result of the calculations depends also on a frequency distribution (how the frequencies of the sinewaves are distributed on the frequency axis) and initial parametres Φ_{min}, Φ_{max}. In Fig. 46 a part of the graph in Fig. 44b is zoomed out near the amplitude minimum at index $ij = 51$. As shown by dashed lines, the actual minimum could be also between the indexes 62 and 63, but it cannot be detected with a current grid.

The performance of the new method was further tested by a variation of initial parametres Φ_{min} and Φ_{max}. The results of several tests are presented in Fig. 47. Φ_{min} was fixed to 0º and Φ_{max} was changed from 1º to 400º degrees with a step of 0.1º (Fig. 47a, b) and 1º (Fig. 47b, d, e). In all cases minimal CF was searched with a phase resolution $\Delta\Phi$ down to 0.1º and a deviation from CF_{min} was calculated. Tests showed that a deviation of the minimum CR detection results depends on the number of frequency components and distribution of these components. Deviation is higher in case of consecutive harmonic frequency components and
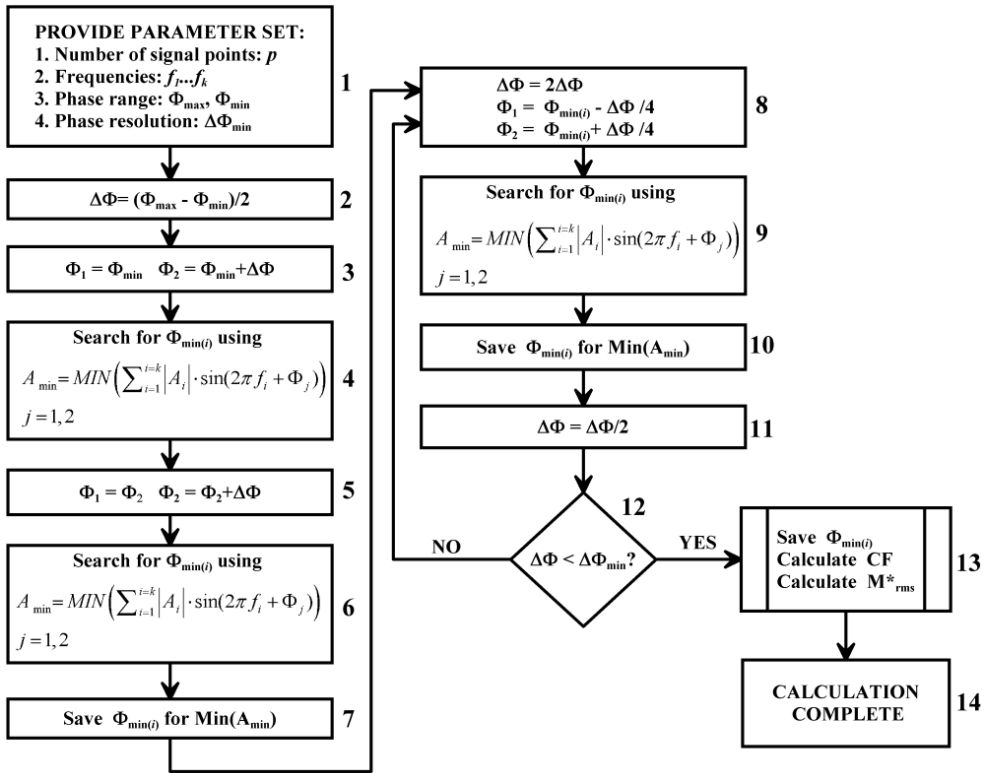
PROVIDE PARAMETER SET:
1. Number of signal points: p
2. Frequencies: $f_l...f_k$
3. Phase range: Φ_{max}, Φ_{min}
4. Phase resolution: $\Delta\Phi_{min}$ — **1**

$\Delta\Phi = (\Phi_{max} - \Phi_{min})/2$ — **2**

$\Phi_1 = \Phi_{min}$ $\Phi_2 = \Phi_{min}+\Delta\Phi$ — **3**

Search for $\Phi_{min(i)}$ using
$$A_{min} = MIN\left(\sum_{i=1}^{i=k}\left|A_i\right|\cdot\sin(2\pi f_i + \Phi_j)\right)$$
$j = 1,2$ — **4**

$\Phi_1 = \Phi_2$ $\Phi_2 = \Phi_2+\Delta\Phi$ — **5**

Search for $\Phi_{min(i)}$ using
$$A_{min} = MIN\left(\sum_{i=1}^{i=k}\left|A_i\right|\cdot\sin(2\pi f_i + \Phi_j)\right)$$
$j = 1,2$ — **6**

Save $\Phi_{min(i)}$ for Min(A_{min}) — **7**

$\Delta\Phi = 2\Delta\Phi$
$\Phi_1 = \Phi_{min(i)} - \Delta\Phi/4$
$\Phi_2 = \Phi_{min(i)} + \Delta\Phi/4$ — **8**

Search for $\Phi_{min(i)}$ using
$$A_{min} = MIN\left(\sum_{i=1}^{i=k}\left|A_i\right|\cdot\sin(2\pi f_i + \Phi_j)\right)$$
$j = 1,2$ — **9**

Save $\Phi_{min(i)}$ for Min(A_{min}) — **10**

$\Delta\Phi = \Delta\Phi/2$ — **11**

12 — $\Delta\Phi < \Delta\Phi_{min}$? — NO / YES

Save $\Phi_{min(i)}$
Calculate CF
Calculate M^*_{rms} — **13**

CALCULATION COMPLETE — **14**

Figure 45. Flowchart of an algorithm for calculation of optimal phases of sine waves - $\Phi_{min(i)}$ of a multisine

Amplitude, (absolute value)
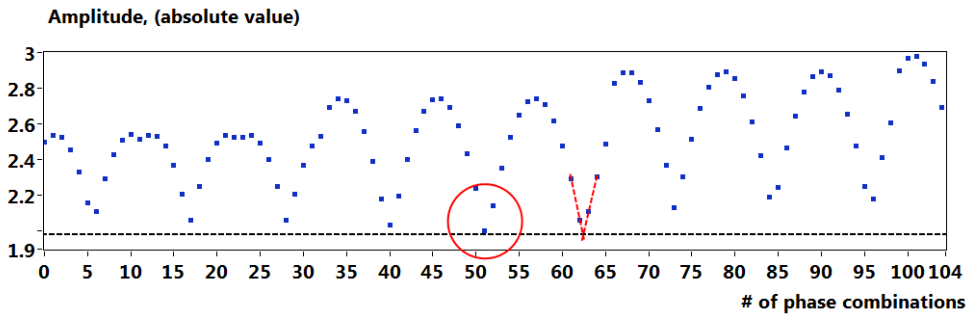
# of phase combinations

Figure 46. Dependency of the absolute values of the amplitudes of multisine on the combination of initial phases zoomed out from Fig. 44b near the index of phase combinations 51

83
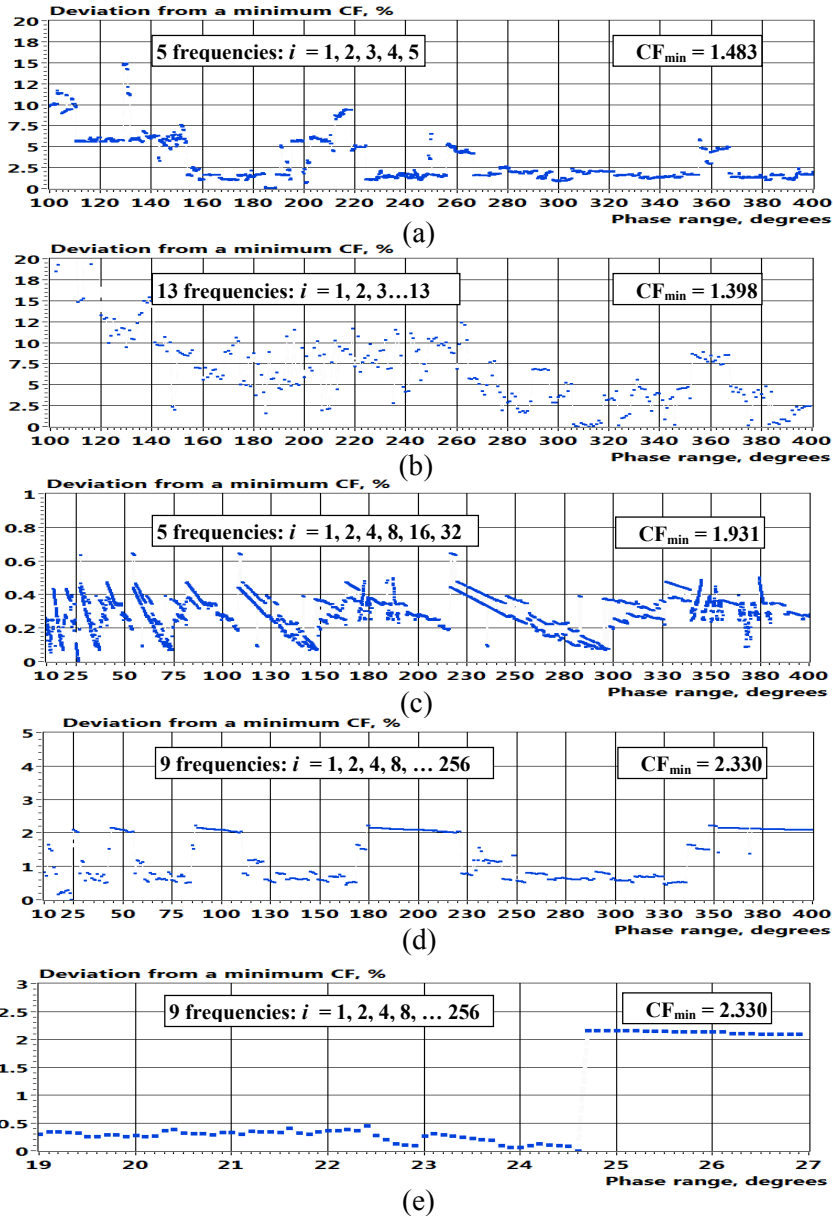
Figure 47. Deviation of the optimized crest factor from its minimum value for the different frequency distributions of multisinewaves (a)…(e)

lower in case of sparse frequency distributions, e.g. in case of binary distribution shown in Fig 47c, d, e. Choosing a proper value for Φ_{max} allows to detect CF_{min} with relative error below 1%. In case of randomly chosen Φ_{max}, a relative error will be typically less than 10 % (consecutive harmonic frequency components and Φ_{max}

between 280 and 360 degrees, see Fig. 47b). Since a number of the calculation steps of the new method is much lower compared to the exhaustive search (eqn. (4.9)), a search of initial parametres for a better result can be done relativly fast, e.g, calculations for the result presented in Fig. 47b take around 20 minutes (LabView software, standard desktop PC). By limiting the searching area and the resolution this time can be reduced.

For the new method the number of the calculation steps searching for an optimal initial phases can be expressed as

$$n_{stp}* = \log_2\left(\frac{|\Phi_{max} - \Phi_{min}|}{\Delta\Phi}\right)2^k + 1 \qquad (4.10)$$

where k is a number of frequency components. In case of k = 13, Φ_{min} = 0°, Φ_{max} = 360° and $\Delta\Phi$ = 0.1°, $n_{stp}* \approx 9.6 \cdot 10^4$. Varying additionally Φ_{max} from 1° to 360° in steps of 1°, increases an overall number of calculations to 3.4×10^7. For a comparison: an exhaustive search with the same $\Delta\Phi$ gives n_{stp} = 1.3×10^7 for k = 3 and n_{stp} = 4.7×10^{42} for k = 13.

An advantage of the new method is that the phase resolution $\Delta\Phi$ has a low impact on the number of calculation steps, e.g. in case of Φ_{max} - Φ_{min} = 360° decreasing a $\Delta\Phi$ from 1° to 0.01° increases a number of calculations less than two times.

Despite the method used, the accuracy of the calculated CF values depends on the density of the signal sampling. It was found that the number of samples per period of the highest frequency component must be at least 10, in order to achieve relative error near 1 %. Close to the Nyquist sampling-rate, the relative error could increase over 20 %. The error depends also on the number of frequency components and their distribution as illustrated in Fig. 48.

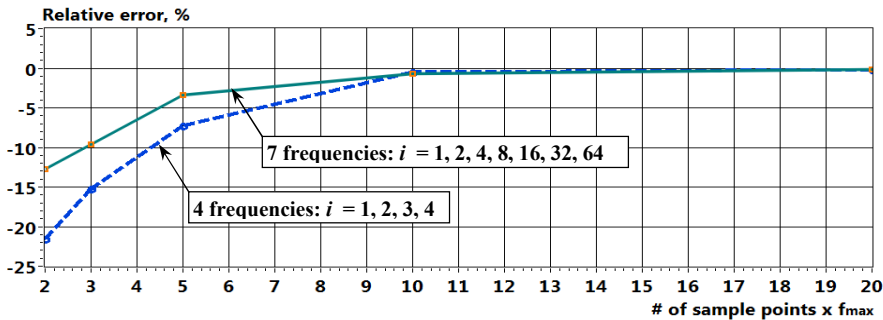Figure 48. Dependency of the relative error of CF calculation on the number of samples per period of the highest frequency component f_{max}

In Fig. 49 the results of the optimization for the consecutive frequency distribution ($i = [1, 2, 3, 4, …, 16]$), binary logarithmic distribution ($i = [1, 2, 4, 8, 16, …, 32768]$) and decimal logarithmic distribution ($i = [1, 10, 100, 1000, 10000]$) are shown.
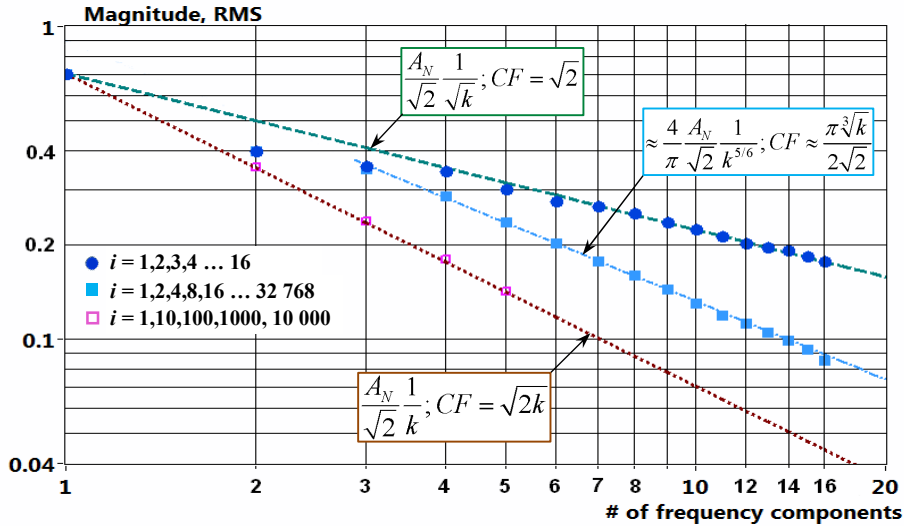
Figure 49. Dependency of the normalized RMS magnitudes of the multisine components M^*_{rms} on the number of frequency components and their distribution

For the number of frequency components below 6, a new method gives the same results as an exhaustive search. For a higher number of components the results were compared with other published data and found to be similar or better (Table 5).

Table 5. Comparison of calculated CF with a reference data, CF_{ref}

List of frequency components	k	CF	CF_{ref}	Reference
1,2,3,4,5,6,7	7	1.40	1.47	[1]
1,3,5,7,9,11,13	7	1.40	1.42	[1]
3,7,11,17,23,29,37 (NSND 2)	7	1.69	1.69	[1]
5,11,19,31,59,103,163 (NSND 4)	7	2.36	2.36	[1]
5,21,37,53,69,85,101	8	1.59	1.64	[4]
1,2,3,4,5…10	10	1.40	1.51	[2]
3,5,7,11,13,17,19,23,29,31	10	1.50	1.57	[2]
10,12,15,18,22,27,33,40,48,58,70,84,100	13	2.00	1.96	[3]
1,2,3,4,5…15	15	1.40	1.80	[2]
3,5,7,11,13,17,19,23,29,31,37,41,43,47,43	15	1.65	1.77	[2]
1,2,3,4,5…16	16	1.41	1.42	[3]

[1]- (Evans and Rees, 2000)
[2]- (Rees and Jones, 1991)
[3]- (Guillaume, Schoukens, Pintelon, and Kollar, 1991)
[4]- (Ong, Kuang, Liam, and Ooi, 2012)

To note in Fig 49, the normalized RMS magnitudes of equally distributed and optimized multisine components are close to the value

$$M*_{rms.ul} = \frac{A_N}{\sqrt{2}} \frac{1}{\sqrt{k}}$$

(4.11)

if $k > 3$. The highest values, which correspond to the $CF = \sqrt{2}$ are marked with a upper dashed line in Fig. 49. In case of very sparse distribution of frequency components, as decimal logarithmic distribution, normalized RMS magnitudes of optimized multisine components tend to the value

$$M*_{rms.ll} = \frac{A_N}{\sqrt{2}} \frac{1}{k}$$

(4.12)

These lowest values, which correspond to the $CF = \sqrt{2k}$ are marked with a dotted line. Normalized RMS magnitudes of the optimized multisine components of all other frequency distributions fall in between these two limiting lines. As an example: it was found, that RMS magnitudes of optimized multisine components of the binary logarithmic frequency distribution tend to the value

$$M*_{rms.bin} \approx \frac{4}{\pi} \frac{A_N}{\sqrt{2}} \frac{1}{k^{5/6}}$$

(4.13)

To note in Fig. 49 and Table 5, in some cases the RMS magnitudes of equally distributed and optimized multisine components are above the value calculated with eqn. (4.11). This means, that in some cases CF of a multisine is less than the CF of the single sinewave ($CF = \sqrt{2}$). Observation of such a waveforms shows an angularity of some of their parts. Considering the fact that a CF of the rectangular waveform is 1 and it can be composed by sinewaves, further improvement of the CF of the multisine seems possible. However, decomposition of a rectangular waveform shows, that the magnitudes of the harmonic components are decaying fast. Therefore a sum of the sinewaves with equal amplitudes can not produce a rectangular waveform.

Nevertheless, improvement of the CF by adding some higher frequency components with lower amplitudes (so called "snow lines") is possible as shown in (Guillaume, Schoukens, Pintelon, and Kollar, 1991). For example: a CF of the multisine with 13 components, shown in Table 5, can be decreased from 1.96 to 1.54 (-21%).

4.1.6 Nonlinear distortions and multisine signals

It was stated in (Rees and Jones, 1991) that if an excitation signal contains an assemblage of sinusoids with the frequencies which are prime number multiplies of

some fundamental, which itself is excluded from the signal, it provides total immunity against harmonic distortions due to even-order non-linearities. Odd-order nonlinearities are also highly reduced. Example of this type of signals is a sequence of frequencies with indexes $i = [3, 5, 7, 11, 13 \ldots]$.

Later analysis showed that it is not possible to eliminate the effect of odd-order nonlinearities simply by adjusting the harmonic content of the test signal. Multisines called *no interharmonic distortion* (NID), and *no sum, no-difference* (NSND) were defined. The NSND signal includes frequency components that are not integer multiples of each other and the input frequencies cannot be obtained as a linear combination of two, three, or four different input frequencies corresponding to NSND orders of two, three, or four, respectively (Huichin, Ingenito, and Suki, 1997). However, comparison of multisines with a different frequency distribution (presented in the first 4 rows of Table 4) by Evans and Rees (Evans and Rees, 2000) shows that the odd multisine ($i = [1, 3, 5, 7, 9, 11, 13]$) generates the smallest error due the nonliearities. It is concluded that there is no benefit in using multisines of increasing sparsity if the main aim is to reduce the effect of odd-order nonlinearities at the test frequencies. The key factor in reducing the influence of odd-order nonlinearities is the signal CF and an odd harmonic multisine provides a lower CF.

4.2   Periodical binary multifrequency signals (BMS)

4.2.1 Introduction

Multifrequency binary waveforms, with two discrete values (i.e. +A and –A or ±1 in case of normalized amplitudes) look similar to the maximum length sequence (MLS) shown in Fig. 27b. However, a sequence of pulses in the period T_p of the binary multifrequency waveform is not distributed by the rule used for generating of MLS waveforms. As a result, the shapes of the spectra of the *binary multifrequency signals* (BMS) differ from the envelope of *sin(f)/f* function. As it is shown in the following sections, the envelope of the spectrum lines of BMS may have decaying, flat or even rising shape. BMS are often also called *discrete-interval binary signals* (DIBS), but in current thesis the first abbreviation is preferred.

The earliest designs for such signals were published by Van den Bos in 1967 although he noted that J.R. Jensen had designed similar multifrequency signals in 1959 by clipping multisines. Enhanced systematic procedures for their construction were developed later in by Van den Bos and J.R. Krol (Van den Bos, 1991).

A spectrum of the periodic BMS waveform may be composed as a sum of spectra of its components (pulses above and below the zero line) as illustrated in Fig. 50. According to the Fourier principle periodic signals can be represented by a
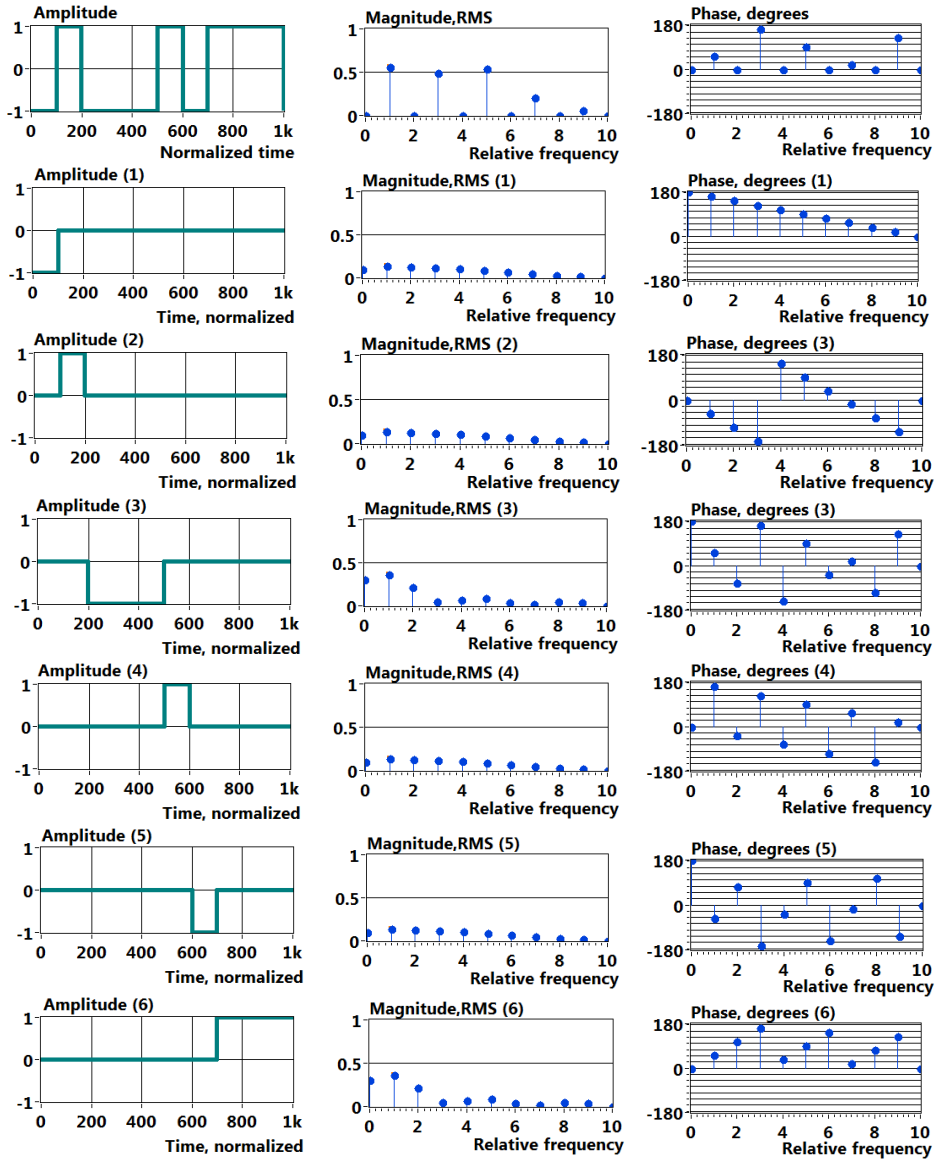
Figure 50. Waveform, magnitude and phase spectra of the BMS (upper row) and waveforms, magnitude and phase spectra of its six components (1)…(6)

set of discrete frequencies (Fourier series sum). This sum depends on magnitudes of the components and also of phases. Four waveform components: (1), (2), (4) and (5) have all excatly the same magnitude spectra, but their contribution to the magnitude spectrum of the BMS waveform depend also on phase spectra of the components. Phase spectra of the waveform components in turn depends on their

polarity and position. The complex spectrum of the BMS is a sum of complex spectra of the its components:

$$\dot{\mathcal{F}}_{BMS} = \sum_{i}^{L} \dot{\mathcal{F}}_{(i)}$$
(4.14)

where L is a number of waveform components.

BMS have always a unity value crest factor $CF = 1$ and the total energy content is 2 times higher than of multisine of the same amplitude, duration and minimum CF ($CF_{min} \approx \sqrt{2}$). However, if a multisine has all the energy spread in wanted spectral lines then BMS has usually about 60 to 80% of energy in these spectral lines. Despite this loss of energy, the RMS values of the desired frequency components of normalized BMS (with amplitudes +1 and -1) are higher than RMS values of comparable multisine signals as shown in the next sections.

4.2.2 Introduction to BMS synthesis

As illustrated in Fig. 50, magnitude spectrum of the BMS waveform depends on the lengths and positions of all components.

First attempts to synthesize BMS with the maximized energy content were described by Van den Bos in 1967 (Van den Bos, 1972). The number of elementary steps of the waveform I_s was taken equal to the number of sampling points and since $I_s > 64$ was considered, optimization via enumeration of all possible combinations was assumed to be unpractical. A computationally simple iterative algorithm was proposed where the change points of the waveform were manipulated using values generated by the random number generator. In each step Fourier coefficients were calculated and the process was continued until a complete run without further improvement occured. It was noted that the described procedure does not necessarily yield the optimum solution and needs repeating for better results. Use of symmetrical parts of the waveform for increasing of the computation speed was also proposed.

Another two step algorithm was prosposed soon (Van den Bos and Krol, 1979), which generates a multisine with the specified harmonic content being as similar as possible to a binary one, takes the sign of the time function, combines the obtained phases with the given amplitudes, generates a new multisine, and so on. The procedure requires two DFT-s in every iteration and produces a BMS which can be shown to be locally best approximate (Van den Bos, 1991).

In (Yang, Wang, Gao, Li, and Wang, 2009) a method for synthesizing of binary BMS with 2^n-th primary harmonics based on Walsh functions is proposed.

4.2.3 Synthesis of BMS via enumeration of all combinations

Computational speed has substantially increased since the first attempts of synthesizing of BMS. That allows extending the limits of synthesis via enumeration

of all combinations. Yet the number of computation steps increases still too fast when the number of signal sample points increases. Considering that a minimum length of the waveform component is equal to one sample interval, a number of all variations $\overline{V}_{max} = (n_{sp})^{n_{sp}}$, where n_{sp} is the number of sample points. Fortunately, not all the variations are needed and there are several possibilities for reducing the number of calculations as explained below.

At first, only these waveform component lengths are usable, which enable to build up the predetermined signal period T_p. This knowledge allows us to prepare arrays of the waveform components, which follow the rule

$$\sum_{i=1}^{i=L} T_k(i) = n_{sp} \tag{4.15}$$

where L is a number of waveform componets an T_k is the lenght of the waveform component in sample points changing in the range from $T_{k.min}$ to $T_{k.max}$ with a step ΔT_k. As an example: an array of waveform components with $n_{sp} = 512$, $T_{k.min} = 0$, $T_{k.max} = 256$, and $\Delta T_k = 4$ has approximately 8.25×10^6 elements, that is more than hundred times less compared to the number of all variations (1.16×10^9) under same conditions. Precalculated arrays are later usable for searching BMS waveforms with different desired shapes of the spectra and different number of spectral components. However, there are also limitations, since the waveforms with more spectral components require typically more waveform components (except when a decaying shape of the spectrum is desired). Longer waveform parts have lower impact on higher frequency area of the spetcrum and vice versa (Fig. 50).

Experiments with a different BMS waveforms showed that for a better mean RMS value, and flatter shape of the spectrum, the number of the waveform components L must be large than a number of desired spectral components k. In case of frequncy distributions containing only odd harmonics (e.g. 1, 3, 5…), $L_{min} \geq k + 1$ and in other cases $L_{min} \geq k + 2$.

Rectangular wave waveform has only two components, $T_{k.max} = T_{k.min} = n_{sp}/2$, and the power of the signal is concentrated into first harmonic. Since the total energy of the fixed lenght BMS waveform is constant, redistribution of the power of the rentangular wave waveform to higher frequency components involves shortening of $T_{k.max}$ so that it becomes less than $n_{sp}/2$. Actual lenght of $T_{k.max}$ of the MBS signal is $< n_{sp}/2$ and depends on the desired spectrum. As an example: in case of only odd harmonics $i = [1, 3, 5]$ $T_{k.max}$ is typically $< n_{sp}/3$, in case of harmonics $i = [3, 5, 7]$ $T_{k.max}$ is typically $< n_{sp}/4$. Use of shorter lenghts of $T_{k.max}$ decreases the amount of calculations substantially.

If the frequency components are odd, then the BMS waveform consists of two sets of pulses with the same configuration, only their signs are opposite as shown in Fig. 51. This allows variation of the properties of waveform components simultaneously for both sets.

Fig. 52 gives a flowchart of waveform parameters manipulation method to create a BMS. In step 1, several initial parameters (n_{sp} – the signal length, number of

points; $B-$ the set of required frequency grid, which are bin numbers according to the DFT standards; $A-$ the set of corresponding relative amplitudes) are provided to create the desired BMS.
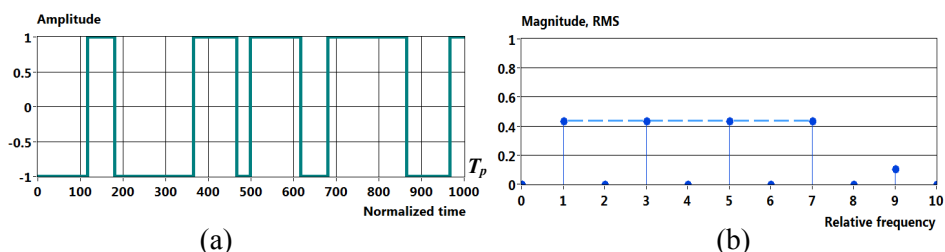

Figure 51. A synthesized binary waveform (a) and its RMS spectrum (b) with four equally emphasized components (frequency bins 1, 3, 5, 7), all of which have 0.436 RMS levels and take 76.2 % of the total signal energy
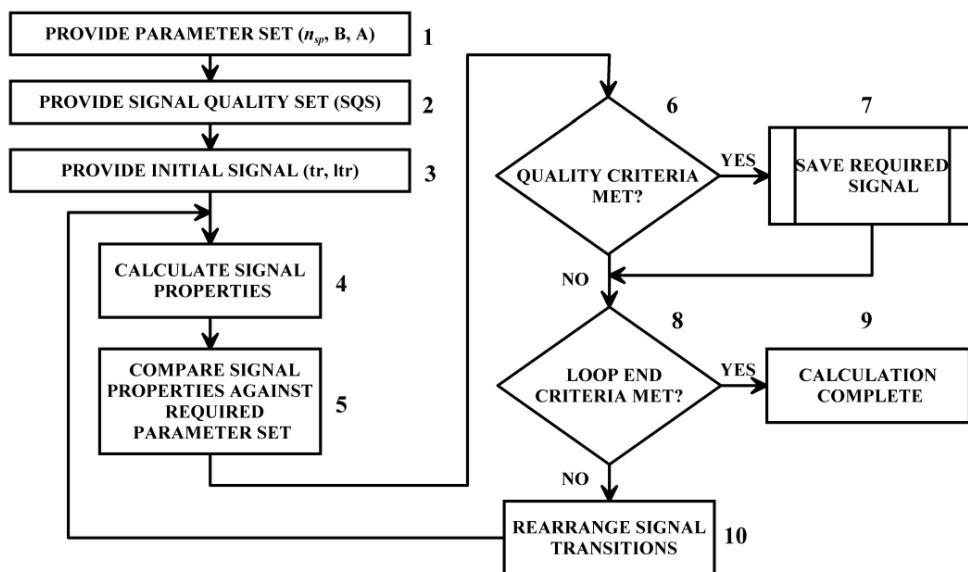

Figure 52. Flowchart of the waveform parameters manipulation method for creating binary waveforms with the required frequency content and spectrum

These parameters are determined on the basis of current spectroscopy requirements. The element values in the set A may be shaped by some curve, if the manipulated magnitude spectrum is required. In step 2, the acceptable level SQS (Signal Quality Set) of inaccuracy of the created spectrum (the corridor into which the discrepancies of the set of actual relative amplitudes should fit) is determined. According to the chosen signal parameters set up in step 1, the initial signal is provided in step 3 on basis of following initial parameters: $tr-$ the total number of

signal transitions, *ltr* – the maximal length of the signal section, where non transitions occur. Looping algorithm begins with step 4, where the spectral properties of the initial signal are calculated. In the next step 5, these parameters are compared against the required parameter set (Fig.53). If the quality criteria are met for the parameter set (step 6), then the actual signal is stored (step 7). This algorithm is presented in (Min, Ojarand, Märtens, Land, et al., 2012).
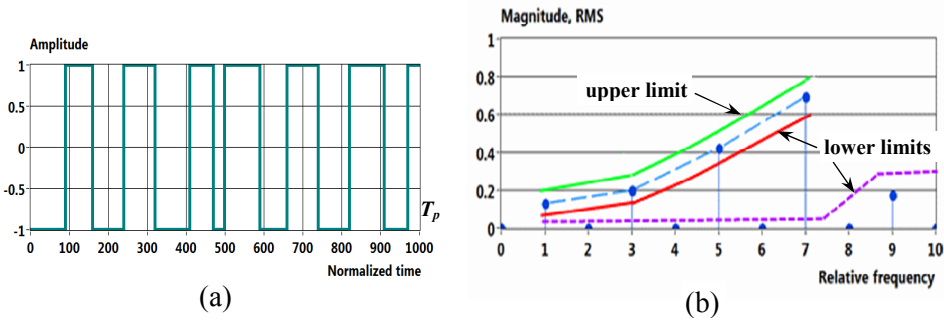

Figure 53. Example of BMS spectrum comparison against required parameter set; waveform (a) and RMS spectrum (b) synthesized for obtaining rising levels for the first four odd frequency bins ($i = [1, 3, 5, 7]$), which occupy 72.5 % of the total signal energy

The number of calculation steps increases with an increase of the required frequency components and corresponding waveform components. Increase of the time step ΔT_k has an opposite influence on a number of calculation steps, however, a large time step gives lower accuracy of the spectrum shaping.

One way out is the use of consecutive calculations starting with large ΔT_k and varying the transition points of the obtained waveform in the next stage with smaller ΔT_k. However, results of this approach can be quaranteed only to be local optima.

4.2.4 One step DFT synthesis of BMS via multisine

Waveform of the BMS *B(t)* may by derived by detecting zero crossings of the multisine waveform

$$B(t) = \text{sign} \sum_{i=1}^{i=n} A_i \cdot \sin(2\pi f_i + \Phi_i) \tag{4.16}$$

Simulations show that in the case of binary frequency distribution ($i = 2^k$) or similar distribution with odd harmonics ($i = [1, 3, 5, 7, 15, …]$), BMS with almost flat RMS spectrum may be obtained with randomly selected phases Φ_i if the number of frequency components k increases. Dependency of the deviation of RMS magnitudes from a mean value on a number of frequency components k is illustrated in Fig. 54 for the case where $\Phi_i = 0$.
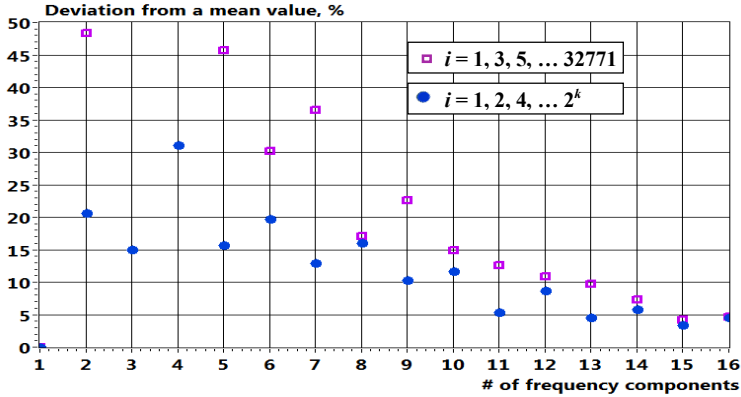
Figure 54. Deviations of RMS spectra of the BMS from its mean RMS value for a different numbers of frequency components k; BMS is obtained from a multisine according to the eqn. (4.16) with $\Phi_i = 0$

With dense frequency distributions, e.g. consecutive harmonics $i = [1, 2, 3, …, k]$ simple detecting of zero crossings of the multisine waveform will not produce a flat RMS spectrum of the BMS.

A flat spectrum of the excitation signal is not always a goal. At first, maximal flatness of the spectrum does not typically coincide with the maximum mean RMS level of frequency components of interest. Secondly, if a response signal from a SUT has a decaying spectrum, excitation signal with a rising shape of the spectrum is usually preferred to improve the SNR of measurements. In some other cases, e.g. if a response signal from a SUT has a rising spectrum, a decaying spectrum of the excitation signal may be necessary to avoid overloading.

A custom shape of spectrum may be obtained via optimization described in the previous section, however, if the number of frequencies k increases, this method becomes very computation resource-hungry and other solutions are needed. One solution is synthesis via multisine. However, unlike with the previously mentioned algorithm (see Section 4.2.2) synthesis may be performed using one DFT transform in each iteration as illustrated in Fig. 55.

In step 1, several initial parameters (n_{sp} - signal length, number of points; B - set of required frequency grid, which are bin numbers according to the DFT standards; A - set of corresponding relative amplitudes; MS - ranges of the phases or amplitudes and corresponding step values of the multisine waveform) are provided to create the desired BMS.
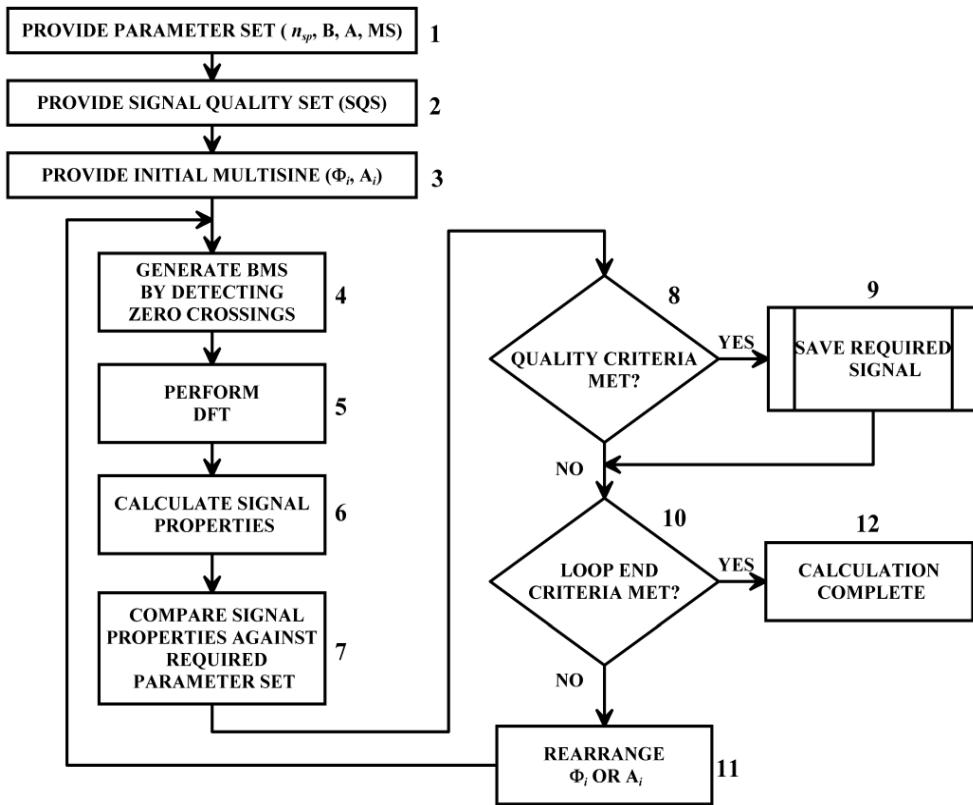
94

Figure 55. Flowchart of the multisine parameters manipulation method for creating binary waveforms with the required frequency content and spectrum

These parameters are determined from the current spectroscopy requirements. The element values in the A may be shaped by some curve, if the manipulated magnitude spectrum is required. In step 2, the acceptable level *SQS* (Signal Quality Set) of inaccuracy of the created spectrum (the corridor into which the discrepancies of the set of actual relative amplitudes should fit) is determined. According to the chosen signal parameters set up in step 1, the initial multisine wave is provided in step 3 with initial phases Φ_i and initial amplitudes A_i. Looping algorithm begins with step 4, where initial BMS is generated by detecting zero crossings of multisine. In the next step DFT is perfomed and the spectral properties of the initial signal are calculated in step 6. In step 7, these parameters are compared against the required parameter set. If the quality criteria are met for the parameter set (step 8), then the actual signal is stored (step 9).

There are two methods of „one step DFT synthesis" via multisine, A and B. In case A amplitudes of the multisine are kept constant and initial phases of the

multisine components are varied. In case B, amplitudes of the multisine components are varied and initial phases are kept constant. If the number of frequency components k is limited to 16, method A provides typically satisfying results. Still this depends also on the distribution of frequencies. Spectrally more sparse distributions have lesser capabilities for magnitude shaping than spectrally denser distributions. If k increases, phase step $\Delta\Phi$ must be also increased to limit the number of calculation steps (which is determined by eqn. (4.9)). However, large phase steps reduce the accuracy of spectrum shaping. Randomly generated initial phases may be also used for large k, however this provides also only a rough estimate.

For the improvement of the results of the spectrum shaping in case of large k (beginning from values $k = 6...10$) method B - variation of the amplitudes A_i of the multisine components can be used. In this case initial phases Φ_i are kept fixed. Values of Φ_i may be obtained from the results of previous calculations (method A) or from the generator of random numbers. Not all the amplitudes of the multisine components are varied in nested loops (as in case of phase variations), but at first the amplitude of the frequency component with highest deviation from desired value is variated. In the next step the amplitude of the frequency component, which has the next highest deviation from desired value is variated and so on. This process is repeated until no further improvement occurs. Typically less than ten iterations are needed.

Dependency of RMS magnitudes of the consecutive and binary rated distributions on the number of frequency components of optimized BMS is illustrated in the following section.

4.3 Efficiency comparison of BMS and multisine

The first part of this section gives a brief summary of the paper presented in appendix B (Ojarand, Land, and Min, 2012) .

As shown in Section 4.1.5, normalized RMS magnitudes of consecutively distributed and optimized multisine components are close to the value calculated by $(A_N / \sqrt{2})(1 / \sqrt{k})$ if the number of frequency componets $k > 3$. The BMS has similar tendency, however, a mean RMS value of the components of the BMS , optimized for a better mean RMS, tend to the value of

$$M_{rms(i).B.eq} = \frac{4}{\pi} \frac{A_N}{\sqrt{2}} \frac{1}{\sqrt{k}}$$

(4.17)

RMS magnitudes of the optimised BMS with consecutively distributed frequency components are approximately $4/\pi$ times higher than RMS magnitudes of the similar optimized multisine waveform. This result is close to the mean RMS values of MLS and signum chirp signals.

In case of logarithmically distributed frequency components the ratio of RMS magnitudes is increasing with number of frequency components. Ratio of RMS

magnitudes of the BMS and multisines at number of frequencies $k = 12$ is 2.27 for the frequency distribution $i = [1, 2, 4, \ldots, 2^k]$ shown in Fig. 56. This ratio yield to power gain of signal components at least 5 times.
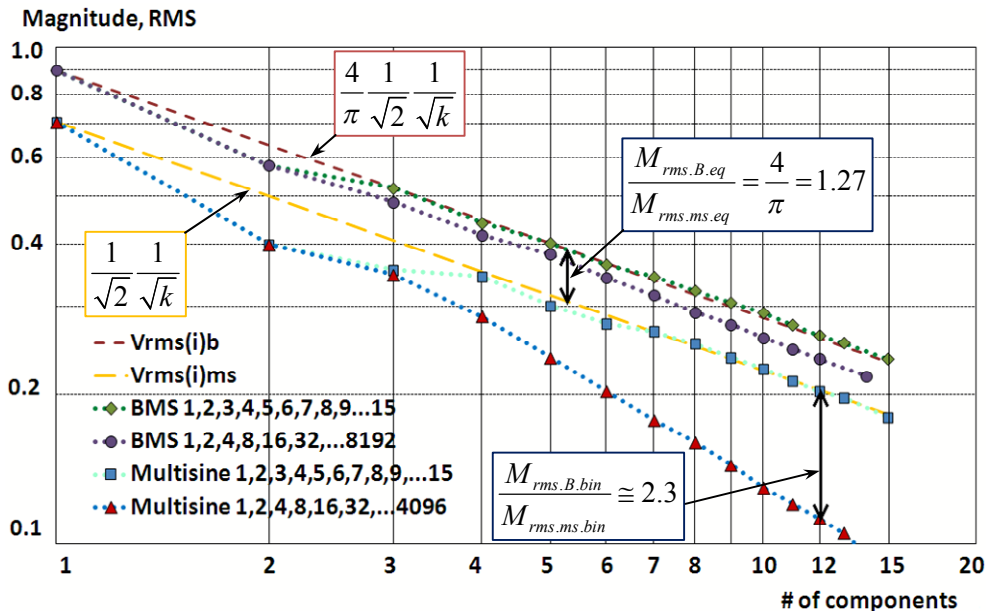
Figure 56. Normalized RMS magnitudes of consecutively distributed and binary rated frequency components of multisines (lower lines) and BMS (upper lines) vs. number of components k

Comparison of the RMS magnitudes of the frequency distributions with prime numbers is given in appendix B.

Another representation of the RMS magnitudes of the excitation signals is how they are changing per frequency decade covered (Fig. 57). Results, obtained by optimization of normalized multisines and BMS show, that BMS with denser frequency distribution allows to cover wider frequency range than the multisine with a sparser frequency distribution. As an example: BMS with binary frequency rate ($i = 1, 2, 4, \ldots, 2^k$) has higher RMS magnitudes than the multisine with decimal frequency rate ($i = 1, 10, 100, \ldots, 10^k$).
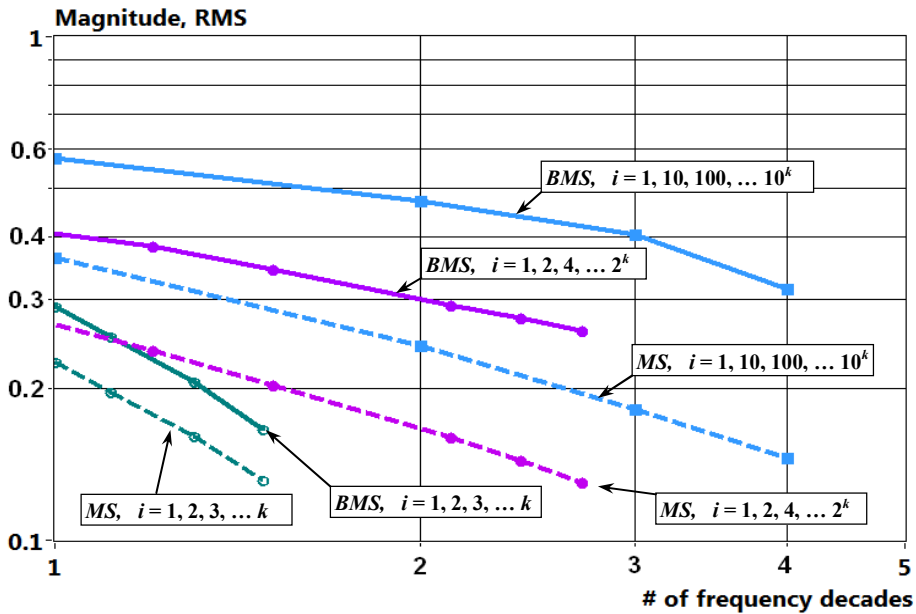
Figure 57. Normalized RMS magnitudes of consecutively and logarithmically distributed frequency components of optimized multisines (MS, dashed lines) and BMS (solid lines) vs. number of frequency decades a signal covers

4.4 Combining time-separated binary signals for better efficiency

This section provides a brief summary of the paper presented in appendix C (Ojarand and Min, 2012) with some additional discussion of the properties of the response signal.

Bio-impedance spectra have a tendency to decrease at higher frequencies (Grimnes and Martinsen, 2008). For example, it is nearly inversely proportional to the frequency in the case of single cell spectroscopy. Pre-emphasizing of higher frequency components in the excitation signal spectrum allows compensating a lower level of the response signal in this area. However, an optimal solution depends also on some other factors, which are discussed below.

For bioimpedance measurements, excitation with a current source is usually considered to be preferable over voltage source. Since the biological objects are sensitive to electric fields, the current flow becomes nonlinear with respect to voltage. Current source will produce negative feedback reducing this nonlinearity (Pliquett, 2010). Moreover, the current density on the electrodes is well controlled, and the voltage drop across the electrodes can be predicted, which opens a possibility for correcting of electrode stray effects.

Real current sources have limitations, especially at the high frequencies, where the stray capacitances degrade significantly the performance of current sources. A disadvantage of active current sources (in comparison to simple current limiting

resistor) is also their higher noise level (Annus, Min, Rist, Ojarand, and Land, 2012).

Typical magnitude spectrum of the impedance of a single cell surrounded by saline suspension is shown in Fig. 40 (Section 4.1.1). Current source should have a rising shape of spectrum for the pre-emphasizing of higher frequency components and a falling shape of the spectrum at lower frequencies to protect the object from over voltages.

When using voltage excitation source, the pre-emphasizing of higher frequency components is not necessary at all, since the current is increasing itself when the impedance is decreasing. One more positive effect of using voltage source is that the rise of impedance in the lower frequency range does not produce any excessive voltage. Notice that rise of impedance in this area is caused by the polarization of electrodes (double layer effect) and does not provide useful information about the properties of object. In some cases, e.g. in the channel of the microfluidic system with a low concentrations of cells and sufficient channel height to cell diameter ratio, the current nonlinearities with respect to voltage are small, and a voltage source with current limiting resistor can be used instead of the more complicated and noisier current source.

In case of EBI measurements, especially in case of cytometry, limits of the excitation voltage and current are different in the lower frequency range (α – dispersion area) and higher frequency range (β – dispersion area) as discussed in the Section 2.4.2. Requirements for the excitation signal source in these two ranges are different and often contradictory. In case of small electrodes, the excitation current in lower frequency area is mainly limited by allowed current density of the electrodes. The excitation voltage is also limited by allowed voltage drop on the electrodes and input range of the measurement circuitry. At higher frequencies a current density limit of electrodes becomes less important since the excitation current passes double-layer capacitance and a rise of the excitation current is beneficial for improving the SNR of measurements. Increase of the excitation voltage may be also required at higher frequencies if the desired maximum current is limited by the conductivity of the saline solution (see Section 2.4.2).

Analysis of the situation described above led to the hypothesis that an excitation source with different properties in lower and higher frequency areas may provide better SNR of measurements. In (Ojarand and Min, 2012) excitation signal with two time-separated parts was proposed. The first part, covering the lower frequency area is a BMS with a flat spectrum, and the second part covering the higher frequency area is a rectangular wave waveform with a decaying spectrum. Computer simulation with a typical equivalent circuit model of the single cell in saline solution shows that the use of two simple binary signals allows to get almost flat spectrum of the response current over three frequency decades (Fig. 58). Replacement of two part excitation signal with a single BMS with eight frequency components (f = [50, 150, 250, 350, 850, 1550, 3200, 6400] kHz decreases RMS magnitudes of the signal by 27 %.

To keep the overall spectrum undistorted, both excitation waveforms must be applied one by one sequentially. The required interval between the two parts of the

signal depends on the characteristics of the object, more specifically on relaxation time-constants formed by the capacitances and resistances of its equivalent circuit. In the present case, the biggest influence has a pair of R_s and C_s relaxation time-constant τ_s of which is around 10 µs (see Fig. 40 in Section 4.1.1.). However, in case of voltage
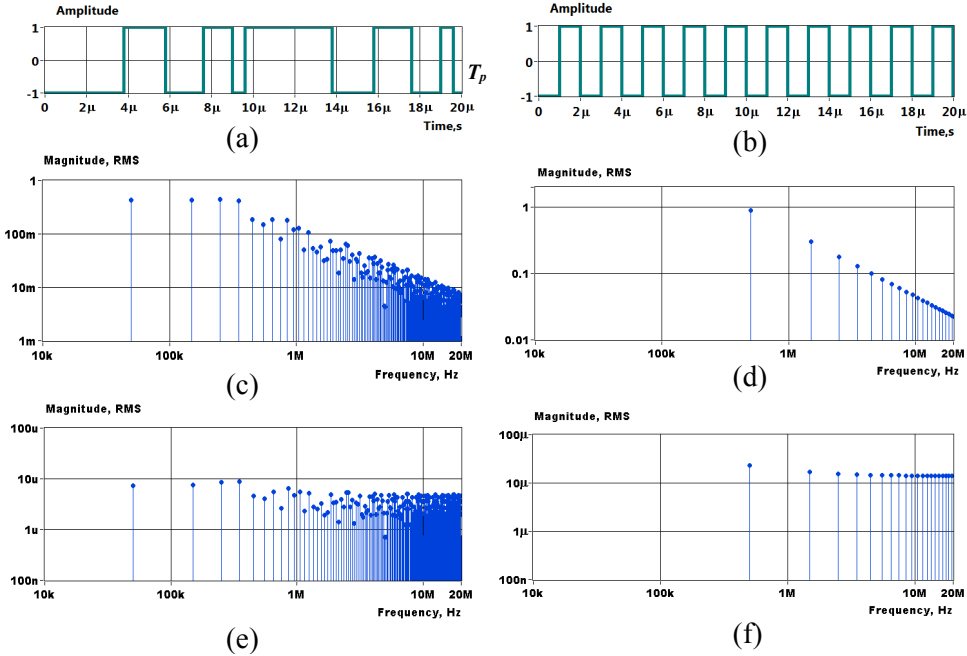
Figure 58. Excitation waveforms (a, b), magnitude spectra of the excitation voltages (c, d), and corresponding magnitude spectra of the response currents (e, f)

excitation source with a current limiting resistor R_a, this resistor may be considered to be connected in parallel with R_s and C_s, in the electrical equivalent circuit since the resistance of the voltage source is near zero. On the positive side, the time constant caused by stray capacitance C_s will be less. However, decreasing of the R_a is limited, since it leads to increase of the current spikes shown in Fig. 59b. A more sophisticated symmetrical circuitry as described in appendix D allows compensation for these current spikes at the input of current measuring circuit. Even so, the current waveform drawn from the signal source remains almost the same.

(a)

(b)

C_{dl} = 2 nF, R_s = 60 kΩ, C_m =1 pF,

R_{cy} =100 kΩ, C_s = 5pF

(c)

Figure 59. Waveforms of the voltage in point A (a) and current (b) in case where R_a = 10 kΩ

4.5   Conclusions of the chapter

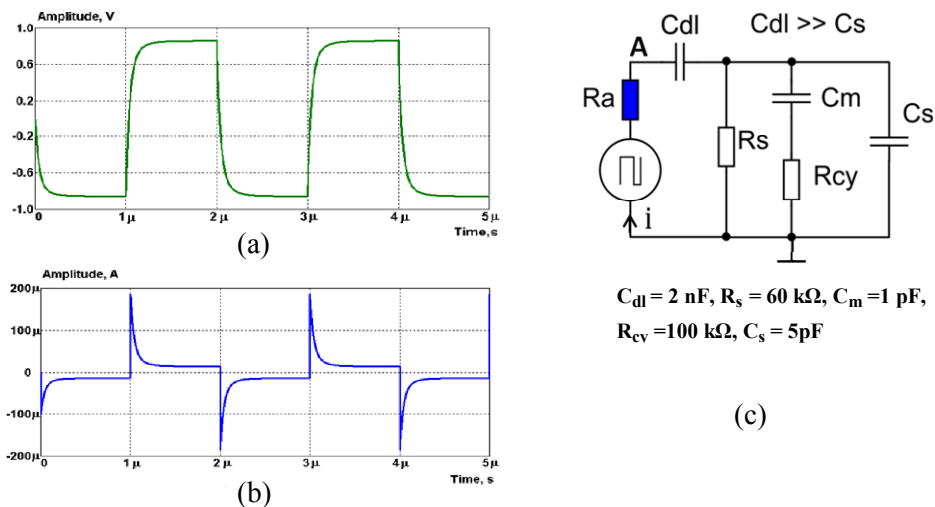For better performance, it is essential to concentrate the signal's energy right on the specific frequencies of interest.

In this chapter the properties of the wideband signals which may have sparse distribution of the frequency components are described and analysed. The first section of the chapter presents a novel method for the minimization of the crest-factor (CF) of the multisine. As in case of other known methods the computed CF may be guaranteed to be a local optimum. Yet the systematic variation of initial parameters, which is possible due to the sparse algorithm, ensures a CF close to the global minimum. For less than six frequency components, a new method gives the same results as an exhaustive search. For a higher number of components the results were compared with other published data and found to be similar or better. Equations characterising the best and worst possible CF are derived. An empirical relationship for the binary frequency distribution is derived. It is shown that regardless of the method used, the accuracy of the calculated CF values depends on the density of the signal sampling. It was found that the number of samples per period of the highest frequency component must be at least 10, in order to achieve a relative error near 1 %. Close to the Nyquist sampling-rate, the relative error could increase over 20 %.

In the second section of the chapter the properties of the binary multifrequency signals (BMS) and two novel methods for the shaping their spectra are described. The first method is based on the enumeration of all possible variations of a waveform. Unlike in case of other similar methods, the number of variations is significantly reduced (at least 200 times). The second method is based on the use of multisine waveform with the desired frequency components. Unlike other known methods, it uses only one DFT in each step of iteration. Dependency of the RMS

magnitudes of consecutive and binary rated distributions on the number of frequency components of optimized BMS is illustrated.

In the third section of the chapter the properties of optimized multisines and BMS with the same spectral distributions are compared and illustrated. The main conclusion is that the mean the RMS of the optimized BMS is always higher than the RMS of similar multisine and that this difference increases considerably in case of spectrally sparse distributions. It is shown that multifrequency binary signals offer the possibility of achieving up to 5 times higher signal power level, for an excitation signal which contains 12 harmonic components of interest, logarithmically distributed over three frequency decades. Considering the simplicity in generating binary sequences, there is no doubt that binary multifrequency excitation signals deserve the greatest attention in the electrical bioimpedance measurements.

Following the conclusion of the second chapter a novel multipart time separated multifrequency excitation signal is presented in the fourth section of the chapter. Computer simulation shows that the RMS values of two-part excitation signal are around 1.3 times higher than the RMS of the BMS covering the same bandwith.

5 PRACTICAL IMPLEMENTATIONS

5.1 Microfluidic device with a differential front-end circuitry

5.1.1 Introduction

The following section is a brief summary of the paper presented in appendix D. (Ojarand, Giannitsis, Min, and Land, 2011) with some additional discussion of the properties of the signal sources.

Impedance spectroscopy is a common approach in assessing passive electrical properties of biological matter, however, serious problems appear in microfluidic devices in connection with distortion free signal acquisition from microelectrodes. The quality of impedance measurements highly depends on the presence of stray capacitances, signal distortions, and accompanying noises. Measurement deficiencies may be minimized with optimized electronics and sensing electrodes. The quality can further be improved with appropriate selection of measuring signals and also with selection of measuring methods such as a choice between current or voltage sources and between differential or single-ended techniques. The microfluidic device that we present here incorporates an impedance sensor, which consists of an array of two sequential pairs of parallel microelectrodes, embedded in a microfluidic channel. All electronics and fluidic components are placed inside a metal holder, which ensures electric and fluidic connections to peripheral instruments. This configuration provides short electric connections and proper shielding. The method that we are using to evaluate the sample's impedance is the differential measurement technique, capable of suppressing the common mode signals and interferences, appearing in the signal-conditioning front-end circuit. Besides, it opens the possibility for compensating stray effects of the electrodes. For excitation we employ wideband signals, such as chirps or multifreqyency signals, which allow fast measurements, essential in the most impedimetric experiments in biology. The impedance spectra cover the frequency range between 10kHz - 10MHz. Two measurement schemes are presented : (i) an in-phase differential method, which employs two transimpedance amplifiers, and (ii) an anti-phase method, which uses one transimpedance amplifier. The sensitivity, SNR and operational bandwidths of these two methods are analysed and compared against other commonly used related circuits.

5.1.2 Impedance electrodes for microfluidic device

In microfluidic devices, both pairs of electrodes can be positioned collinearly along the same side of the microfluidic channel. A drawback of this coplanar arrangement is that the current density and electric field become very inhomogeneous. If the electrodes, however, are placed opposite each other across both sides of the

microfluidic channel, the electric fields produced between the electrodes will be nearly uniform in the middle part of electrodes. Parallel plate electrodes have also good sensitivity and sensing area, and this enhances detection of small impedance changes when cells flow between the electrodes (Wang, Wang, and Jang, 2010). However, it is difficult to position the parallel current electrodes between the voltage sensing electrodes as in the classical four-electrode setup. If these electrodes are placed on the both sides of a microfluidic channel, this will significantly decrease the sensitivity for detection of the impedance changes since the electric field distribution varies mostly at the center of the current electrodes when cells flow between the electrodes.

To ensure low current densities the current electrodes comparable to the dimension of the microchannel were designed. The dimensions of electrodes in our device are $250 \times 200 \ \mu m^2$. The inter-electrode gap is 2.5 mm. This gives small crosstalk between adjacent electrodes. The width of each electrode fits right the width of the channel, which is defined as the area between the two sidewalls. Each microelectrode of the bottom plate is aligned parallel with the microelectrode of the top plate. The opposite end of electrodes have a shape of contact pin, which matches directly with the contact plug, soldered on the circuit board of the analog front-end. This design highly eliminates influence of the electric circuit lengths between the measurand and the analyzer, as the signal conditioning circuitry is very close to the electrodes. The gap between the electrodes, 30 μm, is determined with a transparent double-sided self-adhesive tape (Tesa 4983). Top and side views of the microchannel module are shown on the Fig. 60. The microfluidic module is enclosed in its shielding aluminum case, which is described in the end part of the section.

(a)   (b)
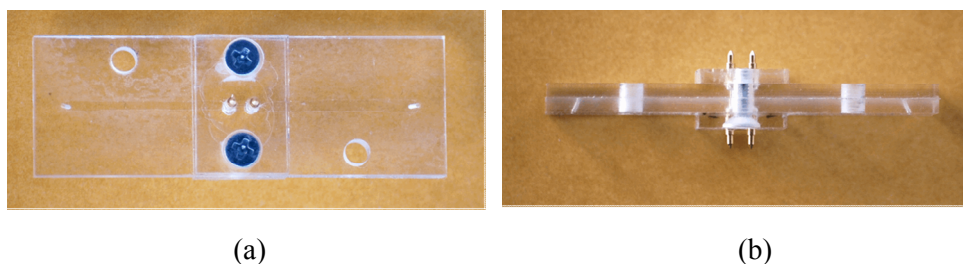
Figure 60. Top view (a) and side view (b) of the microchannel module

5.1.3 *Impedance measurements in microflow cytometer*

The impedance analysis could be performed with impedance analyzers, which provide AC excitation and impedance detection in the same instrument. These instruments are usually complicated devices with large dimensions and cables must be used for connecting of microfluidic devices. Since the input-output impedances of the analyzers and impedances of the cables are not suitable for direct connection to the electrodes in the microfluidic devices, an additional signal conditioning and

impedance matching is necessary. This is accomplished by the front-end device, which usually consists of preamplifiers and excitation voltage or current sources.

The impedance can be measured in a full scale of voltages and currents, which are available for the experiment. However, this approach has sensitivity limits which are directly predicted by the resolution of measuring instruments. To overcome the sensitivity limitations, differential measurement circuitry with two pairs of electrodes is used. Two pairs of electrodes are used to determine the two closely positioned detection volumes enabling to perform differential measurements.

One pair of electrodes measures the electrical signal from the particle whilst the other pair acts as a reference. As the cells pass through the channel, they perturb the electric field in the detection volumes creating positive and negative signals. This signal is processed to provide the impedance. In our microfluidic device we employ a dual two-electrodes setup, which is appropriate for measuring current differences between the two electrode pairs via the use of a front-end circuitry that converts the detected currents to voltage via two identical transimpedance amplifiers, followed by a buffer circuitry which drives the connection cables to an external impedance analyzer measuring differential impedance on the bases of differential current measurement ($dZ = V / dI$). More detailed description of the circuitry can be found in appendix D

5.1.4 Excitation sources

For bioimpedance measurements, excitation with current source is usually considered preferable over sourcing voltage. Since biological objects are sensitive to electric fields, the current flow becomes nonlinear with respect to voltage. Current excitation will produce negative feedback reducing this nonlinearity (Pliquett, 2010). Real current sources have their limitations, especially at the high frequencies, where the stray capacitances degrade significantly their performance (Annus, Min, Rist, Ojarand, and Land, 2012).

A good quality voltage sources can be made in a wide range of frequencies and voltages, which can be converted to passive current-limited source by adding a series resistor. Computer simulation shows, that a noise of the voltage source with a series resistor is typically lower in comparison with the active current source, as illustrated in Fig. 61. Active current source, used for the comparison, is built up with Analog Devices AD8130 differential-to-single-ended amplifier, as described in (Birkett, 2005). A voltage source uses Analog Devices AD4937 low noise, high-speed amplifier as a buffer.

A drawback of using a resistor instead of an active current source is that the current is not constant and should be measured. Yet in the higher frequency range, the current is not constant even in case of active current sources. Considerable changes of the imaginary part of the excitation current (phase shift in other terms) appear typically at frequencies starting from approximately 100 kHz.
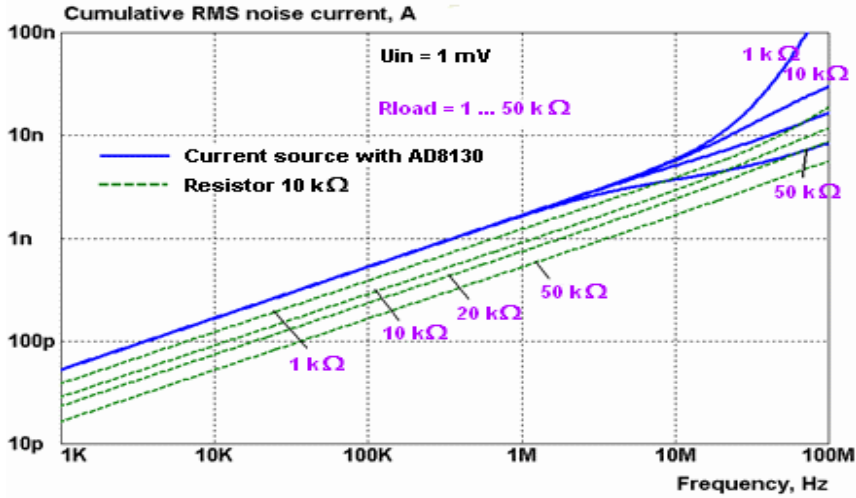
Figure 61. Cumulative RMS noise current of the active current source (solid lines) and voltage source with the 10 kΩ current limiting resistor (dashed lines); the nominal current of the current source is 0.1 μA and the value of the feedback resistor R_s is 10 kΩ; the load resistance varies in the range from 1 kΩ to 50 kΩ

At higher frequencies, the magnitude of the excitation current is also affected. This can be observed also in the noise curves in Fig. 61, e.g. in case of 50 kΩ load, the cumulative RMS noise decays at frequencies above 1 MHz, since the magnitude of the current decays. In the front-end circuitry of the microfluidic device presented in appendix D, a symmetrical differential voltage source with current limiting resistors is implemented.

5.1.5 Current -to-voltage converters and amplifiers

There are two well-known methods for converting a current into voltage. First, we can monitor a voltage drop on the fixed resistor and then use a high impedance voltage follower or amplifier. Secondly, we can use a transimpedance amplifier circuitry shown in Fig. 62. Main characteristics of these two are similar, however, there are also differences. At first, in the case of transimpedance amplifier (TIA), input voltage between the inputs of the op-amp is always near zero on the both inputs. This is not so, if the voltage drop on the resistor is monitored, and this causes small changes in the input capacitances of the op-amp and consequent nonlinearities. Secondly, the transfer characteristic of this type of current-to-voltage converter is nonlinear and the input capacitance C_T has more influence on it. Results of the PSpice modeling for the both converters are shown in Fig.63.

106

(a)   (b)
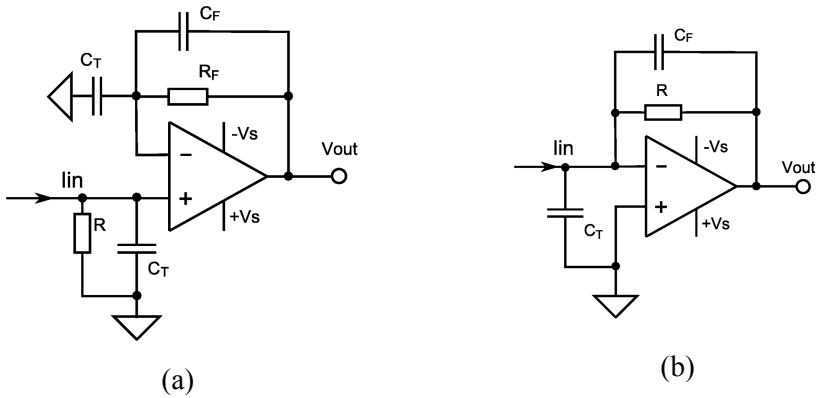
Figure 62. Simplified circuits of the current-to-voltage converter amplifiers, (a) is monitoring a voltage drop on the resistor R, and (b) is a transimpedance amplifier; C_T is a total stray capacitance, C_F is a stray capacitance in parallel with the resistors R and R_F

In the front-end discussed here transimpedance amplifiers (TIA) are implemented. Real TIA has also their limitations more detailed analyze of which is presented in appendix D. The analysis and simulation allows formulation measures for the improved bandwidth and signal-to-noise characteristics of TIA.

(a)   (b)

Figure 63. Bode plots of the current-to-voltage converters gain using in-series resistor R (a) and of the TIA (b); both converters employ the same op-amp OPA656 with $C_T = 2$pF, $C_F = 0.5$ pF, $R_F = 10$ kΩ, the resistance of input current source is 100 kΩ and R varies from 3 kΩ to 100 kΩ

This can be achieved by:

- minimizing the value of the total input capacitance C_T. This reduces the noise gain without limiting the signal bandwidth;
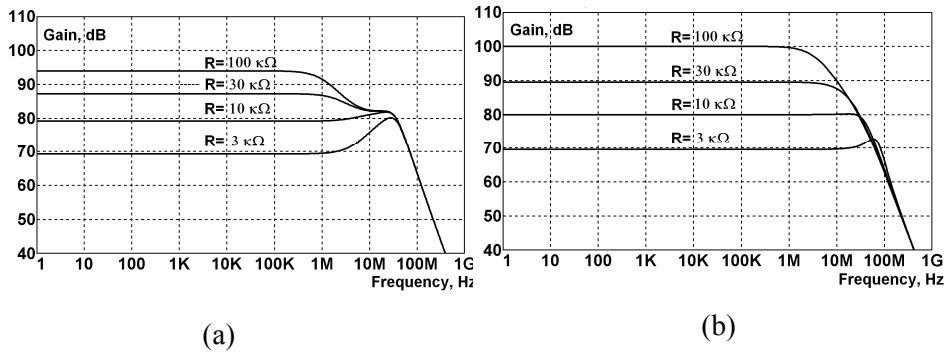- reducing the value of the feedback resistor R_F. Bandwidth is inversely related to the square root value of the feedback resistor. Thus, if the bandwidth is most important, a gain loss can be compensated by the following broadband but low noise voltage gain stage;
- filtering of the TIA output signal to reduce the wideband noise beyond the signal bandwidth. A single pole low-pass filter with a bandwidth twice as the signal bandwidth can easily improve the dynamic range of TIA.

5.1.6 Mechanical design

To ensure proper shielding from external noises, the microchannel module was enclosed inside the aluminum case as shown in photo, Fig. 63. Printed circuit boards (PCB-s) of the front-end electronics are placed on both sides of the microchannel module, an excitation signal part on the bottom side and an input amplifiers part on the top side. Each microelectrode of the bottom plate is aligned parallel with the microelectrode of the top plate. The opposite end of electrodes have a shape of contact pin, which matches directly with the contact plug, soldered on the circuit board of the analog front-end. This design highly eliminates influence of the electric circuit lengths between the electrodes and signal conditioning circuitry. Removable leads cover both sides of the case.

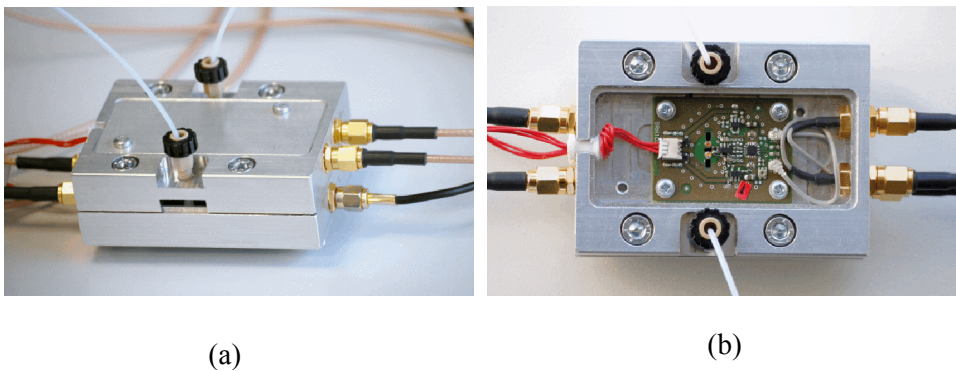(a)   (b)

Figure 64. (a)- the microfluidic device enclosed in its shielding aluminum case, where cabling and fluidic fittings are distinguished, (b) - interior of the microfluidic device where the electronic front-end circuit board is shown

5.1.7 *Excitation signals and signal processing*

Sine wave excitation and phase-sensitive demodulation of the response are common tools for impedance measurement. This method fails if the object changes its electrical properties fast with respect to the time required for a frequency sweep. Such dynamic processes take place in microfluidic devices where cells flow fast between the electrodes with small dimensions. Better solution to cover a wide frequency range within short time interval is the use of multifrequency signals. The multisine signal is the basic solution for this purpose. To test our front-end device an impedance analyzer-spectroscope Model H2FIS (Zurich Instruments, Switcherland) was used. In our tests, we employed 4-frequency multi-sine wave excitation in the frequency range from 3 kHz to 11 MHz. The demodulated output data samples flow into an embedded processor for post processing or to be sent to a host computer.

We can also derive binary multifrequency signals (BMS). Experiment show that the RMS magnitudes of the BMS excitation waveform with four frequency components i = [1, 3, 5, 7] is 15 % more compared to similar multisine signal. In experiments, the arbitrary function generator (AFG3252 Tektronix) and the digital scope (Agilent DSA91304) were used.

The host computer controls the impedance analyzer and performs signal processing and graphical data representation of the measurement results using LabView software.

5.2 Multichannel spectroscopic device

Implementing the above described binary signals enabled us to design and prototype a two-channel spectroscopic device (Fig. 64), which operates with excitation signals with controllable spectra. The electronics is based on Texas Instruments TMS320F28069 Piccolo™ microcontroller, comprising a built-in 12-bit Analogue-to-Digital Converter with a dual sample-and-hold unit. In addition, a Direct Memory Access unit (DMA) is included. An enhanced Pulse Width Modulator (ePWM) is built in to generate complicated pulse width waveforms and sequences of binary level pulses. Also, a FFT routine algorithm has been made available for this microcontroller (Min, Ojarand, Märtens, Paavle, Land, et al., 2012).

A compact and cost effective spectroscopic device has been designed on the bases of above described signal processing methods and mentioned hardware advantages. Requirements in different number of channels have led to the design of a stackable multichannel device. The first device in the stack plays a role of master-device and provides the synchronization for other stacked devices.

The upper limit of the operating frequency range is from 1 kHz to 500 kHz, as it follows from the maximum speed (the Nyquist frequency) of the internal analog-to-digital conversion of the DSP – the sample rate of the internal ADC is 1 MSa/s.

The size of a single unit is 107 × 58 × 23 mm. Power supply for the units is taken from the USB-2 connection and the current consumption is about 150 mA.
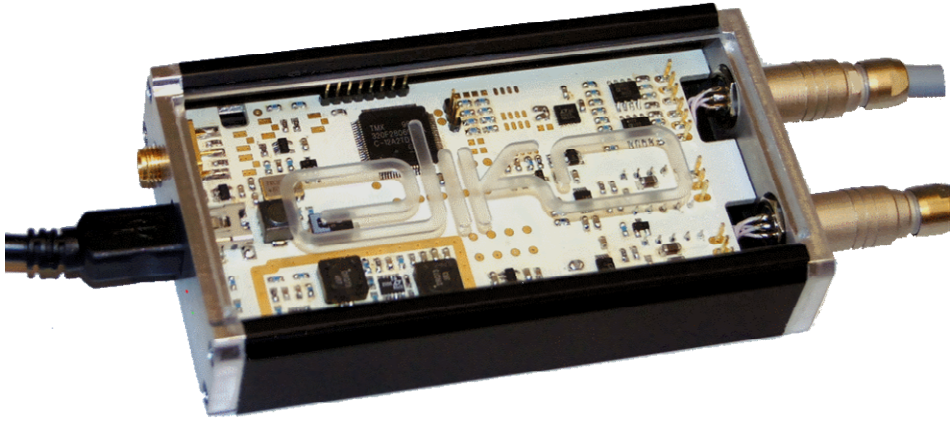
Figure 65. Prototyped spectroscopic device is based on Texas Instruments Piccolo^{TM} microcontroller

Characteristics of the excitation output and signal pick-up input of the unit depend on the used external front-ends, which ensure signal integrity in the measurement chain in the frequency range.

The multifrequency excitation signal (BMS) is generated continuously in time. The maximum number of useful frequency components in the signal is limited to 16. The maximum readout rate of the device is 1000 readings/s that makes the device suitable for the fast and wideband impedance measurements.

Certain solutions used in the device are not described in detail as they are considered intellectual property.

5.3 Conclusions of the chapter

The quality of impedance measurements highly depends on the presence of stray capacitances, noises and interferences, all leading to signal distortions. The novel mechanical design of the experimental microfluidic device and of electronic circuits of the front-end device are introduced to achieve more disturbance proof differential data acquisition. Also multi-frequency binary sequences are proposed for using as excitation signals, which enable to perform fast wide band measurement of impedance deviations on basis of simple and low power electronics.

Experiments show that the low accuracy of the channel part of the microfluidic module limits the efficiency of symmetric measurement circuitry. Testing of our microchannel modules shows unbalance between 10 to 25 %. It is obviously possible to achieve better results improving the fabrication accuracy. It was also

found that such use of only differential measurement data makes fitting of the equivalent circuit parameters complicated, since the parameters which depend on the of properties of the microchannel module were measured in a separate calibration step. It is concluded that for the improvement of the accuracy of measurements the basal impedance and the differential impedance changes should be measured in the same measurement cycle, which can be achieved by additional control of the excitation signal mode (switching between differential and synphase signal modes).

Implementing the above described binary signals (BMS) enabled to design and prototype compact multi-channel spectroscopic device, suitable for carrying out the fast and wideband impedance spectroscopy. Frequency range of this model, however, is not covering the typical β-dispersion area of the single-cell measurements, therefore the cpectroscopic device with wider bandwith is also under development.

CONCLUSION OF THE THESIS

In the process of studying electrical bioimpedance (EBI) measurements, more specifically, the single cell measurements, it became clear that it is a complex task with often contradictory requirements. In short, the measurements should be typically performed over a wide frequency range during a short timeframe and using an excitation signal with a low amplitude. In addition, very high sensitivity of the measurements is often needed. That emphasizes the importance of improving the SNR of measurements.

This thesis concentrates on defining and designing energy efficient, fast wideband excitation signals for improving the SNR of EBI measurements. Other ways to improve the SNR are briefly discussed and several solutions are proposed and analysed in the last chapter of the thesis and in appendix D.

The first chapter gives an overview of EBI measurement basics and the second chapter provides a more detailed survey of the single cells EBI measurement problems, which allows to formulate the requirements for the properties of wideband excitation signals.

The main contributions of the thesis are:

1. Compendious comparison of the efficiency of different wideband excitation signals suitable for fast and wideband EBI measurements.
In the case of limited amplitudes, it is shown that (a) - normalizing the peak value of fixed length waveforms, and (b) - using the mean RMS magnitudes of the spectral components in the frequency range of interest, allows compendious efficiency comparison of different multifrequency excitation waveforms. An undesired deviation from the mean RMS value can be used as an additional quality parameter. The normalized mean RMS magnitudes of main types of the wideband excitation signals are analysed and illustrated for several typical spectral components distributions.

2. A novel method for minimizing the crest-factor (CF) of multisine waveforms.
As in case of other known methods, the computed CF may be guaranteed to be only a local optimum, however, a systematic variation of the initial parameters, which is possible due to the sparing algorithm, ensures a CF close to the global minimum. A brief analysis of the calculation errors and comparison with the results from other sources is provided.

The results obtained with the new method are used for characterising the properties of multisines with different frequency distributions.

3. Two enhanced methods for shaping the spectra of binary multifrequency signals (BMS).

The first method is based on the enumeration of all possible variations of a waveform. Compared to other similar methods, the number of variations is significantly reduced (at least 200 times). The second method is based on the use of multisine waveform with the desired frequency components. Unlike other known methods, it uses only one DFT in each step of iteration.

The results obtained with the new methods are used in characterizing the properties of BMS with different frequency distributions and their comparison with similar multisines. The main conclusion of this comparison is, that the mean useful power of the optimized BMS is always higher than of similar multisine. This advantage increases considerably in case of spectrally sparse distributions.

4. A novel multipart time separated multifrequency excitation signal with improved efficiency.

The design of this signal follows the the fact (decrirbed in the second chapter of the thesis) that the required properties of the excitation signal differ considerably in the low frequency and high frequency areas. The computer simulation shows that power spectrum of the two-part excitation signal is around 1.6 times higher than of the single BMS covering the same bandwith.

5. A novel nonlinearly modulated short chirp signal with better efficiency.

The design of the nonlinearly modulated short chirp signal with a flat magnitude spectrum and 23% better energy efficiency than comparable linearly modulated chirps is introduced.

6. A novel design of the microfluidic device with the symmetrical differential front-end circuitry.

The sensitivity and SNR of measurements depend on the structure of the measurement circuitry and on properties of its parts. The SNR of measurements depends also on mechanical design (design and placement of electrodes, dimensions of the connections, shielding, etc.) The influences of different factors are analysed and a description of the complete experimental microfluidic device is presented.

Directions for further research

Binary multifrequency signals (BMS) deserve primary attention in the development of bio-impedance spectroscopy methods and devices. As shown in the current thesis, the BMS can be generated in a simple way, and the amount of useful excitation energy in these exceeds the energy of comparable sine wave based signals. A drawback in comparison with the multisinewaves, however, is a presence of additional unwanted frequency components. As also shown in the thesis, the shape of the spectrum highly depends on the position of waveform components. This leads to the following two further research topics:

1. Effect of the unwanted frequency components of BMS on the accuracy of impedance measurements.
2. Influence of the deviation of the positions of waveform components and time-discreteness on the spectra of BMS.

Properties of the proposed multi-sectional time separated multifrequency excitation signals show promise in increasing the SNR of the wideband EBI measurements. However, as discussed in the thesis, the results of the measurements depend also on the output impedance of the excitation source and the time delay between the signal parts. This leads to the following further reseach topic:

3. An optimal output resistance of the signal source and the optimal time delay in impedance measurement using multipart multifrequency signals.

Expriments with the microfluidic device presented in the thesis, show that the microfluidic module and the differential excitation source, must be improved. This lead to the following design topics:

4. Design of a microfluidic module for differential impedance measurements with an improved accuracy.
5. Design of a controllable symmetric excitation source for the differential impedance measurements.

REFERENCES

Alkemade, C., Snelleman, W. (1978). A review and tutorial discussion of noise and signal-to-noise ratios in analytical spectrometry-I. Fundamental principles of signal-to-noise ratios. *Spectrochimica Acta, Vol. 338* , p. 383-399.

Annus, P., Land, R., Min, M., Ojarand, J. (2012). Simple Signals for System Identification. In E. Salih Mohammed Salih, *Fourier Transform - Signal Processing.* Intech, p. 257-256.

Annus, P., Min, M., Ojarand, J. (2008). Shortened square wave waveforms in synchronous signal processing. *In: Proc. of the IEEE International Instrumentation and Measurement Technology Conference (I2MTC 2008)* , p. 1259-1262.

Annus, P., Min, M., Märtens, O., Ojarand, J. (2012). *EP 2313001B1. Method and device using shortened square wave waveforms in synchronous signal processing.* European Patent Office.

Annus, P., Min, M., Rist, M., Ojarand, J., Land, R. (2012). Current source considerations for broadband bioimpedance spectroscopy. In E. Olfa Kanoun, *Lecture Notes on Impedance Spectroscopy: Measurement, Modeling and Applications.* London: Taylor & Francis, p. 63-73.

Baranauskas, G., Maggiolini, E., Castagnola, E., Ansaldo, A., Mazzoni, A., Angotzi, G., Vato, A.; Ricci, D.; Panzeri, S., Fadiga, L. (2011). Carbon nanotube composite coating of neural microelectrodes preferentially improves the multiunit signal-to-noise ratio. *J. Neural Eng. 8* , p. 1-12.

Birkett, A. (2005). Bipolar current source maintains high output impedance at high frequencies. *EDN* , p. 128-130.

Blicher, A. (2011). *Electrical aspects of lipid membranes. Ph.D. Thesis.* Copenhagen: University of Copenhagen, Niels Bohr Institute.

Borkholder, D. (1998). *Cell Based Biosensors Using Microelectrodes. Ph.D. Thesis.* Palo Alto: Stanford University.

Brown, A. (2001). *Nerve Cells and Nervous Systems: An Introduction to Neuroscience. 2nd ed.* London: Springer-Verlag.

Cahill, B., Land, R., Nacke, T., Min, M., Beckmann, D. (2011). Contactless Sensing of the Conductivity of Aqueous Droplets in Segmented Flow. *Sensors and Actuators B: Chemical* , p. 286-293.

Cates, J., Graham, G., Omattage, N., Pavesich, E., Setliff, I., Shaw, J., Smith, C.L., Lipan, O. (2011). Sensing the Heat Stress by Mammalian Cells. *BMC Biophysics, 4:16* , p .1-18.

Cheung, K. C., Di Berardino, M., Schade-Kampmann, G., Hebeisen, M., Pierzchalski, A., A., Bocsi, J., Mittag, A., Tárnok, A. (2010). Microfluidic impedance-based flow cytometry. *Cytometry, 77A* , p. 648–666.

Cole, K., Cole, R. (1941). Dispersion and Absorption in Dielectrics. *Journal of Chemical Physics* , p. 341-350.

Dal Maschio, M., Canato, M., Pigozzo, F., Cipullo, A., Pozzato, G., Reggiani, C. (2009). Biophysical effects of high frequency electrical field (4-64 MHz) on muscle fibers in culture. *Basic Applied Myology, 19 (1)* , p. 49-56.

Debye, P. (1929). *Polar molecules.* New York: Chemical Catalog Co.

Di Biasio, A., Ambrosone, L., Cametti, C. (2010). The dielectric behavior of nonspherical biological cell suspensions: an analytic approach. *Biophysical Journal vol.99* , p. 163–174.

Evans, C., Rees, D. (2000). Nonlinear distortions and multisine signals—Part II: Minimizing the Distortion. *IEEE Trans.Instrum. Meas., vol. 49* , p. 610-616.

Fatt, P., Falck, G. (1964). Linear electrical properties of striated muscle fibres obseerved with intracellular electrodes. *Proceedings of the Royal Society of London. Series B, Royal Society (Great Britain)* , p. 69-123.

Foster, K., Schwan, H. (1989). Dielectric properties of tissues and biological materials: a critical review. *Crit Rev Biomed Eng.17(1)* , p. 25-104.

Franceschetti, D., Macdonald, J. (1979). Diffusion of Neutral and Charged Species under Small-Signal A.C. Conditions. *J. Electroanal. Chem. 101* , p. 307-316.

Franks, W., Schenker, I., Schmutz, P., Hierlemann, A. (2005). Impedance Characterization and Modeling of Electrodes for Biomedical Applications. *IEEE Transactions On Biomedical Engineering, Vol. 52, No. 7* , p. 1295-1302.

Geddes, L. (1996). Who introduced the tetrapolar method for measuring resistance and impedance? *IEEE Eng Med Biol.* , p. 133-134.

Gersing, E. (1998). Impedance spectroscopy on living tissue for determination of the state of organs. *Bioelectrochemistry and Bioenergetics, V.45, Issue 2* , p. 145-149.

Godfrey, K. R. (1991). Introduction to binary signals used in system identification. *Proc. Int. Conf. Control, vol. 1* , p. 161-166.

Gowrishankar, T., Weaver, J. (2003). An approach to electrical modeling of single and multiple cells. *Proc Natl Acad Sci U S A. 100(6)* , p. 3203–3208.

Gözen, I., Dommersnes, P., Czolkos, I., Jesorka, A., Lobovkina, T., Orwar, O. (2010). Fractal avalanche ruptures in biological membranes. *Nat Mater.,9(11)* , p. 908-912.

Grimnes, S., Martinsen, Ø. G. (2005). Cole electrical impedance model – a critique and an alternative. *IEEE Trans. Biomed. Eng ., 52(1)* , p. 132-135.

Grimnes, S., Martinsen, Ø. G. (2008). *Bioimpedance and Bioelectricity Basics.* Oxford: Elsiver.

Grimnes, S., Martinsen, Ø. G. (2007). Sources of error in tetrapolar impedance measurements on biomaterials and other ionic conductors. *J. Phys. D: Appl. Phys. 40* , p. 9-14.

Grimnes, S., Martinsen, Ø.-G. (2010). Alpha-dispersion in human tissue. *Journal of Physics: Conference Series 224* , p. 1-4.

Guillaume, P., Schoukens, J., Pintelon, R., Kollar, I. (1991). Crest-factor minimization using nonlinear Chebyshev approximation methods. *IEEE Trans. Instrum. Meas. v.40* , p. 982-989.

Gustafsson, B., Jankowska, E. (1976). Direct and indirect activation of nerve cells by electrical pulses applied extracellularly. *J. Physiol.,258(1)* , p. 33-61.

Huang, C. L.-H. (1993). Charge inactivation in the membrane of intact frog striated muscle fibres. *Journal of Physiology, v.468* , p. 107-124.

Huichin, Y., Ingenito, E., Suki, B. (1997). Dynamic properties of lung parenchyma: mechanical contributions of fiber network and interstitial cells. *Journal of Applied Physiology, vol. 83 no. 5* , p. 1420-1431.

Huigen, E., Peper, A., Grimbergen, C. (2002). Investigation into the origin of the noise of surface electrodes. *Med Biol Eng Comput.40(3)* , p. 332-338.

IEC60601-1 (ed 3.0). (2005). *Medical electrical equipment— part1: general requirements for basic safety and essential performance.* Geneva: International Electrotechnical Commission.

Ivorra, A. (2003). *Bioimpedance Monitoring for physicians: an overview.* Barcelona: Centre Nacional de Microelectrònica.

Ivorra, A., Genesca, M., Sola, A., Luis, P., Villa, R., Hotter, G., Aguilo, J. (2005). Bioimpedance dispersion width as a parameter to monitor living tissues. *Physiological Measurement, v.26* , p. 1-9.

Jackson, W., Duling, B. (1983). Toxic Effects of Silver-Silver Chloride Electrodes on Vascular Smooth Muscle. *Journal of the American Heart Association. Circulation Research* , p. 105-108.

Kaatze, U. (2005). Electromagnetic Wave Interactions with Water and Aqueous Solutions. In K. Kupfer, *Electromagnetic Aquametry.* Berlin: Springer, p. 16-37.

Karrenberg, U. (2007). *An interactive Multimedia Introduction to Signal Processing.* Berlin: Springer-Verlag.

Krassen, H., Pliquett, U., Neumann, E. (2007). Nonlinear current-voltage relationship of the plasma membrane of single CHO cells. *Bioelectrochemistry. v.70(1)* , p. 71-77.

Kraszewski, A. (2005). Recent Developments in Electromagnetic Aquametry. In K. Kupfer, *Electromagnetic Aquametry.* Berlin: Springer, p. 7-8.

Lasia, A. (1999). Electrochemical Impedance Spectroscopy and its Applications. In B. Conway, *Electrochemical Impedance Spectroscopy and Its Applications, Modern Aspects of Electrochemistry.* New York: Kluwer Academic/Plenum, p. 143-248.

Macdonald, J. (1987). Impedance Spectroscopy and its Use in Analyzing the Steady-State AC Response of Solid and Liquid Electrolytes. *J. Electroanal. Chem. 223* , p. 25-50.

Macdonald, J. (2012). Three to six ambiguities in immittance spectroscopy data fitting. *J. Phys.: Condens. Matter 24* , p. 1-10.

Malleo, D., Nevill, J., Van Ooyen, A., Schnakenberg, U., Lee, L., Morgan, H. (2010). Note: Characterization of electrode materials for dielectric spectroscopy. *Rev Sci Instrum., 81(1).6104* , p. 1-3.

Malmivuo, J., Plonsey, R. (1995). *Biolectromagnetism - Principles and Applications of Bioelectric and Biomagnetic Fields.* New-York: Oxford University Press.

Maswiwat, K., Wachner, D., Warnke, R., Gimsa, J. (2007). Simplified equations for the transmembrane potential induced in ellipsoidal cells of rotational symmetry. *J. Phys. D: Appl. Phys., 40.* , p. 914–923.

Mazzeo, B., Flewitt, A. (2007). Two- and four-electrode, wide-bandwidth, dielectric spectrometer for conductive liquids: Theory, limitations, and experiment. *J. Appl. Phys. 102, 104106* , p. 1-6.

McAdams, E., Jossinet, J., Subramanian, R., McCauley, R. (2006). Characterization of gold electrodes in phosphate buffered saline solution by impedance and noise measurements for biological applications. *Proceedings of the 28th IEEE EMBS Annual International Conference* , p. 4594 - 4597.

McAdams, E., Lackermeier, A., McLaughlin, J., Macken, D., Jossinet, J. (1995). The linear and non-linear electrical properties of the electrode-electrolyte interface. *Biosensors & Bioelectronics, 10* , p. 67-74.

McIntyre, C., Grill, W. (2002). Extracellular stimulation of central neurons: influence of stimulus waveform and frequency on neuronal output. *J Neurophysiol, 88(4)* , p. 1592-1604.

Mercanzini, A., Colin, P., Bensadoun, J.-C., Bertsch, A., Renaud, P. (2009). In Vivo Electrical Impedance Spectroscopy of TissueReaction to Microelectrode Arrays. *IEEE Transactions on biomedical engineering, vol. 56, no. 7* , p. 1909-1918.

Merino, O. (2006). *A Short History of Complex Numbers.* Kingston: University of Rhode Island.

Min, M., Ojarand, J., Märtens, O., Paavle, T., Land, R., Annus, P., Rist, M., Reidla, M., Parve, T. (2012). Binary Signals in Impedance Spectroscopy. *Proceedings of the 2012 34th Annual International Conference of the IEEE Engineering in Medicine and Biology Society (EMBC 2012)* , p. 1-4.

Min, M., Parve, T., Annus, P., Paavle, T. (2006). Method of Synchronous Sampling in Multifrequency Bioimpedance Measurements. *Proc. of the 23rd IEEE Instrumentation and Measurement Technology Conference (IMTC/06)* , p. 1699-1703.

Min, M., Parve, T., Kukk, V., Kuhlberg, A. (2002). An Implantable Analyser of Bio-Impedance Dynamics: Mixed Signal Approach. *IEEE Transactions on Instrumentation and Measurement, Vol. 51, No. 4* , p. 674-678.

Mittelmann, H. D., Pendse, G., Rivera, D. E., Lee, H. (2006). Optimization-based design of plant-friendly multisine signals using geometric discrepancy criteria. *Comput.Optim. Appl.,vol.38* , p. 173-190.

Moussy, F., Harrison, D. (1994). Prevention of the rapid degradation of subcutaneously implanted Ag/AgCl reference electrodes using polymer coatings. *Anal. Chem. 66(5)* , p. 674-679.

Nahvi, M., Hoyle, B. (2009). Electrical Impedance Spectroscopy Sensing for Industrial Processes. *IEEE Sensors Journal, 2009, vol. 9* , p. 1808-1816.

Nelson, S., Trabelsi, S. (2011). Sensing grain and seed moisture and density from dielectric properties. *Int. J. Agric & Biol. Eng. Vol. 4 No.1* , p. 1-7.

Neuman, M. (2000). Biopotential Electrodes. Ed: J. Bronzino, *The Biomedical Engineering Handbook: Second Edition.* CRC Press LLC, p. 48.1-13.

Nikovski, P. (2011). Practical Synthesis Of Irrational Impedance Based On Solutions Of The Quadratic Equation. *IU-JEEE Vol. 11(2)* , p. 1391-1398.

Ohm, G. S. (1827). *Die galvanische Kette : mathematisch bearbeitet.* Berlin: Riemann.

Ojarand, J., Min, M. (2012). Simple and Efficient Excitation Signals for Fast Impedance Spectroscopy. *Electronics and Electrical Engineering, No. 2(128)* .

Ojarand, J., Annus, P., Land, R., Parve, T., Min, M. (2010). Nonlinear Chirp Pulse Excitation for the Fast Impedance Spectroscopy. *Electronics and Electrical Engineering, 4.* , p. 73-76.

Ojarand, J., Giannitsis, A., Min, M., Land, R. (2011). Front-end electronics for impedimetric microfluidic devices. SPIE Bioelectronics, Biomedical, and Bioinspired Systems V; and Nanotechnology, V. *In: Proceedings of SPIE,*

vol.8068R. Bellingham, Washinghton, USA.: International Society For Optical Engineering. p. 1-15.

Ojarand, J., Land, R., Min, M. (2012). Comparison of Spectrally Sparse Excitation Signals for Fast Bioimpedance Spectroscopy. In the context of cytometry. *In: Proc. 7th International Workshop on Medical Measurements and Applications (MeMeA2012). IEEE* , p. 214-218.

Ong, M. S., Kuang, Y. C., Liam, P. S., Ooi, M. P.-L. (2012). Multisine With Optimal Phase-Plane Uniformity for ADC Testing. *EEE Trans.- Instrum. Meas., vol. 61, no. 3* , p. 566-578.

Paavle, T., Min, M., Ojarand, J., Parve, T. (2010). Short-time chirp excitation for using in wideband characterization of objects:an overview. *In: Proceedings of the 12th Biennial Electronics Conference BEC2010* , p. 253-256.

Pajkossy, T. (2005). Impedance spectroscopy at interfaces of metals and aqueous solutions — Surface roughness, CPE and related issues. *Solid State Ionics, 176.* , p. 1997-2003.

Pethig, R., Kell, D. (1987). The passive electrical properties of tissues and cell suspensions. *Phys Med Biol.3(8)* , p. 33–70.

Plessey Semiconductor. (2011). *PS25101 EPIC Ultra High Impedance ECG Sensor. Data Sheet 291346.* Swindon, UK: Plessey Semiconductors Ltd.

Pliquett, U. (2010). Bioimpedance: A Review for Food Processing. *Food Engineering Reviews, vol.2* , p. 74-94.

Pliquett, U., Frense, D., Schönfeldt, M., Frätzer, C., Zhang, Y., Cahill, B., Metzen, M., Barthel, A., Nacke, T., Beckmann, D. (2010). Testing miniaturized electrodes for impedance measurements within the β-dispersion – a practical approach. *J. Electr. Bioimp., vol. 1* , p. 41-55.

Pliquett, U., Gallo, S., Hui, S., Gusbeth, C., Neumann, E. (2005). Local and transient structural changes in stratum corneum at high electric fields: contribution of Joule heating. *Bioelectrochemistry. 67(1)* , p. 37-46.

Pliquett, U., Schönfeldt, M., Barthel, A., Frense, D., Nacke, T., Beckmann, D. (2011). Front end with offset-free symmetrical current source optimized for time domain impedance spectroscopy. *Physio. Meas.32(7)* , p. 927-944.

Prodan, E., Prodan, C., Miller, J. H. (2008). The dielectric response of spherical live cells in suspension: an analytic solution. *Biophys. J., (95)* , p. 4174-4182.

Pucihar, G., Krmelj, J., Reberšek, M., Napotnik, T., Miklavčič, D. (2011). Equivalent Pulse Parameters for Electroporation. *IEEE Transactions on Biomedical Engineering , vol. 58, no. 11* , p. 3279-3288.

Rauscher, C. (2008). *Fundamentals of Spectrum Analysis. Sixth edition.* München: Rohde & Schwarz.

Rees, D., Jones, D. (1991). Design and application of non-binary low peak factor signals for system dynamic measurement. *Int. Conference on Control, Edinburgh, UK, vol., 1991* , p. 644 – 650.

Rees, D., Jones, D., Evans, D. (1992). Practical considerations in the design of multisine test signals for system. *IEEE Conference on Instrumentation and Measurement Technology* , p. 174-179.

Richter, K., Haslbeck, M., Buchner, J. (2010). The heat shock response: life on the verge of death. *Mol Cell. 40(2)* , p. 253-256.

Riistama, J. (2010). *Characterisation of Wearable and Implantable Physiological Measurement Devices. Ph.D. Thesis.* Tampere: Tampere University of Technology.

Ron, A., Singh, R., Fishelson, N., Shur, I., Socher, R., Benayahu, D., Shacham-Diamand, Y. (2008). Cell-based screening for membranal and cytoplasmatic markers using dielectric spectroscopy. *Biophys Chem.,135(1-3)*, p. 59-68.

Scharfetter, H., Lackner, H., Rosell, J. (2001). Magnetic induction tomography:hardware for multi-frequency measurements in biological tissues. *Physiological Measurement, vol. 22, no. 1* , p. 131-146.

Schroeder, M. (1970). Synthesis of low peak-factor signals and binary sequences of low autocorrelation. *IEEE Trans. Information Theory, vol. 16* , p. 85-89.

Schwan, H. P. (1968). Linear and nonlinear electrode polarization and biological materials. *Annals of the New York Academy of Sciences, 148* , p. 269–288.

Schwan, H. P. (1999). The Practical Success of Impedance Techniques from an Historical Perspective. *Annals of the New York Academy of Sciences, v.873* , p. 1-12.

Schwan, H., Takashima, S. (1991). Dielectric Behavior of Biological Cells and Membranes. *Bull.Inst.Chem.Res., Kyoto Univ., Vol. 69, No.4* , p. 459-475.

Schwartz, G. (1962). A theory of the low-frequency dielectric dispersion of colloidal particles in electrolyte solution. *J. Phys. Chem.,v. 66* , p. 2636-2642.

Shinwari, M., Zhitomirsky, D., Deen, I., Selvaganapathy, P., Deen, M., Landheer, D. (2010). Microfabricated Reference Electrodes and their Biosensing Applications. *Sensors 10, no. 3* , p. 1679-1715.

Smith, S. (1999). *The Scientist and Engineer's Guide to Digital Signal Processing.* San Diego: California Technical Publishing.

Stoy, R., Foster, K., Schwan, H. (1982). Dielectric properties of mammalian tissues from 0.1 to 100 MHz: a summary of recent data. *Phys. Med. Biol., v.27* , p. 501-513.

Sun, T., Morgan, H. (2010). Single-cell microfluidic impedance cytometry: a review. *Microfluidics and Nanofluidics.Volume 8, Number 4* , p. 423-443.

Sun, T., Bernabini, C., Morgan, H. (2010). Single-Colloidal Particle Impedance Spectroscopy: Complete Equivalent Circuit Analysis of Polyelectrolyte Microcapsules. *Langmuir26 (6). Journal of the American Chemical Society* , p. 3821–3828.

Tai, C., de Groat, W., Roppolo, J. (2005). Simulation analysis of conduction block in unmyelinated axons induced by high-frequency biphasic electrical currents. *IEEE Trans Biomed Eng., 52(7)* , p. 1323-1332.

Takashima, S. (1985). Passive electrical properties and voltage dependent membrane capacitance of single skeletal muscle fibers. *Pflügers Archiv European Journal of Physiology. volume 403, Number 2* , p. 197-204.

Udal, A., Kukk, V., Velmre, E. (2009). Critical Analysis of Uncertainty Relations Based on Signal Duration and Spectrum Width. *Electronics and Electrical Engineering v.94(6)* , p. 31-34.

Urbanova, V., Li, Y., Vytras, K., Yvert, B., Kuhn, A. (2011). Macroporous microelectrode arrays for measurements with reduced noise. *Journal of Electroanalytical Chemistry, vol. 656* , p. 91-95.

Valsa, J., Vlach, J. (2011). RC models of a constant phase element. *Int. J. Circ. Theor. Appl. Vol. 20, No. 3* , p. 619-626.

Van den Bos, A. (1972). *Estimation of parameters of linear systems using periodic test signals. Doctor of Technical Sciences Thesis.* Delft: Delft university Press.

Van den Bos, A. (1991). Periodic test signals-properties and use. *In Proc. of International Conference Control '91, vol.1* , p. 545 - 549.

Van den Bos, A., Krol, R. (1979). Synthesis of Discrete-Interval Binary Signals with Specified Fourier Amplitude Spectra. *International Journal of Control, 1979, Vol. 30, No. 5* , p 871-884.

Vedru, J., Gordon, R. (2010). Model of an Inductive Sensor of Cardiac Activity Attached to Patient. *Journal of Physics: Conference Series, 2010, 244(1), 012010.*, p. 1-4.

Velmre, E. (2010). Thomas Johann Seebeck and his contribution to the modern science and technology. *In proceeding of: Electronics Conference (BEC), 2010 12th Biennial Baltic* , p. 17-24.

Wang, H., Pilon, L. (2012). Intrinsic limitations of impedance measurements in determining electric double layer capacitances. *Electrochimica Acta 63.* , p. 55-63.

Wang, J.-W., Wang, M.-H., Jang, M.-S. (2010). Effects of electrode geometry and cell location on single-cell impedance measurement. *Biosensors and Bioelectronics, 25* , p.1271–1276.

Wang, X., Becker, F., Gascoyne, P. (2010). The fractal dimension of cell membrane correlates with its capacitance: A new fractal single-shell model. *Chaos, v. 20, 043133* , p. 1-7.

Weaver, J. (2000). Electroporation of Cells and Tissues. *IEEE Trans. On Plasma Science, Vol. 28, No. 1* , p. 24-33.

Yang, Y., Wang, J., Gao, Z., Li, D., Wang, J. (2009). Waveform synthesis of multi-frequency sinusoids with 2nth primary harmonics based on Walsh functions. *Proc. IEEE Biomedical Circuits and Systems Conference , Bejing, China* , p. 129-132.

Yao, J., Gillis, K. (2012). Quantification of noise sources for amperometric measurement of quantal exocytosis using microelectrodes. *Analyst, 137* , p. 2674-2681.

**List of publications directly related to thesis topic
(copies are added in Appendices)**

A. Ojarand, J., Annus, P., Land, R., Parve, T., Min, M. (2010). Nonlinear Chirp Pulse Excitation for the Fast Impedance Spectroscopy. Electronics and Electrical Engineering, 4 (100), p.73 - 76.

B. Ojarand, J., Land, R., Min, M. (2012).Comparison of Spectrally Sparse Excitation Signals for Fast Bioimpedance Spectroscopy. In the context of cytometry. In: Proc. 7th International Workshop on Medical Measurements and Applications (MeMeA2012): Budapest, Hungary, May 18-19, 2012, IEEE 2012, p. 214-218.

C. Ojarand, J., Min, M. (2012). Simple and Efficient Excitation Signals for Fast Impedance Spectroscopy. Electronics and Electrical Engineering, No. 2(128), (Accepted for publication).

D. Ojarand, J., Giannitsis, A.T., Min, M., Land, R. (2011). Front-end electronics for impedimetric microfluidic devices. Bioelectronics, Biomedical, and Bioinspired Systems V; and Nanotechnology V,In: Proc. SPIE'2011, Vol.8068, 80680R, 15 pp. doi: 10.1117/12.886553.

List of other publications related to topic

1. Min, M., Ojarand, J., Märtens, O., Paavle, T, Land, R., Annus, P., Rist, M., Reidla, M., Parve, T. (2012). Binary Signals in Impedance Spectroscopy. Proceedings of the 2012 34th Annual International Conference of the IEEE Engineering in Medicine and Biology Society (EMBC 2012) (1 - 4). New Jersey: IEEE Conference Publications.

2. Annus, P., Min, M., Ojarand, J., Paavle, T., Land, R., Ellervee, P., Parve, T. (2011). Multisine and Binary Multifrequency Waveforms in Impedance Spectrum Measurement - A Comparative Study. In: Proceedings of the 5th European IFMBE MBEC 2011, Budapest, 14-18 Sept. , 2012, Volume 37, Part 1, Part 13, p.1265-1268, DOI: 10.1007/978-3-642-23508-5_327.

3. Annus, P., Land, R., Min, M., Ojarand, J. Simple Signals for System Identification. In: Fourier Transform - Signal Processing, edited by Salih Mohammed Salih, InTech, 2012, Ch.11, p.257-276. ISBN: 978-953-51-0453-7.

4. Annus, P., Min, M., Rist, M., Ojarand, J., Land, R. (2012). Current source considerations for broadband bioimpedance spectroscopy. In: Lecture Notes on Impedance Spectroscopy: Measurement, Modeling and Applications, edited by Olfa Kanoun, London: Taylor & Francis, 2012, p.63 – 73.

5. Min, M., Land, R., Annus, P., Ojarand, J. (2011). Chirp pulse excitation in the impedance spectroscopy of dynamic subjects - Signal modelling in time and frequency domain. Lecture Notes on Impedance Spectroscopy: measurement, Modeling and Applications, edited by Olfa Kanoun, London: Taylor & Francis, 2011, p. 79-82.

6. Min, M., Paavle, T., Ojarand, J. (2011). Time-Frequency Analysis of Biological Matter Using Short-Time Chirp Excitation. In: Proceedings of the European Conference on Circuit Theory and Design 2011 (ECCTD'11), Linköping, Sweden, August 29-31, 2011. IEEE, 2011, p. 585 - 588.

7. Paavle, T., Min, M., Ojarand, J., Parve, T. (2010). Short-time chirp excitation for using in wideband characterization of objects:an overview. In: Proceedings of the 12th Biennial Baltic Electronics Conference BEC2010. IEEE, 2010, p. 253-256.

8. Annus, P., Min, M., Ojarand, J. (2008). Shortened square wave waveforms in synchronous signal processing. In: Proceedings of the IEEE International Instrumentation and Measurement Technology Conference (I2MTC 2008), 12-15 May 2008, Victoria, British Columbia, Canada, 2008 , IEEE 2008, p.1259 - 1262.

9. Invention: Method and device using shortened square wave waveforms in synchronous signal processing; Authors: Paul Annus, Mart Min, and Jaan Ojarand. EP 2 313 001 B1. Date of publication and mention of the grant of the patent: 01.02.2012

10. Invention: Method and device for broadband analysis of systems and substances; Authors: Raul Land, Paul Annus, Mart Min, Olev Märtens, Jaan Ojarand; Priority number: P201100054; Priority Priority date: 30.08.2011

APPENDIX A

Ojarand, J., Annus, P., Land, R., Parve, T., Min, M. (2010).
Nonlinear Chirp Pulse Excitation for the Fast Impedance Spectroscopy.
Electronics and Electrical Engineering, 4 (100), p.73 - 76.

SIGNAL TECHNOLOGY

T 121 ——————————————

SIGNALŲ TECHNOLOGIJA

Nonlinear Chirp Pulse Excitation for the Fast Impedance Spectroscopy

J. Ojarand, P. Annus
Competence Center ELIKO,
Teaduspargi 6/2, 12618 Tallinn, Estonia, phone: +372 6202166, e-mail: jaan.ojarand@eliko.ee

R. Land, T. Parve, M. Min
Tallinn University of Technology, Department of Electronics,
Ehitajate tee 5, 19086 Tallinn, Estonia s, phone: +372 6202158, e-mail: raula@ttu.ee

Introduction

Excitation with a short duration pulse is often used to perform the fast spectroscopy – to cover the wide frequency range within short timeframe [1-5].

Variety of well known short excitation waveforms can produce wideband spectral distribution of power e.g. rectangular pulses, pseudo-random maximum length sequence (MLS) of rectangular pulses, Gaussian pulses and its derivatives, sinc and others [1-6]. Though a number of different waveforms are used, the chirp wave is expected to be the most suitable one in many cases [2-5]. The power spectral density (PSD) of the chirp excitation pulse can cover tailored frequency range within given duration in time domain [4-5]. Recently shorter chirp pulses, having only some of cycles or even a fraction of a single cycle, have been analyzed and proposed to be used for the broadband spectroscopy of dynamic impedance. These short waveforms are named "titlets" by the authors [5].

Linear chirp is a well-known wideband excitation waveform, where the instantaneous frequency f_i, changes linearly during the excitation interval T_{exc}

$$f_i(t) = ktf_0,\qquad (1)$$

where f_0 is the starting frequency (at time $t = 0$), and k is the rate of the frequency increase or chirp rate. The instantaneous frequency could also be defined in terms of the derivative of the phase θ

$$f_i(t) = \frac{1}{2\pi}\frac{d\theta(t)}{dt}.\qquad (2)$$

Chirps with a nonlinear rate of the frequency change are also known [7,8]. Unlike the linear chirp, which has a constant chirp rate, a nonlinear chirp has varying chirp rate during the excitation interval. Spectral properties of the chirp waveform depend on

quickening (or slowing) of the frequency change i.e. acceleration or deceleration of the frequency change.

Rayleigh energy criterion and Parseval's theorem infer that for a linear chirp with a constant bandwidth, PSD must be proportional to pulse width. Consequently, under conditions of constant bandwidth, the PSD must be inversely proportional to chirp rate. Furthermore, the principle of stationary phase infers that the major contribution to the spectrum at any frequency f is made by that part of the signal which has instantaneous frequency f_i. This means that for the nonlinearly modulated chirp, the PSD in the particular frequency range is inversely proportional to the chirp rate in that particular frequency [9].

In the field of impedance spectroscopy an equal spectral density at all frequencies of interest is desirable though smooth PSD curve above level of 0.5 is often also satisfactory. It is also considered necessary that most of the excitation energy will fall into bandwidth of interest [2-4].

Since the spectrum at any frequency f is made by that part of the signal which has corresponding instantaneous frequency, f_i it is possible to shape the spectral density curve by controlling the speed of the frequency change of the chirp. This principle is usable also for titlets - short chirp waveforms.

It is possible to control the chirp rate by combining several exponential signals with different slopes when driving the voltage controlled sinusoidal oscillator (VCO) as described below.

Nonlinearly Modulated Chirp Excitation

Nonlinearly modulated chirp excitation is defined in general as a waveform where the instantaneous frequency f_i changes nonlinearly during the excitation interval T_{exc}. If the growth (or reduction) of the frequency change is exponential then the frequency of the signal varies exponentially as a function of time t:

$$f_i(t) = k^t f_0. \qquad (3)$$

The advantage of using an exponential relationship is in ease of realization, Fig. 1. depicts a simplified structure of the exponentially modulated chirp waveform source.
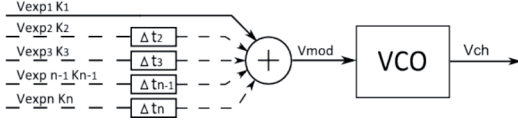

Fig. 1. Exponentially modulated chirp waveform source

Output signal Vch of the VCO can be expressed as follows

$$V_{ch} = V_p \sin(2\pi(f_0 t + \int_0^t K_f V_{\text{mod}} dt)), \qquad (4)$$

where V_p – a peak amplitude of the signal; K_f – the frequency sensitivity of the VCO in Hz/V. In current study V_p is kept constant at the 1V level. Peak value of the modulating signal V_{mod} is also kept at the 1V level. Input voltages V_{exp} can be expressed as follows

$$V_{\text{exp}} = V_o e^{kt} = V_o e^{t/\tau}, \qquad (5)$$

where V_o express an initial voltage; k – growth constant; τ – the e-folding time. $\tau = 1/k$ and is called „time-constant" later in this paper.

In the simplest case only one exponentially changing voltage V_{exp} drives a VCO. However, it was found, that by combining two or more exponential signals with different growth factors it is possible to generate chirp waveforms with substantially steeper slope of spectral curve above the cut-off frequency, compared to linearly modulated chirp or nonlinearly modulated chirp with one exponentially changing voltage V_{exp}.

Linearly modulated chirps have typically -40 dB/decade fall of the amplitude spectrum curve above the cut-off frequency [2–5], Simple, exponentially modulated chirp marked as Exp.1 has similar characteristics (Fig. 2). Spectrum of the chirp marked as Exp.2 using combination of two exponential signals for modulating the VCO has -60 dB/decade fall of the amplitude above the cut-off frequency. As it can be seen, spectral curves of the exponentially modulated chirps are also more flat in a usable frequency bandwidth.
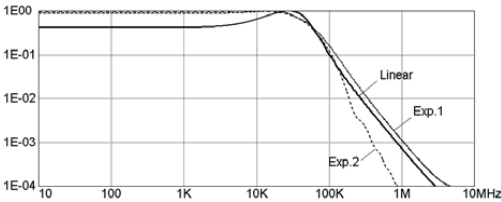

Fig. 2. Normalized RMS spectral density of the exponentially modulated single cycle titlets

All chirps described in this paper are short, one cycle chirps – one cycle titlets.

Further investigation shows, that combination of three exponential signals allows to control the shape of the spectral density curve more flexibly. As it was noted before the peak amplitude of the modulating signal V_{mod} is kept constant, variables are the time delays Δt_n, time-constant τ, direction and sign of the exponential signals and the frequency sensitivity of the VCO, K_f. Resulting waveforms of the modulating signals used in following examples are shown in Fig. 3. Time-constant τ of the signal Exp.1 is 11 µs. Exp.2 is a sum of upward-sloping exponential signal V_1 with τ_1=12 µs and downward-sloping exponential signal V_2 with τ_2=12 µs, delay Δt_2=5 µs. Exp.3 is a sum of upward-sloping exponential signal V_1 with τ_1=3 µs and downward-sloping exponential signals V_2 and V_3 with τ_2=12 µs, τ_3=5 µs, delays Δt_2= Δt_3= 4 µs.
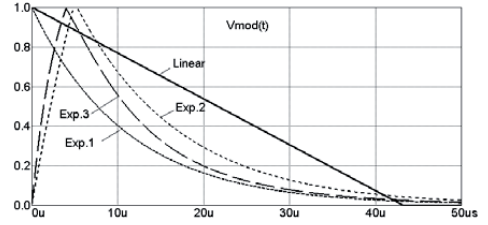

Fig. 3. Modulating waveforms

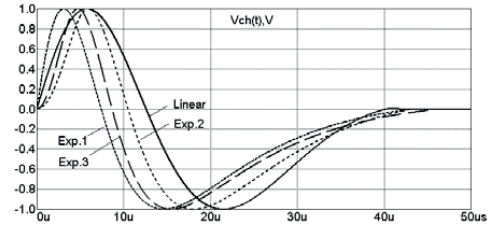Corresponding waveforms of titlets at the output of the VCO are shown in Fig. 4.

Fig. 4. Titlet waveforms

Frequency sensitivity K_f of the VCO for the linear titlet is 46.5 kHz/V, 92.7 kHz/V for the Exp.1 titlet, 69 kHz/V for the Exp.2 titlet and 80.5 kHz/V for the Exp.3 titlet.

PSD and Energy Distribution of Linearly and Exponentially modulated titlets

Computer simulation give following PSD curves presented in Fig. 5. and Fig. 6. Peak amplitudes of all waveforms are same, +/- 1V. Duration of signals is in the region of 40-50 µs and was varied intentionally to get the same cut-off frequency where PSD falls to the level of 0.5 (Fig. 6).

The shape of the signal was varied by changing the parameters of the modulating signals to achieve two goals: maximize the energy content and get a flat

and smooth PSD curve in the frequency range of interest.

As it can be seen in Figs 2 and 5, a multislope exponential modulating signal allows substantially steeper slope above the cut-off frequency. However, looking at the situation in the linear scale, see Fig. 6 effect is not so impressive any more. Exponentially modulated titlets perform better than linearly modulated waveforms, but the difference between the simplest Exp.1 and Exp.3 is not significant. However, it must be noted that by changing the parameters of the modulating signal in case of Exp.3, it is possible to raise the first part of the PSD curve above the level of 0.9, but this will drop accordingly the last part of the PSD curve, and this means that overall bandwidth will be narrower.
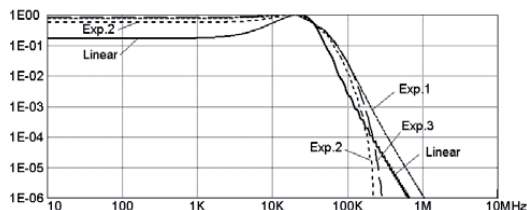

Fig. 5. Normalized PSD of linearly and exponentially modulated titlets, logarithmic scale

PSD curves, where the spectra are normalized separately for each signal are not suitable for the comparison of the energy content of different signals since the maximum values are not equal. To compare the spectral content of different signals, they must be normalized against one of them. PSD curves normalized against the maximum of the linear titlet are presented in Fig. 7.

According to Parseval's theorem, the total energy in the frequency domain must be the same as in time time domain. Due to the higher frequency components, a certain part of the signal energy falls outside of the useful bandwidth. Summing up of the PSD values using a small predetermined frequency interval Δf over the full frequency range and dividing the sum of the useful frequency range with total sum, we can find the ratio of useful energy content to the total energy content of the excitation signal. Computer simulation using Δf =10Hz and full bandwidth of 320 kHz gives following results for the one cycle titlets:

1. Linear titlet – 73 % *,
2. Exp.1 titlet – 73 %,
3. Exp.2 titlet – 76%,
4. Exp.3 titlet – 72 %.

* Note: energy from the starting frequency which is below 0.5 level is excluded.

The slope of distribution curve above the cut-off frequency characterizes the ratio of the energies laying in the desired frequency range and above of it. However, it is also important to pay attention also to the PSD in the desired frequency range.
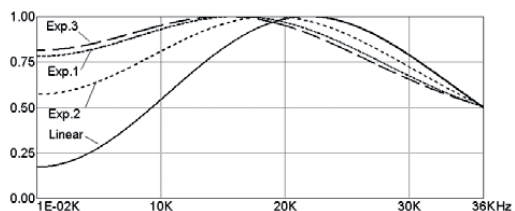

Fig. 6. Normalized PSD of linearly and exponentially modulated titlets, linear scale
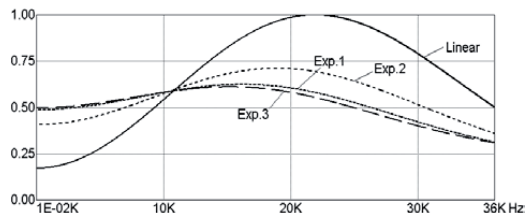

Fig. 7. PSD of linearly and exponentially modulated titlets, linear scale, normalized against the maximum value of the linear titlet

Most likely it is more adequate to compare distribution of the energy of different waveforms in the frequency range of interest since in the field of impedance spectroscopy better signal to noise ratio is usually more important than small power loss outside of the useful frequency range. We can compare the energy content of different waveforms in the frequency range of interest. Computer simulation using frequency interval Δf =10Hz and cut-off frequency 36kHz, gives following results:

1. Linear titlet – 60 % *,
2. Exp.1 titlet – 83 %,
3. Exp.2 titlet – 78%,
4. Exp.3 titlet – 83 %.

* Note: energy from the starting frequency which is below 0.5 level is excluded.

Conclusions

Nonlinear modulation of the VCO allows to shape the PSD curve of the chirp excitation waveforms. Usage of the exponential modulation signals improves one cycle chirp's energy content in the usable frequency range by more than 20 %, compared to its linear counterpart.

Acknowledgements

References

1. **Nahvi, M., Hoyle, B.S**. Electrical Impedance Spectroscopy Sensing for Industrial Processes// IEEE Sensors Journal. –

2009. – No. 12 (9). – P. 1808–1816.

2. **Min M., Giannitsis A. T., Land R., Cahill B. P., Pliquett U., Nacke T., Frense D., Gastrock G., Beckmann D.** Comparison of rectangular wave excitations in broad band impedance spectroscopy for microfluidic applications // IFMBE Proceedings, Vol.25: VII World Congress on Medical Physics and Biomedical Engineering. – Munich (Germany), 2009. – P. 85–88.

3. **Min M., Pliquett U., Nacke T., Barthel A., Annus P., Land R.**. Signals in bioimpedance measurement: different waveforms for different tasks // IFMBE Proceedings, Vol. 17: 13th Int. Conf. on Electrical Bioimpedance (ICEBI'2007). – Graz (Austria), 2007. – P. 181–184.

4. **Min, M., Land, R., Annus, P., Ojarand, J.** Chirp Pulse Excitation in the Impedance Spectroscopy of Dynamic Subjects: signal modelling in time and frequency domain // Transactions on Systems, Signals and Devices. – Aachen: SHAKER Verlag (Germany), 2010. – in print (2p.).

5. **Min M., Land R., Paavle T., Parve T., Annus P**. Broadband spectroscopy of a dynamic impedance// Journal of Physics: Proceedings ICEBI2010. – London: IOP, 2010. – in print (4p).

6. **Annus, P., Min, M., Ojarand, J.** Shortened square wave waveforms in synchronous signal processing// Proceedings I²MTC2008. – Victoria, British Columbia (Canada), 2008. – P. 1259 – 1262.

7. **Skolnik M.I**. Radar Handbook (3rd edition). – McGraw–Hill, 2008. – 1352 p.

8. **Darowicki K., Slepski P**. Determination of electrode impedance by means of exponential chirp signal // Electrochemistry Communications. – 2004. – No. 6. – P.898–902.

9. **Doerry A.W**. Generating Nonlinear FM Chirp Waveforms for Radar (Research Report). – Sandia National Laboratories (New Mexico, USA), 2006. – 34 p.

J. Ojarand, P. Annus, R. Land, T. Parve, M. Min. Nonlinear Chirp Pulse Excitation for the Fast Impedance Spectroscopy // Electronics and Electrical Engineering. – Kaunas: Technologija, 2010. – No. 4(100). – P. 73–76.

Wideband excitation is used to perform the fast spectroscopy – to cover the wide frequency range within short timeframe. Power spectrum of the chirp excitation pulse can cover tailored frequency range within given duration in the time domain. Linear chirp is a well-known wideband excitation waveform, where the instantaneous frequency varies linearly with time. Chirps with nonlinear relationship between time and frequency are also well known. This group of waveforms shape the power spectrum differently from its linear counterpart. The paper describes the results of the study of spectral properties of the nonlinearly modulated chirp signals, where the frequency of the signal varies according to multi-slope nonlinear relationship over the time. The advantage of this type of chirp signals is that the power spectrum of these signals has substantially steeper slope above the cut-off frequency, compared to its common linear and nonlinear counterparts. Ill. 7, bibl. 9 (in English; abstracts in English, Russian and Lithuanian).

Я. Ояранд, П. Аннус, Р. Ланд, Т. Парве, М. Мин. Нелинейный „chirp" сигнал для быстродействующей импеданс спектроскопии // Электроника и электротехника. – Каунас: Технология, 2010. – № 4(100). – С. 73–76.

Широкополосный генератор используется для получения результата в быстрой импеданс спектроскопии, целью которой является покрытие широкой полосы частот за короткий промежуток времени. Спектр мощности возбуждающего „chirp" сигнала может покрывать необходимый частотный диапазон в течении отведенного времени во временной области. Широко известен линейный чирп-сигнал (сигнал с линейной частотной модуляцией). „Chirp" сигнал с нелинейной зависимостью частоты от времени также хорошо известен и имеет форму спектра мощности отличную от спектра мощности линейного „chirp" сигнала. Данная работа описывает результаты исследований спектральных особенностей нелинейного „chirp" сигнала. Изменение частоты такого сигнала задано несколькими отличающимися друг от друга временными зависимостями. Достоинство рассматриваемых сигналов состоит в лучшем распределении энергетического спектра. Ил. 7, библ. 9 (на английском языке; рефераты на английском, русском и литовском яз.).

J. Ojarand, P. Annus, R. Land, T. Parve, M. Min. Netiesinių „chirp" signalų taikymas greitojo impedanso spektroskopijoje // Elektronika ir elektrotechnika. – Kaunas: Technologija, 2010. – Nr. 4(100). – P. 73–76.

Plačiajuostis generatorius naudojamas rezultatams gauti greitojo impedanso spektroskopijoje, kuria siekiama aprėpti platų dažnių diapazoną per trumpą laiko momentą. Galios spektras gali per nustatytą laiką aprėpti reikiamą dažnių diapazoną, esant „chirp" žadinimo signalui. Taikomas plačiai žinomas tiesinis „chirp" signalas (su tiesine dažnine moduliacija). Netiesinis „chirp" signalas taip pat taikomas ir turi galios spektro formą, kuri skiriasi nuo tiesinio „chirp" signalo formos. Aprašyti netiesinio „chirp" signalo spektriniai tyrimai. Nustatyta, kad, pasikeitus tokio signalo dažniui, patys signalai skiriasi tik laiko parametrais. Il. 7, bibl. 9 (anglų kalba; santraukos anglų, rusų ir lietuvių k.).

APPENDIX B

Ojarand, J., Land, R., Min, M. (2012).

Comparison of Spectrally Sparse Excitation Signals for Fast Bioimpedance Spectroscopy. In the context of cytometry.

In: Proc. 7th International Workshop on Medical Measurements and Applications (MeA2012): Budapest, Hungary, May 18-19, 2012. IEEE, 2012, p. 214-218.

Comparison of Spectrally Sparse Excitation Signals for Fast Bioimpedance Spectroscopy

In the context of cytometry

Jaan Ojarand, Raul Land, Mart Min

Thomas Johann Seebeck Department of Electronics
Tallinn University of Technology
Tallinn, Estonia
E-mail: jaan@elin.ttu.ee

Abstract—This paper presents a comparative study of multifrequency excitation signals that are suitable for fast bioimpedance spectroscopy. If properties of an object are changing fast or if the objects are moving fast, e.g. cells flowing within microfluidic channels, the excitation signal should cover the frequency range of interest in short timeframes. However, since shorter signals carry less energy this reduces the signal-to-noise ratio performance. To enhance performance, it is essential to concentrate the signal's energy right on the specific frequencies of interest. Taking into account properties of the biological matter allows us to use more efficient spectrally sparse excitation signals. We also demonstrate that properly designed binary multifrequency excitation signals offer better performance in comparison to multisinewave signals.

Keywords- excitation signals; perturbation signals; multi-frequency signals; spectrally sparse signals; multisine; fast impedance spectroscopy; bioimpedance spectroscopy; crest factor; microfluidics.

I. INTRODUCTION

Impedance spectroscopy is a common approach in assessing passive electrical properties of biological matter, e.g. single cells and cell solutions. However, the quality of impedance measurements highly depends on the presence of noises and interferences, which cause signal distortions.

In microfluidic cytometers interfacial double-layer near microelectrodes affects the impedance and, in combination with intrinsic stray impedance, impacts the measurement [1, 2]. A single cell consists only of small fraction of the volume of its suspending solution, and because of this the sensitivity of measurements must be high [3]. Typical electric equivalent model for a single cell in suspension between two microelectrodes is shown in Fig.1 (a). The suspension resistance R_s and stray capacitance C_s are parallel to cell membrane resistance R_m, cytoplasm resistance R_{cy}, and cell membrane capacitance C_m. Assuming that the membrane resistance R_m is high compared to the resistance of the cytoplasm R_{cy}, this electric equivalent circuit can be simplified to this of Fig.1 (b).
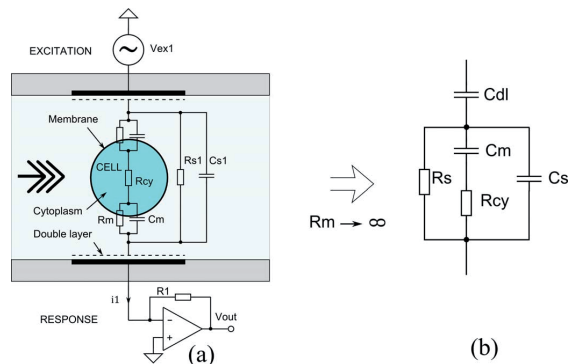

Figure 1.   Typical equivalent circuit model for a single cell in suspension between the electrodes (a) and its simplified equivalent circuit (b)

The signal-to-noise ratio (SNR) of the measured response signal depends directly on the energy of the excitation signal, more exactly, is proportional to the RMS value of the signal. However, the low peak value of the excitation signal may be requested due to several factors. In the case of measuring biological objects the most important factors are the safety limit, the distortions originated by nonlinearities of an object [4] and nonlinearities of interfacial double-layers. To avoid the nonlinearities which are due to the double-layers, the voltage drop on the electrodes should be kept below ±50 mV [5].

The energy content of a wideband excitation signal of fixed amplitude depends also on several other factors including, (a) the duration of the signal itself, and (b) the distribution of energy within the frequency range of interest. In the case of microfluidic devices, within which suspended objects are flowing relatively fast, the excitation signal should cover the whole frequency range of interest within short timeframes. Since a shorter waveform carries less energy, and the amplitude of the signal, as explained, should not exceed specific limit, the only way of improving the efficiency of the excitation signal is by means of concentrating most of its energy right on the frequencies of interest.

II. Spectrally Sparse Excitation Signals

A. Multisine waves

Spectrally sparse signals possess discrete power density spectrum (PSD). Well-known example of this type of signal is the multisine wave. A multisinewave excitation (later here as multisine), $S_{exc}(t)$, between the frequencies f_i to f_n, of n sinusoidal components, can be expressed as

$$s_{exc}(t) = \sum_{i=1}^{i=n} A_i \cdot \sin(2\pi f_i + \Phi_i), \qquad (1)$$

where A_i is the amplitude of the i-th component, and Φ_i is the initial phase of the i-th component.

To avoid spectral leakage, when performing Discrete Fourier Transform (DFT), the multisine must satisfy the following conditions:
(i) the window length to equal the period of the signal,
(ii) an integer number of samples to exactly fit within the window,
(iii) the sampling frequency to satisfy the Nyquist criterion.

Extra periods of the same multisine may be included in the total measurement record since they do not influence the PSD. If the amplitudes A_i of all components are kept on same value, A_N, then the RMS magnitude of the multisine divided over the square root of n remains constant, and the RMS magnitudes of all components equal each other:

$$V_{rms(i)ms} = A_N \frac{1}{\sqrt{2}} \sqrt{\frac{1}{n}}. \qquad (2)$$

In this case the RMS magnitude of the sum of the sine waves depends only on the number of components. However, the amplitude of the sum of the sinusoidal components depends also on the initial phases, Φ_i, of the components. The ratio of the peak value to the RMS value, of the excitation signal, is called peak factor (PF), or crest-factor (CF). The difference of these two factors is in definition of the peak value. In the case of using PF, the peak value is defined as $(V_{pk+} - V_{pk-})/2$, and in the case of using CF, the peak value is defined by the maximum value of absolute values of V_{pk+} and V_{pk-}. [6]. Varying the values of initial phases allows one to find the lower PF and CF values. There is much research done in the direction of achieving the best set of phases, Φ_i, for multisines that contain up to 40 frequencies [7] or even more. Occasionally, the signal designers, ignore the discrepancy between PF and CF. However, if in the process of optimizing a multisine, for achieving minimum peak value, one ignores the difference between PF and CF, this might cause significant asymmetry, with respect to zero, especially in the case of using just few sinusoidal components.

We have developed a novel recursive algorithm, which performs relatively fast and high phase resolution (below 0.1°) search of near optimal phases for multisines with up to 16 components. This algorithm was mainly used for comparing performance of the signals that are presented below. In several cases, this algorithm allows to achieve lower and more accurate CF values compared to the results which are available in other published sources [7, 8].

The accuracy of the calculated CF values highly depends on the density of the signal sampling. We found that the number of samples per period of the highest frequency component must be at least 10, in order to achieve relative error near 1 %. Close to the Nyquist sampling-rate, the relative error will increase up to 50 %. The error depends also on the number of frequency components and their positioning on the frequency axis. Detailed description of the CF optimization algorithm is out of scope of this paper.

B. Performance indicies

In addition to the PF and CF there are more performance indices like PIPS (Performance Index for Perturbation Signals) and other proposed for excitations, which are often also called perturbation signals [8]. Main motivation for searching signals with lower CF is that the allowed maximum peak value of the excitation signal is given (fixed). We found that, in this case, normalizing the peak value of fixed length signals relative to A_N (which is taken equal to 1), with equal or near equal RMS magnitudes of components allows compendious performance comparison of different excitation signals. The RMS values of components of a normalized multisine can be calculated as

$$V_{rms}^* = \frac{1}{\sqrt{2}} \frac{A_N}{Max(|A_i +|, |A_i -|)}. \qquad (3)$$

C. Number of multifrequency components

Optimal number of the excitation signal components depends on the dielectric properties of the cells. The polarization of cell membranes which is observed on the spectrum as β-dispersion exhibits a characteristic frequency between several kHz up to some MHz [1]. Results of PSpice modeling of the equivalent circuit, using some typical values of the components, which are appropriate for the microfluidic unit, which is described in the reference [3], are plotted in Fig. 2.

This basic model is a good approximation not only for cell suspensions but also for tissues. More sophisticated are frequency dependent R and C in order to create a constant phase element (CPE). The latest fits measurement data better. However, the physical meaning of the CPE is still subject of controversy [10]. Due to the nature of the cells there is no resonance across β-dispersion band or even at lower frequencies, where is the α-dispersion located. Because magnitude and phase curves vs. frequency are smooth and cover usually not more than 2-3 decades, according to equation (2) it is beneficial the use spectrally sparse multifrequency signals with limited number of frequency components.

Accuracy of the model fitting depends on the number of frequency components n as it is illustrated in Fig.3 for the C_m values as in Fig.2. A number of fittings m is 1000 and 10% of Gaussian white noise was added to the impedance values before the fitting was performed using LabVIEW software.
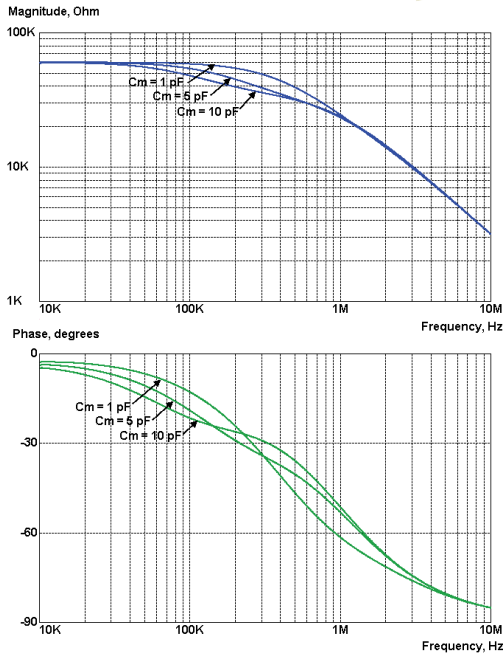
Figure 2. Spectra of magnitude and phase of the impedance, for different values of membrane capacitance Cm. The electric equivalent of this model is shown in Fig 1 (b), Cdl = 10nF, Cs = 5 pF, Rs = 60 kΩ and Rcy = 100 kΩ .
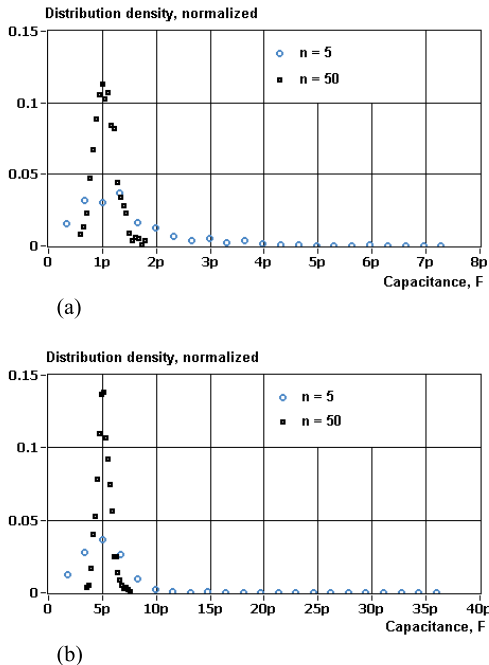

(a)

(b)

Figure 3. Normalized distribution density of the fitted Cm values of 1pF (a) and 5pF (b) for the number of frequency componets n=5 and n=50.

It was stated in [7] that if excitation signal contains an assemblage of sinusoids with the frequencies which are prime number multiplies of some fundamental, which itself is excluded from the signal, then it provides total immunity against harmonic distortions due to even power non-linearities. Odd power nonlinearities are also highly reduced. In our comparison we included also this type of multisines (see Fig. 7).

D. Binary multifrequency signals (BMS)

Multifrequency binary waveforms, with only two discrete values (i.e. +A and –A), are much simpler to generate, and can be effective too [9, 11-14], even more effective than the sine wave is [14]. This type of excitation signals have always a unity value crest factor CF = 1 and the total energy content is √2 times higher than of multisine of the same duration. However, if a multisine has all the energy spread in wanted spectral lines then BMS has usually about 60 to 70% of energy in these spectral lines. [14]. Despite this loss of energy, the RMS values of the desired frequency components of normalized BMS (with amplitudes +1 and -1) are higher than RMS values of comparable multisine signals.

BMS can be synthesized in several ways. At first it can be derived by detecting zero crossings of the multisine signal. This operation can be described by the following formula:

$$b_{exc}(t) = sign \sum_{i=1}^{i=n} A_i \cdot \sin(2\pi f_i + \Phi_i). \qquad (4)$$

It was found that in a logarithmic distribution of frequency components and for $n > 10$, well optimized multisines allow synthesize BMS with almost flat spectra as it is shown in Fig. 4. In some cases described optimization of multisines does not provide satisfying results for the BMS. The magnitudes of
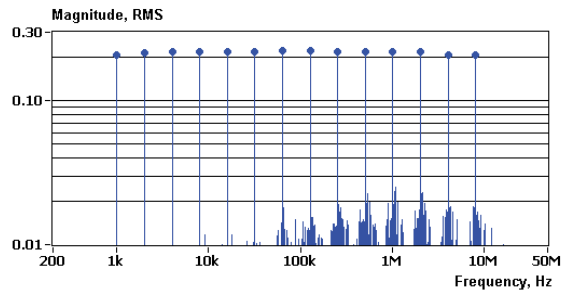

Figure 4. RMS spectrum of BMS with 14 binary rated frequencies 1, 2, 4, 8, 16, 32, 64, 128, 256, 512, 1024, 2048, 4096, 8192 kHz . Mean RMS value of all components is 0.218and deviation from mean value +/- 3,4 %.
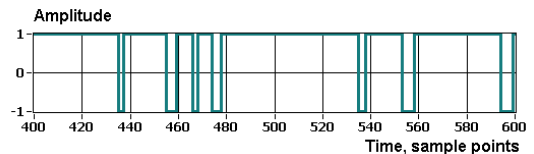

Figure 5. A slice of the vaweform of BMS with 14 binary rated frequencies, zoomed out between the sample points from 400 to 600. Total number of samples is 81920.

BMS spectral components can be adjusted by manipulating iteratively with amplitudes of the origin multisine signal. This method allows also pre-emphasizing of the shape of spectra to match the frequency response of an object [14].For the specific case, which is plotted on Fig. 2, it is desirable to increase the magnitudes of lower frequency components in the excitation signal spectrum, which allow improving the SNR in this area.

If the number of components $n < 10$, manipulating of all phase combinations of origin multisine, as described in reference [3], or direct varying the durations of the pulses of binary signal can be also used for finding desired shapes of the spectra .

III. COMPARISION OF RMS VALUES OF NORMALIZED MULTISINES AND BINARY MULTIFREQUENCY SIGNALS.

For the comparison of RMS values, the frequency components peak values of the multisine were kept between +1 and -1 and the amplitudes of the binary signals determined as +1 and -1. As it can be noticed in Fig 6, normalized RMS magnitudes of equally distributed and optimized multisine

components are close to the value calculated by equation (2) if $n > 3$. The BMS has similar tendency, but however, RMS values of the components tend to the value of

$$V_{rms(i)b} = \frac{4A_N}{\pi\sqrt{2}}\sqrt{\frac{1}{n}} . \tag{5}$$

Normalized RMS magnitudes of multisines and BMS distributed by prime numbers are shown on Fig. 7. In both cases normalized RMS magnitudes of multisines are considerably lower than RMS magnitudes of BMS. In case of equally distributed frequency components, the ratio of RMS limits is given as

$$\frac{V_{rms(i)b}}{V_{rms(i)ms}} = \frac{4}{\pi} . \tag{6}$$

Since the energy is proportional to power of two of RMS magnitude, this yields to signal energy gain up to 1.62 times.
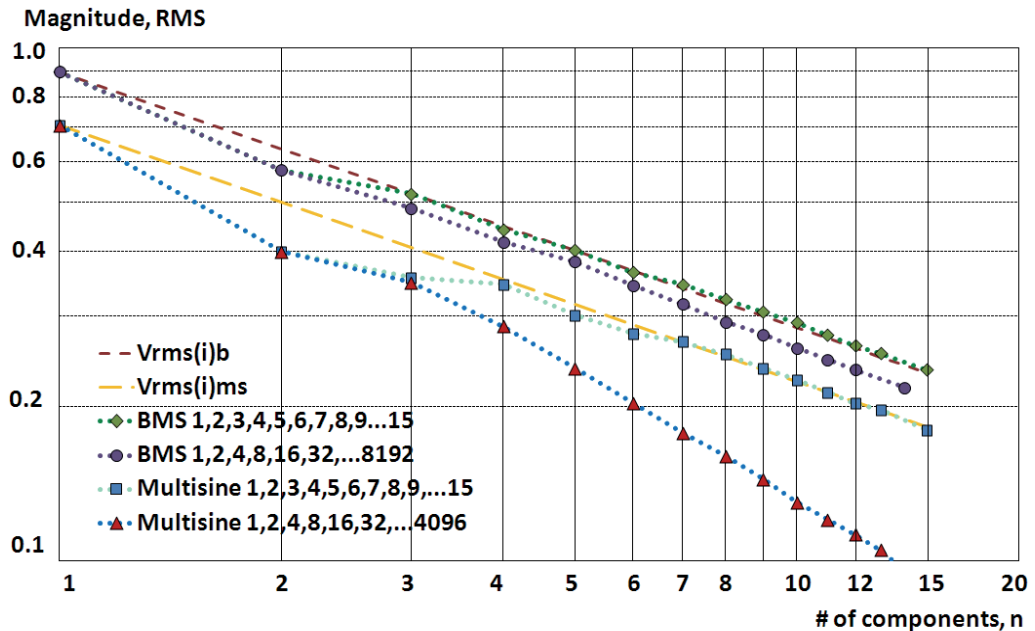
Figure 6.   Normalized RMS magnitudes V *rms of equally distributed and binary rated frequency components of multisines (lower lines) and BMS (upper lines) vs. number of components n .

In case of logarithmically distributed frequency components which are suited better for bioimpedance measurements, the ratio of RMS magnitudes is increasing with number of frequency components. Ratio of RMS magnitudes of the BMS

and multisines at number of frequencies n=12 is 2.27 for the frequency distributions shown in Fig. 6, and 2.24 for the frequency distributions shown in Fig. 7. These ratios yield to signal energy gain at least 5 times.
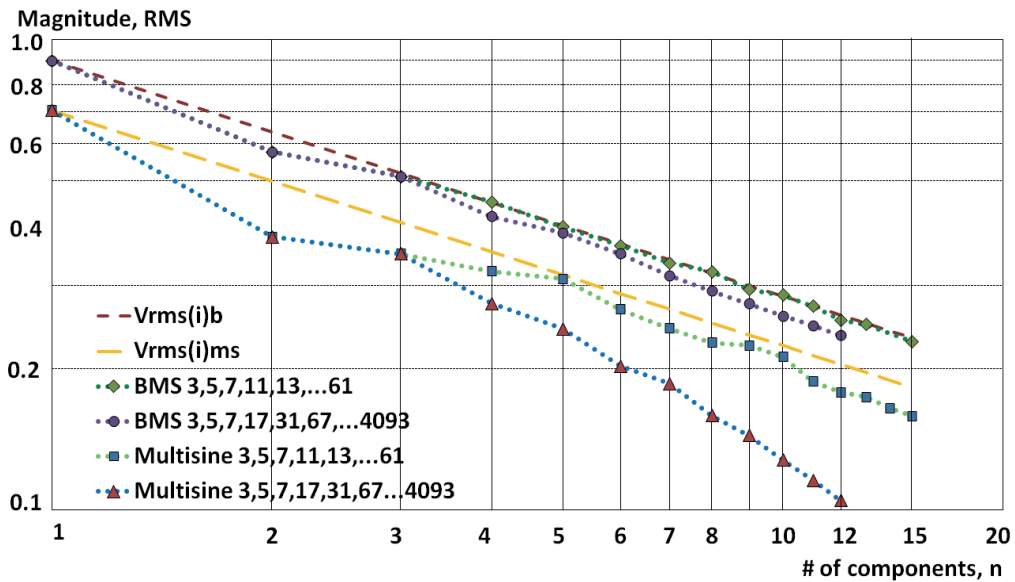
Figure 7. Normalized RMS magnitudes V^{*}_{rms} of equally distributed and near logarithmically distributed frequency components with prime numbers for multisines (lower lines) and BMS (upper lines) vs. number of components n.

IV. CONCLUSION

We showed that multifrequency binary signals offer the possibility of achieving up to 5 times higher signal energy level, for an excitation signal which contains 12 harmonic components of interest, which are logarithmically distributed over three frequency decades. Considering the simplicity in generating binary sequences, there is no doubt that binary multifrequency excitation signals deserve the greatest attention in the electrical bioimpedance measurements.

REFERENCES

[1] H. P. Schwan, Determination of Biological Impedances In Physical Techniques in Biological Research, Nastuk W.L., Ed., Academic Press, New York, vol. 6, 1963, pp.323-406.

[2] B. A. Mazzeo, "Parasitic capacitance influence of potential-sensing electrodes on four-electrode liquid impedance measurements," Journal of Applied Physics, 105, 2009, pp. 094106-1-5.

[3] J. Ojarand, A. T. Giannitsis, M. Min, R. Land. "Front-end electronics for impedimetric microfluidic devices," In: Proc. SPIE'2011, Vol.8068, 80680R, Bioelectronics, Biomedical, and Bioinspired Systems V; and Nanotechnology V, 2011, pp. 80680R-1-15.

[4] U. Pliquett, "Bioimpedance: A Review for Food Processing," Food Engineering Reviews, Springer, 2010 pp.74–94.

[5] D. A. Borkholder, "Cell Based Biosensors Using Microelectrodes," Ph.D. Thesis, Stanford University, 1998, pp.57-61.

[6] E. Van der Ouderaa, J. Schoukens, and J. Renneboog, "Peak factor minimization using a time-frequency swapping algorithm," IEEE Trans. - Instrum. Meas., vol. 37, no. 1, 1988, pp. 145–147.

[7] D. Rees, D. L. Jones, "Design and application of non-binary low peak factor signals for system dynamic measurement," Int. Conference on Control, Edinburgh, UK, 1991, vol., 1991, pp. 644 – 650.

[8] M. S. Ong, Y. C. Kuang, P. S. Liam, M. P-L. Ooi. "Multisine With Optimal Phase-Plane Uniformity for ADC Testing," IEEE Trans. - Instrum. Meas., vol. 61, no. 3, 2012, pp. 566-578.

[9] K. R. Godfrey, A. H. Tan, H. A. Barker, B. Chong. "A survey of readily accessible perturbation signals for system identification in the frequency domain," Control Engineering Practice, 13 (11).,2005, pp. 1391-1402.

[10] U. Pliquett, "Electricity and biology," in Proc. 2008 Int. Biennial Baltic Electronics Conference (BEC2008), Tallinn, Estonia, 2008, pp. 11-20.

[11] R. Pintelon, J. Schoukens, System identification: a frequency domain approach. Piscataway, NJ, USA, IEEE Press, 2001.

[12] Y. Yang, J. Wang , Z. Gao, D. Li and J. Wang "Waveform synthesis of multi-frequency sinusoids with 2nth primary harmonics based on Walsh functions," Proc. IEEE Biomedical Circuits and Systems Conference , Bejing, China, 2009, pp. 129–132.

[13] A. Van Der Bos and R. Krol, "Synthesis of discrete-interval binary signals with specified Fourier amplitude spectra," Int J Control 30:, 1979, pp. 871–884.

[14] R. Land, B. P. Cahill, T. Parve, P. Annus, M. Min, "Improvements in Design of Spectra of Multisine and Binary Excitation Signals for Multi-frequency Bioimpedance Measurement", Proc. IEEE 33rd Medicine and Biology Society Conference (EMBC'11), Boston, USA, Aug. 30 - Sept. 3, 2011, pp. 4038 - 4041.

APPENDIX C

Ojarand, J., Min, M. (2012).

Simple and Efficient Excitation Signals for Fast Impedance Spectroscopy.

Electronics and Electrical Engineering, No. 2(128) (Accepted for publication).

Simple and Efficient Excitation Signals for Fast Impedance Spectroscopy

J. Ojarand, M. Min

Th. J. Seebeck Dept. of Electronics, Tallinn University of Technology
Ehitajate tee 5, 19086 Tallinn, Estonia, phone: +372 6202166, e-mail jaan@elin.ttu.ee

Introduction

Using of simple binary waveforms in fast bioimpedance spectroscopy is discussed in the paper. The use of excitation waveforms discussed here is not limited for biological objects, however, bioimpedance spectroscopy is a common field where fast and sensitive measurements are required. Electrical bio-impedance spectra are used to characterize the structure of tissues and cell cultures [1]. Also single cells can be detected and their behavior characterized even if the parameters of which are changing fast, e.g. when the cells are flowing within microfluidic channels [2] or nerve cells are fired. Only milliseconds can be allowed to avoid significant dynamic errors in last case.

The signal-to-noise ratio (SNR) of the measured response signal depends directly on the energy of the excitation signal, more exactly, is proportional to the RMS value of the signal. However, the level of the excitation signal may be low due to nonlinearities of both, object and interfacial double layers. In the case of measuring biological objects the most important factors are safety limit and distortions originated by nonlinearities of an object [3] and interfacial double-layers. To avoid the nonlinearities which are due to double-layers, the voltage drop on the electrodes should be kept below ±50 mV [4]. Since shorter signals carry less energy this also reduces the SNR performance.

Classically multi-frequency sine waves or sine wave based chirps are used in fast impedance measurements [1, 5-7]. However, it is found out that some binary waveforms can not only be generated in a simple way, but also the amount of useful excitation energy in these exceeds the energy of comparable sine wave based signals [5, 7-9]. Energy of the binary waveforms can be concentrated onto selected separate frequencies. At the same time, not only the frequencies of selected signal components but also their levels are controllable. We can optimize the binary excitation waveform depending on the predicted shape of the frequency response of impedance under study [5-8].

Bio-impedance spectra have a tendency to decrease at higher frequencies [1]. For example, it is nearly inverse proportional to the frequency in the case of single cell spectroscopy. Pre-emphasizing of higher frequency components in the excitation signal spectrum allows compensating a lower level of the response signal in this area. However, an optimal solution depends also on some other factors, which are discussed below.

Impedance measurement architecture

A simplified architecture of the bio-impedance spectroscopy system is presented in Fig. 1. An excitation signal source (generator of excitation waveform) has inputs for timing and duration control (from t_1 to t_2) and for frequency range setting (from f_1 to f_n). The binary signal from this generator is used as an input excitation for the complex impedance $\dot{Z}$ under study, as well as a reference signal source. For the differential measurement the reference impedance $\dot{Z}_{ref}$ is placed in the reference signal path. In the signal conditioning block, amplification, filtering and signal level matching for the signal processing block is performed. Discrete or fast Fourier transforms (DFT or FFT) are used for obtaining the amplitude and phase spectra $|\dot{Z}(f)|$ and $\Phi(f)$ of the impedance $\dot{Z}$.
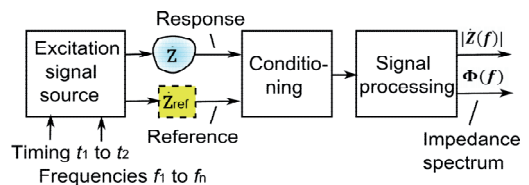

Fig. 1. A simplified architecture of the spectroscopy system designed for measurement and analysis of complex bio-impedance $\dot{Z}$

To measure unknown impedance, we can use one of two simple approaches: either we apply a known voltage excitation across the object and then measure the current flowing through it, or we inject a known current injection into that object and measure the voltage across it. We can also measure both values, current and voltage simultaneously. There are also other methods, like bridge balancing etc, but these are not described here.

The impedance of an object can be characterized by its electrical equivalent, which, on the other hand, can be represented as the frequency-dependent complex vector

$$\dot{Z}(j\omega) = \text{Re}(\dot{Z}(j\omega)) + j\,\text{Im}(\dot{Z}(j\omega)) =$$
$$|\dot{Z}(\omega)|\exp(j\Phi_z(\omega)), \tag{1}$$

where $\omega = 2\pi f$, $|\dot{Z}(\omega)| = (\text{Re}(\dot{Z}(j\omega))^2 + \text{Im}(\dot{Z}(j\omega))^2)^{1/2}$, and $\Phi(\omega) = \text{arctg}(\text{Im}(\dot{Z}(j\omega))/\text{Re}(\dot{Z}(j\omega)))$. Using the current excitation I_{exc} through the object and measuring the response voltage V_z, we can find out the impedance spectrum of it as

$$\dot{Z}(j\omega) = \mathcal{F}(V_z(t))/\mathcal{F}(I_{exc}(t)) \tag{2}$$

In case of using voltage excitation source V_{exc} the impedance spectrum can be found in a similar way

$$\dot{Z}(j\omega) = \mathcal{F}(V_{exc}(t))/\mathcal{F}(I_z(t)) \tag{3}$$

Current source versus voltage source

For bioimpedance measurements, excitation with a current source is usually considered to be preferable over sourcing of voltage. Since the biological objects are sensitive to electric fields, the current flow becomes nonlinear with respect to voltage. Current source will produce negative feedback reducing this nonlinearity [3]. Moreover, the current density on the electrodes is well controlled, and the voltage drop across the electrodes can be predicted, which opens a possibility for correcting of electrode stray effects [3].

Despite of these advantages of the current source excitation method, more parameters should be taken into account to estimate the overall performance of different methods and their practical realizations.

Real current sources have limitations, especially at the high frequencies, where the stray capacitances degrade significantly the performance of current sources. Active current sources work reasonably well up to some MHz. As it is shown in [9] a simple resistor has been used as a current source, while not comparable at lower frequencies, much better performance has been reached potentially at higher frequencies. Disadvantage of active current sources (in comparison to resistor) is also their higher noise level.

There is one more important difference in using of current or voltage excitation sources. Typical magnitude spectrum of the impedance of a single cell surrounded by saline suspension is shown in Fig.3. In the case of using current source it should have a rising shape of spectrum for the pre-emphasizing of higher frequency components and a falling shape of the spectrum at lower frequency area to protect the object from over voltages.

In the case of using voltage excitation source, the pre-emphasizing of higher frequency components is not necessary at all, since the current is increasing itself when the impedance is decreasing. As it is illustrated below, the waveforms with falling spectra are more energy efficient and easier to design, then the waveforms with rising spectra. One more positive effect of using voltage source is that the rise of impedance in the lower frequency area of frequency range does not produce any excessive voltage.
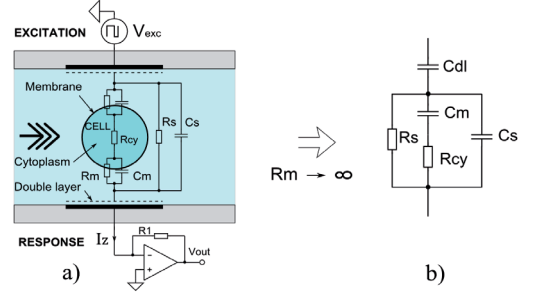
Fig. 2. Simplified electrical model of a single cell in suspension between the electrodes – a and its equivalent circuit – b
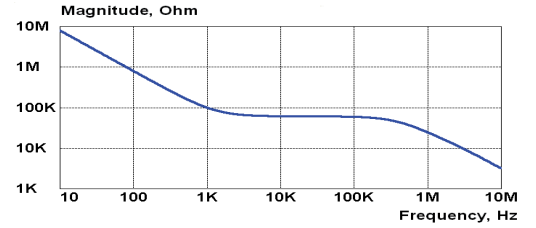
Fig. 3. A magnitude spectrum of the impedance of a single cell in saline suspension shown in Fig.2. Cdl = 2nF, Cm= 1 pF, Cs = 5pF, Rs = 60 kΩ and Rcy = 100 kΩ

Please notice that rise of impedance in this area is caused by the polarization of electrodes (double layer effect) and does not provide useful information about the properties of object.

In some cases, e.g. in the channel of the microfluidic system with a low concentrations of cells and sufficient channel height to cell diameter ratio, the current nonlinearities with respect to voltage are small, and a voltage source can be used instead of the more complicated and noisier current source.

Simple energy efficient binary waveforms

Energy content of the optimized binary waveforms exceeds the energy of comparable sine wave based signals [5-8]. However, as it is shown in [8] the mean RMS magnitudes of frequency components $V_{rms(i)b}$ is decreasing proportionally to the square root of $1/n$, where n is a number of all frequency components.

$$V_{rms(i)b} = \frac{4A_N}{\pi\sqrt{2}}\sqrt{\frac{1}{n}} \tag{4}$$

It means, that the binary waveform with 4 frequency components (bins of spectrum) have two times more

energy in each spectral bin than the binary waveform with 8 frequency bins and same duration. Benefit of the excitation signal with more frequency bins is that it gives more detailed shape of the spectrum of the response signal or covers a wider frequency range in the same timeframe. For the better SNR performance some minimum number of frequency components should be used according to the nature of object and level of additive noise accompanying the response signal. If the spectrum of the response signal is smooth and characteristic changes fall into 1-2 frequency decades, as illustrated in Fig.3, the waveform with 5 to 10 frequency components is sufficient.

The simplest binary waveform which almost fulfills the requirements described above in the case of using voltage excitation, is the simple rectangular signal (meander). The spectrum of this waveform contains odd harmonics (1st, 3rd, 5th, 7th, 9th, etc) which are declining with frequency by 1/f rule (Fig. 4b). Energy content of the first 4 frequency bins compared to the total energy of the signals is 95 % and 98,6 % for the first 15 bins.
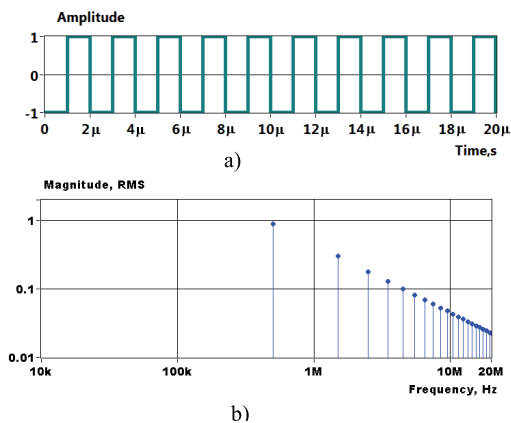

a)

b)

Fig. 4. Waveform and magnitude spectrum of the rectangular signal

If the duration of the cycle of the waveform is chosen so that the first frequency bin of the magnitude spectrum is placed on the knee of the impedance spectrum curve (see Fig.3), then the spectrum of the response current is almost flat (as illustrated in Fig.5a). Shifting the first frequency bin lower does not give flat spectrum anymore as it shown in Fig. 5b. RMS magnitudes of the response current are also significantly lower (except the first frequency bin).

Effective solution for covering of lower frequency area is using of specially designed binary waveforms which have flat spectrum in this area. A binary waveform which is shown in Fig.6, has a flat spectrum of first 4 frequency bins (1st, 3rd, 5th, 7th harmonics) and allows getting magnitudes of the response current near to 10 µA. Please notice, that rectangular waveform with a longer period (Fig. 5b) provides lower magnitudes of the response current in this area.

Though the description of the methods for designing of binary multifrequency waveforms is out of the scope of this paper, however, it must be noted that such type of excitation signals allow versatile adapting the shape of the excitation spectrum to the spectrum of the object to be measured.

a)

b)
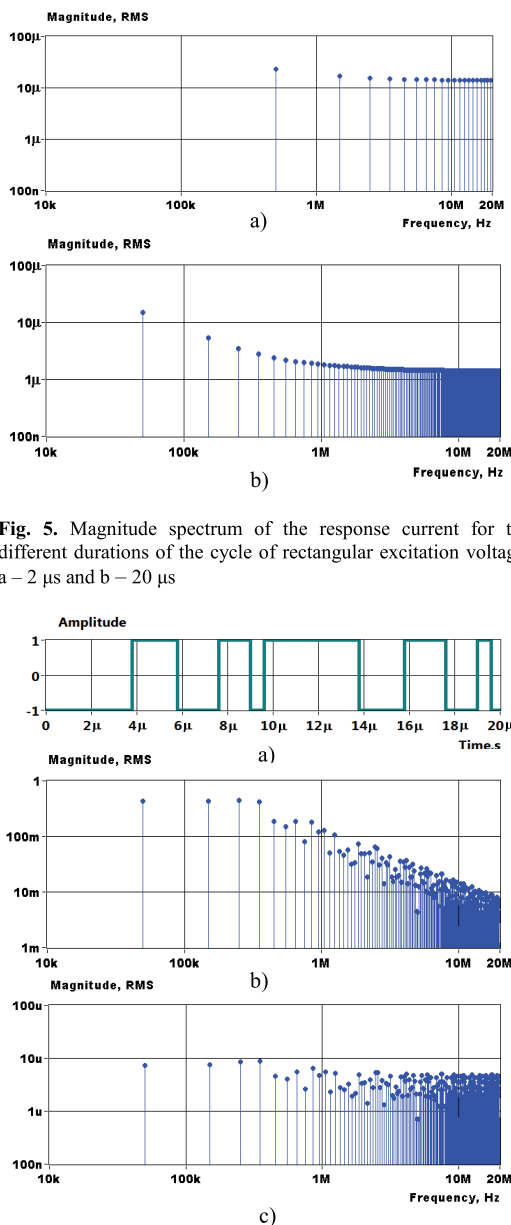
Fig. 5. Magnitude spectrum of the response current for the different durations of the cycle of rectangular excitation voltage: a – 2 µs and b – 20 µs

a)

b)

c)
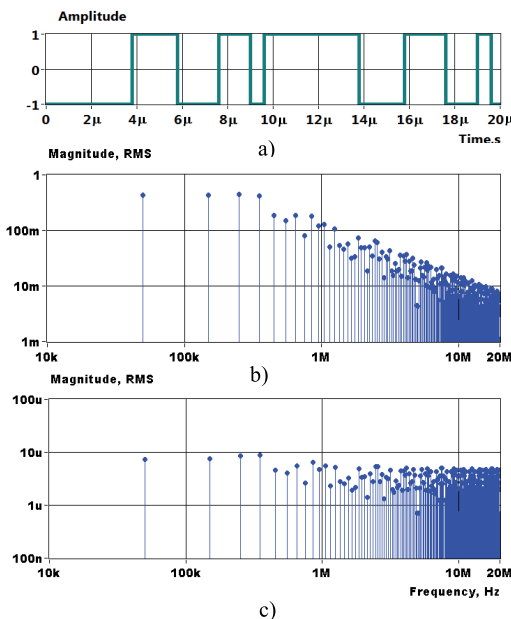
Fig. 6. Excitation waveform – a, magnitude spectrum of the excitation voltage – b, and corresponding magnitude spectrum of the response current – c

Two simple waveforms illustrated in Fig. 4 and 6 cover the frequency range over 3 decades in a short timeframe. However, to keep the overall spectrum undistorted, both excitation signals must be applied one by one sequentially. Required interval between the two parts of the signals depends on the characteristics of an object, more specifically on relaxation time-constants formed by

the capacitances and resistances of its equivalent circuit (see Fig. 2). In current case the biggest influence has a pair of R_s and C_s, relaxation time-constant τ_s of which equals as

$$\tau_s = 2\pi R_s C_s \qquad (5)$$

As a rule of thumb, time-interval of 3τ is sufficient for avoiding cross-disturbances (τ_s is about 10 μs in our case). Since the durations of the excitation pulses are less than τ_s this time interval could be less than 3 τ_s. In practice this time-constant is also decreased by output resistance of the excitation source and usually more than one period of excitation signals is used for improving SNR by averaging. In the last case a short time interval between the two signal portions becomes inconsiderable.

Conclusions

Simple binary waveforms can not only be generated in a simple way, but also the amount of useful excitation energy in these exceeds the energy of comparable sine wave based signals. This type of signals allows also versatile adapting (matching) of the shapes of the spectra of the object and excitation signal.

Using of voltage excitation sources rather than current ones allows us to use simple and energy efficient rectangular signals and also simple matching with a bio-impedance spectra becomes achievable.

Using a waveform with two separate parts allows to maximize the RMS magnitudes of response signals and to improve the signal-to-noise-ratio of measurements. The drawback is that a time delay is neccessary between the two signal parts. Despite of this delay more than three frequency decades beginning from 50 kHz can be covered during less than 100 μs.

Acknowledgements

References

1. **Grimnes S., Martinsen Ø. G.** Bioimpedance and Bio-electricity Basics – Elsevier-Academic Press, 2008. – 471 p.
2. **Ojarand J., Giannitsis A. T., Min M., Land R.** Front-end electronics for impedimetric microfluidic devices // Proc. SPIE'2011, Vol.8068, 80680R, Bioelectronics, Biomedical, and Bioinspired Systems V; and Nanotechnology V, 2011. – P. 80680R-1-15. DOI: 10.1117/12.886553.
3. **Pliquett U.** Bioimpedance: A Review for Food Processing //Food Engineering Reviews, Springer, 2010, – P. 74–94. DOI: 10.1007/s12393-010-9019-z.
4. **Borkholder D. A.** Cell Based Biosensors Using Microelectrodes, Ph.D. Thesis, - Stanford University, 1998. – P.57-61.
5. **Land R., Cahill B. P., Parve T., Annus P., Min M.** Improvements in Design of Spectra of Multisine and Binary Excitation Signals for Multi-frequency Bioimpedance Measurement //Proc. IEEE 33rd Annual International Conference of the IEEE EMBS, 2011. – P. 4038-4041. DOI: 10.1109/IEMBS.2002.1137013.
6. **Ojarand J., Land R., Parve T., Annus P.** Nonlinear Chirp Pulse Excitation for the Fast Impedance Spectroscopy //Electronics and Electrical Engineering, 4, Kaunas, 2010. – P. 73 – 76.
7. **Annus P. Min M., Ojarand J., Paavle T., Land R., Ellervee T., Parve T.** Multisine and Binary Multifrequency Waveforms in Impedance Spectrum Measurement A Comparative Study //Proc.5 th European IFMBE MBEC, 2011.– P. 1265-1268.
8. **Ojarand J, Min M., Land R.** Comparison of Spectrally Sparse Excitation Signals for Fast Bioimpedance Spectroscopy. In the context of cytometry //Accepted paper for the Workshop on Medical Measurements and Applications (MeMeA2012).
9. **Annus P., Min M., Ojarand J., Land R.** Current source considerations for broadband bioimpedance spectroscopy. //Lecture Notes on Impedance Spectroscopy. Measurement, Modeling and Applications,Vol. 2. Editor: Olfa Kanoun. CRC Press/Balkema Book, 2012. – P.63-73.

J. Ojarand, M. Min. Simple and Efficient Excitation Signals for Fast Impedance Spectroscopy // Electronics and Electrical Engineering. – Kaunas: Technologija, 20XX. – No. 2(128). – P. XX–XX.

This paper deals with using of simple but energy efficient binary multififrequency excitation waveforms for fast bioimpedance spectroscopy. Binary waveforms can not only be generated in a simple way, but also the amount of useful excitation energy in these exceeds the energy of comparable sine wave based signals. This type of signals allows also versatile adapting (matching) of the shapes of the spectra of the object and excitation signal. Ill. 6, bibl. 9, tabl. 0 (in English; abstracts in English and Lithuanian).

Autorius(-iai). Straipsnio pavadinimas // Elektronika ir elektrotechnika. – Kaunas: Technologija, 20XX. – Nr. 2(128). – P. XX–XX.

Santrauka. Il. 6, bibl. 9, lent. 0 (anglų kalba; santraukos anglų ir lietuvių k.).

APPENDIX D

Ojarand, J., Giannitsis, A.T., Min, M.; Land, R. (2011).

Front-end electronics for impedimetric microfluidic devices.

Bioelectronics, Biomedical, and Bioinspired Systems V; and Nanotechnology V, In: Proc. SPIE'2011, Vol.8068, 80680R, 15 pp. doi: 10.1117/12.886553.

Front-end electronics for impedimetric microfluidic devices

Jaan Ojarand*[a,b], Athanasios T. Giannitsis[b], Mart Min[b], Raul Land[b]

[a]Competence Centre ELIKO, Teaduspargi 6/2, 12618 Tallinn, Estonia

[b]Technical University of Technology, Ehitajate tee 5, 19086 Tallinn, Estonia

ABSTRACT

Impedance spectroscopy is a common approach in assessing passive electrical properties of biological matter, however, serious problems appear in microfluidic devices in connection with distortion free signal acquisition from microelectrodes. The quality of impedance measurements highly depends on the presence of stray capacitances, signal distortions, and accompanying noises. Measurement deficiencies may be minimized with optimized electronics and sensing electrodes. The quality can further be improved with appropriate selection of measuring signals and also with selection of measuring methods such as a choice between current or voltage sources and between differential or single-ended techniques. The microfluidic device that we present here incorporates an impedance sensor, which consists of an array of two sequential pairs of parallel microelectrodes, embedded in a microfluidic channel. All electronics and fluidic components are placed inside a metal holder, which ensures electric and fluidic connections to peripheral instruments. This configuration provides short electric connections and proper shielding. The method that we are using to evaluate the sample's impedance is the differential measurement technique, capable of suppressing the common mode signals and interferences, appearing in the signal-conditioning front-end circuit. Besides, it opens the possibility for compensating stray effects of the electrodes. For excitation we employ wideband signals, such as chirps or multifreqyency signals, which allow fast measurements, essential in the most impedimetric experiments in biology. The impedance spectra cover the frequency range between 10kHz - 10MHz. This is essential for accessing information relating to β-dispersion, which characterizes the cell's structural properties. We present two measurement schemes: (i) an in-phase differential method, which employs two transimpedance amplifiers, and (ii) an anti-phase method, which uses one transimpedance amplifier. In this study we analyze and compare the sensitivity, signal-to-noise-ratio, and operational bandwidths of these two methods against other commonly used related circuits.

Keywords: impedance spectroscopy, microfluidic device, front-end electronics, signal conditioning, excitation signal.

1. INTRODUCTION

Impedimetric microfluidic devices target to facilitate dielectric measurements of tiny fluidic volumes. The measuring fluid may be an electrolyte, cell suspension or microparticles, biochemical solution of metabolites, proteins, and nucleic acids. The impedance sensor relies on electrochemical, voltammetric, or impedance principles. Although microfluidics in conjunction with impedance spectroscopy is not fully developed yet, the potentiality of this combination is huge because i) increases the speed of analysis, ii) automates the measurement without affecting the sample, and iii) enables to characterize microscopic objects in fluids by means of information carried by a multitude of frequencies. To date there are no commercially available impedimetric microfluidic devices available, as this technology is not yet fully developed, but it is only under systematic research in laboratories mostly. Microfluidics, in conjunction with impedance spectroscopy, motivates researchers in producing workable prototype devices of diverse functionalities in the direction of cytometry mostly. The goal is to achieve sensitivity, resolution and functionality, comparable to this of big analytical instruments.

The measuring apparatus of impedimetric microfluidic devices consist of a miniaturized impedance sensor that offers electrical impedance measurability. Such an impedance sensor can be combined with signal conditioning and processing electronics of mixed signal circuits, and processing units like DSP processors or FPGA. Upon data processing, the information can be monitored on external computer via the use of virtual instrument software.

*jaan.ojarand@eliko.ee; phone +372 26202166; fax +372 6202151; elin.ttu.ee

1.1 Advantages of adopting impedance spectroscopy in microfluidics

Impedance measurement of solutions can be highly enhanced by measuring small amounts. In contrast to conventional laboratorial vessels, the microfluidic devices offer the possibility of processing small liquid volumes, with the further advantage of mixing the compounds, at first, inside the device. In comparison to other monitoring methods (as for instance optical fluorescence, for instance) the use of the completely electrical impedance spectroscopy highly reduces the measurement time, due to the exclusive use of electrical information, which requires reduced computations for data processing. In addition, the feasibility of integrating electronics directly on the microfluidic devices, and the possibility of adjusting the measurement directly by online, increases the measurement throughput and makes microfluidic concept very attractive.

Notable technical advantages that characterize commercial microfluidic devices are compactness, portability, modularity, reconfigurability, reduced electronic noise, reduced power consumption, and simplified integration of the electronic components onto a hybrid chip. In addition, the microfluidic devices are tightly enclosed, which reduces the possibility of contamination of liquid samples during operation. Further to their measuring capabilities, microfluidic devices may also contain built-in transducers that can route, transport, dispense, or mix fluidic samples in a controllable manner. Due to their small fluidic volumes, impedimetric microfluidic devices offer efficient control of fluid translocation and precision in impedance measurements.

Key manufacturing advantages that make commercial microfluidic devices competitive is achievable mass production, affordable replacement cost, short manufacturing time, and broad range of supporting computer aided design and simulation software. Impedimetric microfluidic devices can be manufactured affordably and be maintained simply. Their microchannels can be cleaned and sterilized with chemical cleaners. Alternative to chemical cleaners, ultraviolet radiation and heat can sterilize them. Capillary plasma can dissolve organic remains from inside the microchannels.

1.2 Material compatibility

The material compatibility concerns the safety of a microfluidic device in avoiding reaction with the measuring substances that are imported inside its channels. The chemical inactivity of the fabrication materials, against chemical solutions, is very momentous for the sustainability of the device and the liquid sample. Bare electrodes made of platinum or gold, as in our device, avoid chemical reactions with the measuring solutions at large.

It is possible, however, that ions or neutral molecules may be adsorbed on electrodes and hence affect the measuring current. The rate of adsorption is usually rapid. To include adsorption in the electrical response, it is necessary to know the relationship between the surface concentration of the adsorbed ions and the average concentration of the electrolyte. The surface concentration can then be related to the average concentration of the electrolytic solution through electrochemical diffusion equations.

To prevent adhesion of substances in microfluidic channels, surfactants like poloxamer copolymers can be added inside the solution to isolate it from contact with the channel walls.

The microfluidic channel of the device presented here is made of transparent polycarbonate. The height of the channel, 30 μm, is determined with a transparent double-sided self-adhesive tape (Tesa 4983) which consists of Polyethylene Terephthalate (PET) backing and a modified acrylic adhesive. This tape, which is characterized as a biocompatible material, defines the sidewalls of the microfluidic channel and seals it tightly [1].

2. IMPEDIMETRIC IMPLEMENTATION IN MICROFLUIDIC DEVICE

There are different requirements in the impedance measurement of electrolytic solutions, in comparison to usual solid dielectrics or metals. Electrolytic solutions demonstrate negligible electronic conductivity as they are dominated by ionic conductivity and nearly negligible electronic conductivity. .

The impedance of an electrolytic solution, made of non-polar solvent, is ruled by its ionic conductance. Along the interface of a bare impedance electrode that is in contact with such electrolytic solution the ions accumulate uniformly due to the attraction from the electrode potential, and build up an ionic double layer capacitance, which adds to the measuring impedance. The higher the concentration of the electrolyte, the thinner the double layer is. In DC or low

frequencies this double layer capacitance interferences the impedance measurement, whilst at frequencies above few tens of kHz this double layer capacitance becomes insignificant due to the easy penetration of the high frequency signals. In the common case of measuring aqueous electrolytes, a monolayer of water molecules develops on the electrode-electrolyte interface, due to alignment of the water dipoles in direction perpendicular to the electrode plate, and screens the ions of the solution from the contacting electrode. This monolayer adds another capacitance, called Stern, in series with the ionic one. Beyond this, the ionic layer, now called Gouy-Chapman, will extend back into the solution in a decaying manner. Both these capacitances screen the near DC to kHz range impedance measurements.

2.1 Impedance electrodes for microfluidic device

In 1963, Schwan proposed the four-electrode method with two current-passing electrodes and two high impedance potential electrodes that highly reduce electrode polarization effect [2]. In microfluidic devices both pairs of electrodes can be positioned collinearly along the same side of the microfluidic channel. A drawback of this coplanar arrangement is that the current density and electric field become very inhomogeneous. If the electrodes, however, are placed opposite each other across both sides of the microfluidic channel, the electric fields produced between the electrodes will be nearly uniform in the middle part of electrodes. Parallel plate electrodes have also good sensitivity and sensing area, and this enhances detection of small impedance changes when cells flow between the electrodes [3]. However, it is difficult to position the parallel current electrodes between the voltage sensing electrodes as in the classical four-electrode setup. If these electrodes are placed on the both sides of a microfluidic channel, this will significantly decrease the sensitivity for detection of the impedance changes since the electric field distribution varies mostly at the center of the current electrodes when cells flow between the electrodes.

It is shown that in the classical four-electrode setup the electrode polarization still affects the impedance measurement due to the presence of small current leakage through the voltage sensing electrodes [4]. The influence of electrode polarization could be reduced via increasing the area of electrodes, but however, this will reduce the sensitivity of the impedance measurement since the initial impedance between the electrodes decreases. As it can be seen on the simplified equivalent circuit model shown on Fig. 1, the resistance Rs and capacitance Cs are connected in parallel with the cell resistances, Rm and Rcy, and the capacitances Cm.
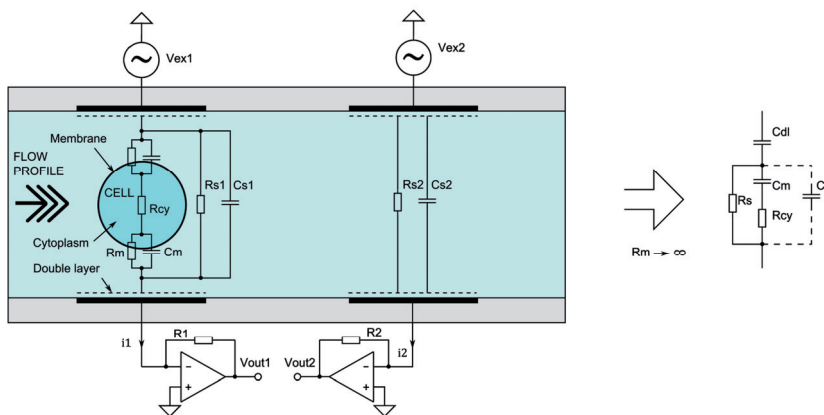
Figure 1. Simplified equivalent circuit model for a single cell in suspension between the electrodes (a). Rm and Cm are the resistance and capacitance of the cell membrane, respectively, Rcy is a resistance of the cell cytoplasm; Rs and Cs are the resistance and capacitance of the suspension respectively and Cdl is a capacitance of the double-layer.

The electrode-electrolyte interface area can be also increased by using electrochemical treatments that produce a porous or fractal electrode surface with a large effective surface area [5].The microfluidic device that we present in this article incorporates an impedance sensor, which consists of an array of two sequential pairs of parallel plate microelectrodes. These two pairs of electrodes are used for the differential measurements.

To ensure low current densities in our microfluidic device, we designed the current electrodes comparable to the dimension of the microchannel. The dimensions of electrodes in our device are 250 x 200 μm^2. The inter-electrode gap is 2.5 mm. This gives small crosstalk between adjacent electrodes. The width of each electrode fits right the width of the channel, which is defined as the area between the two sidewalls. Each microelectrode of the bottom plate is aligned parallel with the microelectrode of the top plate. The opposite end of electrodes have a shape of contact pin, which matches directly with the contact plug, soldered on the circuit board of the analog front-end. This design highly eliminates influence of the electric circuit lengths between the measurand and the analyzer, as the signal conditioning circuitry is very close to the electrodes. The gap between the electrodes, 30 μm, is determined with a transparent double-sided self-adhesive tape (Tesa 4983). Top and side views of the microchannel module are shown on the Fig. 2.

(a)   (b)

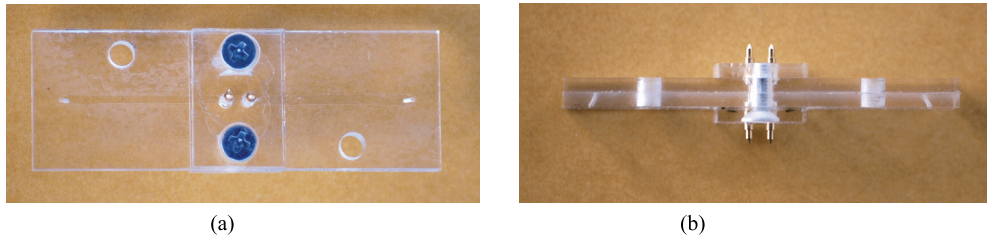Figure 2. Top view (a) and side view (b) of the microchannel module. Length of the unit is 53 mm and width is 18 mm.

The microfluidic module is enclosed in its shielding aluminum case, which is described in the end part of the article.

2.2 Impedance measurements in microflow cytometer

For measuring the impedance, it is essential to apply either constant amplitude AC voltage across the fluidic volume and measure the current response, or apply fixed current of fixed amplitude and measure the voltage response. Analysis of the dielectric β-dispersion yields information on membrane capacitance, cytoplasm conductivity, and cytoplasm permittivity of the biological cells as a function of frequency. It is important to cover all frequencies where this dispersion comes out. The frequency range of interest, when investigating the β-dispersion of cells in a standard saline solution, is usually located in an intermediary region ranging from 100 kHz to 10 MHz, where the signal obtained is dominated by the channel bulk impedance [6],[7].

To avoid distortions the measurements should be performed within the linear region of the current-to-voltage characteristic. The linearity of the current-to-voltage characteristic depends on the current density on the electrodes (order of μA/cm2) and the voltage level applied. To avoid nonlinearities, the voltage drop on the electrodes should be kept below ±50 mV [8].

The impedance analysis could be performed with impedance analyzers, which provide AC excitation and impedance detection in the same instrument. These instruments are usually complicated devices with large dimensions and cables must be used for connecting of microfluidic devices. Since the input-output impedances of the analyzers and impedances of the cables are not suitable for direct connection to the electrodes in the microfluidic devices, an additional signal conditioning and impedance matching is necessary. This is accomplished by the front-end device, which usually consists of preamplifiers and excitation voltage or current sources. It is well known that the overall system signal-to-noise ratio (SNR) depends mostly on parameters of the first preamplifier stage. This stage must have also low input leakage currents and small input capacitances. The voltage source must have low and current source high output impedance over the full frequency range required. Connections to the electrodes must be as short as possible to avoid the overall significant deterioration of the performance of measurements. Short connections to the electrodes have also minimum sensitivity to the external noise.

The impedance can be measured in a full scale of voltages and currents, which are available for the experiment. However, this approach has sensitivity limits which are directly predicted by the resolution of measuring instruments and

noises. In a microfluidic device which, is aimed on measuring the impedance of single cells, the sensitivity of the measurement is limited by several factors:

i)   cell volume is only a small fraction of the detection volume;

ii) the stray impedance of liquid is surrounding the cell;

iii) double layer capacitance disturbs measurements.

To overcome the sensitivity limitations, differential measurement circuitry with two pairs of electrodes is widely used during last decade [7], [9], [10], [11]. As shown in Fig.1, two pairs of electrodes are used to determine the two closely positioned detection volumes enabling to perform differential measurements. One pair of electrodes measures the electrical signal from the particle whilst the other pair acts as a reference. As the cells pass through the channel, they perturb the electric field in the detection volumes creating a positive and negative signals. This signal is processed to provide the impedance. Employing differential current measurements increases the sensitivity of the impedance measurement, because we do not measure full-scale or basal impedance, but can focus right in the range of the detected impedance variation. This provides higher sensitivity in comparison to other common impedance methodologies, such as absolute impedance measurements, or incremental impedance measurements. The differential impedance setup is convenient in measuring slight changes of impedance due to small concentrations in the measurand solution, or due to presence of small suspended objects like particles or cells. In our microfluidic device we employ a dual two-electrodes setup, which is appropriate for measuring current differences between the two electrode pairs via the use of a front-end circuitry that converts the detected currents to voltage via two identical transimpedance amplifiers, followed by a buffer circuitry which drives the connection cables to an external impedance analyzer measuring differential impedance on the bases of differential current measurement ($dZ=V / dI$). The front-end circuitry was designed in two variants, one with in-phase excitation, on both electrode pairs which is similar to commonly used differential circuit (see Fig. 4 and 7 below). Another variant, where upper two voltage excitation electrodes have 180^0 phase difference, gets current difference from bottom electrodes which are tied together (see Fig. 3 and 7 below).

3. FRONT-END CIRCUITRY

3.1 Excitation sources

For bioimpedance measurements, excitation with current source is considered to be preferable over sourcing voltage. Since biological objects are sensitive to electric fields, the current flow becomes nonlinear with respect to voltage. Current excitation will produce negative feedback reducing this nonlinearity [12]. Moreover, the current density on the electrodes is well controlled, and the voltage drop across the electrodes can be predicted, which opens a possibility for correcting of electrode stray effects [12]. Despite of these advantages of the current source excitation method, more parameters should be accounted. One important parameter is the signal-to-noise ratio.

Real current sources have their limitations, especially at the high frequencies, where the stray capacitances degrade significantly their performance. Active current sources work reasonably well up to some MHz, on the other hand, the working range of passive current sources, while not comparable at lower frequencies, can reach potentially higher frequencies at acceptable quality. Good quality voltage sources can be made in a wide range of frequencies and voltages, which can be converted to passive current source by adding a series resistor. Still several problems are apparent. Voltage source is limited by power supply range. It can be doubled in bridged connection, but achieving voltages over some tens of volts is usually not feasible in embedded electronics. Resistor on the other hand needs to be usually much larger then impedance under examination, which could severely limit achievable current levels. Disadvantage of active current sources in comparison to resistive source is also their higher noise levels, for example, in the 10 MHz frequency range a cumulative RMS noise of the active current source can reach 10 times higher than of the passive source [13].

In some cases, e.g. in the channel of the microfluidic system with a low concentrations of cells and sufficient channel height-to-cell diameter ratio, current nonlinearities with respect to voltage are probably small, and a voltage source can be used instead of the more complicated current sources.

In our front-end we use voltage sources based on ADA4937 low noise, ultralow distortion and high speed differential amplifiers. A simplified circuit of first variant of the exitation source is shown in Fig. 3. The ADA4937 differs from conventional op-amps in that it has two outputs whose voltages move in opposite directions. Like an op-amp, it relies on open-loop gain and negative feedback to force these outputs to the desired voltages. It behaves much like a standard voltage feedback op-amp, which makes it easier to perform single-ended-to-differential conversions, common-mode level shifting, and amplifications of differential signals. The ADA4937 architecture results in outputs that are highly balanced over a wide frequency range without requiring tightly matched external components. The common-mode feedback loop forces the signal component of the output common-mode voltage to zero. This results in nearly perfectly balanced differential outputs that are identical in amplitude and are exactly 180° apart in phase. These outputs are connected to top electrodes of the microfluidic channel Vex- and Vex+ via resistors R8 and R9. These 10 Ω resistors, potentiometer P2 and capacitor C3 allow to compensate the initatial phase difference which is caused by the unsymmetry of electrode pairs. The range of this phase correction is typically ± 2 to 5 degrees. Resistors R2,R3,R5 are used for matching the input impedance to the impedance of 50 Ω coaxial cables. Potentiometer in parallel with the resistor R1 is intended for compensation of initial differential mode gain unsymmetry, which is caused by the unsymmetry of electrode pairs. Correction range of this circuitry is typically ± 10 %. The second stage, which uses also ADA4937 differential amplifier, repeats the excitation voltages Vex+ and Vex- of the top electrodes and drives the coaxial cables connected to the outputs OUT- and OUT+. The frequency bandwidth of the op-amps could reach over 1 GHz, therefore the capacitors C1 and C2 are used to limit it because too wide bandwidth increases the total RMS noise.

The second variant of the excitation source is similar, but the excitation voltage for the both electrode pairs is supplied from the same output of the first stage U1. The magnitude and phase balancing components are not used in this case. Simplified circuit of this excitation voltage source is shown on Fig. 4.

Figure 3. Simplified circuit of the differential excitation voltage source, variant 1.

Figure 4. Simplified circuit of the excitation voltage source, variant 2.

3.2 Current -to-voltage converters and amplifiers

There are two well known methods for converting a current into voltage. At first we can monitor a voltage drop on the fixed resistor and then use a high impedance voltage follower or amplifier. Secondly we can use a transimpedance amplifier circuitry shown in Fig.5. Main characteristics of these two ones a similar, however there are also some differences. At first, in the case of transimpedance amplifier, input voltage between the inputs of the op-amp is always zero on the both inputs. This is not so, if the voltage drop on the resistor is monitored, and this causes small changes in the input capacitances of the op-amp and consequent nonlinearities. Secondly, the transfer characteristic of this type of current-to-voltage converter is nonlinear and the input capacitance C_T has more influence on it. Results of the PSpice modeling for the both converters are shown in Fig.6.

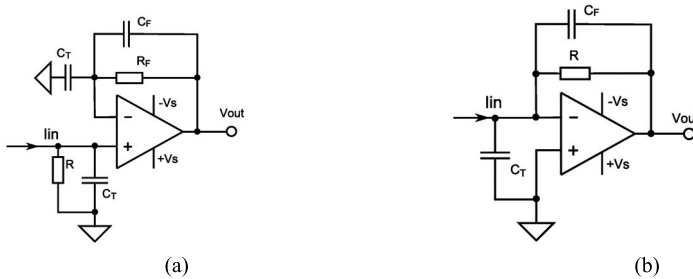(a)   (b)

Figure 5. Simplified circuits of the current-to-voltage converter amplifiers, (a) is monitoring a voltage drop on the resistor R, and (b) is a transimpedance amplifier. C_T is a total stray capacitance, C_F is a stray capacitance in parallel with the resistors R and R_F.

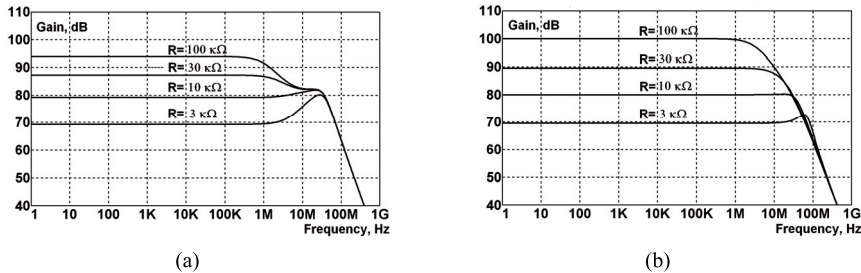(a)   (b)

Figure 6. Bode plots of the current-to-voltage converters gain using in-series resistor R (a) and of the transimpedance amplifier (b). Both converters employ the same op-amp OPA656 with $C_T = 2pF$, $C_F=0$, 5 pF, $R_F=10$ kΩ, the resistance of input current source is 100 kΩ and R varies from 3 kΩ to 100 kΩ.

In our front-end we use transimpedance amplifiers (TIA). The voltage at the input node is maintained to zero volts (virtual ground) because the current through the feedback resistor R_F balances with the measured current I_{in}. Advantage of this circuitry is that requirements for the common mode rejection ratio (CMMR) of the amplifier are not high and it does not degrade the impedance of a current source. However, a real TIA has also their limitations [14], [15].

The TIA with equivalent current and noise sources e_n (t) and in $i_n(t)$ is shown in Fig.7. I_{in} is the current of the current source, R_S the output resistance of the current source, C_T the total input capacitance (including the input capacitance C_{in} of the amplifier), R_F is the feedback resistor and C_F is a capacitor connected in parallel to the feedback resistor and includes also the stray capacitance. The noise gain (NG) transfer function for this circuit is expressed by:

$$NG = \frac{1 + sR_F(C_T + C_F)}{1 + sC_F R_F}.$$ (1)

In order to maintain the stability, a feedback capacitor C_F is placed across R_F to create a pole at f_P in the noise gain function (1). The noise gain's zero is defined by:

$$f_Z = \frac{1}{2\pi(R_F \| R_S)(C_T + C_F)} \cong \frac{1}{2\pi R_F C_T} .$$ (2)
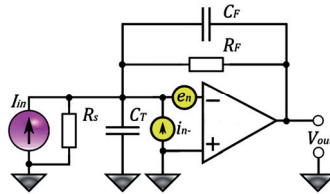

Figure 7. A Circuit of TIA with current and voltage noise sources.

The higher the values of R_F and C_T, the sooner the NG peaking starts and the higher the value of C_T, the higher the value of the high frequency noise gain is. Resistor R_F sets the TIA gain, K, and bandwidth, BW, and also influences the stability of the TIA. C_F influences the noise gain, TIA stability and BW. We modeled the TIA circuit with PSpice by applying low noise and high gain-bandwidth product, JFET op-amps OPA656 and OPA657. Fig. 7 shows modeling results of the cumulative RMS noise of OPA657. Thermal noise spectral densities of some resistors are also shown for comparison.
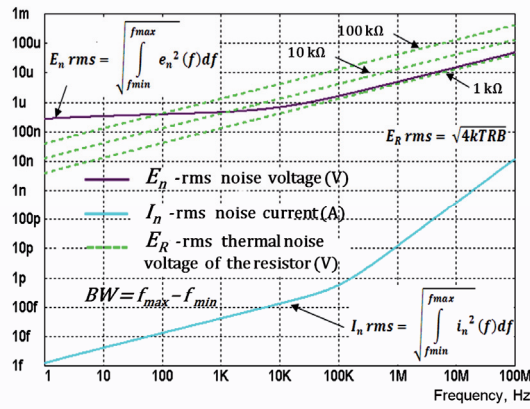

Figure 8. Cumulative RMS noises of the OPA657.

The internal noise sources of op-amps are normally uncorrelated and the noise components can be combined to root-sum-squares. The total output RMS noise E_{nT} can be estimated by:

$$E_{nT} = \sqrt{E_n^2 + E_{ni}^2} + E_{nR}^2$$ (3)

E_{ni} is an output voltage component that results from the current noise and equals: $E_{ni} = i_n Z_F$. Z_F is the total impedance of R_F and C_F and E_{nR} is the thermal noise of the feedback resistor R_F. Fig. 9 shows modeling results of the TIA by using

OPA656 with various values of the stray capacitances added on the input capacitance. The higher value of C_T gives also higher value for high frequency noise, as expected.
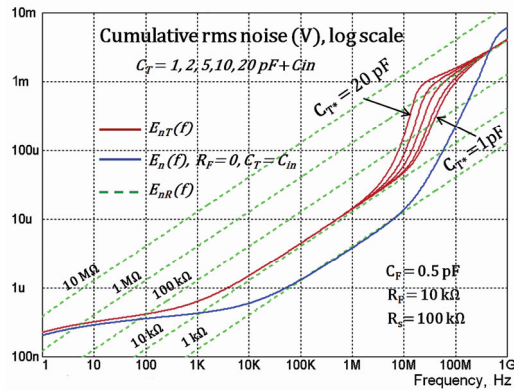

Figure 9. Total cumulative RMS noises of the TIA with different stray capacitances C_{T*}.

Fig. 10 illustrates the influence of the gain of TIA using OPA656. The total cumulative noise is normalized against the gain of $K_n = 10$ kΩ.
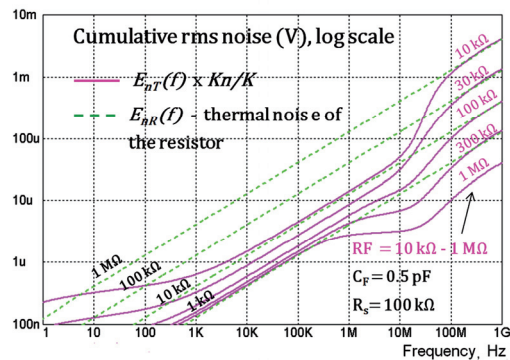

Figure 10. Total cumulative RMS noises of TIA with different values of RF normalized against Kn=10 kΩ.

Higher values of R_F give higher value of the thermal noise, but the signal-to-noise ratio is proportional to the gain of TIA. As a result, the higher value of the resistor R_F improves the overall SNR. However, the bandwidth of TIA decreases at the same time as, shown in Fig. 6 (b). The gain K equals R_F only at the low frequency region. It must be also noted that if the value of R_F becomes greater than the characteristic value R_{ch}, the amplifier's current noise will cause more output noise than the voltage noise of amplifier. The characteristic value R_{ch} equals:

$$R_{ch} = e_n(f)/i_n(f) \tag{4}$$

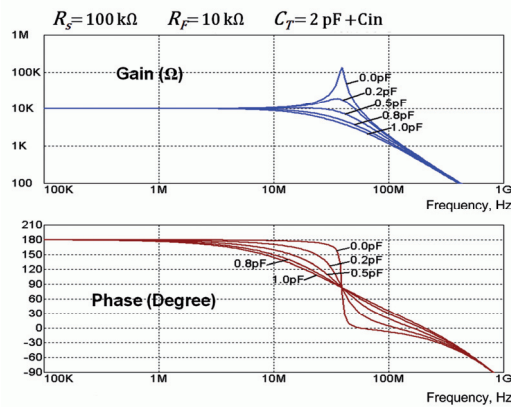The influence of the capacitance C_F to the stability and bandwidth of TIA is illustrated in Fig. 11.

Figure 11. Gain and phase vs. frequency of the TIA using OPA656 with different values of the CF.

If the capacitance C_F is below 0.5 pF, the TIA becomes unstable. The analysis and simulation presented here allow formulation measures for the improved bandwidth and signal-to-noise characteristics of TIA. This can be achieved by:

  i)   minimizing the value of the total input capacitance C_T. This reduces the noise gain without limiting the signal bandwidth;

  ii)   reducing the value of the feedback resistor R_F. Bandwidth is inversely related to the square root value of the feedback resistor. Thus, if the bandwidth is most important, a gain loss can be compensated by the following broadband but low noise voltage gain stage;

  iii) filtering of the TIA output signal to reduce the wideband noise beyond the signal bandwidth. A single pole low-pass filter with a bandwidth twice as the signal bandwidth can easily improve the dynamic range of TIA.

Simplified circuits of the current-to-voltage converters, which were designed according to these principles are shown in Fig.11. As shown in [7], for the circuitry with transimpedance amplification stage with a gain of 2 R_F followed by a differential gain of G_{diff} as presented in Fig. 12 (a), the sensitivity at the electronic output to an impedance change in low frequency area is clearly a function of the interface impedance. This impedance is determined by the double layer capacitance C_{dl}. The impedance is high and the currents are small in this region. To evaluate cell parameters in this lower frequency range, different compensation techniques have been considered, including calibration or global fitting methods. The electrode material and the effective surface in contact with the electrolyte can also be modified to increase the interface capacitance and reduce the related pole frequency. However, this is not usually necessary for the investigating of the β-dispersion region.

In the intermediate to high frequency range, the electrode interface capacitance is considered as shorted and we only consider the channel bulk impedance in parallel with the stray capacitances. The stray capacitances take into account the current paths found in parallel with the detection or reference volume. Since this capacitances C_s is small, the channel can be considered to be resistive and the current change in the measurement channel can be found as:

$$\Delta I = -\frac{V_{in}}{Z_c^2} \Delta Z \qquad (5)$$

where Z_c is the impedance of the channel.

As shown in [7], in the case of small disparities between the measurement and reference stray capacitances, the transfer function at the output of the differential gain stage is:

$$\frac{V_{out(\Delta C)}}{V_{in}} = j\omega R_F \Delta C_s G_{diff} \qquad (6)$$

In the intermediate frequency range, we have a resistive plateau, which permits unbiased impedance measurements of the channel. At high frequencies, the stray currents increase, and if they are not balanced, this could saturate the dynamic range of the amplifiers, especially the first amplifier stages of transimpedance amplifiers (TIA).

To decrease the risk of saturation of TIA-s and to increase the sensitivity of measurement, we designed a circuitry shown on Fig. 12 (b). Excitation voltage is supplied to the upper pair of electrodes 180° apart in phase and the lower electrodes are connected together. In this configuration only the difference of currents ΔI between two electrode pairs reaches the input of TIA which allows to increase the gain of the TIA and voltage amplifier U2. Since the common impedance Zc of the channel and the common stray capacitance Cs do not influence directly the difference of the currents, this allows to increase the sensitivity for measuring the current changes caused by cells flowing between the electrodes.
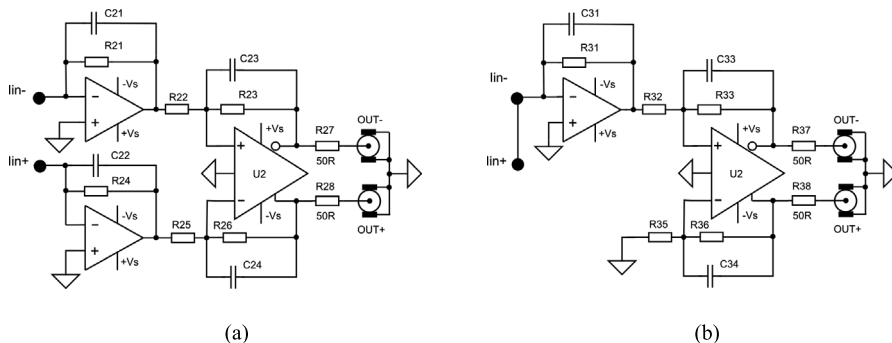

Figure 12. Simplified circuits of the current-to-voltage converters amplifiers, (a) - for use with the antiphase voltage source shown in Fig. 3 and (b) - for the use with the common phase voltage source shown in Fig. 4.

Balance of the currents depends also on the geometrical symmetry of the electrode pairs and the channel itself. Testing of our microchannel units (Fig. 2) shows unbalance between 10 to 25 %. This is mainly caused by inaccuracies of the placement of electrodes. Such the unbalance allows to increase the sensitivity up to 10 times. It is obviously possible to achieve better results improving the fabrication accuracy, the increase of sensitivity is however limited by noises.

There are different sources of noises. In the front-end part the thermal noise of resistors and electronic amplifier is present. Increasing the gain limits increases the frequency bandwidth (Fig. 6) and also the noises (Fig. 8 and 9), unfortunately. Noise sources are present also in the microfluidic channel, e.g. due to charge instability at electrode surfaces and fluctuation of particle positions in the channel [7]. Another class of noises is caused by external electromagnetic fields (EMF).

3.3 Mechanical design

To ensure proper shielding from external noises, we enclosed the microchannel module inside the aluminum case as shown in Fig. 13 and 14. Printed circuit boards (PCB-s) of the front-end electronics are placed on both sides of the microchannel module, an excitation signal part on the bottom side and an input amplifiers part on the top side. Each microelectrode of the bottom plate is aligned parallel with the microelectrode of the top plate. The opposite end of electrodes have a shape of contact pin, which matches directly with the contact plug, soldered on the circuit board of the analog front-end. This design highly eliminates influence of the electric circuit lengths between the electrodes and signal conditioning circuitry. Both sides of the case are covered by removable leads.
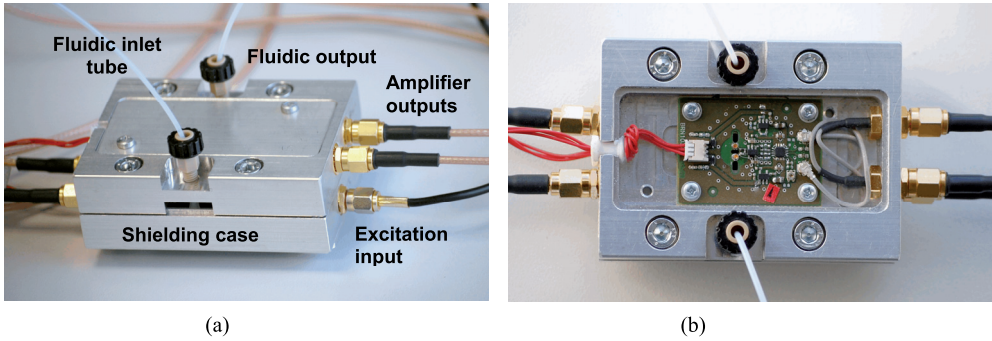
(a)   (b)

Figure 13. The possibility of configuring the signal condition front-end closely to the impedance electrodes offers critical advantage, as highly reduces stray capacitances from the measuring circuit. (a)- the microfluidic device enclosed in its shielding aluminum case, where cabling and fluidic fittings are distinguished, (b) - interior of the microfluidic device where the electronic front-end circuit board is shown.
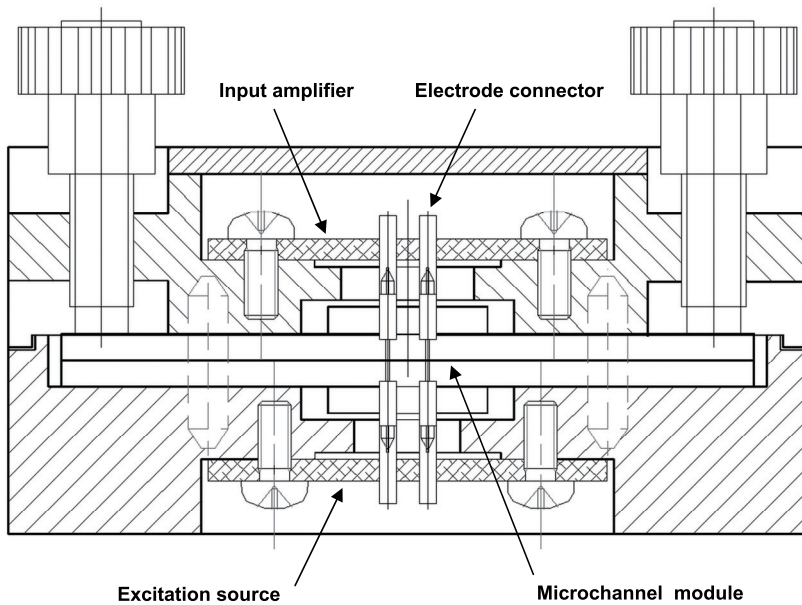

Figure 14. Cross-section view of the aluminum case with the microchannel module and PCB-s of the front-end electronics.

3.4 Impedance instrumentation

To test our front-end device we are used an impedance analyzer-spectroscope Model H2FIS Zurich Instruments, Switcherland. This analyzer has two individual input-output channels, frequency range from 0.7 µHz to 50 MHz, input AC voltage range 1.5V and differential inputs with 14 bit, 210 MSamples/s analog-to-digital (A/D) converters. The response signal to be measured is supplied to the one of high-frequency analog inputs, in which it gets amplified to a specific range, then filtered, and digitized. The resulting samples are fed into the digital signal processing block for demodulation by means of up to 8 dual-phase synchronous demodulators. The numerical oscillators generate sine and cosine signal pairs that are used for demodulating of the input samples and also for generating of the high-frequency output signals. For this purpose, the output mixers generate a weighted sum of outputs, which generate the multifrequency signal used as excitation signal. In our tests we employ 4-frequency multi-sine wave excitation in the frequency range from 3 kHz to 11 MHz. The demodulated output data samples flow into an embedded processor for post processing or to be sent to a host computer. The host computer controls the impedance analyzer and performs signal processing and graphical data representation of the measurement results using LabVIEW software.

In the case of unavailability of an impedance analyzer, the excitation signals can be easily supplied via a signal generator, or an arbitrary function generator, and the response can be recorded with a digital scope. This method, however, requires synchronization between the generator and the scope. The resolution and the accuracy of measurements in this setup are usually poorer since the A/D converters of the digital scopes have lower resolution (order of 8 bits), furthermore the synchronous demodulators are not available. In our experiments we also use arbitrary function generator (AFG3252 Tektronix), digital scope (Agilent DSA91304) and LabVIEW software for automation of measurements. Arbitrary function generator allows us to use also different excitation signals like chirps and binary multi-frequency signals.

3.5 Implementation of signal processing

Sine wave excitation and phase-sensitive demodulation of the response are common tools for impedance measurement. In many applications, bio-impedance spectroscopy utilizes a frequency sweep over the range of interest (frequency domain), either with logarithmic or linear spacing of the frequencies. Both real and imaginary parts (or magnitude and phase) of the impedance are of interest, where the role of the imaginary part has been often underestimated. This method fails if the object changes its electrical properties fast with respect to the time required for a frequency sweep. Such dynamic processes take place in microfluidic devices where cells flow fast between the electrodes with small dimensions.

Linear chirp is a well-known wideband excitation waveform, where the instantaneous frequency changes linearly at the constant during the excitation interval T_{exc}. Nonlinear chirps with varying of the frequency change are also known. This type of short chirps have better energy content over the excitation frequency range [16]. However, since the excitation energy depends proportionally on duration of the excitation pulse [17], it is reasonable to use longer excitation pulses for obtaining better SNR.

Another possibility to cover wide a frequency range within short time interval is to use multifrequency signals. Though the multi-sine signal is the basic solution for this purpose, it is technically quite complicated to generate and is not very effective in the usage of available signal range. The reason is that the sum of sine waves has relatively pure crest factor (CF) – a relation of the peak value to the average root-mean-square (RMS) level of the signal. For example if we take a 4-frequency multi-sine signal with the frequencies of $1f_1$, $3f_1$, $5f_1$ and $7f_1$, where f_1 is the frequency of the first component, and taking amplitudes of all signals equal to 1V with zero value initial phases, then the peak amplitude of the signal will be 2,94 V and CF reaches 2,08. However, changing the values of the initial phases will allow obtain lower CF values. We checked all possible phase combinations with the resolution of 1degree using LabVIEW software, and as a result, for the initial phases 0, 79, 199 and 139 degrees we got the peak amplitude 2,05V and CF= 1,45 for the multi-sine signal. There is much research done on this topic to achieve near optimum phase relationships for multi-sine signals containing up to 40 frequencies [18].

Crest factor of a single sine wave with unit amplitude (A=1) is 1,414, but for the square wave with the same unit amplitude it is only 1. It leads to the idea of creating binary multifrequency signals, as proposed in [19]. We can also derive binary multifrequency signals by detecting zero crossings of multi-sine signal according to the following formula:

$$b_{exc}(t) = sign \sum_{i=1}^{i=n} Ai \cdot \sin(2\pi f_i + \Phi_i) \tag{7}$$

where n is a number of frequencies and Φ_i is initial phase of the i-th signal. Using such a 4-frequency multisine signal as described above, and optimizing the initial phases so that the deviation of the magnitudes will be minimal, we get a binary signal shown in Fig. 15 (a). All possible phase combinations with the resolution of 1degree are checked using LabVIEW software. The magnitude spectrum of the binary multifrequency signal is shown in Fig. 15 (b). Mean value of the magnitudes is 562 mV with deviation of the magnitudes 2,8 mV (0.5 %). Initial phases are 0, 78, 211 and 28 degrees. Normalizing the magnitude of the optimized multisine against 1 V we will get 1/2.05 = 488 mV. It appears that under similar conditions the amplitude of the binary multifrequency signal components is 15 % more compared to similar multisine signal.
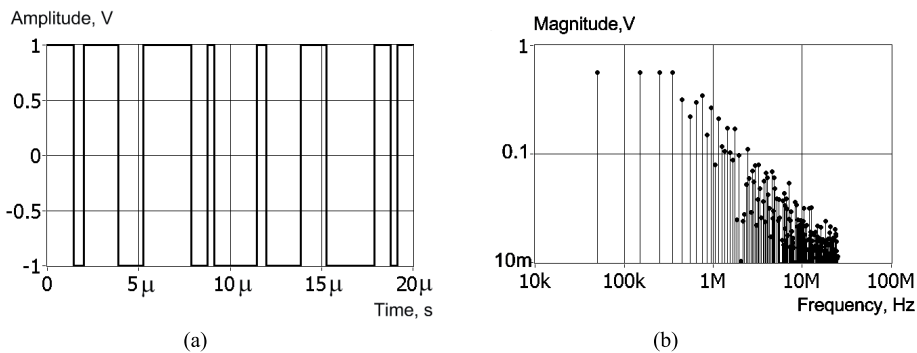

Figure 15. Waveform of the 1f, 3f, 5f, 7f binary multifrequency signal (a) and its magnitude spectrum (b) for f=50 kHz.

Binary multifrequency waveform can be continuously repeated without changes in the spectrum.

4. CONCLUSIONS AND OUTLOOK

Impedance spectroscopy is expected for years already to be a promising technique for characterization of cells and cell cultures in microfluidic devices. However, practical achievements are not so good yet, serious problems have appeared with distortion free signal acquisition from microelectrodes. The quality of impedance measurements highly depends on the presence of stray capacitances, noises and interferences, all leading to signal distortions. The authors introduced novel versions of electronic circuits for front-end techniques to achieve more disturbance proof differential data acquisition. Also multi-frequency binary sequences are proposed for using as excitation signals, which enable to perform fast and wide band measurement of impedance deviations on the bases of simple and low power electronics. As a result, we have developed further the technique for impedance spectroscopy to fulfill the theoretical expectations in the microfluidic technology practice.

5. ACKNOWLEDGEMENTS

REFERENCES

[1] Mazzuferi, M., Bovolenta, R., Bocchi, M., Braun, T., Bauer, J., Jung, E., Iafelice, B., Guerrieri, R., Destro, F., Borgatti, M., Bianchi, N., Simonato, M. and Gambari, R., "The biocompatibility of materials used in printed circuit board technologies with respect to primary neuronal and K562 cells," Biomaterials 31(6), 1045-1054, (2010).

[2] Schwan, H. P., [Determination of Biological Impedances In Physical Techniques in Biological Research], Nastuk W.L., Ed., Academic Press, New York, vol. 6, 323-406, (1963).

[3] Wang, J.W, Wang M.H, Jang L.S., "Effects of electrode geometry and cell location on single-cell impedance measurement," Biosensors and Bioelectronics, 25(6), 1271-1276, (2010).

[4] Mazzeo, B. A., "Parasitic capacitance influence of potential-sensing electrodes on four-electrode liquid impedance measurements," Journal of Applied Physics, 105, 094106, (2009).

[5] Malleo, D., Nevill, J.T., Van Ooyen, A., Schnakenberg, U., Lee, L.P. and Morgan H., "Note: Characterization of electrode materials for dielectric spectroscopy," Rev Sci Instrum., 81(1), 6104, (2010).

[6] Schwan, H.P., "Electrical Properties of Tissues and Cell Suspensions: Mechanisms and Models", Annual International Conference of the IEEE Engineering in Medicine and Biology Society, Vol. 1, 70a-71a, (1994).

[7] Gawad, S., Cheung, K., Seger, U., Bertsch, A., and Renaud, P., "Dielectric spectroscopy in a micromachined flow cytometer: theoretical and practical considerations," Lab on a Chip, vol. 4, 241-251, (2004).

[8] Borkholder, D. A., "Cell Based Biosensors Using Microelectrodes," Ph.D. Thesis, Stanford University, 57-61, (1998).

[9] Holmes, D., Morgan, H., "Single cell impedance cytometry for identification and counting of CD4 T-cells in human blood using impedance labels," Analytical Chemistry, 82(4),1455-1461, (2010).

[10] Holmes, D., Pettigrew, D., Reccius, C.H., Gwyer, J.D, van Berkel, C., Holloway, J., Davies, D.E., Morgan, H., "Leukocyte analysis and differentiation using high speed microfluidic single cell impedance cytometry," Lab on a Chip vol. 9, 2881–2889, (2009).

[11] Valero, A., Braschler, T., Renaud, P., "A unified approach to dielectric single cell analysis: impedance and dielectrophoretic force spectroscopy," Lab on a Chip, vol.10, 2216-2225, (2010).

[12] Pliquett, U., "Bioimpedance: A Review for Food Processing," Food Engineering Reviews, Springer, 74–94, (2010).

[13] Annus, P., Min, M., Rist, M., Ojarand, J. and Land, R., "Current source considerations for broadband bioimpedance spectroscopy," Proc. International Workshop on Impedance Spectroscopy, Chemnitz, Germany, in press (2010).

[14] Baker, B.C., "Comparison of noise performance between a FET transimpedance amplifier and switched integrator," Burr-Brown Application Bulletin, Burr-Brown Corporation, (1993).

[15] Sobering, T.J., "Op Amp Noise Analysis, "Technote, Revised 11/19/02, SDE Consulting, (1999).

[16] Ojarand, J., Land, R., Parve, T., Annus, P., "Nonlinear Chirp Pulse Excitation for the Fast Impedance Spectroscopy," Electronics and Electrical Engineering, 4, Kaunas, 73 – 76, (2010).

[17] Paavle, T., Min, M., Ojarand, J., Parve, T., "Short-time chirp excitations for using in wideband characterization of objects: An overview," Electronics Conference (BEC), 12th Biennial Baltic, 253 – 256, (2010).

[18] Rees, D., Jones, D.L., "Design and application of non-binary low peak factor signals for system dynamic measurement," Int. Conference on Control, Edinburgh, UK, 1991, vol., 644 – 650, (1991).

[19] Yang, Y., Wang, J., Gao, Z., Li, D. and Wang, J. "Waveform synthesis of multi-frequency sinusoids with 2nth primary harmonics based on Walsh functions," Proc. IEEE Biomedical Circuits and Systems Conference, Bejing, China, 129–132, (2009).

CURRICULUM VITAE

Personal data

Name	Jaan Ojarand
Date and place of birth	24.11.1951, Tallinn, Estonia

Contact information

Address	Mäealuse 2/1, Tallinn 12618
Phone	(+372) 5024723
E-mail	jaan.ojarand@eliko.ee

Education

2008- ….	Ph.D. studies in Information and Communication Technology, Tallinn University of Technology
1974- 1980	Diploma engineer studies in automation and telecommunication in Tallinn Technical University
1967-1971	Radio technician studies at Tallinn Polytechnicum

Languages   Estonian, English, Russian

Professional Employment

2007-	ELIKO Competence Centre in Electronics-, Info- and Communication Technologies, researcher
1993-2007	Mikrotehnika PLC, technical director, chairman
1986-1993	Design Bureau of the Institute of Cybernetics (EKTA), research group leader
1983-1986	Design Bureau of the Institute of Cybernetics (EKTA), project manager

1978- 1983	Design Bureau of the Institute of Cybernetics (EKTA), design engineer

Defended theses

„Calibration System for initial verification of CM1800 analog sub-assemblies" Tallinn Technical University, 1980.

Honours & Awards

Estonian state award in science and technology, 1988.

Main areas of scientific work/Current research topics

Natural Sciences and Engineering.

Wideband excitation based characterization of substances.
Methods and technical solutions of measurement of impedance.

Other research projects

Low noise synchronization solutions in signal processing technology.
Research of the adaptively oversampled and modulated conversion and processing algorithms of signal.
Energy efficient electronic systems.

ELULOOKIRJELDUS

Isikuandmed

Ees- ja perekonnanimi	Jaan Ojarand
Sünniaeg ja -koht	24.11.1951, Tallinn
Kodakondsus	Eesti

Kontaktandmed

Aadress	Mäealuse 2/1, Tallinn 12618
Telefon	(+372) 5024723
E-posti aadress	jaan.ojarand@eliko.ee

Hariduskäik

2008- ….	Doktorantuur, Info-ja kommunikatsiooni-tehnoloogia, Tallinna Tehnikaülikool
1974- 1980	Tallinna Polütehniline Instituut, automaatika ja telemehaanika eriala
1967-1971	Tallinna Polütehnikum, keskeriharidus raadioaparatuuri tootmise eriala

Keelteoskus	Eesti, Inglise, Vene

Teenistuskäik

2007-	ELIKO Tehnoloogia Arenduskeskus OÜ, teadur
1993-2007	Mikrotehnika OÜ, tehnikadirektor, juhataja
1986-1993	TA Küberneetika Instituudi Erikonstrueerimisbüroo (EKTA), grupijuht
1983-1986	TA Küberneetika Instituudi Erikonstrueerimisbüroo (EKTA), juhtiv konstruktor

| 1978- 1983 | TA Küberneetika Instituudi Erikonstrueerimisbüroo (EKTA), insener-konstruktor |

Kaitstud lõputööd

„Mõõtekompleks CM-1800 analoogmoodulite lõppkontrolliks", Tallinna Polütehniline Instituut, 1980.

Teaduspreemiad ja -tunnustused

ENSV riiklik preemia teaduse ja tehnika alal, 1988.

Teadustöö põhisuunad /käesolevad uurimisteemad

Loodusteadused ja tehnika, info- ja kommunikatsioonitehnoloogia.
Ainete iseloomustamine lairiba ergutussignaalide abil.
Impedantsi mõõtmise meetodid ja tehnilised lahendused.

Teised uurimisprojektid

Väikese müraga sünkroniseerimisahelad signaalitöötluses.
Adaptiivselt ülevõendatud ja moduleeritud signaalide muundamise ja töötlemise algoritmide uurimine.
Energiasäästlikud elektroonikasüsteemid.

DISSERTATIONS DEFENDED AT
TALLINN UNIVERSITY OF TECHNOLOGY ON
INFORMATICS AND SYSTEM ENGINEERING

1. **Lea Elmik**. Informational Modelling of a Communication Office. 1992.

2. **Kalle Tammemäe**. Control Intensive Digital System Synthesis. 1997.

3. **Eerik Lossmann**. Complex Signal Classification Algorithms, Based on the Third-Order Statistical Models. 1999.

4. **Kaido Kikkas**. Using the Internet in Rehabilitation of People with Mobility Impairments – Case Studies and Views from Estonia. 1999.

5. **Nazmun Nahar**. Global Electronic Commerce Process: Business-to-Business. 1999.

6. **Jevgeni Riipulk**. Microwave Radiometry for Medical Applications. 2000.

7. **Alar Kuusik**. Compact Smart Home Systems: Design and Verification of Cost Effective Hardware Solutions. 2001.

8. **Jaan Raik**. Hierarchical Test Generation for Digital Circuits Represented by Decision Diagrams. 2001.

9. **Andri Riid**. Transparent Fuzzy Systems: Model and Control. 2002.

10. **Marina Brik**. Investigation and Development of Test Generation Methods for Control Part of Digital Systems. 2002.

11. **Raul Land**. Synchronous Approximation and Processing of Sampled Data Signals. 2002.

12. **Ants Ronk**. An Extended Block-Adaptive Fourier Analyser for Analysis and Reproduction of Periodic Components of Band-Limited Discrete-Time Signals. 2002.

13. **Toivo Paavle**. System Level Modeling of the Phase Locked Loops: Behavioral Analysis and Parameterization. 2003.

14. **Irina Astrova**. On Integration of Object-Oriented Applications with Relational Databases. 2003.

15. **Kuldar Taveter**. A Multi-Perspective Methodology for Agent-Oriented Business Modelling and Simulation. 2004.

16. **Taivo Kangilaski**. Eesti Energia käiduhaldussüsteem. 2004.

17. **Artur Jutman**. Selected Issues of Modeling, Verification and Testing of Digital Systems. 2004.

18. **Ander Tenno**. Simulation and Estimation of Electro-Chemical Processes in Maintenance-Free Batteries with Fixed Electrolyte. 2004.

19. **Oleg Korolkov**. Formation of Diffusion Welded Al Contacts to Semiconductor Silicon. 2004.

20. **Risto Vaarandi**. Tools and Techniques for Event Log Analysis. 2005.

21. **Marko Koort**. Transmitter Power Control in Wireless Communication Systems. 2005.

22. **Raul Savimaa**. Modelling Emergent Behaviour of Organizations. Time-Aware, UML and Agent Based Approach. 2005.

23. **Raido Kurel**. Investigation of Electrical Characteristics of SiC Based Complementary JBS Structures. 2005.

24. **Rainer Taniloo**. Ökonoomsete negatiivse diferentsiaaltakistusega astmete ja elementide disainimine ja optimeerimine. 2005.

25. **Pauli Lallo.** Adaptive Secure Data Transmission Method for OSI Level I. 2005.

26. **Deniss Kumlander**. Some Practical Algorithms to Solve the Maximum Clique Problem. 2005.

27. **Tarmo Veskioja**. Stable Marriage Problem and College Admission. 2005.

28. **Elena Fomina**. Low Power Finite State Machine Synthesis. 2005.

29. **Eero Ivask**. Digital Test in WEB-Based Environment 2006.

30. **Виктор Войтович**. Разработка технологий выращивания из жидкой фазы эпитаксиальных структур арсенида галлия с высоковольтным p-n переходом и изготовления диодов на их основе. 2006.

31. **Tanel Alumäe**. Methods for Estonian Large Vocabulary Speech Recognition. 2006.

32. **Erki Eessaar**. Relational and Object-Relational Database Management Systems as Platforms for Managing Softwareengineering Artefacts. 2006.

33. **Rauno Gordon**. Modelling of Cardiac Dynamics and Intracardiac Bio-impedance. 2007.

34. **Madis Listak**. A Task-Oriented Design of a Biologically Inspired Underwater Robot. 2007.

35. **Elmet Orasson**. Hybrid Built-in Self-Test. Methods and Tools for Analysis and Optimization of BIST. 2007.

36. **Eduard Petlenkov**. Neural Networks Based Identification and Control of Nonlinear Systems: ANARX Model Based Approach. 2007.

37. **Toomas Kirt**. Concept Formation in Exploratory Data Analysis: Case Studies of Linguistic and Banking Data. 2007.

38. **Juhan-Peep Ernits**. Two State Space Reduction Techniques for Explicit State Model Checking. 2007.

39. **Innar Liiv**. Pattern Discovery Using Seriation and Matrix Reordering: A Unified View, Extensions and an Application to Inventory Management. 2008.

40. **Andrei Pokatilov**. Development of National Standard for Voltage Unit Based on Solid-State References. 2008.

41. **Karin Lindroos**. Mapping Social Structures by Formal Non-Linear Information Processing Methods: Case Studies of Estonian Islands Environments. 2008.

42. **Maksim Jenihhin**. Simulation-Based Hardware Verification with High-Level Decision Diagrams. 2008.

43. **Ando Saabas**. Logics for Low-Level Code and Proof-Preserving Program Transformations. 2008.

44. **Ilja Tšahhirov**. Security Protocols Analysis in the Computational Model – Dependency Flow Graphs-Based Approach. 2008.

45. **Toomas Ruuben**. Wideband Digital Beamforming in Sonar Systems. 2009.

46. **Sergei Devadze**. Fault Simulation of Digital Systems. 2009.

47. **Andrei Krivošei**. Model Based Method for Adaptive Decomposition of the Thoracic Bio-Impedance Variations into Cardiac and Respiratory Components. 2009.

48. **Vineeth Govind**. DfT-Based External Test and Diagnosis of Mesh-like Networks on Chips. 2009.

49. **Andres Kull**. Model-Based Testing of Reactive Systems. 2009.

50. **Ants Torim**. Formal Concepts in the Theory of Monotone Systems. 2009.

51. **Erika Matsak**. Discovering Logical Constructs from Estonian Children Language. 2009.

52. **Paul Annus**. Multichannel Bioimpedance Spectroscopy: Instrumentation Methods and Design Principles. 2009.

53. **Maris Tõnso**. Computer Algebra Tools for Modelling, Analysis and Synthesis for Nonlinear Control Systems. 2010.

54. **Aivo Jürgenson**. Efficient Semantics of Parallel and Serial Models of Attack Trees. 2010.

55. **Erkki Joasoon**. The Tactile Feedback Device for Multi-Touch User Interfaces. 2010.

56. **Jürgo-Sören Preden**. Enhancing Situation – Awareness Cognition and Reasoning of Ad-Hoc Network Agents. 2010.

57. **Pavel Grigorenko**. Higher-Order Attribute Semantics of Flat Languages. 2010.

58. **Anna Rannaste**. Hierarcical Test Pattern Generation and Untestability Identification Techniques for Synchronous Sequential Circuits. 2010.

59. **Sergei Strik**. Battery Charging and Full-Featured Battery Charger Integrated Circuit for Portable Applications. 2011.

60. **Rain Ottis**. A Systematic Approach to Offensive Volunteer Cyber Militia. 2011.

61. **Natalja Sleptšuk**. Investigation of the Intermediate Layer in the Metal-Silicon Carbide Contact Obtained by Diffusion Welding. 2011.

62. **Martin Jaanus**. The Interactive Learning Environment for Mobile Laboratories. 2011.

63. **Argo Kasemaa**. Analog Front End Components for Bio-Impedance Measurement: Current Source Design and Implementation. 2011.

64. **Kenneth Geers**. Strategic Cyber Security: Evaluating Nation-State Cyber Attack Mitigation Strategies. 2011.

65. **Riina Maigre**. Composition of Web Services on Large Service Models. 2011.

66. **Helena Kruus**. Optimization of Built-in Self-Test in Digital Systems. 2011.

67. **Gunnar Piho**. Archetypes Based Techniques for Development of Domains, Requirements and Sofware. 2011.

68. **Juri Gavšin**. Intrinsic Robot Safety Through Reversibility of Actions. 2011.

69. **Dmitri Mihhailov**. Hardware Implementation of Recursive Sorting Algorithms Using Tree-like Structures and HFSM Models. 2012.

70. **Anton Tšertov**. System Modeling for Processor-Centric Test Automation. 2012.

71. **Sergei Kostin**. Self-Diagnosis in Digital Systems. 2012.

72. **Mihkel Tagel**. System-Level Design of Timing-Sensitive Network-on-Chip Based Dependable Systems. 2012.

73. **Juri Belikov**. Polynomial Methods for Nonlinear Control Systems. 2012.

74. **Kristina Vassiljeva**. Restricted Connectivity Neural Networks based Identification for Control. 2012.

75. **Tarmo Robal**. Towards Adaptive Web – Analysing and Recommending Web Users` Behaviour. 2012.

76. **Anton Karputkin**. Formal Verification and Error Correction on High-Level Decision Diagrams. 2012.

77. **Vadim Kimlaychuk**. Simulations in Multi-Agent Communication System. 2012.

78. **Taavi Viilukas**. Constraints Solving Based Hierarchical Test Generation for Synchronous Sequential Circuits. 2012.

79. **Marko Kääramees**. A Symbolic Approach to Model-based Online Testing. 2012.

80. **Enar Reilent**. Whiteboard Architecture for the Multi-agent Sensor Systems. 2012.